POLITECNICO DI MILANO
DEPARTMENT OF AEROSPACE SCIENCE AND TECHNOLOGY
DOCTORAL PROGRAMME IN AEROSPACE ENGINEERING

NON-KEPLERIAN MODELS FOR MISSION ANALYSIS SCENARIOS ABOUT SMALL SOLAR SYSTEM BODIES

Doctoral Dissertation of:
Fabio Ferrari

Supervisor:
Prof. Michèle Lavagna

Tutor:
Prof. Franco Bernelli

The Chair of the Doctoral Program:
Prof. Luigi Vigevano

Year 2016 – XXIX Cycle

Dedicato alla persona che, più di tutte, avrebbe apprezzato, indagato e discusso il significato di ogni singola parola, virgola, equazione.
Dedicato a te, papà.

Acknowledgements

Here comes the hardest part of writing a thesis. So many people to acknowledge and just a few of them to be selected here.

The first mention goes to my advisor and mentor Prof. Michèle Lavagna. I am extremely thankful to her for believing in me and for entrusting me with countless opportunities. I thank her for charging me with responsibilities, some of which were very exceptional for a researcher in its early career. She is a passionate teacher and tireless worker and I must thank her for any academic and working achievement I might have reached. I hope we will continue to work together in such a fruitful manner.

I thank my PhD-mates Paolo and Riccardo and all the research group at PoliMi for walking (and running) through this PhD journey together. I owe thanks to all academic researchers to whom I collaborated with during these years, inside and outside PoliMi. Special thanks go to Dr. Ian Carnelli and to the whole Asteroid Impact Mission team for the great work done together on this fascinating space mission.

I would like to thank Dr. Rüdiger Jehn and Dr. Paolo Tanga for their invaluable work as reviewer of this thesis. Their comments and advices were very inspirational and improved a lot the quality of the text, its readability and the clarity of the technical content.

I must thank my other half of the apple (the better one!) Elisabetta, my mom Lucia, my brother Vincenzo. Without their unconditional support and encouragement through good times and bad, I would have never reached the end of this work. A special thank to my dad, Dino, to whom this work is dedicated.

Many others deserve my gratitude and can not be acknowledged here. This is a special thank you to all of them.

Fabio

Abstract

THE thesis work focuses on the implementation of non-Keplerian models and their applications to space mission analysis scenarios. Non-Keplerian dynamics are used to accurately reproduce the gravity field around small Solar System bodies such as asteroids or comets and to conveniently exploit their gravitational environment for trajectory design purpose. Compared to Earth or other planets in the Solar System, small celestial bodies are characterized by very weak and irregular gravity field. This turns into a highly challenging mission analysis to be solved when designing a space mission. The mass distribution of such bodies is modeled by means of either mass-concentrated or shape-based models. Mass-concentrated models have the significant advantage to require less computational effort and also, they naturally simulate the effect of having a non-uniform density distribution and the presence of voids in the internal structure of the celestial body. The mass-concentrated model is obtained here by means of asteroid N-body gravitational aggregation. Shape-based models can reproduce to higher fidelity the gravity field around homogeneous small bodies, given their shape and density distribution, at the cost of a higher computational effort required, compared to mass-concentrated models. Relevant solutions, of interest for space mission scenarios aimed at the exploration of asteroids or comets, are found by using nonlinear system dynamics techniques applied to non-Keplerian astrodynamics problems. Such solutions include periodic motion and invariant manifolds associated to equilibrium or periodic solutions in the proximity of such bodies. Mission analysis scenarios are studied for the case of exploration of binary

asteroid systems. Investigated scenarios include landing about a binary asteroid with a two-lobed elongated primary, designed through a patched three-body approach. Close-proximity operations in the context of the Asteroid Impact Mission (AIM) are investigated and suitable solutions are presented to land a probe on the smaller asteroid of a binary couple. The last scenario studies formation flying dynamics in the proximity of libration point orbits associated to a binary system.

Table of Contents

List of Figures

List of Tables

"and everything under the sun is in tune
but the sun is eclipsed by the moon.
– There is no dark side of the moon really.
Matter of fact it's all dark. –"

Waters, *Eclipse*

CHAPTER 1

Introduction

Non-Keplerian gravity models are the present and future frontier of astrodynamics. They provide unique opportunities for mission analysis and open to a great variety of design solutions not available whenever a single point-mass gravity source is dealt with. From the space mission design point of view, the modeling of the gravitational environment through the use of multiple or non-spherical gravity sources can be effectively exploited to design convenient orbital paths, to meet challenging requirements due to on-board payloads, to decrease the cost of manoeuvres to be provided by the spacecraft. The use of non-Keplerian dynamics to fly space missions was largely studied in the second half of the 20th century and found interesting applications since the launch of the International Sun/Earth Explorer 3 (ISEE-3) in 1978. ISEE-3 was the first spacecraft placed into a Halo orbit around the L1 Lagrangian point of the Sun-Earth system (SE-L1) and the first spacecraft whose mission analysis was designed using a three-body strategy [35]. The Sun-Earth L1 point is located between the Earth and the Sun and moves with the same angular velocity of Earth and Sun as they revolve around the barycentre of their system. For this reason, the L1 point was the ideal location to place ISEE-3 to study the solar wind approaching the Earth. After ISEE-3, other missions were designed to target three-body trajecto-

ries: missions to SE-L1 served mainly for Sun observation, while SE-L2 (located behind the Earth, along the Sun-Earth line) for deep space observation. Other missions such as Hiten (1990) [133] were used as demonstrator for low-cost transfers in the Earth-Moon system using three-body dynamics.

In the last few decades the space community has put a lot of effort into the exploration of small Solar System bodies, such as asteroids and comets. Motivated by a great scientific interest, the exploration of small celestial bodies represents the current and future frontier to extend the mankind's knowledge on how our Solar System was formed and how it evolves. In addition, small bodies represent an ideal place for technology demonstration missions as they can serve as a test bench for deep-space In-Orbit-Demonstration (IOD) experiments. Due to their peculiar properties, small celestial bodies provide the unique opportunity of having a natural low-gravity environment that can be used to study gravitational dynamics and for many technological-related applications.

This thesis is focused towards studying and deepening the knowledge of non-Keplerian dynamics to provide useful insights to support mission analysis and spacecraft design. More in detail, non-Keplerian systems are used to model the dynamics in the proximity of a small Solar System body. Since the work aims at space design applications, *restricted* models are considered to be representative of the dynamics of a spacecraft. Such models focus on the dynamics of a body (spacecraft), which moves under the gravitational attraction of massive bodies, without influencing their motion. This is true for bodies (spacecraft) whose mass is negligible with respect to the mass of gravity sources (celestial bodies) and it is a common working assumption in the field of astrodynamics and spacecraft design.

1.1 Small bodies and non-Keplerian dynamics

Small Solar System bodies such as asteroids and comet nuclei are known to possess very irregular mass distribution and, consequently, a very irregular gravity field. Also, such bodies have a very weak gravity field, compared to that of more massive objects as Sun, planets and their major natural satellites. Recently, the European Rosetta mission [131] showed how challenging comet landing can be. In 2014 Rosetta landed the Philae lander on the surface of comet 67P/Churyumov-Gerasimenko [125], an extremely irregular body whose shape and mass distribution were completely unknown during the design phase of the mission. The comet's gravity field was too weak to keep the lander on the surface after touch down and did not pre-

vent it from bouncing a couple of times before coming to a rest. From the dynamics point of view, irregular field means highly chaotic motion, with dynamics extremely sensitive to initial conditions. From the spacecraft design point of view, this means that a very small deviation in the state, which can be due e.g. to navigation or manoeuvre errors, can result in a very large discrepancy in the subsequent motion. This is very relevant for the case of close-proximity operations and for example when collision avoidance or soft-landing constraints are to be considered. In such case the chaotic nature of the environment can lead to real world trajectories that does not satisfy the constraints (colliding or not landing on the asteroid), even when they are fulfilled by the nominal trajectory. For these reasons, the effective design of trajectories to fly a spacecraft in the proximity of an asteroid requires the knowledge of the physical, inertial and dynamical properties of the target body. Due to their non-spherical mass distribution, a simple Keplerian model is not suitable to accurately represent the dynamics around small bodies. In some cases, when the mass distribution is very far from being spherical, the Keplerian model can lead to very inaccurate results, which are not acceptable for mission analysis design applications. This motivates the use of non-Keplerian dynamics to model the environment in the close proximity of such objects.

A recent example of a mission that makes use of non-Keplerian dynamics is the Asteroid Impact Mission (AIM), the European contribution to the Asteroid Impact and Deflection Assessment (AIDA), a joint mission between the European Space Agency (ESA) and the National Aeronautics and Space Administration (NASA) aimed to rendezvous with binary asteroid (65803) Didymos. AIM, whose launch is planned in 2020, is currently under study and foresees the use of manifold dynamics associated to the three-body system of Didymos binary asteroid to safely land a probe on the smaller asteroid of the couple [42, 44]. More in detail, the dynamics of the probe in the proximity of the binary asteroid are studied using a three-body model with non-spherical gravity sources: since the mass distribution of the asteroids is expected to be very irregular, shape-based models are used to model the two asteroids.

1.2 Historical review

The history of non-Keplerian dynamics started in the 17th century, with first studies by Newton on the Three-Body Problem (3BP) published in its *Philosophiæ Naturalis Principia Mathematica*, also known as *Principia* (1687). Newton studied the motion of the Moon around the Earth and in-

troduced the effects of the Sun (third body) in the attempt of correcting the error of the two-body model prediction. In the following centuries, a lot of mathematicians contributed to the understanding of the 3BP and its reductions, as one of the most interesting and challenging problems in dynamics. About a hundred years later, in 1772, Lagrange showed in his *Essai sur le Problème des Trois Corps* the existence of analytical solutions in the general 3BP when the three bodies are constrained to remain in an equilateral triangle or collinear formation [118]. In the same year, Euler formulated for the first time the Restricted Three-Body Problem (R3BP) and introduced the synodic (rotating) reference frame. Being a *restricted* problem, the R3BP studies the motion of a particle, moving under the gravitational attraction of two massive bodies, called primaries, without influencing their motion. Euler identified the three collinear libration points associated to the rotating problem and, after him, Lagrange identified the two equilateral ones. In 1836 Jacobi discovered the integral of motion associated to the problem formulated by Euler. Then, in 1878, Hill was the first to give a physical meaning to the Jacobian integral, by introducing the concept of Zero Velocity Curves (ZVC) and showing how the energy of the particle constrains and bounds its motion within the three-body system. After such early analytical studies, once the mathematical formulation of the R3BP was clearly established, the focus of researchers moved to the investigations of the solutions associated to such problem. The ground breaking contribution, which opened to the era of studies on solutions in such systems, came from Poincaré. In his work *Les Méthodes Nouvelles de la Mécanique Céleste* [108], Poincaré proved that the Jacobian integral is the only integral of motion and an infinite number of periodic solutions exist in the R3BP. The knowledge of periodic motion is very important to understanding the dynamics of a complex dynamical environment such as the one generated by multiple gravitational sources. Poincaré identified periodic solutions as the only way the inaccessible problem of the three bodies can be made accessible and fully understood. Poincaré's work motivated mathematicians towards analytical and numerical investigations of periodic orbits in the R3BP. The search for periodic solutions in complex non-Keplerian systems represents one of the most promising and challenging problems in modern astrodynamics. The most popular problems investigated was (and so are nowadays) the Circular Restricted Three-Body Problem (CR3BP) and the Elliptic Restricted Three-Body Problem (ER3BP). In the CR3BP the primaries moves on circular paths around the barycentre of the system, while the ER3BP represents a generalization of CR3BP for the case of elliptical orbits of primaries. These problems gained popularity due to the fact that

they are able to represent with a higher accuracy with respect to the simple Keplerian model the motion of observable celestial bodies (e.g. the motion of the Moon in the Sun-Earth system). The most relevant results obtained in the first half of the 20th century in terms of periodic motion in R3BP are well summarized by Moulton [97] and Szebehely [128].

The advent of numerical computing in the latter part of the 20th century has provided a great boost to the study and analysis of such a complex dynamical system. A great milestone in the history of R3BP was related to the discovery of periodic motions in the proximity of collinear libration points, by Farquhar [34]. Periodic motion near Lagrangian points represented a step forward into the space mission design era: it opened to a new variety of solutions, able to meet new space mission objectives and to promote new ideas for future mission opportunities. Also, from the dynamical investigations point of view, Farquhar's work on three-dimensional periodic solutions about libration points in the Earth-Moon three-body system started a new era. Farquhar found three-dimensional periodic orbits in the proximity of libration points and named them 'Halo' orbits. More comprehensive works came from Farquhar and Kamel [36], Breakwell and Brown [13], Howell and Breakwell [74] and Howell [73], who extended the computation of a single orbit to a family of Halo orbits and to different values of mass ratio of the primaries. The contribution due to Howell [72], who applied the method of differential corrections to find periodic motion in the CR3BP, is of great importance to the development of numerical algorithms to exactly compute periodic orbits. After them a lot of researchers, after numerical investigations, revealed the existence of many different kind of families of periodic orbits, both around libration points and primaries, computed in the frame of the CR3BP. Among them, relevant contributions to periodic motion in the CR3BP include the work by Richardson [114], who developed an analytical method to find initial guesses for periodic solutions and the work by Goudas [61] and Hénon [68] who published studies on the restricted three-body problem. Peculiar solutions such as orbits in resonance with motion of the primaries are also of great interest [2, 135], since these solutions are periodic not only in the synodic (rotating) frame of the three-body system, but also in the inertial frame. Finally, the work by Guzzetti et al. [52, 66] includes a comprehensive survey of orbit families in the Earth-Moon system and their properties. In general, classical methods of nonlinear dynamics analysis, applied to astrodynamics problems are implemented to find peculiar solutions in non-Keplerian systems. As mentioned, a lot of examples exist in the literature: a collection of these methods can be found in the work by Schaub and Junkins [118], Koon et

al. [82] and Parker and Anderson [105].

A further step into the analysis of realistic models of the dynamics is represented by the ER3BP. The ER3BP is a better approximation, compared to the CR3BP, of the dynamics of a particle in the proximity of two attractors, whose two-body motion is not circular. The non-zero eccentricity of the orbits of primaries is the most notable perturbation leading the orbit not to be periodic [105]. Compared to the widely studied CR3BP, periodic motion in the ER3BP remains still to be largely explored. Different kinds of orbits were targeted in the past, with the main focus either on systematic analysis of the elliptical problem (e, μ) space dependency [15, 79, 86, 99, 117] or on finding multi-revolution orbits about collinear libration points [17, 87, 106, 107]. Relevant studies on periodic motion under ER3BP include also the work by Gurfil and Kasdin [63] and Palacian et al. [104].

Small Solar System bodies

It is a long time since mankind discovered the existence of celestial bodies other than planets and their satellites in our Solar System. Due to their observability with the naked eye, comets were known since the ancient times in history. The first asteroid known was Ceres, discovered by Giuseppe Piazzi in 1801, from the Astronomical Observatory of Palermo. For a long time, remote observation from ground was the only way to study asteroids and comets and still today the largest amount of data available relies upon remote surveys. Optical observations plays a fundamental role to the detection and discovery of new bodies and to estimate their physical properties. Some information can be extracted from magnitude and light curve (fluctuation in the reflected light) data. Optical observations are very useful to detect binary systems and are used to estimate the size, shape and spin state of the object. Also, information on the surface temperature and composition can be extracted by studying the spectrum of the body. In addition to optical survey, a powerful technique for remote observation of asteroids and comets is radar observation. This technique allows for a precise determination of the object's orbit and for a very precise reconstruction of its shape and spin state through radio telescopes observation. A complete survey of techniques and results achieved through remote sensing is reported in the books [12, 57, 89, 93].

The *in situ* exploration of small Solar System bodies began in 1986, when an international cooperation between ESA, the Japanese Institute of Space and Astronautical Science (ISAS) and the Soviet Union's space agency (in a joint cooperation with France) launched five probes, the so

called Halley Armada, towards comet 1P/Halley. The closest flyby performed by the European Giotto spacecraft at a distance of 596 km from the comet nucleus provided the first close-up colour images of the nucleus of a comet and of a small Solar System body. The first high-resolution images of asteroids came from NASA's Galileo spacecraft, which performed flybys near asteroids (951) Gaspra in 1991 and (243) Ida in 1993. Galileo was also the first to image a binary asteroid system, after the discovery of Dactyl, the small moon of asteroid Ida. After that, NASA's Near Earth Asteroid Rendezvous (NEAR-Shoemaker) mission flew past asteroid (253) Mathilde in 1997 and successfully performed rendezvous with asteroid (433) Eros in 2000. This was the first close rendezvous with an asteroid and, after remaining on a bounded orbit around Eros for approximately one year, NEAR-Shoemaker achieved the first soft-landing on an asteroid surface in 2001. In the same year, NASA's Deep Space 1 performed a flyby of comet 19P/Borrely, after having flown by asteroid (9969) Braille in 1999. NASA's Stardust mission performed a flyby of asteroid (5535) Annefrank in 2002 and then flew past comet 81P/Wild in 2004. Stardust was able to collect a sample of comet dust and return it to Earth on 2006. The first sample-return mission from an asteroid is the Hayabusa mission by the Japan Aerospace eXploration Agency (JAXA), which successfully performed a rendezvous with asteroid (25143) Itokawa in 2005. Hayabusa collected a small sample of asteroidal surface after touch down and returned it back to Earth in 2010. In 2005 NASA's Deep Impact reached comet 9P/Tempel and released an impactor on the nucleus. The effects of the impact were observed in a subsequent flyby performed by the Stardust spacecraft. Afterwards, the Deep Impact spacecraft performed a flyby of comet 103P/Hartley in 2010. NASA's DAWN mission performed rendezvous with asteroids (4) Vesta in 2011 and (1) Ceres in 2015. To date, the latest mission reaching a small body is ESA's Rosetta mission. Launched in 2004, Rosetta performed the first rendezvous ever achieved with a comet, when reaching comet 67P/Churyumov-Gerasimenko after a ten-years trip, in 2014. On its way to the comet, Rosetta flew past asteroids (2867) Šteins in 2008 and (21) Lutetia in 2010. After rendezvous with the comet, Rosetta remained approximately two years on bounded orbit around it and released the first cometary lander (Philae) on the comet's surface in 2014. Currently, two sample-return missions are heading towards asteroids. The Japanese Hayabusa 2 was launched in 2014 and is on its path to asteroid (162173) Ryugu (formerly designated 1999 JU_3), where it will release a lander, the Mobile Asteroid Surface SCOuT (MASCOT), after rendezvous in 2018. A sample of asteroidal surface will be then returned back to Earth in 2020. The sec-

ond ongoing mission is NASA's OSIRIS-REx mission, launched in 2016. It will rendezvous with asteroid (101955) Bennu (formerly 1999 RQ_{36}) in 2018 and return a sample back to Earth in 2023. Studies for future mission opportunities include the AIDA mission, aimed at the exploration and deflection assessment of binary asteroid (65803) Didymos. AIDA is a joint cooperation between ESA, which contributes with AIM and NASA, which contributes with the Double Asteroid Redirection Test (DART). The mission is currently under study and planned to be launched in 2020, in order to rendezvous (AIM) and impact (DART) with Didymos binary in 2022 [1].

Nowadays, due to the large accessibility of the Near Earth Asteroid (NEA) population to spacecraft, such bodies represent the current frontier of space exploration. For this reason, the study of non-Keplerian dynamics has extended to the modeling of gravity field produced by such celestial bodies. Few strategies are usually adopted to model the gravity field about asteroids. Classic methods consider harmonic expansion of gravitational potential [80] to model the irregularities of a simple Keplerian field. Shape-based methods are used to model the asteroid as objects with specific shapes, such as homogeneous ellipsoids [119] or polyhedra [123, 137]: in this case their distribution of mass is not spherical and the gravity field in its proximity is computed accordingly. Other methods use a number of masses (mascon models) to reproduce the mass distribution of the body. The mascon method was first developed to explain the anomalies of the Moon's gravity field [98]. The inclusion of concentrations of mass in the nearly spherical mass distribution of the Moon helped in the development of a highly accurate lunar gravity model. A similar technique is used to reproduce the gravity field of asteroids [25, 50, 58]. The applicability of each method depends on the information available on the body's mass distribution and on the level of accuracy required by the application. Typically, each model fits a specific class of asteroids and application range. In general, the determination of mass and bulk density of small body is a very difficult task [71] and very little is known about their internal mass distribution.

1.3 Dissertation overview

Despite the large number of studies on the topic, the full comprehension of the general dynamics in non-Keplerian systems is still far to be reached. Few studies exist concerning general properties of such systems. Com-

[1] At the time of writing this thesis, AIM design underwent phase A and B1. Phase B2 and subsequent ones are currently awaiting for ESA ministry assembly approval.

pared to the vast literature on the topic, this thesis aims at deepening and harmonizing existing knowledge on non-Keplerian dynamics and their applications to mission analysis scenarios to small celestial bodies. After this introductory chapter, the work is presented as follows.

Chapter 2 deals with the background knowledge and recalls mathematical formulations of non-Keplerian dynamical models under study. The formulation of Circular and Elliptic Restricted Three-Body Problem is recalled and the major properties of such models are discussed. Restricted and unrestricted N-Body problems are also recalled, with emphasis on applications of such problems studied in this work. The problem of reproducing the mass distribution of non-spherical objects is discussed and techniques related to shape-based models are recalled, together with N-body mascon formulation. Finally, the formulation used to model the main perturbing effect related to the asteroidal environment (solar radiation pressure) is recalled.

Chapter 3 describes the implementation of numerical methods in use to find solutions of the dynamics relevant to the mission analysis scenarios under study. First, a general-purpose method for targeting trajectories and solutions within non-Keplerian models is described. The general software architecture in terms of functional structure is presented, together with the lower level details concerning the description of methods implemented in each functional block. The applicability of such method is discussed for the dynamical cases under study. An example of implementation of such general-purpose method is shown for the case of periodic orbit investigation. Applications related to periodic motion in the CR3BP, ER3BP and small body dynamics are detailed. Finally, the numerical implementation of N-body gravitational dynamics method, developed to support aggregation dynamics simulation, is presented.

A survey of solutions relevant to mission analysis scenarios under study is presented in Chapter 4. The existence and properties of periodic motion is discussed for the case of CR3BP, ER3BP and small body dynamics. New libration point periodic solutions, sorted by number of revolutions around equilibrium point, are shown for the ER3BP case. Results from the asteroid aggregation scenario are also shown for the case of small/medium sized asteroid aggregation.

Chapter 5 reports the discussion of three mission analysis scenarios under study, related to space missions to binary asteroid systems. The first concerns a space mission to explore a binary asteroid with a two-lobed primary. The applicability of such model within the Solar System asteroidal population is discussed. The relative dynamics and kinematics between asteroids is studied and trajectory design within the binary system is per-

formed by means of a patched three-body approach. The concept of Surface Of Equivalence (SOE) is introduced to deal with the patched problem and a design strategy to land a probe on the primary asteroid is discussed. The second mission analysis scenario under study reproduces the AIM scenario. This is related to the design of a ballistic landing of a small and passive probe on the secondary of Didymos binary. The dynamical model in use is described and its validity discussed. The strategy to land the probe is discussed and motivated. Landing results are reported for the realistic mission analysis case, including the study of robustness of chosen solution. The last case study is a formation flying scenario. Three spacecraft are considered at the vertexes of an equilateral triangle, flying around libration point orbits associated to three-body dynamics of binary systems. The study identifies orientations of the formation suitable to satisfy natural formation keeping properties. Formation keeping performance is quantified by means of performance factors and results are found by means of combined Monte Carlo and global optimization analyses and subsequently interpreted according to monodromy matrix analysis. As for the relative motion between primaries in the binary system, both CR3BP and ER3BP are studied.

Concluding remarks and future work opportunities are eventually discussed in Chapter 6.

CHAPTER 2

Non-Keplerian Dynamical Models

This chapter deals with the background knowledge needed to approach the topics presented in this thesis. The mathematical formulation of non-Keplerian dynamical models in use is presented and the properties of each system are discussed when relevant to the case of spacecraft trajectory design.

The most relevant Non-Keplerian models for space mission applications include Circular and Elliptic Restricted Three-Body Problems, whose formulations are recalled in Section 2.1. Section 2.2 discusses applications of the N-Body Problem (NBP), both in terms of restricted problem, with a high fidelity model of the Solar System built by using a high number of gravity sources, and in terms of unrestricted problem, whose application in used for simulating asteroid aggregation processes. The latter problem is deepened in Section 2.3, where strategies to model the gravity field produced by small celestial bodies such as asteroids and comets are discussed. The mathematical modeling of the perturbing effect the Solar Radiation Pressure (SRP) has on the orbital motion of a spacecraft is eventually recalled in Section 2.4.

2.1 The Restricted Three-Body Problem

The general or Unrestricted Three-Body Problem (also referenced as 3BP) studies the mutual gravitational interaction between three point-mass bodies. Space mission applications require the study of the motion of a spacecraft under the gravitational attraction of celestial bodies of the Solar System, such as Sun, planets or asteroids. In such case, the unrestricted problem can be simplified into a *restricted* problem. The Restricted Three-Body Problem (R3BP) studies the motion of a small body (also referenced as third body), which moves under the gravitational attraction of two massive bodies, called primaries. The dynamics of the primaries are not influenced by the presence of the third body. Such model is valid when the mass of the third body (m) is negligible compared to that of the primaries (M_1, M_2)

$$m \ll M_1, M_2 \tag{2.1}$$

Primaries are also referenced as P_1 and P_2 in the following, which refer to M_1 and M_2 respectively and with $M_1 > M_2$. Since the primaries are influenced by their mutual attraction only, they follow a two-body solution and their relative motion is a conic section. More in detail, bounded relative motion between primaries is considered for astrodynamics applications, meaning circular or elliptical paths around the barycentre of the system. Depending on the motion of the primaries, the dynamical model is referenced either as CR3BP or as ER3BP. The different relative motion between the primaries strongly influences the dynamical properties of the system. Mathematical formulations of CR3BP and ER3BP are recalled in sections 2.1.1 and 2.1.2.

2.1.1 The Circular Restricted Three-Body Problem

The main features and mathematical formulation of the CR3BP, with notation in use throughout this thesis, are recalled here. The classical formulation of the Restricted Three-Body Problem considers three bodies as point masses and studies the motion of the third body (m), which moves under the gravitational attraction of the primaries P_1, P_2, without influencing their motion (restricted problem). In the Circular Restricted Three-Body Problem, the two primaries are constrained to move on circular orbits around the centre of mass of their two-body system.

Equations of motion in the inertial frame

Consider the inertial frame (X,Y,Z) centred in the barycentre of the system, with primaries moving on the (X,Y) plane and Z parallel to the specific an-

gular momentum vector associated to their two-body motion. The equation of motion of the third body reads as

$$\ddot{\boldsymbol{R}} = \frac{GM_1}{\|\boldsymbol{R}_1\|^3}\boldsymbol{R}_1 + \frac{GM_2}{\|\boldsymbol{R}_2\|^3}\boldsymbol{R}_2 \tag{2.2}$$

where G denotes the universal gravitational constant. $\boldsymbol{R}$ is the position vector of the third body with respect to the barycentre of the system in the inertial reference frame. $\boldsymbol{R}_1$ and $\boldsymbol{R}_2$ are the relative distances between the third body and, respectively P_1 and P_2:

$$\boldsymbol{R}_1 = \boldsymbol{R}_{P_1} - \boldsymbol{R} \tag{2.3a}$$

$$\boldsymbol{R}_2 = \boldsymbol{R}_{P_2} - \boldsymbol{R} \tag{2.3b}$$

$\dot{\boldsymbol{R}}$ and $\ddot{\boldsymbol{R}}$ indicate respectively the first and second derivative of $\boldsymbol{R}$ with respect to time.

Equations of motion in the rotating frame

As mentioned, the position of the primaries is solution of their two-body interaction and it does not depend on $\boldsymbol{R}$. Accordingly, $\boldsymbol{R}_{P_1}$ and $\boldsymbol{R}_{P_2}$ are known functions of time. Being on circular orbits, they move with the same angular velocity ω around the barycentre of their two-body system, with $\boldsymbol{\omega}$ directed as the Z axis. In such case it is possible to write the equation of motion of the third body with respect to a specific frame, in order to eliminate its explicit dependence on time. This can be done by using a reference frame that is centred in the barycentre of the two primaries and rotates together with them with the same angular velocity $\boldsymbol{\omega}$. This frame is referenced as *rotating* or *synodic* (x, y, z) frame in the following. The position of the primaries is fixed in this rotating frame, which is chosen such to have both primaries lying on its x axis, as shown in Figure 2.1. More in detail, P_1 is located on the negative x axis, while P_2 is on the positive x axis.

In order to write Eq. (2.2) in the rotating frame, the inertial coordinates are converted to the rotating ones. In the following, upper case letters identify vectors in the inertial frame and lower case ones refer to the rotating frame. Since inertial and rotating coordinates differ for a rotation around Z=z axis, the position vectors in the rotating frame can be retrieved by means of the time-dependent rotation matrix $\mathbf{T}_\omega(t)$, defined as

$$\mathbf{T}_\omega(t) = \begin{bmatrix} \cos(\omega t) & \sin(\omega t) & 0 \\ -\sin(\omega t) & \cos(\omega t) & 0 \\ 0 & 0 & 1 \end{bmatrix} \tag{2.4}$$

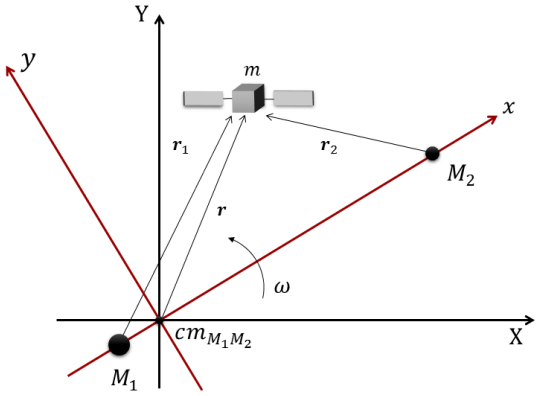

Figure 2.1: *Inertial (X,Y) and rotating (x, y) frame*

Accordingly, the position vector $\boldsymbol{r}$ of the third mass in rotating frame can be written as

$$\boldsymbol{r} = \begin{Bmatrix} x \\ y \\ z \end{Bmatrix} = \mathbf{T}_\omega(t)\boldsymbol{R} \tag{2.5}$$

Since $\mathbf{T}_\omega(t)$ is a rotation matrix, it can be inverted and its inverse is equal to its transpose

$$\mathbf{T}_\omega^{-1}(t) = \mathbf{T}_\omega^T(t) = \begin{bmatrix} \cos(\omega t) & -\sin(\omega t) & 0 \\ \sin(\omega t) & \cos(\omega t) & 0 \\ 0 & 0 & 1 \end{bmatrix} \tag{2.6}$$

consequently

$$\boldsymbol{R} = \mathbf{T}_\omega^T(t)\boldsymbol{r} \tag{2.7}$$

Note that $\mathbf{T}_\omega(t)$ preserves the norm of vectors

$$\|\boldsymbol{R}\| = \|\boldsymbol{r}\| \tag{2.8}$$

The velocity vector of the third body in the inertial frame is written as function of rotating frame coordinates, by derivating Eq. (2.7)

$$\dot{\boldsymbol{R}} = \dot{\mathbf{T}}_\omega^T(t)\boldsymbol{r} + \mathbf{T}_\omega^T(t)\dot{\boldsymbol{r}} \tag{2.9}$$

Analogously, the acceleration vector is written as

$$\ddot{\boldsymbol{R}} = \ddot{\mathbf{T}}_\omega^T(t)\boldsymbol{r} + 2\dot{\mathbf{T}}_\omega^T(t)\dot{\boldsymbol{r}} + \mathbf{T}_\omega^T(t)\ddot{\boldsymbol{r}} \tag{2.10}$$

Equations (2.7) and (2.10) are substituted into Eq. (2.2) and the equation of motion is written as function of rotating frame coordinates

$$\begin{aligned}&\ddot{\mathbf{T}}_{\omega}^{T}(t)\boldsymbol{r}+2\dot{\mathbf{T}}_{\omega}^{T}(t)\dot{\boldsymbol{r}}+\mathbf{T}_{\omega}^{T}(t)\ddot{\boldsymbol{r}}=\\&=G\mathbf{T}_{\omega}^{T}(t)\left(\frac{M_1}{\|\boldsymbol{r}_{\mathrm{P}_1}-\boldsymbol{r}\|^3}(\boldsymbol{r}_{\mathrm{P}_1}-\boldsymbol{r})+\frac{M_2}{\|\boldsymbol{r}_{\mathrm{P}_2}-\boldsymbol{r}\|^3}(\boldsymbol{r}_{\mathrm{P}_2}-\boldsymbol{r})\right)\end{aligned} \tag{2.11}$$

where $\boldsymbol{r}_{\mathrm{P}_1}$ and $\boldsymbol{r}_{\mathrm{P}_2}$ are constant vectors identifying the position of primaries in the rotating frame, directed as the negative and positive x axis. Equation (2.11) can be simplified by knowing that

$$\mathbf{T}_{\omega}(t)\mathbf{T}_{\omega}^{T}(t)=\mathbf{I} \tag{2.12a}$$

$$\mathbf{T}_{\omega}(t)\dot{\mathbf{T}}_{\omega}^{T}(t)=\begin{bmatrix}0&-\omega&0\\\omega&0&0\\0&0&0\end{bmatrix} \tag{2.12b}$$

$$\mathbf{T}_{\omega}(t)\ddot{\mathbf{T}}_{\omega}^{T}(t)=-\omega^2\mathbf{I} \tag{2.12c}$$

By right-multiplying each term of (2.11) for $\mathbf{T}_{\omega}(t)$, substituting expressions (2.12a), (2.12b) and (2.12c) and rearranging the equation, the following is obtained

$$\begin{aligned}\ddot{\boldsymbol{r}}=\omega^2\mathbf{I}\boldsymbol{r}-2\omega\begin{bmatrix}0&-1&0\\1&0&0\\0&0&0\end{bmatrix}\dot{\boldsymbol{r}}+\\+G\left(\frac{M_1}{\|\boldsymbol{r}_{\mathrm{P}_1}-\boldsymbol{r}\|^3}(\boldsymbol{r}_{\mathrm{P}_1}-\boldsymbol{r})+\frac{M_2}{\|\boldsymbol{r}_{\mathrm{P}_2}-\boldsymbol{r}\|^3}(\boldsymbol{r}_{\mathrm{P}_2}-\boldsymbol{r})\right)\end{aligned} \tag{2.13}$$

When the components of position vectors of the three bodies are written as

$$\boldsymbol{r}_{\mathrm{P}_1}=\begin{Bmatrix}-x_{\mathrm{P}_1}\\0\\0\end{Bmatrix}\qquad\boldsymbol{r}_{\mathrm{P}_2}=\begin{Bmatrix}x_{\mathrm{P}_2}\\0\\0\end{Bmatrix}\qquad\boldsymbol{r}=\begin{Bmatrix}x\\y\\z\end{Bmatrix} \tag{2.14}$$

the scalar form of Eq. (2.13) has the form

$$\begin{cases}\ddot{x}=\omega^2x+2\omega\dot{y}-G\left(\frac{M_1}{r_1^3}(x+x_{\mathrm{P}_1})+\frac{M_2}{r_2^3}(x-x_{\mathrm{P}_2})\right)\\\ddot{y}=\omega^2y-2\omega\dot{x}-Gy\left(\frac{M_1}{r_1^3}+\frac{M_2}{r_2^3}\right)\\\ddot{z}=-Gz\left(\frac{M_1}{r_1^3}+\frac{M_2}{r_2^3}\right)\end{cases} \tag{2.15}$$

where r_1 and r_2 represent the norm of relative position vectors between the third body and the primaries

$$r_1 = \|\boldsymbol{r}_{\mathrm{P}_1} - \boldsymbol{r}\| = \sqrt{(x + x_{\mathrm{P}_1})^2 + y^2 + z^2} \tag{2.16a}$$

$$r_2 = \|\boldsymbol{r}_{\mathrm{P}_2} - \boldsymbol{r}\| = \sqrt{(x - x_{\mathrm{P}_2})^2 + y^2 + z^2} \tag{2.16b}$$

Nondimensional equations of motion in the rotating frame

The equations of motion of the third body contain parameters related to the primaries and their motion. Such parameters are not independent from each other and the system can be reduced to a simpler form, by using nondimensional variables. The conservation of linear momentum allows finding a relation between coordinates of primaries in the rotating frame

$$-M_1 x_{\mathrm{P}_1} + M_2 x_{\mathrm{P}_2} = 0 \rightarrow x_{\mathrm{P}_1} = \frac{M_2}{M_1} x_{\mathrm{P}_2} \tag{2.17}$$

the primaries are on circular orbits around the barycentre of the system. The distance between P_1 and P_2 is constant and equal to

$$d = x_{\mathrm{P}_1} + x_{\mathrm{P}_2} \tag{2.18}$$

substituting it into Eq. (2.17)

$$x_{\mathrm{P}_1} = \frac{M_2}{M_1}(d - x_{\mathrm{P}_1}) \tag{2.19}$$

the position of primaries is written as function of their relative distance d and masses

$$\begin{cases} -x_{\mathrm{P}_1} = -\frac{M_2}{M_1+M_2} d \\ x_{\mathrm{P}_2} = \left(1 - \frac{M_2}{M_1+M_2}\right) d \end{cases} \tag{2.20}$$

The angular velocity is associated to the two-body motion of the primaries and is computed as

$$\omega = \sqrt{\frac{G(M_1 + M_2)}{d^3}} \tag{2.21}$$

The major parameters in Eq. (2.15) are now expressed as function of relative distance and mass of primaries. It is convenient to normalize the equations of motion according to such values. More in detail, the nondimensional form of the problem is normalized to the distance between the

primaries, angular velocity and total mass of the system. The following unit parameters are chosen

$$\begin{aligned} &\tilde{d} = 1 && \text{[length units]} \\ &(\tilde{M}_1 + \tilde{M}_2) = 1 && \text{[mass units]} \\ &\tilde{\omega} = 1 && \text{[rad/time units]} \end{aligned}$$

Nondimensional quantities are labeled here with superscript $\tilde{}$. The physical quantities of the problem are written as function of the parameter μ, which is defined as the mass ratio between the primaries, as follows

$$\mu = \frac{M_2}{M_1 + M_2} \tag{2.22}$$

Accordingly, the following relations are found

$$\begin{cases} \tilde{M}_1 = 1 - \mu \\ \tilde{M}_2 = \mu \\ -\tilde{x}_{\mathrm{P}_1} = -\mu \\ \tilde{x}_{\mathrm{P}_2} = 1 - \mu \end{cases} \tag{2.23}$$

Finally, since $\tilde{G}$ becomes equal to one, the nondimensional equations of motion for the third body are written

$$\begin{cases} \ddot{\tilde{x}} = \tilde{x} + 2\dot{\tilde{y}} - \frac{1-\mu}{\tilde{r}_1^3}(\tilde{x} + \mu) - \frac{\mu}{\tilde{r}_2^3}(\tilde{x} - (1-\mu)) \\ \ddot{\tilde{y}} = \tilde{y} - 2\dot{\tilde{x}} - \tilde{y}\left(\frac{1-\mu}{\tilde{r}_1^3} + \frac{\mu}{\tilde{r}_2^3}\right) \\ \ddot{\tilde{z}} = -\tilde{z}\left(\frac{1-\mu}{\tilde{r}_1^3} + \frac{\mu}{\tilde{r}_2^3}\right) \end{cases} \tag{2.24}$$

with

$$\tilde{r}_1 = \sqrt{(\tilde{x} + \mu)^2 + \tilde{y}^2 + \tilde{z}^2} \tag{2.25a}$$

$$\tilde{r}_2 = \sqrt{(\tilde{x} - (1-\mu))^2 + \tilde{y}^2 + \tilde{z}^2} \tag{2.25b}$$

System (2.24) can be written in a more compact form, by defining the pseudo-potential function associated to the nondimensional form of the problem

$$\tilde{U}(\tilde{x}, \tilde{y}, \tilde{z}) = \frac{1}{2}(\tilde{x}^2 + \tilde{y}^2) + \frac{1-\mu}{\tilde{r}_1} + \frac{\mu}{\tilde{r}_2} \tag{2.26}$$

The pseudo-potential function $\tilde{U}(\tilde{x}, \tilde{y}, \tilde{z})$ depends only on the position of the third body in the rotating frame and includes both the gravitational potential due to the primaries' attraction and the centrifugal potential due to

the rotation of the non-inertial synodic frame, which depends only on the distance the particle has from the roation axis (z axis). Using the expression of $\tilde{U}$, system (2.24) becomes

$$\begin{cases} \ddot{\tilde{x}} - 2\dot{\tilde{y}} = \tilde{U}_{\tilde{x}} \\ \ddot{\tilde{y}} + 2\dot{\tilde{x}} = \tilde{U}_{\tilde{y}} \\ \ddot{\tilde{z}} = \tilde{U}_{\tilde{z}} \end{cases} \tag{2.27}$$

where the notation $\tilde{U}_{(\cdot)}$ indicates the partial derivative of the pseudo-potential function with respect to the variable $(\cdot)$. As expected, the equations of motion in the rotating frame show no explicit dependence on time. Also, the dynamics depend on the choice of the primaries only through the parameter μ.

Equilibrium solutions

The rotating CR3BP is known to have five equilibrium points, called *libration* or *lagrangian* points. The equilibrium condition implies that the velocity is null. The libration points are stationary points for the pseudo-potential $\tilde{U}$, associated to energy minima or maxima, and they are found by equating its gradient to zero

$$\boldsymbol{\nabla}\tilde{U}(\tilde{x}, \tilde{y}, \tilde{z}) = \mathbf{0} \tag{2.28}$$

More into detail, Eq. (2.28) is written in scalar form as

$$\tilde{U}_x = 0 \tag{2.29a}$$

$$\tilde{U}_y = 0 \tag{2.29b}$$

$$\tilde{U}_z = 0 \tag{2.29c}$$

The location of libration points is fixed in the rotating frame. Equation 2.29c leads to $\tilde{z} = 0$ and therefore all libration points lay in the (x, y), as shown in Figure 2.2. Three of them (L1, L2 and L3) are called *collinear* points and are located on the x axis. The remaining two (L4 and L5) are called *triangular* or *equilateral* points, since they form equilateral triangles with the two primaries.

Equation 2.29b gives the location of the two equilateral points along the y direction, with $\tilde{y} = 0$ for the case of the three collinear points. Equation 2.29a results in a quintic equation, which provides the position of the five equilibrium points along the x direction. As mentioned, the equilateral points (L4 and L5) lie at the vertex of an equilateral triangle with primaries

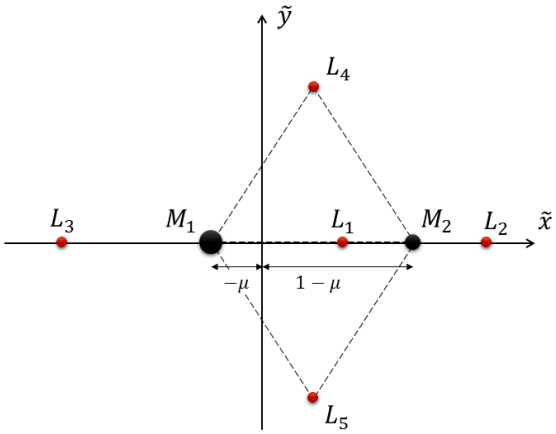

Figure 2.2: *Primaries and libration points in the rotating frame, expressed in non dimensional coordinates*

occupying the remaining vertexes. In the nondimensional rotating frame, the position of the equilateral point is written as function of the mass ratio μ

$$\boldsymbol{r}_{L_4} = \begin{Bmatrix} -\mu + \frac{1}{2} \\ \frac{\sqrt{3}}{2} \\ 0 \end{Bmatrix} \qquad \boldsymbol{r}_{L_5} = \begin{Bmatrix} -\mu + \frac{1}{2} \\ -\frac{\sqrt{3}}{2} \\ 0 \end{Bmatrix} \tag{2.30}$$

The study of the stability of the system around these points, allows their classification as stable or unstable equilibrium solutions. Theoretically, if the dynamical system is in an equilibrium state, it remains in that state as $t \to \infty$. When real problems are considered, disturbances must be taken into account: from a qualitative point of view, if the perturbed motion remains confined in a small neighborhood of the equilibrium point, then the equilibrium solution is named stable, otherwise, if the perturbed trajectory departs from the equilibrium point, it is named unstable. In the case of CR3BP, collinear points are known to be saddle points for the pseudo-potential (unstable), while triangular points are stable under the following condition [128]

$$\mu < 0.03852 \tag{2.31}$$

This implies that the largest primary must be at least roughly 25 times more massive than the smaller primary. This condition is well verified in all gravitational three body systems that include the Sun as primary, as well as for the Earth-Moon system ($\mu \cong 0.01215$) and most of binary asteroid systems.

Energy considerations

The CR3BP, when written in the rotating frame, possesses an integral of motion, called *Jacobi integral*. It can be demonstrated that the following quantity is conserved during the motion of the third body in the rotating frame (see [128] for the complete derivation)

$$\frac{1}{2}(\dot{\tilde{x}}^2 + \dot{\tilde{y}}^2 + \dot{\tilde{z}}^2) - \tilde{U}(\tilde{x}, \tilde{y}, \tilde{z}) = \text{const} \tag{2.32}$$

such quantity is related to the specific mechanical energy of the third body, being the sum of kinetic ($\tilde{E}_k$) and pseudo-potential ($\tilde{E}_p$) energy contributions

$$\begin{cases} \tilde{E} = \tilde{E}_k(\dot{\tilde{x}}, \dot{\tilde{y}}, \dot{\tilde{z}}) + \tilde{E}_p(\tilde{x}, \tilde{y}, \tilde{z}) \\ \tilde{E}_k = \frac{1}{2}(\dot{\tilde{x}}^2 + \dot{\tilde{y}}^2 + \dot{\tilde{z}}^2) \\ \tilde{E}_p = -\tilde{U}(\tilde{x}, \tilde{y}, \tilde{z}) \end{cases} \tag{2.33}$$

Note that $\tilde{U}$ is the pseudo-potential energy of the problem within the rotating system, since it includes a contribution due to the non-inertial motion of the frame. The Jacobi integral of motion is often expressed through the *Jacobi constant* C, which is related to such energy and it is defined as

$$C = -2\tilde{E} \tag{2.34}$$

Note that, due to their opposite sign, if the energy increases, Jacobi constant decreases and vice versa.

Very useful insights on the qualitative behaviour of the motion of the third body can be assessed by means of energetic considerations and Jacobi constant evaluation. More in detail, C can be used to establish regions of motion in the three-body system, where the particle can or cannot be moving when provided with a given energy. Such regions are delimited by Zero Velocity Surfaces (also referenced as Hill's curves) and correspond to the locus of points where the particle, for a given C, has zero velocity in the rotating frame. The basics of Hill's curves analysis are briefly summarized here. The interested reader can refer to [118, 128] for further details. Qualitatively, at a very low energy, if the particle is close to one of the attractors, its motion is bounded in the close proximity of it. In such case the particle does not have enough energy to either escape from the three-body system or to be caught in the close proximity of the other primary. The lowest level of energy that allows the third body to travel between the two primaries is known to be that corresponding to the L1 point E_{L_1}. With energy increased above that of the L2 point E_{L_2}, the particle can escape the three-body system. Higher energy correspond to L3 point E_{L_3} and even higher to the

equilateral points $E_{L_4} = E_{L_5}$, which are reachable at the cost of a very high energy to be provided to the particle.

State Transition Matrix

The concept of State Transition Matrix (STM) is recalled here. As it will be clear from Chapter 3, the STM is a fundamental ingredient for numerical methods of nonlinear system dynamics. Consider a general system of nonlinear differential equations

$$\dot{\boldsymbol{X}} = \boldsymbol{f}(\boldsymbol{X}) \tag{2.35}$$

where $\boldsymbol{X}$ indicates the n-dimensional state vector. The system (2.35) can be linearized and written as first-order variational equations

$$\boldsymbol{\delta}\dot{\boldsymbol{X}} = \mathbf{A}(t)\boldsymbol{\delta X} \tag{2.36}$$

where $\boldsymbol{\delta X}$ represent the vector of small variations associated to the n-dimensional state while the system matrix $\mathbf{A}(t)$ is the Jacobian matrix of the system which, in general, can be written as

$$\mathbf{A}(t) = \frac{\partial \boldsymbol{f}}{\partial \boldsymbol{X}} \tag{2.37}$$

Variations of the initial state at time t_0 can be correlated to variations of the state at any time t, by introducing the concept of State Transition Matrix. The STM is the $n \times n$ matrix defined as

$$\boldsymbol{\Phi}(t, t_0) = \frac{\partial \boldsymbol{X}}{\partial \boldsymbol{X_0}} \tag{2.38}$$

and then

$$\boldsymbol{\delta X}(t) = \boldsymbol{\Phi}(t, t_0)\boldsymbol{\delta X}(t_0) \tag{2.39}$$

The STM is a solution of the first-order variational equations (2.36)

$$\dot{\boldsymbol{\Phi}}(t, t_0) = \mathbf{A}(t)\boldsymbol{\Phi}(t, t_0) \tag{2.40}$$

at initial time t_0, the STM equals the $n \times n$ identity matrix

$$\boldsymbol{\Phi}(t_0, t_0) = \mathbf{I_n} \tag{2.41}$$

STM in CR3BP

In the case of CR3BP, the system of equations (2.27) can be written as first-order variational equations, in the form (2.36). The matrix $\mathbf{A}(t)$ reads

$$\mathbf{A}(t) = \begin{bmatrix} \mathbf{0} & \mathbf{I} \\ \mathbf{U}_{xx} & 2\boldsymbol{\Omega} \end{bmatrix} \tag{2.42}$$

$\mathbf{A}(t)$ is a 6×6 matrix and its four 3×3 submatrices are

$$\begin{aligned}
\mathbf{0} &= \text{zero matrix} \\
\mathbf{I} &= \text{identity matrix} \\
\mathbf{U}_{xx} &= \text{matrix of second partials of pseudo-potential function } \tilde{U} \\
\mathbf{\Omega} &= \begin{bmatrix} 0 & 1 & 0 \\ -1 & 0 & 0 \\ 0 & 0 & 0 \end{bmatrix}
\end{aligned}$$

The STM matrix can be numerically computed by solving Eq. (2.40) with initial conditions from Eq. (2.41), and using the expression of $\mathbf{A}(t)$ in Eq. (2.42).

2.1.2 The Elliptic Restricted Three-Body Problem

The Elliptic Restricted Three-Body Problem (ER3BP) considers the primaries moving on ellipses around the barycentre of the system. Such problem is a generalization of the simpler CR3BP for $e \neq 0$. With analogy to the CR3BP formulation in Section 2.1.1, the equations of motion of the ER3BP are recalled here.

Equations of motion in the rotating frame

Eq. (2.2) is valid both for the case of circular and elliptic problem. The equations of motion in the rotating frame are written considering that $\omega = \omega(t)$ is now time dependent and no longer constant as for the case of CR3BP, with $\dot{\omega} \neq 0$. Also, when seen from the rotating frame, the positions of the primaries are no longer constant and pulsate along the x axis: $x_{\mathrm{P}_1} = x_{\mathrm{P}_1}(t)$ and $x_{\mathrm{P}_2} = x_{\mathrm{P}_2}(t)$. Accordingly, (2.15) is written as

$$\begin{cases}
\ddot{x} = \omega(t)^2 x + 2\omega(t)\dot{y} + \dot{\omega}(t) y - G\left(\dfrac{M_1}{r_1(t)^3}(x + x_{\mathrm{P}_1}(t)) + \right. \\
\qquad\qquad \left. + \dfrac{M_2}{r_2(t)^3}(x - x_{\mathrm{P}_2}(t))\right) \\
\ddot{y} = \omega(t)^2 y - 2\omega(t)\dot{x} - \dot{\omega}(t) x - G y \left(\frac{M_1}{r_1(t)^3} + \frac{M_2}{r_2(t)^3}\right) \\
\ddot{z} = -G z \left(\frac{M_1}{r_1(t)^3} + \frac{M_2}{r_2(t)^3}\right)
\end{cases} \tag{2.43}$$

with

$$r_1(t) = \|\boldsymbol{r}_{\mathrm{P}_1}(t) - \boldsymbol{r}\| = \sqrt{(x + x_{\mathrm{P}_1}(t))^2 + y^2 + z^2} \tag{2.44a}$$

$$r_2(t) = \|\boldsymbol{r}_{\mathrm{P}_2}(t) - \boldsymbol{r}\| = \sqrt{(x - x_{\mathrm{P}_2}(t))^2 + y^2 + z^2} \tag{2.44b}$$

Unlike the CR3BP case, this system is no more autonomous, since it explicitly depends on time. Instantaneously, system (2.43) is formally identical to system (2.15), except for the terms $\dot{\omega}y$ and $\dot{\omega}x$ that appear at the right-hand side of, respectively, first and second equation.

Nondimensional equations of motion in the rotating frame

As done for the circular case, information on the known motion of the primaries can be used to obtain a reduced form of system (2.43). The relative distance between P_1 and P_2 is no longer constant and it is solution of the two-body problem between them, to be written as function of either true or eccentric anomaly

$$d(t) = \frac{p}{1 + e\cos\theta(t)} = a(1 - e\cos E(t)) \tag{2.45}$$

where p is the semi-latus rectum of the conic solution, θ is the true anomaly, E is the eccentric anomaly and e is the eccentricity of the two-body orbit of the primaries. The angular velocity $\omega(t)$ is also written according to the two-body solution

$$\omega(t) = \sqrt{\frac{G(M_1 + M_2)}{d(t)^3}} \tag{2.46}$$

Equivalently, the angular velocity can be written as

$$\omega(t) = \frac{h}{d(t)^2} \tag{2.47}$$

where h is the specific angular momentum of the orbit

$$h = \sqrt{G(M_1 + M_2)a(1 - e^2)} \tag{2.48}$$

with a being the semi-major axis of the two-body solution. Two strategies are commonly adopted to nondimensionalize the problem. Both strategies start from the nondimensional set adopted for the circular case, except for the choice of the unit length. The first strategy considers the characteristic length to be the semi-major axis a of the two-body solution. Superscript $\hat{}$ is used here to refer to nondimensionalization according to a. In this case, the nondimensional angular velocity $\hat{\omega}$ is written as

$$\hat{\omega} = \frac{\hat{h}}{\hat{d}^2} = \frac{\sqrt{1 - e^2}}{(1 - e\cos E)^2} \tag{2.49}$$

accordingly, its derivative is written as

$$\dot{\hat{\omega}} = -2e\frac{\sqrt{1-e^2}}{(1-e\cos E)^4}\sin E \tag{2.50}$$

The positions of primaries are expressed as

$$\begin{cases} -\hat{x}_{\mathrm{P}_1} = -\mu(1-e\cos E) \\ \hat{x}_{\mathrm{P}_2} = (1-\mu)(1-e\cos E) \end{cases} \tag{2.51}$$

Substituting, the nondimensional equations of motion are written as

$$\begin{cases} \ddot{\hat{x}} = \hat{\omega}^2\hat{x} + 2\hat{\omega}\dot{\hat{y}} + \dot{\hat{\omega}}\hat{y} - \left(\frac{(1-\mu)[\hat{x}+\mu(1-e\cos E)]}{\hat{r}_1^3} + \frac{\mu[\hat{x}-(1-\mu)(1-e\cos E)]}{\hat{r}_2^3}\right) \\ \ddot{\hat{y}} = \hat{\omega}^2\hat{y} - 2\hat{\omega}\dot{\hat{x}} - \dot{\hat{\omega}}\hat{x} - \left(\frac{(1-\mu)\hat{y}}{\hat{r}_1^3} + \frac{\mu\hat{y}}{\hat{r}_2^3}\right) \\ \ddot{\hat{z}} = -\left(\frac{(1-\mu)\hat{z}}{\hat{r}_1^3} + \frac{\mu\hat{z}}{\hat{r}_2^3}\right) \end{cases} \tag{2.52}$$

as done for the circular case, the nondimensional pseudo-potential associated to the problem is defined as

$$\hat{U}(\hat{x},\hat{y},\hat{z},t) = \frac{1}{2}\hat{\omega}^2(\hat{x}^2+\hat{y}^2) + \frac{1-\mu}{\hat{r}_1} + \frac{\mu}{\hat{r}_2} \tag{2.53}$$

and the equations of motion are written in a more compact form as

$$\begin{cases} \ddot{\hat{x}} - 2\hat{\omega}\dot{\hat{y}} = \hat{U}_{\hat{x}} + \dot{\hat{\omega}}\hat{y} \\ \ddot{\hat{y}} + 2\hat{\omega}\dot{\hat{x}} = \hat{U}_{\hat{y}} - \dot{\hat{\omega}}\hat{x} \\ \ddot{\hat{z}} = \hat{U}_{\hat{z}} \end{cases} \tag{2.54}$$

A different nondimensionalization strategy considers the characteristic length to be the instantaneous distance between primaries. Unlike the previous case, the position of primaries in the rotating frame is fixed here and their relative distance equals one at any time. This nondimensional frame is then not only rotating but also pulsating along the x direction. Formally, the equations of motion does not differ from system (2.27), which is valid instantaneously. When referring to the rotating-pulsating frame, it can be useful to refer to equations of motion in terms of true anomaly rather than time. In this case, time derivatives are replaced by derivatives with respect to true anomaly θ

$$\frac{d(\cdot)}{dt} = \frac{d(\cdot)}{d\theta}\frac{d\theta}{dt} \tag{2.55}$$

with

$$\frac{d\theta}{dt} = \frac{h}{d^2} \tag{2.56}$$

Superscript $\check{}$ is used here to refer to variables in the rotating-pulsating nondimensional frame. Nondimensional equations of motion, in terms of true anomaly variation, are written as

$$\begin{cases} \check{x}'' - 2\check{y}' = \check{U}_{\check{x}} \\ \check{y}'' + 2\check{x}' = \check{U}_{\check{y}} \\ \check{z}'' = \check{U}_{\check{z}} \end{cases} \tag{2.57}$$

where $(\cdot)'$ and $(\cdot)''$ indicate first and second derivative with respect to the true anomaly θ. The pseudo-potential function $\check{U}(\check{x}, \check{y}, \check{z}, \theta)$ associated to the problem is defined as

$$\check{U}(\check{x}, \check{y}, \check{z}, \theta) = \frac{1}{1 + e\cos\theta}\left[\frac{1}{2}(\check{x}^2 + \check{y}^2 - \check{z}^2 e\cos\theta) + \right. \\ \left. + \frac{1-\mu}{\check{r}_1} + \frac{\mu}{\check{r}_2}\right] \tag{2.58}$$

the interested reader can refer to [64] for further details.

STM in ER3BP

As done for the circular case, details on the STM computation are discussed here for the elliptic case. More in detail, the formulation related to motion in terms of time variations, as expressed in system 2.54, is considered. As mentioned, the system is non-autonomous and the six-dimensional state vector associated to position and velocity of the third body in the rotating frame must be augmented to introduce information of the motion of the primaries. To this goal, the eccentric anomaly related to the two-body motion of primaries is included in the seven-dimensional state vector

$$\boldsymbol{X} = [\hat{x}, \hat{y}, \hat{z}, \dot{\hat{x}}, \dot{\hat{y}}, \dot{\hat{z}}, E]^T \tag{2.59}$$

The variational equations associated to the problem are written as

$$\dot{\boldsymbol{\delta X}} = \mathbf{A}(t)\boldsymbol{\delta X} \tag{2.60}$$

where $\mathbf{A}(t)$ is the 7×7 Jacobian of the system

$$\mathbf{A}(t) = \begin{bmatrix} \mathbf{0} & \mathbf{I} & \mathbf{0} \\ \mathbf{U}_{\boldsymbol{XX}} + \dot{\hat{\omega}}\boldsymbol{\Omega} & 2\hat{\omega}\boldsymbol{\Omega} & \boldsymbol{\Gamma} \\ \mathbf{0} & \mathbf{0} & \sigma \end{bmatrix} \tag{2.61}$$

the first row of $\mathbf{A}(t)$ expresses the derivatives of the velocities $\dot{\hat{x}}, \dot{\hat{y}}, \dot{\hat{z}}$ with respect to the full state $\boldsymbol{X}$ and it is made of three submatrices

$$\begin{aligned} \mathbf{0} &= (3 \times 3) \text{ zero matrix} \\ \mathbf{I} &= (3 \times 3) \text{ identity matrix} \\ \mathbf{0} &= (3 \times 1) \text{ zero matrix} \end{aligned}$$

the second row contains the derivatives of the accelerations

$$\begin{aligned} \mathbf{U}_{\boldsymbol{XX}} &= (3 \times 3) \text{ matrix of second partials} \\ &\quad \text{of } \hat{U} \text{ with respect to position} \\ \boldsymbol{\Omega} &= \begin{bmatrix} 0 & 1 & 0 \\ -1 & 0 & 0 \\ 0 & 0 & 0 \end{bmatrix} \\ \boldsymbol{\Gamma} &= (3 \times 1) \text{ matrix of derivatives of} \\ &\quad \text{accelerations with respect to E} \end{aligned}$$

the last row contains the derivatives of $\dot{E}$ with respect to the full state

$$\begin{aligned} \mathbf{0} &= (1 \times 3) \text{ zero matrix} \\ \sigma &= (1 \times 1) \text{ derivative of } \dot{E} \text{ with respect to E} \end{aligned}$$

Being the STM $\boldsymbol{\Phi}(t, t_0)$ solution of Equation 2.60, its components can be computed numerically by solving the system

$$\begin{cases} \dot{\boldsymbol{\Phi}}(t, t_0) = \mathbf{A}(t)\boldsymbol{\Phi}(t, t_0) \\ \dot{\boldsymbol{\Phi}}(t_0, t_0) = \mathbf{I} \end{cases} \tag{2.62}$$

2.2 The N-Body Problem

The N-body problem studies the dynamics of N point-mass bodies under their reciprocal gravitational attraction. Despite being a well known mathematical problem, with an established mathematical formulation, the full comprehension of its solutions and dynamical behaviour is still very far from being reached. It was proved that no analytical solution exists for $N > 2$ and the problem is characterized by a highly non-linear (chaotic) behaviour, which is reflected in a strong dependency of the solution on initial state of any body.

2.2.1 The Unrestricted N-Body Problem

The classic Newton's law expresses the gravitational interactions between the N bodies, with each body moving under the gravitational attraction of all remaining N-1 bodies

$$m_i \ddot{\boldsymbol{R}}_i = G \sum_{j=1, j\neq i}^{N} \frac{m_i m_j}{\|\boldsymbol{R}_{ij}\|^3} \boldsymbol{R}_{ij} \qquad \forall i = 1 : N \tag{2.63}$$

with $\boldsymbol{R}_i$ representing the position vector of the centre of mass of body i in an inertial frame and $\boldsymbol{R}_{ij} = \boldsymbol{R}_j - \boldsymbol{R}_i$, while m_i represents its mass and G is the universal gravitational constant. Applications of the unrestricted N-Body problem are used in this work of thesis to simulate asteroid aggregation dynamics, to find suitable mass distribution models for an asteroid. Further detail on the numerical implementation of the unrestricted N-Body problem in this kind of application is provided in Section 3.4 and 4.2.

2.2.2 The Restricted N-Body Problem

As mentioned in Section 2.1, restricted problems finds real world applications on astrodynamics problems related to spacecraft trajectory design. In such case, the focus is on the motion of a small body (spacecraft) under the gravitational field generated by massive gravity sources, such as celestial bodies in the Solar System. In this case, the following assumption holds

$$m_{S/C} \ll m_i \qquad \forall i = 1 : N - 1 \tag{2.64}$$

meaning that the spacecraft does not influence the motion of the remaining N-1 bodies. Applications of the restricted N-Body problem are implemented in this work to provide a real world model of the Solar System. The position of each celestial body, when relevant to the application, is provided with high accuracy by using planetary ephemerides retrieved from JPL's existing database (for the case of planets and planetary satellites) or by using JPL's Horizons system (for the case of asteroids and comets) [77].

2.3 Small bodies

Few strategies can be adopted to model the gravity field about asteroids. Classic methods consider a spherical mass distribution of the asteroid and include harmonic expansion of gravitational potential [80] to model the irregularities of the field. These methods work well when the mass distribution of the gravity source is spherical or very close to be spherical,

as in the case of planets and large natural planetary satellites. However, such methods can be very inaccurate for the case of asteroids and comets, especially during close-proximity operations. As for the case of spherical harmonics, the series is known to converge exactly to the actual gravity field only outside of the sphere circumscribing the small body (or Brillouin sphere) [121]. This clearly does not fit with the need to design close proximity or landing trajectories about elongated or non-convex bodies, which is often the case in the NEA population. Also, a lot of series coefficients must be known to have a good estimate of the gravity field and such information is hardly available for a mostly unknown celestial object. A recent strategy models the gravity field according to shape information available on the asteroid/comet after optical and radar observation. If a shape model of the body is available, the best technique is to represent it as an homogeneous polyhedron [123, 137], based on such shape model. When a detailed shape model is not available, simpler models of its shape can be used, such as tri-axial ellipsoids [119]. A further class of methods makes use of mass-concentrated models, also known as mascon models. These methods model the mass distribution of the celestial body using multiple point-mass sources and accordingly, the gravity field is the sum of multiple central fields. The accuracy of each method depends on the modeled target body and on the application. Typically, each model fits a specific class of asteroids and application range.

In the following, the most suitable models for small celestial bodies applications are recalled and discussed. Section 2.3.1 recalls the techniques to model small bodies through shape-based models, while Section 2.3.2 discusses the mascon model strategy and introduces a methodology to obtain the final asteroid model based on multi-body N-body asteroid aggregation simulation.

2.3.1 Shape-based models

The use of shape-based models is currently the most advanced technique concerning refined and high-accuracy models of irregularly-shaped bodies. Since they are built using shape information, such models are able to reproduce the irregularities of the field produced by the irregular shape of the target body. If accurate shape and mass distribution information is available, the model can virtually reproduce a real-world model of the target body, by means of accurate shape and density distribution modeling. Due to their usefulness within astrodynamics problems and for mission analysis of spacecraft orbiting in the close-proximity of small celestial bodies,

ellipsoid and polyhedron models are recalled here. Due to the very little knowledge about interior mass or density distribution of asteroids and comets [71], the case of uniform density distribution is studied.

Ellipsoid model

The implementation is based on the method proposed by Scheeres [119] and models the gravity potential of an ellipsoid of constant density ρ, with semi-axes α, β, γ, aligned respectively to the x, y and z axes of the reference frame, and with $\alpha \geq \beta \geq \gamma$. The reference (x, y, z) is then aligned to the principal axes of inertia of the ellipsoid. The shape of the ellipsoid is delimited by

$$\left(\frac{x}{\alpha}\right)^2 + \left(\frac{y}{\beta}\right)^2 + \left(\frac{z}{\gamma}\right)^2 = 1 \tag{2.65}$$

the dimensional potential outside of the ellipsoid is written as

$$U_{\text{ell}}(x, y, z) = -G\rho\pi\alpha\beta\gamma \int_{\lambda(x,y,z)}^{\infty} \varphi(x, y, z; u) \frac{du}{\Delta(u)} \tag{2.66}$$

where G is the universal gravitational constant and

$$\varphi(x, y, z; u) = \frac{x^2}{\alpha^2 + u} + \frac{y^2}{\beta^2 + u} + \frac{z^2}{\gamma^2 + u} - 1 \tag{2.67}$$

$$\Delta(u) = \sqrt{(\alpha^2 + u)(\beta^2 + u)(\gamma^2 + u)} \tag{2.68}$$

with parameter λ being solution of

$$\varphi(x, y, z; \lambda(x, y, z)) = 0 \tag{2.69}$$

In order to include the effect of the ellipsoid gravity source into the equations of motion of the surrounding particle, the acceleration vector is computed as the gradient of the potential function $U_{\text{ell}}(x, y, z)$

$$\boldsymbol{a}_{\text{ell}} = \boldsymbol{\nabla} U_{\text{ell}}(x, y, z) = -2G\rho\pi\alpha\beta\gamma \begin{Bmatrix} x \int_{\lambda}^{\infty} \frac{du}{(\alpha^2+u)\Delta(u)} \\ y \int_{\lambda}^{\infty} \frac{du}{(\beta^2+u)\Delta(u)} \\ z \int_{\lambda}^{\infty} \frac{du}{(\gamma^2+u)\Delta(u)} \end{Bmatrix} \tag{2.70}$$

for completeness, the Jacobian of acceleration vector, namely the second partials of potential, is reported here

$$\boldsymbol{\nabla} \boldsymbol{a}_{\text{ell}} = \mathbf{U}_{\text{ell}_{\boldsymbol{xx}}} = -2G\rho\pi\alpha\beta\gamma \begin{bmatrix} U_{xx} & U_{xy} & U_{xz} \\ U_{xy} & U_{yy} & U_{yz} \\ U_{xz} & U_{yz} & U_{zz} \end{bmatrix} \tag{2.71}$$

with

$$U_{xx} = \int_{\lambda}^{\infty} \frac{du}{(\alpha^2+u)\Delta(u)} - \frac{2x^2}{(\alpha^2+\lambda)^2\Delta(\lambda)\psi} \tag{2.72a}$$

$$U_{yy} = \int_{\lambda}^{\infty} \frac{du}{(\beta^2+u)\Delta(u)} - \frac{2y^2}{(\beta^2+\lambda)^2\Delta(\lambda)\psi} \tag{2.72b}$$

$$U_{zz} = \int_{\lambda}^{\infty} \frac{du}{(\gamma^2+u)\Delta(u)} - \frac{2z^2}{(\gamma^2+\lambda)^2\Delta(\lambda)\psi} \tag{2.72c}$$

$$U_{xy} = -\frac{2xy}{(\alpha^2+\lambda)(\beta^2+\lambda)\Delta(\lambda)\psi} \tag{2.72d}$$

$$U_{xz} = -\frac{2xz}{(\alpha^2+\lambda)(\gamma^2+\lambda)\Delta(\lambda)\psi} \tag{2.72e}$$

$$U_{yz} = -\frac{2yz}{(\beta^2+\lambda)(\gamma^2+\lambda)\Delta(\lambda)\psi} \tag{2.72f}$$

and with ψ

$$\psi = \frac{x^2}{(\alpha^2+\lambda)^2} + \frac{y^2}{(\beta^2+\lambda)^2} + \frac{z^2}{(\gamma^2+\lambda)^2} \tag{2.73}$$

Polyhedron model

The computation of gravity contribution due to a polyhedron of constant density ρ is recalled here. The derivation is based on the method proposed by Werner and Scheeres [137]. The dimensional potential function U_{poly} indicates the exact potential of an object, according to its shape model. The contributions due to all faces and edges of the polyhedron are summed together

$$U_{\text{poly}}(x,y,z) = -\frac{1}{2}G\rho\left(\sum_{f\in\text{faces}} \boldsymbol{r}_f \cdot \mathbf{F}_f \cdot \boldsymbol{r}_f \omega_f - \sum_{e\in\text{edges}} \boldsymbol{r}_e \cdot \mathbf{E}_e \cdot \boldsymbol{r}_e L_e \right) \tag{2.74}$$

where G is the universal gravitational constant. $\boldsymbol{r}_f$ and $\boldsymbol{r}_e$ are vectors from the field point to face f and edge e. $\mathbf{F}_f$ is the dyad associated to face f of the polyhedron model

$$\mathbf{F}_f = \hat{\boldsymbol{n}}_f \hat{\boldsymbol{n}}_f \tag{2.75}$$

with $\hat{\boldsymbol{n}}_f$ as the unitary vector normal to face f. Analogously, $\mathbf{E}_e$ is the dyad associated to edge e of the polyhedron

$$\mathbf{E}_e = \hat{\boldsymbol{n}}_{f_1} \hat{\boldsymbol{n}}_e^{f_1} + \hat{\boldsymbol{n}}_{f_2} \hat{\boldsymbol{n}}_e^{f_2} \tag{2.76}$$

where f_1 and f_2 denotes the two faces sharing the edge e. $\hat{\boldsymbol{n}}_e^{f_1}$ is the unit vector normal to the edge e and to $\hat{\boldsymbol{n}}_{f_1}$ and pointing opposite with respect

to the centre of face f_1. The term L_e represents the potential of a wire associated to the edge e

$$L_e = \ln \frac{r_1^e + r_2^e + l_e}{r_1^e + r_2^e - l_e} \tag{2.77}$$

where r_1^e and r_2^e are vectors from the field point to the vertexes at the ends of edge e, while l_e is the length of edge e. Parameter ω_f is the solid angle associated to the face f, when viewed from the field point

$$\omega_f = 2 \arctan \frac{\boldsymbol{r}_1^f \cdot \boldsymbol{r}_2^f \times \boldsymbol{r}_3^f}{r_1^f r_2^f r_3^f + r_1^f \boldsymbol{r}_2^f \cdot \boldsymbol{r}_3^f + r_2^f \boldsymbol{r}_2^f \cdot \boldsymbol{r}_1^f + r_3^f \boldsymbol{r}_1^f \cdot \boldsymbol{r}_2^f} \tag{2.78}$$

where $\boldsymbol{r}_1^f, \boldsymbol{r}_2^f$ and $\boldsymbol{r}_3^f$ are vectors from the field point to the three vertexes of the triangular face f and r_1^f, r_2^f, r_3^f are their norms. As done for the ellipsoid model, the acceleration and its Jacobian are reported here

$$\boldsymbol{a}_{\text{poly}} = \boldsymbol{\nabla} U_{\text{poly}}(x, y, z) = G\rho \left(\sum_{f \in \text{faces}} \mathbf{F}_f \cdot \boldsymbol{r}_f \omega_f - \sum_{e \in \text{edges}} \mathbf{E}_e \cdot \mathbf{r}_e L_e \right) \tag{2.79}$$

$$\boldsymbol{\nabla} \boldsymbol{a}_{\text{poly}} = \mathbf{U}_{\text{poly}_{\boldsymbol{xx}}} = -G\rho \left(\sum_{f \in \text{faces}} \mathbf{F}_f \omega_f - \sum_{e \in \text{edges}} \mathbf{E}_e L_e \right) \tag{2.80}$$

Figure 2.3 shows an example of polyhedral model of comet 67P/Churyumov-Gerasimenko, as compared to a high resolution picture taken by the Rosetta spacecraft in 2014.

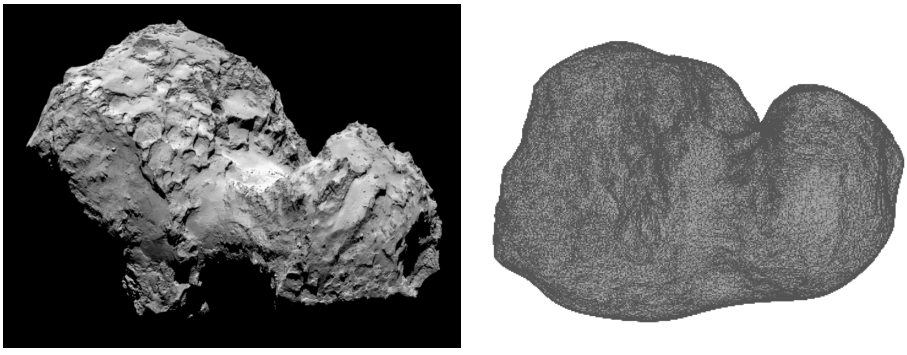

(a) (b)

Figure 2.3: *Comet 67P/Churyumov-Gerasimenko (a) picture from Rosetta spacecraft (credits: ESA, 2014) (b) polyhedral shape model.*

2.3.2 N-mascon models

In the late 1970s, Chapman [19] used the term "rubble pile" to indicate a gravitational aggregate of boulders. Although a non-negligible fraction of objects of more than 50 km diameter could be monolithic [12], recent studies and observations support the idea that many comet nuclei and asteroids between 100 m and 100 km in size may be gravitational aggregates [111]. Celestial bodies of this class can have up to 40% porosity, or void fraction. For this reason, homogeneous mass models of asteroids are usually not the best choice to model gravitational aggregates with high accuracy since internal voids can significantly affect the outer field. To this goal, the target body is modeled here using a mass-concentrated model, also referenced as *mascon* model in the following. The basic idea is to model the mass distribution of the target body by means of N concentrated masses. In such a way, the outer gravity field is expressed as the sum of N central bodies

$$\ddot{\boldsymbol{r}} = G \sum_{i=1}^{N} \frac{m_i}{\|\boldsymbol{r}_i\|^3} \boldsymbol{r}_i \qquad \forall i = 1 : N \tag{2.81}$$

where $\boldsymbol{r}$ is the position vector of the particle subjected to the field in the (x, y, z) body-fixed frame, while $\boldsymbol{r}_i$ is the distance between the particle and the i-th mass m_i

$$\boldsymbol{r}_i = \boldsymbol{R}_i - \boldsymbol{r} \tag{2.82}$$

with $\boldsymbol{R}_i$ being the position of m_i in the body-fixed frame. The positions $\boldsymbol{R}_i$ of each i-th concentrated mass are fixed with respect to the body-fixed frame and they represent the mass distribution of the object. How the masses are displaced in the body-fixed frame and the values of each mass m_i are related to the target body to be modeled. The N masses can be distributed according to a specific mass distribution of the target body, or outer field to be reproduced. A classical method fits N equal masses within the shape of the target body on an evenly spaced grid [58]. Since this method displaces all masses uniformly within the shape of the body, it represent a simplification of analytical shape-based models and not a valid alternative for the case of gravitational aggregates. The simple gridded method can be improved by introducing a non-uniform distribution of masses, with $m_i \neq m_j$. To this goal, optimization can be applied, with position $\boldsymbol{R}_i$ and masses m_i as free parameters of the optimizer and with a given outer field as reference. The optimal mascon approach is implemented using a genetic algorithm to minimize the difference between the outer field generated by the N mascon model and the real-world known field [25]. The last strategy for mass displacements and m_i definition, is by simulating the asteroid

aggregation process. Such strategy is suitable for the case of gravitational aggregates, or "rubble pile" asteroids: the mass distribution of the asteroid is provided as output of a realistic aggregation scenario.

Applications related to mascon models are studied in this work of thesis. A two-mascon model is used to reproduce a space mission scenario around a two-lobed asteroid in Section 5.1. Further details on the numerical implementation of the N-body gravitational aggregation model are provided in Section 3.4.1, while results coming from numerical simulations are discussed in Section 4.2.

2.4 Non-gravitational perturbations: SRP

The model of the dynamics of a spacecraft flying in the Solar System can be refined by including orbital perturbations due to non-gravitational effects. Among these, one of the most relevant effect for space applications is provoked by the SRP. Concerning applications discussed in this work, the perturbation is computed according to a very simple cannonball model [24]. The acceleration due to the SRP is estimated as

$$a_{SRP} = \frac{P(1 + C_r)A}{c \cdot m} \tag{2.83}$$

where P is the amount of power received from the Sun per square meter, C_r is the reflectivity coefficient, A is the cross-section area, c is the speed of light constant and m is the mass of the spacecraft.

CHAPTER 3

Numerical Methods for Nonlinear System Dynamics

One of the most crucial aspect when dealing with non-Keplerian dynamics is the capability to identify effective solutions, suitable for the mission analysis application under design. The great effort devoted by the astrodynamics community to the problem of finding solutions to restricted three-body systems has enhanced the understanding of such chaotic systems. However, the full comprehension of general non-Keplerian dynamics is far to be reached and the capability to predict the dynamical behaviour of an object moving in such environment is very poor, except for very confined applications related mainly to R3BP. The reason is due to the nature of the problem, to its strong nonlinearity and to the absence of general analytical solutions. Numerical methods play a fundamental role in finding such solutions and nowadays, represent the most powerful tool the designer can use for mission analysis design.

This chapter discusses the problem of finding solutions associated to non-Keplerian systems and presents the numerical methods used to compute the trajectories and orbits throughout this thesis work. Typical examples related to mission analysis applications concern the search for periodic

solutions. Section 3.1 presents the software architecture of a general purpose method to address such problem. Although the software implementation proposed here is presented with a clear focus towards the computation of periodic orbits, its application can be easily extended to the finding of any wanted trajectory. The numerical tool includes and harmonizes three main blocks of libraries, which implement the three fundamental ingredients to compute periodic orbits: initial guess generation, correction and continuation. The methods and techniques are general and can be applied to any nonlinear dynamical system. Nomenclature and notation refer to nonlinear dynamical system theory: see [67] for a detailed and rigorous description of nonlinear dynamical system theory and [72, 82, 121] for the theory applied to astrodynamics problems. Since the purpose of this work is to study astrodynamics applications, the research is focused towards two main kind of non-Keplerian systems, which are very popular for spacecraft applications: the restricted three-body problem and gravity field around small celestial bodies. Applications of the implemented software architecture to periodic motion identification are shown in Section 3.2. The most relevant solutions for space mission applications are summarized and the suitability of the different methods proposed is discussed for each specific case: initial guess generation, correction and continuation methods are customized to the specific solution to be targeted. Examples of algorithms used to find periodic motion are presented. The algorithm in use for computation of invariant manifold solutions is presented in Section 3.3. The last part of the chapter (Section 3.4) is dedicated to an application indirectly related to spacecraft trajectory design. An innovative numerical method used to solve the unrestricted N-body problem is presented. Since it is an unrestricted problem, its solutions are not directly used for spacecraft trajectory design. Instead, they are used to generate suitable N-body mascon models that represent the mass distribution of an asteroid. Spacecraft trajectories can be designed at a subsequent phase, using the software architecture presented in Section 3.1 under the dynamics associated to the N-body mascon gravity field (Section 2.3.2).

3.1 Software architecture for restricted problems

Part of the thesis work was devoted to the implementation and validation of a general purpose software to be used for astrodynamics applications. The software was implemented to support the thesis work and to provide relevant dynamical solutions (orbits and trajectories) under non-Keplerian dynamics. The current section discusses in more detail the general method-

ology used, the software architecture of the numerical tool implemented and its applicability to astrodynamics problems. Given the framework of the dynamics to be considered, the goal is to build a general tool for trajectory design. A set of *initial conditions* unequivocally identifies the evolution of the dynamics (initial value problem) and the resulting solution, or trajectory, can always be retrieved by starting from the same set of initial conditions. For this reason, searching for specific trajectories means searching for sets of initial conditions associated to these solutions.

Concerning existing numerical methodologies and implementations for finding periodic motion in non-Keplerian systems, the majority of them are based on the correction algorithm implemented by Howell [72]. Few methods are used to provide initial guess to find a periodic solution after differential corrections: Lo [85] showed how to look for initial guess conditions in the centre subspace associated to a libration point, Howell and Campbell [75] showed how to use bifurcation maps to find new families of solutions starting from other families of orbits. Bifurcation problems are detailed by Keller [81], for general nonlinear systems. A comprehensive implementation, called AUTO [27], exists for continuation and bifurcation problems in ordinary differential equations. Examples of its implementation to find periodic solutions in the CR3BP are given in [16, 28, 29]. Compared to AUTO, the proposed implementation aims to a much more astrodynamics-related tool, with the scope of creating a tool to support space mission analysis and design. As compared to existing studies, the proposed software architecture aims at generalizing and harmonizing existing techniques into a unique and multi-purpose tool. According to the current state of the art, no general-purpose tools able to handle different systems and dynamics are available. Classical and recent techniques for non-linear system dynamics are used and integrated together to build new algorithms, in the attempt of creating more efficient schemes, that can be customized to the properties of the system.

As mentioned, specific applications related to periodic motion identification are presented. For any dynamical system, a periodic motion is found when the dynamics repeat themselves in a certain time (period). Consider the general nonlinear dynamical system

$$\dot{\boldsymbol{X}} = \boldsymbol{f}(\boldsymbol{X}) \tag{3.1}$$

with $\boldsymbol{X}$ being the state vector. Let then

$$\boldsymbol{X_s} = \boldsymbol{\Gamma_s}(t) \tag{3.2}$$

be a solution of system (3.1). If the function $\boldsymbol{\Gamma_s}(t)$ is periodic in time with

period T

$$\boldsymbol{\Gamma_s}(t) = \boldsymbol{\Gamma_s}(t+T) \tag{3.3}$$

then $\boldsymbol{X_s}$ is a periodic solution of the system of differential equations (3.1). Analogously, concerning initial conditions of the initial value problem, at time $t = t_{\text{in}}$ the state $\boldsymbol{X}(t_{\text{in}})$ corresponds to a periodic solution for the dynamical system if after a certain time T

$$\boldsymbol{X}(t_{\text{in}}) = \boldsymbol{X}(t_{\text{in}}+T) \tag{3.4}$$

since in this system the particle is periodically coming back (with period T) to the same point in the state space. A catalogue of periodic orbits (stored as sets of initial conditions) relevant for space mission applications, was generated for rapid trajectory design. Also, guidelines related to the applicability of numerical methodologies to the different dynamics under study were investigated. The ultimate goal is to enhance the comprehension of non-Keplerian dynamics, in order to foresee a priori what kind of periodic solutions can be expected to be found in a specific system.

As discussed, non-Keplerian dynamics are strongly non-linear, meaning that solutions are highly dependent on their initial conditions (i.e., the initial state of the bodies involved) and small variations of them can lead to very different trajectories. For this reason, *correction* algorithms are needed to correct initial conditions, to find those corresponding to a specific solution. The choice of the *initial guess* to be provided to the corrector is crucial to guarantee the method to converge to the aimed solution. In the case of families of solutions (solutions sharing some properties or behaviour in the dynamical system), such an initial guess is often provided by using information available on other members of the family, i.e., by *continuation* from other solutions close to the aimed one. The proposed integrated method for periodic motion computation includes and harmonizes three main sets of libraries (or blocks), which implement the three fundamental ingredients to compute periodic orbits: initial guess generation (Section 3.1.1), correction (Section 3.1.2) and continuation (Section 3.1.3). Methodologies to deal with nonlinear system dynamics are also implemented: all libraries make use of routines developed for the computation of relevant quantities such as State Transition Matrix (STM) and variational equations, implemented for each of the different dynamical system under study. More in detail, the linearized system matrix associated to variational equations is written analytically for each dynamical system and the STM is computed numerically based on this information, as described in Chapter 2. A more detailed description of the methods and their applicability to astrodynamics problems is discussed in the following.

The connection and exchange of information between each block is schematically shown in Figure 3.1. The whole process is initiated by a given initial guess, which is corrected to find the first periodic orbit solution. Then, this information is used to generate a new initial guess, to find the next member of the family. Different methods and strategies are implemented in each block. The suitable combination of methods is selected according to the nature of solution to be found and to the dynamics of the problem.

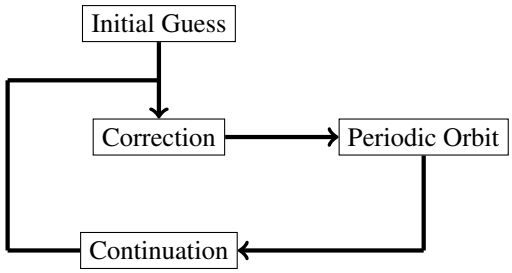

Figure 3.1: *Schematics of software architecture implemented*

3.1.1 Initial guess

The term *initial guess* refers to a set of initial conditions used as first guess to find, after correction, another set of initial conditions, the latter associated to the aimed periodic orbit. The initial conditions set typically includes the state of the massless body (spacecraft) subjected to the gravity field, the state of the gravity sources and other relevant properties of the system under study (e.g. mass ratio or eccentricity of primaries for the case of three-body systems). In the following the initial conditions set is referenced using the notation $\boldsymbol{X}_g$. Depending on the case, the initial guess is provided according to different strategies.

Catalog of available data

This represents the quickest way to find the initial guess when a catalogue of periodic solutions is available. It allows to retrieve solutions in the catalogue or solutions close to orbits included in the catalogue.

Center manifold associated to an equilibrium point

This powerful technique is suitable to initiate the family of certain classes of orbits such as planar or vertical Lyapunov, which emanate directly from the centre manifold of the equilibrium point. Periodic and quasi-periodic

orbits live in the centre manifold phase space associated to collinear libration points. The centre manifold directions are found by analyzing the eigenstructure of the linearized system near the libration point, which can be written in the form

$$\boldsymbol{\delta \dot{X}} = \mathbf{A}\boldsymbol{\delta X} \tag{3.5}$$

being $\boldsymbol{\delta X}$ the linearized state and $\mathbf{A}$ the system matrix. The eigenvectors associated to the complex conjugate eigenvalues of the system matrix $\mathbf{A}$ represent the directions tangent to the centre manifold subspace. The initial guess $\boldsymbol{X}_g$ is found by moving a small step towards the centre manifold direction near the libration point [85], such that

$$\boldsymbol{X}_g = \boldsymbol{P} + \mathbf{E}\boldsymbol{\rho} \tag{3.6}$$

where $\boldsymbol{P}$ is the state vector associated to the libration point (with zero velocity). $\mathbf{E}$ is a matrix that collects the eigenvectors of $\mathbf{A}$ associated to the centre manifold

$$\mathbf{E} = \begin{bmatrix} \boldsymbol{v}_1 & \boldsymbol{v}_2 & \dots & \boldsymbol{v}_n \end{bmatrix} \tag{3.7}$$

where n is the size of the centre subspace associated to the problem. $\boldsymbol{\rho}$ is a $(n \times 1)$ vector, used as a weight to define how far the guess is taken from $\boldsymbol{P}$ and to select preferred directions in the centre subspace. This parameter shall be carefully tuned according to the specific case considered and it should be small enough so that linearized system represents a good approximation of the non-linear problem. Lastly, the initial conditions set should include a guess for the period of the orbit to be found. This information is retrieved using the eigenvalue frequency $\|\lambda_i\|$ associated to the centre manifold selected

$$T = \frac{2\pi}{\|\lambda_i\|} \tag{3.8}$$

.

Center manifold associated to a periodic orbit

Relevant motion, of interest for space applications, can be found in the proximity of a periodic orbit, when a centre manifold subspace exists in its vicinity (e.g. quasi-periodic tori near Halo orbits [4]). With analogy to the previous case, the guess if found in the direction of the centre eigenvectors associated to the linearized system. In this case the analysis is performed by studying the eigenstructure of the monodromy matrix associated to the periodic orbit.

Bifurcations

A bifurcation is typically identified by a sudden change of the properties of the periodic solution along its family (e.g. modifications in the eigenstructure of the monodromy matrix). This technique is suitable to initiate the family of certain classes of orbits which emanates from bifurcations of other families. An example is given here for the case of Halo family: Hénon [68] showed that these particular orbits are the results of a bifurcation of the planar Lyapunov family. No Halo orbits exist at energies lower than the bifurcating one, hence no Halo orbit can be found in the centre subspace in the vicinity of the libration points. The monodromy matrix associated to any Lyapunov orbit smaller than the bifurcating one (the one having critical amplitude) has four centres, one stable and one unstable eigenvalue. Focusing on the centre eigenvalues, two of them are real and their value is equal to one, the other two are a complex conjugates pair with unitary norm. Both couples of centre eigenvalues represent bounded motion in the proximity of the orbit and in particular the real unit eigenvalues represent the periodic orbit, while the two complex conjugates represent quasi-periodic motion nearby the Lyapunov. As the amplitude of the Lyapunov orbit increases and approaches the critical amplitude, the conjugate pair moves on the unit circle, approaching the real value of one. Hence, the monodromy matrix of the critical Lyapunov has four real eigenvalues equal to one. At this specific point, the quasi-periodic motion disappears while two periodic motions are present: the first one is the in-plane motion (Lyapunov orbit) while the second one has an out-of-plane component (Halo orbit).

Bifurcation maps are extremely useful to understand connections between families of orbits and to help identify new families. The problem of bifurcation in such nonlinear systems is extremely complex, since the properties of the dynamics can exhibit large variations depending on the energy of the particle and on the parameters characterizing the gravity source (mass ratio between primaries, eccentricity of their relative orbit, shape/mass distribution of the gravity source,...).

Poincaré maps

A very effective strategy to explore the complexity of non-Keplerian dynamical systems, is to make use of Poincaré maps. In few words the Poincaré map helps representing in a simpler way the dynamics, allowing for an easy identification of relevant solutions. Examples of such solutions are periodic and quasi-periodic orbits, heteroclinic and homoclinic connec-

tions between solutions about equilibrium points.

Consider the general dynamical system (3.1) and its n-dimensional flow ϕ. Let Σ be a hyperplane transversal to the flow. The Poincaré map $\mathcal{M}$ is defined as the set of points that intersects the hyperplane

$$\mathcal{M}(\boldsymbol{X}) = \phi(T_\Sigma, \boldsymbol{X}) \tag{3.9}$$

For the case of finding periodic motion, T_Σ is the time the flow takes to first return on the hyperplane where the initial conditions set $\boldsymbol{X}_0$ belongs to. The hyperplane Σ is also called Poincaré section. Figure 3.2(a) shows schematically the Poincaré map generated by the intersection between the dynamical flow and the Poincaré section Σ. Figure 3.2(b) shows an example of a numerically computed Poincaré map.

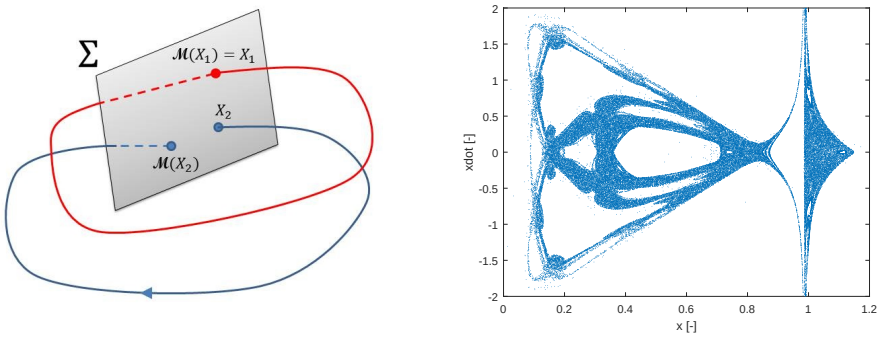

(a) (b)

Figure 3.2: *(a) Poincaré map generated by the intersection between the dynamical flow and the Poincaré section Σ (b) example of Poincaré map on (x-$\dot{x}$) section*

Periodic orbits are represented on the map as fixed points if T_Σ is equal to the period of the orbit, as they return on the Poincaré section with the same state they initially have. The red curve in figure 3.2(a) is an example of periodic orbit on a Poincaré map: after one period, the flow intersects the Poincaré section exactly at the starting point $\boldsymbol{X}_1$. The periodicity condition is fulfilled when the flow after one period is equal to the initial point and reads as

$$\mathcal{M}(\boldsymbol{X}_i) = \phi(T_i, \boldsymbol{X}_i) = \boldsymbol{X}_i \tag{3.10}$$

A different example of use of Poincaré maps is shown in Section 5.1, where a map is used to find intersections between stable and unstable manifolds in the patched three-body problem.

Analytical approximations

The last method recalled here refers to the use of analytical or semi-analytical methods to approximate periodic solutions near libration points. A widely used method is that proposed by Richardson [114], where Halo orbits are targeted based on a third-order analytical approximation.

3.1.2 Correction

Two main strategies exist to perform correction on the initial guess, to find the initial conditions associated to the aimed periodic solution.

Differential corrections

Based on the classical algorithm proposed by Howell [72], differential corrections algorithms are the most widely used technique for numerical correction of solutions. Modifications and customization are applied depending on the solution to be found and the dynamics to be investigated. The methods are based on the definition of constraints to be satisfied and free variables that can be modified by the corrector. The choice of free variables vector $\boldsymbol{\chi}$ and constraint condition $\boldsymbol{F}(\boldsymbol{\chi}) = \mathbf{0}$ depends on the orbit to be found and on the dynamics of the system. Typically, periodicity constraint is enforced, by ensuring that the initial conditions set repeats itself after a certain time (period of the orbit). In case of unique solution of the constrained problem (number of constraints equal to number of free variables), a multi-variable iterative Newton's method is employed:

$$\boldsymbol{\chi}_{k+1} = \boldsymbol{\chi}_k - \mathbf{J}(\boldsymbol{\chi}_k)^{-1}\boldsymbol{F}(\boldsymbol{\chi}_k) \tag{3.11}$$

Where subscript $_k$ refers to current iteration and $\mathbf{J}(\boldsymbol{\chi})$ is the Jacobian matrix of the problem, found by computing the derivatives of the constraints with respect to the free variables. Since both constraints and free variables are built using the state vector $\boldsymbol{X}$ of the spacecraft, the Jacobian matrix is usually written using the components of the STM Φ_{ij}, which are, by definition, the partial derivatives of the state $\partial X_i/\partial X_j$. In case time is free to vary, time derivatives of the state that appear into $\mathbf{J}(\boldsymbol{\chi})$ are computed directly from equations of motion (3.1). The STM for the problem under study is computed numerically based on variational equations associated to the dynamics. In case of a under-constrained problem (free variables exceed the number of constraints), the solution is found by minimizing the variation of free variables between two consecutive iterations:

$$\boldsymbol{\chi}_{k+1} = \boldsymbol{\chi}_k - \mathbf{J}(\boldsymbol{\chi}_k)^T \left[\mathbf{J}(\boldsymbol{\chi}_k)\mathbf{J}(\boldsymbol{\chi}_k)^T\right]^{-1} \boldsymbol{F}(\boldsymbol{\chi}_k) \tag{3.12}$$

Common implementations for astrodynamics applications include different choice of shooting techniques:

- single-shooting: in this case, the initial state of the spacecraft is integrated forward into a single arc and the solution is found whenever the trajectory returns at its initial state.
- multiple-shooting: the initial guess trajectory in discretized into a series of patch points. The initial state at each patch point is integrated independently and the complete solution is made by several arcs, patched together. In this case, the constraint vector includes not only the periodicity constraint, but also continuity constraint between each arc. Multiple-shooting algorithms are in general more powerful than single-shooting ones: both of them search for the solution using a linear approximation (variational equations) of the initial guess trajectory and multiple shorter arcs reduce the errors coming from linearization, compared to a single long arc. Figure 3.3 shows an example of multiple-shooting iterations, with the corrected solution that quickly converges to a periodic orbit.

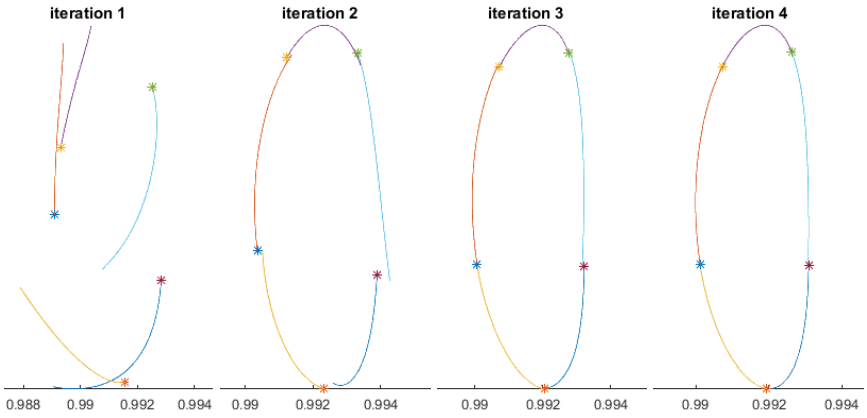

Figure 3.3: *Multiple-shooting iterations*

Depending on whether the dynamics have symmetries, the correction strategy can exploit such symmetry through the mirror theorem. In these cases, it is sufficient to generate a portion of the orbit, to automatically have the complete one. Additional constraints must be enforced to ensure symmetry. In this case, symmetry constraints replace periodicity constraints. The implementation includes the distinction between fixed and variable time

schemes. From the numerical point of view, the difference is made simply by defining the period as constraint or free variable. This distinction is extremely important for the case of time-dependent systems, such as the ER3BP or the gravity field of a spinning asteroid. The need of considering the additional constraint of a fixed-period algorithm can challenge the corrector or, in some cases, lead to an over-constrained problem.

Optimization algorithms

Finding periodic solutions is equivalent to solving a boundary value problem (BVP). As an alternative to the use of differential corrections, the BVP can be solved using optimization algorithms, with periodicity satisfied by minimizing the difference between parameters in the initial conditions set, evaluated at initial time and after one period.

3.1.3 Continuation

Continuation methods provide the initial guess to find the next orbit in the family. Two main strategies are applied.

Single/multiple-parameter continuation

This method is very simple and provides the initial guess for the new orbit by simply varying one or multiple parameters in the initial conditions set. The new (varied) parameter shall be kept fixed by the corrector (it is put into the constraint set), in order to find the new solution. Typical choice of parameters to be continued include the initial position of the spacecraft, the energy (to find similar orbits at different energy levels) and period (to find a family of orbits within a certain period range). Single/multiple-parameter methods are greatly useful to find solutions within different dynamical systems. In this case, the continuation parameter can be the mass ratio between primaries, the eccentricity of their orbit (to find periodic solutions in the ER3BP), or the geometry/mass distribution of the gravity source (for the case of shape-based models of asteroids).

An example regarding Halo orbit generation is given here. To obtain the first guess for the Halo orbit, starting from the six-dimensional state corresponding to initial conditions of the bifurcating Lyapunov, a small step Δz is provided in the out-of-plane direction. The new z state is kept fixed by the corrector. The value of Δz shall be chosen carefully, since it depends on the choice of the system and on the method used to correct the initial guess to the actual initial conditions of the Halo orbit. Depending on the sign of Δz, northern ($\Delta z > 0$) or southern ($\Delta z < 0$) Halo is generated.

Pseudo-arclength continuation

This method is a special case of multiple-parameter continuation. Parameters to be continued are not chosen a priori, but the free variable vector is continued along the direction tangent to the targeted orbital family, i.e., in the direction of the next member of the family. This method is very efficient and typically is more robust than single/multiple-parameter continuation, since it does not require any a priori knowledge (or prediction) of the evolution of the family.

The basic idea of the algorithm is reported here. The next orbit of the family is associated to new initial conditions $\boldsymbol{X}_{0_n}$, which are computed starting from the available member of the family $\boldsymbol{X}_0$. In general, the new initial conditions are found by moving from $\boldsymbol{X}_0$ of a step $\boldsymbol{\rho}$ in the state space

$$\boldsymbol{X}_{0_n} = \boldsymbol{X}_0 + \boldsymbol{\rho} \tag{3.13}$$

In the case of pseudo-arclength continuation, $\boldsymbol{\rho}$ in taken in the direction tangent to the family of orbits. All orbits in the family satisfy the constrained problem defined by the differential correction algorithm. Accordingly $\boldsymbol{\rho}$ is the vector lying on the null space of the system matrix.

Concerning the example given above on CR3BP single-shooting corrector, the initial conditions of the new orbit read as

$$\boldsymbol{X}_{0_n} = \boldsymbol{X}_0 + \rho \begin{Bmatrix} n_1 \\ 0 \\ n_2 \\ 0 \\ n_3 \\ 0 \end{Bmatrix} \tag{3.14}$$

where ρ can be tuned by the user and indicates how far the new orbit shall be with respect to the old one in the state space, while n_1, n_2 and n_3 are the first three components of the null vector of system matrix of (3.25).

3.2 Periodic motion in restricted problems

The most common non-Keplerian models, to be used for space mission design applications are presented here and the problem of finding periodic solutions associated to each of them is discussed. The applicability of the different techniques available is investigated, depending on the kind of dynamics and relevant parameters involved. As mentioned in the introductory

section, the main focus is on CR3BP, ER3BP and small celestial body models.

3.2.1 The Circular Restricted Three-Body Problem

The CR3BP is the most studied non-Keplerian system and a wide variety of studies on periodic motion exists. Due to the acquired knowledge on the problem, a lot of different families of periodic orbits are known to exist. Relevant contributions include the work by Breakwell and Brown [13], who computed families of orbits in the Earth-Moon system. Later, Howell [72–74] extended their work to compute families for different systems, and study their properties depending on the mass ratio μ between primaries. Recent works by Guzzetti et al. [66] and Folta et al. [52] include a comprehensive survey of orbit families in the Earth-Moon system and their properties. Here, a list of the most relevant to space mission design applications is reported, and the applicability of the aforementioned numerical methods to find periodic solutions is discussed for each of them.

- Halo: perhaps the most popular orbit in the CR3BP. The Halo family is known to bifurcate from the planar Lyapunov family. In this case, either single- or multiple-shooting corrector, with pseudo-arclength continuation represent a suitable choice to find the whole Halo family. Due to the symmetry of the problem, the mirror theorem can be exploited and it is sufficient to find half orbit, provided that it crosses orthogonally the (x,z) plane in the synodic frame. Halo orbits exist around all collinear libration points (L1, L2, L3).

- Planar Lyapunov: this family emanates directly from the centre manifold associated to a collinear point (either L1, L2 or L3). The orbits are planar and lie on the (x,y) plane of the synodic frame. The family can be easily continued by single parameter continuation (e.g. x coordinate). As for the case of Halo orbit, the mirror theorem can be exploited.

- Vertical Lyapunov: as the planar family, it emanates directly from the centre manifold of a libration point, with the difference of having a three-dimensional out-of-plane motion. The family evolves through the out-of-plane component and therefore a z-continuation (or pseudo-arclength) can be used to find the whole family. Unlike the planar family, vertical Lyapunov can be found around the equilateral points (L4, L5) as well.

- Axial: this family can be generated starting from bifurcations in both vertical and planar Lyapunov families: the Axial family connect the two bifurcating planar and vertical Lyapunov orbits.

- Other libration point orbits: many other families of orbits exist in the CR3BP. Examples are short and long period orbits around triangular points, Butterfly and Horseshoe orbits. Each family possess its peculiar properties, but general and robust methods such as multiple-shooting with pseudo-arclength continuation can be used successfully.

- Primary-centred: all previously-listed orbits are libration point orbits. In addition, orbits around primaries can be of great interest for space mission applications. A typical example is that of Direct Retrograde Orbits (DRO), which are of extreme interest due to their convenient stability properties. The general numerical scheme proposed applies.

- Resonant: these kinds of orbits possess peculiar properties in terms of period that is, by definition, a multiple of the synodic period of the primaries. Unlike the previously listed orbits, these are not arranged in a continuous family, but can be found among all families. To be found, it is crucial to use a fixed-time corrector, starting from a given orbit of similar period.

Single-shooting for periodic motion in the CR3BP

An example is provided here for the case of a periodic orbit about a collinear libration point in the CR3BP, using a single-shooting algorithm. Since the equations of CR3BP (2.27) are symmetric with respect to the (x, z) plane in the rotating frame, it is reasonable to assume that a periodic orbit about collinear libration points crosses the (x, z) plane perpendicularly. Such symmetry is used to simplify the problem and to speed up the corrector. Periodicity is related to the orthogonality of the trajectory with respect to (x, z) plane. Orthogonality (or periodicity) constraint reads as

$$y = \dot{x} = \dot{z} = 0 \tag{3.15}$$

When starting from the (x, z) plane, the initial state for a periodic orbit is

$$\boldsymbol{X}_0 = \begin{Bmatrix} x_0 \\ 0 \\ z_0 \\ 0 \\ \dot{y}_0 \\ 0 \end{Bmatrix} \tag{3.16}$$

Since the problem is symmetric with respect to the (x, z) plane, and the periodic orbit will return to its initial state after one period, the trajectory returns on the (x, z) plane after half period, with

$$\boldsymbol{X}_h = \begin{Bmatrix} x_h \\ 0 \\ z_h \\ 0 \\ \dot{y}_h \\ 0 \end{Bmatrix} \tag{3.17}$$

where the subscript $_h$ refers to the state after half period of the orbit. If T is the period of the orbit, then $T_h = T/2$. The initial guess $\boldsymbol{X}_g$ provided to the corrector is integrated in the CR3BP and checked after half period. An initial guess for the half period T_{h_g} shall also be provided. The correction algorithm can operate to modify the initial states x_0, z_0 and $\dot{y}_0$, or the integration time T_h until constraints are satisfied. The free variables vector is written as

$$\boldsymbol{\chi} = \begin{Bmatrix} x_0 \\ z_0 \\ \dot{y}_0 \\ T_h \end{Bmatrix} \tag{3.18}$$

The constraint condition $\boldsymbol{F}(\boldsymbol{\chi})$ refers to the state after half period and is written as

$$\boldsymbol{F}(\boldsymbol{\chi}) = \begin{Bmatrix} y_h(\boldsymbol{\chi}) \\ \dot{x}_h(\boldsymbol{\chi}) \\ \dot{z}_h(\boldsymbol{\chi}) \end{Bmatrix} = \boldsymbol{0} \tag{3.19}$$

The problem of finding the initial conditions for a periodic orbit is reduced to the non-linear constrained problem

$$\begin{cases} \boldsymbol{X}_h = \boldsymbol{f}(\boldsymbol{X}_0, T_h) \\ \boldsymbol{F}(\boldsymbol{\chi}) = 0 \end{cases} \tag{3.20}$$

Overall, the problem has three constraints and four free variables. To find solutions to the under-constrained problem (3.20) and solve for $\boldsymbol{\chi}$, Eq. (3.12) is used. To this goal, the Jacobian of the problem $\mathbf{J}(\boldsymbol{\chi})$ is required. Since the Jacobian contains the partial derivatives of the state, the STM after half period is used. The impact of a slight variation in the initial state is related to the change in the state after half period, through the State Transition Matrix $\Phi(T_h, 0)$

$$\boldsymbol{\delta X}_h = \boldsymbol{\Phi}(T_h, 0)\boldsymbol{\delta X}_0 \tag{3.21}$$

assuming that $\boldsymbol{X}_0$ corresponds to the state at time $t = 0$. In addition, the state after half period depends on the time T_h: another term shall be included to Eq. (3.21).

$$\boldsymbol{\delta X}_h = \boldsymbol{\Phi}(T_h, 0)\boldsymbol{\delta X}_0 + \begin{Bmatrix} \frac{\partial x}{\partial t} \\ \frac{\partial y}{\partial t} \\ \frac{\partial z}{\partial t} \\ \frac{\partial \dot{x}}{\partial t} \\ \frac{\partial \dot{y}}{\partial t} \\ \frac{\partial \dot{z}}{\partial t} \end{Bmatrix}_{T_h} \delta T_h \tag{3.22}$$

which is equivalently written as

$$\boldsymbol{\delta X}_h = \boldsymbol{\Phi}(T_h, 0)\boldsymbol{\delta X}_0 + \dot{\boldsymbol{X}}_h \delta T_h \tag{3.23}$$

Equation (3.23) is expressed in matrix form and it is equivalent to six scalar equations. Among these, the three equations representing the constraints can be extracted. Also, knowing that the corrector is allowed to change only x_0, z_0, $\dot{y}_0$, and T_h then

$$\delta y_0 = \delta \dot{x}_0 = \delta \dot{z}_0 = 0 \tag{3.24}$$

Variations related to constraint variables can be written as

$$\begin{cases} \delta y_h = \Phi_{21}\delta x_0 + \Phi_{23}\delta z_o + \Phi_{25}\delta \dot{y}_0 + \dot{y}_h \delta T_h \\ \delta \dot{x}_h = \Phi_{41}\delta x_0 + \Phi_{43}\delta z_o + \Phi_{45}\delta \dot{y}_0 + \ddot{x}_h \delta T_h \\ \delta \dot{z}_h = \Phi_{61}\delta x_0 + \Phi_{63}\delta z_o + \Phi_{65}\delta \dot{y}_0 + \ddot{z}_h \delta T_h \end{cases} \tag{3.25}$$

or equivalently, in matrix notation

$$\delta \boldsymbol{F}(\boldsymbol{\chi}) = \mathbf{J}(\boldsymbol{\chi})\delta\boldsymbol{\chi} \tag{3.26}$$

with

$$\mathbf{J}(\boldsymbol{\chi}) = \begin{bmatrix} \Phi_{21} & \Phi_{23} & \Phi_{25} & \dot{y}_h \\ \Phi_{41} & \Phi_{43} & \Phi_{45} & \ddot{x}_h \\ \Phi_{61} & \Phi_{63} & \Phi_{65} & \ddot{z}_h \end{bmatrix} \tag{3.27}$$

which represent a system of three equations and four unknowns. Note that $\Phi_{i,j}$ is the (i, j) element of the STM. Alternatively to solving the under-constrained problem, a common choice is to operate on only three out of the four free variables, while fixing either x_0 or z_0 and consequently

$$\delta x_0 = 0 \qquad \text{or} \qquad \delta z_0 = 0 \tag{3.28}$$

In such case, the problem has equal number of constraints and free variables and Eq. (3.11) can be used to solve the constrained system. The choice of fixing x_0 or z_0 depends on the kind of orbit the corrector is targeting. For example, $\delta x_0 = 0$ can be imposed to find Lyapunov orbits, while $\delta z_0 = 0$ to find Halo orbits. In case $\delta x_0 = 0$ is chosen, the system becomes

$$\begin{cases} \delta y_h = \Phi_{23}\delta z_0 + \Phi_{25}\delta\dot{y}_0 + \dot{y}_h\delta T_h \\ \delta\dot{x}_h = \Phi_{43}\delta z_0 + \Phi_{45}\delta\dot{y}_0 + \ddot{x}_h\delta T_h \\ \delta\dot{z}_h = \Phi_{63}\delta z_0 + \Phi_{65}\delta\dot{y}_0 + \ddot{z}_h\delta T_h \end{cases} \tag{3.29}$$

which is now a system of three equations in the three unknowns δz_0, $\delta\dot{y}_0$ and δT_h.

3.2.2 The Elliptic Restricted Three-Body Problem

The role of eccentricity in the R3BP is extremely relevant. From the dynamical point of view, compared to the CR3BP, the ER3BP is no longer autonomous, being the dynamics of the latter time-dependents. This fact highly challenges the problem of finding periodic solutions. For an orbit to be periodic in the CR3BP, it is sufficient to replicate its six-dimensional state, after a certain time (period of the orbit). The circular problem is known to have an infinite number of periodic solutions which can be collected into families of orbits with continuously varying period. This is not true for the elliptic problem. Due to its explicit time dependency, it is not sufficient for an orbit in the ER3BP to replicate its six-dimensional state:

the whole dynamics shall be replicated, including the time-dependent position of primaries. For this reason the ER3BP admits only isolated periodic orbits, with well-determined periods. Since the time dependency of the problem is due to the motion of the primaries, orbits in the ER3BP must be periodic with a period commensurable to that of the primaries. From the computational point of view, periodic solutions can be found through fixed-time differential correction, starting from a resonant orbit in the CR3BP and applying single-parameter continuation to slightly vary the eccentricity of the system. The constraints to build the corrector must be chosen wisely depending on the aimed orbit, and making sure not to over-constraint the problem. After considering the increased complexity of the problem, general methodologies presented in the previous section can be applied.

When considering nondimensional equations of motion 2.54, primaries moves with normalized period of 2π: accordingly, periodic solutions of the ER3BP must have period of $T = 2\pi N$, with $N \in \mathbb{N}^+$. Since the orbit is periodic with period equal or multiple to that of the rotating frame, it is periodic both in the rotating and in the inertial frame. The criterion for an orbit to be periodic in the ER3BP was firstly given by [97], after merging together the aforementioned period constraint and his considerations on the symmetry of the problem

> *if the infinitesimal body crosses the x-axis perpendicularly when the finite bodies are at an apse, its motion is symmetrical with respect to the x-axis.*

The formalization of the periodicity condition is due to [116], who generalized it for the motion of *n* point-masses in the so called *Mirror Theorem*:

> *if n point-masses are acted upon by their mutual gravitational forces only, and at a certain epoch each radius vector from the (assumed stationary) centre of mass of the system is perpendicular to every velocity vector, then the orbit of each mass after that epoch is a mirror image of its orbit prior to that epoch*

According to [97] and [116], a sufficient condition for the motion in the ER3BP to be periodic is that it has two perpendicular crossings with the $(\hat{x}, \hat{z})$ plane, which shall occur when the primaries are at an apse.

Single-shooting for periodic motion in ER3BP

Periodic orbits in the ER3BP are generated starting from orbits in the CR3BP with same period, through differential corrections and eccentricity continuation techniques. In agreement with the Mirror Theorem [116], the dif-

ferential correction algorithm is implemented to target two perpendicular crossings with the (x, z) plane. More in detail, a fixed-time single-shooting algorithm is implemented, based on the algorithm proposed by Howell [72] and adapted for the case of ER3BP. The initial guess is taken on the (x, z) plane, at a time the primaries are at an apse. The correction algorithm targets the second perpendicular crossing, that occurs after π or multiples of π, i.e., when the primaries happen to be at an apse again. The time between the two perpendicular crossings is half of the orbital period of the periodic solution. In this case, it is sufficient to find half of the orbit, and to propagate it forward for the remaining half period to have the full periodic solution. With reference to Section 3.1.2, the vector of free variables is written as

$$\boldsymbol{\chi} = \begin{Bmatrix} x_0 \\ z_0 \\ y_0' \end{Bmatrix} \tag{3.30}$$

where the subscript 0 indicates conditions at initial time, corresponding to initial true anomaly f_0 that equals either 0 (periapsis) or π (apoapsis). At the end of the trajectory (half orbit), the state must satisfy the following constraint condition, defined such to have perpendicular crossing on the (x, z) plane

$$\boldsymbol{F}(\boldsymbol{\chi}) = \begin{Bmatrix} y_h \\ x_h' \\ z_h' \end{Bmatrix} = \mathbf{0} \tag{3.31}$$

with subscript h indicating the state after half period of the orbit, corresponding to true anomaly $f_h = f_0 + N\pi$. The goal is to compute a solution for the free variable vector $\boldsymbol{\chi}$ that satisfies the constraint condition $\boldsymbol{F}(\boldsymbol{\chi}) = \mathbf{0}$. The result is found iteratively through the multi-variable Newton's method (3.11). The Jacobian matrix $\mathbf{J}(\boldsymbol{\chi})$ of the problem is found by computing the derivatives of the constraint with respect to the free variables

$$\mathbf{J}(\boldsymbol{\chi}) = \frac{\partial \boldsymbol{F}(\boldsymbol{\chi})}{\partial \boldsymbol{\chi}} = \begin{bmatrix} \frac{\partial y_h}{\partial x_0} & \frac{\partial y_h}{\partial z_0} & \frac{\partial y_h}{\partial y_0'} \\ \frac{\partial x_h'}{\partial x_0} & \frac{\partial x_h'}{\partial z_0} & \frac{\partial x_h'}{\partial y_0'} \\ \frac{\partial z_h'}{\partial x_0} & \frac{\partial z_h'}{\partial z_0} & \frac{\partial z_h'}{\partial y_0'} \end{bmatrix} = \begin{bmatrix} \Phi_{21} & \Phi_{23} & \Phi_{25} \\ \Phi_{41} & \Phi_{43} & \Phi_{45} \\ \Phi_{61} & \Phi_{63} & \Phi_{65} \end{bmatrix} \tag{3.32}$$

with Φ_{ij} being the element (i, j) of the STM $\boldsymbol{\Phi}(f_h, f_0)$.

3.2.3 Small celestial bodies

The goal is to develop a method able to find periodic motion around a small body of any given shape/mass distribution. In this case, periodic solutions would be found through variable-time differential correction. The initial guess is provided by a periodic orbit in the simple Keplerian model, to be corrected and continued through single/multiple-parameter continuation. The continuation is related here to the change in shape of the primary. For example, for a constant density ellipsoidal asteroid, continuation can be achieved by slightly changing the mass distribution from spherical, to ellipsoidal. In this case the continuation parameters could be the semi-major axes of the ellipsoid. The general idea applies to any shape of the gravity source, which is initially decomposed into a single simple shape (or into a cluster of multiple simple shapes), whose geometry is steadily continued until the more complex polihedral shape is reached. As for the ER3BP case, despite the increased complexity of the problem, numerical methods proposed here can be successfully exploited to seek periodic motion.

Multiple-shooting for periodic motion around small celestial bodies

In this case, no symmetries in the dynamical environment can be exploited since, in general, the mass distribution of the small celestial body is not symmetric and the initial guess to be provided is a complete orbit. The initial guess is divided into N_p segment, each associated to a patch point. With reference to Section 3.1.2, the vector of free variables contains the state of each patch point. Also, since no time constraints are imposed to find the solution, the integration times associated to each patch segment is included in the $7N_p$-long free variables vector

$$\boldsymbol{\chi} = \begin{Bmatrix} \boldsymbol{X}_1 \\ \boldsymbol{X}_2 \\ \vdots \\ \boldsymbol{X}_{N_p} \\ T_1 \\ T_2 \\ \vdots \\ T_{N_p} \end{Bmatrix} \tag{3.33}$$

In order to represent a unique solution, each arc must be fully connected to its neighbor arcs. At each patch point, the state must satisfy the following

constraint condition

$$\boldsymbol{F}(\boldsymbol{\chi}) = \begin{Bmatrix} \boldsymbol{X}_1^f - \boldsymbol{X}_2 \\ \vdots \\ \boldsymbol{X}_{N_p}^f - \boldsymbol{X}_1 \end{Bmatrix} = \boldsymbol{0} \tag{3.34}$$

which results in a $6N_p$-long vector. $\boldsymbol{X}_i^f$ represent the final state after integrating initial state $\boldsymbol{X}_i$ for the integration time T_i. The last constraint in Eq. (3.34) (the last six scalar elements of constraint vector) is the periodicity condition since it enforces connection between the last (N_p) and the first arc. As mentioned, the goal of the corrector is to find a solution for the free variable vector $\boldsymbol{\chi}$ that satisfies the constraint condition $\boldsymbol{F}(\boldsymbol{\chi}) = \boldsymbol{0}$. Since the number of constraints is lower than the number of free variables, the system is under-constrained and the result is found iteratively using Eq. (3.12). As usual, the Jacobian matrix $\mathbf{J}(\boldsymbol{\chi})$ of the problem is found by computing the derivatives of the constraint with respect to the free variables

$$\mathbf{J}(\boldsymbol{\chi}) = \frac{\partial \boldsymbol{F}(\boldsymbol{\chi})}{\partial \boldsymbol{\chi}} = $$

$$= \begin{bmatrix} \frac{\partial \boldsymbol{X}_1^f}{\partial \boldsymbol{X}_1} & -\frac{\partial \boldsymbol{X}_2}{\partial \boldsymbol{X}_2} & \boldsymbol{0} & \dots & \boldsymbol{0} & \frac{\partial \boldsymbol{X}_1^f}{\partial T_1} & \boldsymbol{0} & \dots & \dots \\ \boldsymbol{0} & \frac{\partial \boldsymbol{X}_2^f}{\partial \boldsymbol{X}_2} & -\frac{\partial \boldsymbol{X}_3}{\partial \boldsymbol{X}_3} & \boldsymbol{0} & \dots & \boldsymbol{0} & \frac{\partial \boldsymbol{X}_2^f}{\partial T_2} & \boldsymbol{0} & \dots \\ & \vdots & & & \vdots & & & \vdots & \\ \dots & \boldsymbol{0} & \frac{\partial \boldsymbol{X}_i^f}{\partial \boldsymbol{X}_i} & -\frac{\partial \boldsymbol{X}_{i+1}}{\partial \boldsymbol{X}_{i+1}} & \boldsymbol{0} & \dots & \boldsymbol{0} & \frac{\partial \boldsymbol{X}_i^f}{\partial T_i} & \boldsymbol{0} \\ & \vdots & & & \vdots & & & \vdots & \\ -\frac{\partial \boldsymbol{X}_1}{\partial \boldsymbol{X}_1} & \boldsymbol{0} & \dots & \boldsymbol{0} & \frac{\partial \boldsymbol{X}_{N_p}^f}{\partial \boldsymbol{X}_{N_p}} & \boldsymbol{0} & \dots & \boldsymbol{0} & \frac{\partial \boldsymbol{X}_{N_p}^f}{\partial T_{N_p}} \end{bmatrix} \tag{3.35}$$

The quantity $\frac{\partial \boldsymbol{X}_i^f}{\partial \boldsymbol{X}_i}$ is the STM between initial time t_i at patch point i and final time after integration $t_i + T_i$

$$\frac{\partial \boldsymbol{X}_i^f}{\partial \boldsymbol{X}_i} = \boldsymbol{\Phi}(t_i + T_i, t_i) \tag{3.36}$$

Knowing that $\frac{\partial \boldsymbol{X}_2}{\partial \boldsymbol{X}_2}$ is a 6×6 identity matrix $\mathbf{I}_6$ and $\frac{\partial \boldsymbol{X}_i^f}{\partial T_i} = \dot{\boldsymbol{X}}_i^f$, Eq. (3.35) is written as

$$\mathbf{J}(\boldsymbol{\chi}) = \begin{bmatrix} \boldsymbol{\Phi}_1 & -\mathbf{I}_6 & \mathbf{0} & \dots & \mathbf{0} & \dot{\boldsymbol{X}}_1^f & \mathbf{0} & \dots & \dots \\ \mathbf{0} & \boldsymbol{\Phi}_2 & -\mathbf{I}_6 & \mathbf{0} & \dots & \mathbf{0} & \dot{\boldsymbol{X}}_2^f & \mathbf{0} & \dots \\ & \vdots & & & \vdots & & & \vdots & \\ \dots & \mathbf{0} & \boldsymbol{\Phi}_i & -\mathbf{I}_6 & \mathbf{0} & \dots & \mathbf{0} & \dot{\boldsymbol{X}}_i^f & \mathbf{0} \\ & \vdots & & & \vdots & & & \vdots & \\ -\mathbf{I}_6 & \mathbf{0} & \dots & \mathbf{0} & \boldsymbol{\Phi}_{N_p} & \mathbf{0} & \dots & \mathbf{0} & \dot{\boldsymbol{X}}_{N_p}^f \end{bmatrix} \tag{3.37}$$

where $\boldsymbol{\Phi}_i = \boldsymbol{\Phi}(t_i + T_i, t_i)$.

3.3 Stable and unstable manifolds in restricted problems

In previous sections the techniques to find periodic motion in a general nonlinear dynamical system were discussed. As discussed, periodic motion is associated to the centre manifold subspace of a periodic orbit or of an equilibrium solution. Here, solutions related to stable and unstable manifold subspaces are discussed and the numerical technique in use to find such solutions are presented. As for the case of centre manifold, stable and unstable manifolds can be associated both to equilibrium and to periodic orbit solutions. The algorithm to compute invariant manifolds does not depend on this distinction, except for the eigenstructure to be analyzed. When manifold associated to an equilibrium solution is sought, the eigenstructure of system matrix $\mathbf{A}$, associated to the linearized system in the vicinity of the equilibrium point is studied. In case of manifold of a periodic orbit, the associated monodromy matrix is studied. In both cases, the eigenpairs of the monodromy (or system) matrix are computed. In order to compute stable and unstable manifolds, stable and unstable subspace must be present in the eigenstructure of the monodromy (or system) matrix. This is not the case for stable orbits, whose eigenstructure is made of centre manifold only.

To provide an example, the computation of stable manifolds associated to a periodic orbit is described here. The same method can be easily generalized for the case of unstable manifolds and for the case of solutions associated to equilibrium points. The first step consists in identifying the eigenvector associated to the stable (or unstable) eigenvalues of the monodromy matrix. The manifold solution is computed moving along the stable (or unstable) eigendirection, which is tangent to the manifold. The initial

conditions of the manifold can be written as

$$\boldsymbol{X}_0 = \boldsymbol{X}_{\text{orb}} + \varepsilon \boldsymbol{\Phi}(t, t_0)\boldsymbol{v} \tag{3.38}$$

where $\boldsymbol{X}_{\text{orb}}$ represent the state on the orbit where the manifold is departing from (or the equilibrium point). The scalar ε represent the distance in the state space between the point on the orbit and the starting point of the manifold and it shall be carefully tuned by the user, depending on the dynamics and on the kind of orbit to be found. $\boldsymbol{\Phi}(t, t_0)$ is the STM where t_0 represent the initial time while t is the local time associated to the point on the orbit where the manifold is departing from (identity matrix in the case of equilibrium solution). Finally, $\boldsymbol{v}$ is the stable (or unstable) eigenvector of the monodromy matrix. Initial conditions for the manifolds are computed for all desired points in the orbit. Once all initial conditions for the manifolds are computed, they are integrated backward in time (forward in case of unstable manifolds) to find the manifolds trajectories.

3.4 The unrestricted N-body aggregation method

As mentioned in Section 2.3.2, recent studies and observations support the theory of "rubble pile" asteroids. According to this, small and medium size asteroids may be gravitational aggregates of boulders. Such aggregates have very low tensile strength, possessing no cohesive force other than gravity. This evidence motivates the present work. The goal of the method presented here is to obtain a N-body model of the asteroid mass distribution by studying it as a gravitational aggregate. The physical problem is modeled as a classical unrestricted N-body problem, with mutual gravitational interaction between all bodies (Section 2.2.1). Each boulder is modeled as a rigid body: collision detection is implemented and contact forces are included to describe the dynamics of the colliding bodies.

From the numerical point of view, the N-body problem is usually approached using two main classes of codes: N-body integrators and N-body simulators [96]. Integrators solve the Newtonian equations of motion by computing all N to N gravitational interactions between bodies. Simulators incorporate models of dynamical or physical effects to partially estimate the behaviour of the N bodies. As a consequence, the high accuracy of numerical integrators is associated with long computational time, whereas simulators are usually faster. The selection of the algorithm is strictly dependent on the application, namely on the physical phenomenon that must be reproduced. Concerning the accretion of planetesimal and asteroid aggregation processes, relevant implementations include tree codes [112, 113, 126],

hybrid codes [1], adaptive algorithms of optimal orders [110], systolic algorithms [30] and, more in general, symplectic codes [18, 32, 138]. At the time being, typical capabilities of N-body integration software include the handling of a few hundred bodies with simple (spherical) shape. Collisions and contact interaction between bodies are often resolved by interfacing with hydrodynamics codes or by implementing hard/soft sphere collision models [94, 111].

This section presents an innovative method used to model the N-body gravitational and contact behaviour of a cluster of complex-shaped bodies. The problem is implemented using the open source Chrono::Engine (C::E) simulation library [90, 130], which is able to handle the contact and collision of large numbers of complex-shaped objects. From a computational standpoint, the problem is characterized by the need to consider long-time simulations of a large number of interacting bodies, simultaneously subjected to gravity and contact forces. Gravity implies many-to-many interaction, which depends on the inverse of the distance squared. Contact forces require collision detection and the handling of non-smooth problems. C::E was selected for its peculiar ability to efficiently and effectively simulate the collision and interaction of large numbers of irregularly-shaped bodies. In the following, only the aspects related to the N-body gravitational dynamics are deepened, since they are relevant for the case of numerical method for non-Keplerian dynamics, which is the topic of this chapter. As they are out of the scope of this thesis work, the complete multi-body model and contacts handling strategy are not detailed here. The interested reader can refer to [51] for further details on the multi-body model, including a more detailed description of contact model and collision dynamics implemented.

3.4.1 N-body gravitational dynamics

The method is used to obtain a mass distribution model asteroids after N-body aggregation. In order to obtain different classes of bodies, the method allows to investigate the effects that different initial conditions sets have on the physical properties of the final aggregate. Initial conditions are given to initiate the relative distance and velocity between bodies and also to initiate their absolute state with respect to a given inertial frame (XYZ). The dynamics of the system is allowed to have a predefined orbital angular momentum about the origin O of the aforementioned inertial frame. In this case, all bodies rotate about O with a constant angular velocity $\mathbf{\Omega}$. System (2.63), representing the equations of motion for the centre of mass of each body, can be equivalently written in a rotating frame (xyz) that rotates

with angular velocity $\mathbf{\Omega}$ with respect to the inertial frame

$$m_i\ddot{\mathbf{r}}_i = G\sum_{j=1,j\neq i}^{N}\frac{m_i m_j}{\|\mathbf{r}_{ij}\|^3}\mathbf{r}_{ij} - m_i\mathbf{\Omega}\times(\mathbf{\Omega}\times\mathbf{r}_i) - 2m_i\mathbf{\Omega}\times\dot{\mathbf{r}}_i \qquad \forall i = 1:N \tag{3.39}$$

where $\mathbf{r}_i$ is the position vector of body i in the rotating frame and $\mathbf{r}_{ij} = \mathbf{r}_j - \mathbf{r}_i$. The effect of the rotation is included by adding Coriolis and centrifugal terms to the equation of motion of the centre of mass of the i-th body. The addition of a predefined orbital angular momentum to the system is used here to simulate a realistic asteroidal aggregation process, e.g. re-accumulation dynamics of asteroidal fragments after a collision event. In this case, all fragments initially belong to a unique asteroid that spins with a certain angular velocity about its principal inertia axes. After a collision with an external body occurs, fragments are created and scattered away from the main body, but they keep part of the orbital angular momentum they had before the collision when they were part of a unique body. The aggregation phase simulated here can be applied to the subsequent re-accumulation phase, as well as to other asteroid aggregation scenarios.

The code is classified as a numerical *integrator*, since it implements all N to N gravitational interactions between bodies. More in detail, the code implements equations (3.39). From the numerical point of view, system (3.39) is an initial value problem and its solution strongly depends on the choice of the initial conditions set, namely the initial relative state of each body and angular velocity of the rotating frame. An important feature of gravitational interaction, to be considered from the numerical point of view, is that it is characterized by slow dynamics: for the case of N bodies, the shortest characteristic time can be estimated as follows [112]

$$T \sim \frac{1}{\sqrt{G\rho}} \tag{3.40}$$

More in detail, a particle under the attraction of mass M at distance r is known to orbit around it with orbital period proper of Keplerian solutions:

$$T \sim \frac{1}{\sqrt{GM/r^3}} \tag{3.41}$$

In the case of N-body interactions, the fastest dynamics in the system are found when two bodies happen to be very close to each other. The limiting case can be found by assuming r as minimum distance between the two bodies (characteristic size of the body) and M as mass of the body. In

this case, the standard Keplerian form can be written as (3.40), where $\rho \sim M/r^3$ is the material density of the bodies. A constraint for the numerical integrator is derived from (3.40): since the dynamics are slow, there is no need of having extremely small time steps of integration. To catch the correct dynamical behaviour of the system, the integrator time step shall satisfy

$$t_{step} < \frac{T}{2} = \frac{1}{2\sqrt{G\rho}} \tag{3.42}$$

For typical values of asteroid material density ranging from 1000 to 4000 kg/m^3 [111], the maximum time step results in the order of 10^3 s.

3.4.2 Degrees of freedom

Several parameters have to be set to initiate the simulation of the asteroid aggregation process. To simulate realistic scenarios it is important to carefully select the physical properties of the N bodies and to consistently initiate their dynamics. Initial conditions play an extremely important role when dealing with N-body dynamics. The set of initial conditions includes the initial state of all N bodies. As described in Section 3.4.1, the state of all bodies is expressed in a rotating frame that rotates with angular velocity $\mathbf{\Omega}$ with respect to an inertial reference. In addition, the relative state of each body, namely their position and orientation, as well as their linear and angular velocity, are initialized with respect to the rotating reference frame. Initial conditions are given at initial simulation time, or t_0 in the following.

From the numerical point of view, the choice of the number of bodies is crucial, since it has a great impact on the computational effort. For an integrator, the cost of evaluating gravity is N^2. For this reason, typical capabilities of numerical integrators are often limited to few hundreds of bodies. The computational cost can be reduced by clustering the gravitational effect of bodies through domain decomposition. In this case, the cost can be reduced to $N \log N$ (N-body simulators [112]).

An example of a complete set up of the numerical simulation and analysis of asteroid aggregation results, is provided in Section 4.2.

3.4.3 Identification of aggregate's shape

When a stable aggregate is found, after its stabilization, the aggregate is considered as a single asteroid. The shape of the aggregate is found as the envelope of all bodies in the aggregate using an Alpha-Shape algorithm [33]. Intuitively, the Alpha-Shape algorithm finds the enveloping surface of the aggregate by rolling a sphere of radius α over the cluster of

points representing the vertexes of the bodies. The value of α influences the final result since it constrains the path of the rolling sphere, with $\alpha = \infty$ being equivalent to the convex hull representation. For this reason, α must be accurately chosen, based on characteristic size information on the final aggregate.

CHAPTER 4

Non-Keplerian Solutions for Astrodynamics Problems

In order to support mission analysis and trajectory design, relevant solutions were generated for the most common systems related to space mission applications. Solutions presented here are computed using techniques discussed in Chapter 3.

As mentioned, the software architecture of Section 3.1 is used to find spacecraft trajectories within restricted problems. Among these, catalogues of periodic orbits were built to quickly provide orbits to the designer, to be selected according to specific requirements or mission objectives. Some of them are presented here, with particular emphasis on new solutions identified in the ER3BP and in the proximity of small celestial bodies. A survey of periodic orbits is presented in Section 4.1: ER3BP solutions are classified according to their resonance properties in Section 4.1.2 and correlated with well-known CR3BP solutions. Examples of periodic motion near small celestial bodies are also shown in Section 4.1.3.

Section 4.2 shows results obtained from an N-body aggregation simulation, using the numerical method introduced in Section 3.4. The simulation scenario aims at reproducing the asteroid aggregation process, with refer-

ence to available data from asteroids in the NEA population.

4.1 Periodic orbits

Examples of periodic motion computation is reported here. Attention is paid to new solutions found in the Sun-Earth and Earth-Moon ER3BP and within the binary asteroid system 65803 Didymos. Properties of families of orbits around collinear libration points in the CR3BP are discussed to support the investigation of ER3BP periodic motion.

4.1.1 The Circular Restricted Three-Body Problem

The orbital period ranges within Halo, planar and vertical Lyapunov families around collinear libration points are reported for the case of Earth-Moon and Sun-Earth CR3BP. Table 4.1 shows orbital period ranges for Halo families computed around L1, L2 and L3 in both Earth-Moon and Sun-Earth system. Orbital periods are expressed in nondimensional form, as recalled in Section 2.1.1, with 2π being the nondimensional period of revolution of primaries. In both systems, the orbital period of L1 and L2 families is shown to be significantly lower than L3 family, the latter being on the order of one revolution of primaries. Planar and Vertical Lyapunov families have in general higher periods with respect to Halo orbits as they can became very large. For the case of L1 and L2 families, orbital periods ranges between approximately 3 nondimensional units, up to 5-7 nondimensional units. Results found are in agreement with data reported reported in [52, 66].

Table 4.1: *Nondimensional orbital period for Halo families computed in the CR3BP.*

	T [nondim]	
Libration Point	Earth-Moon	Sun-Earth
L1	1.84 - 2.78	1.52 - 3.06
L2	1.77 - 3.41	1.87 - 3.10
L3	6.15 - 6.23	6.28 - 6.28

4.1.2 The Elliptic Restricted Three-Body Problem

A survey of periodic motion in the ER3BP is presented here. The orbits are classified depending on the number of revolutions they perform around collinear libration points during one revolution of the primaries. Examples from both Earth-Moon (eccentricity $e = 0.0554$) and Sun-Earth

($e = 0.0167$) systems are shown. Resonant motion in the CR3BP is identified to be used as initial guess to compute periodic orbits in the ER3BP. Table 4.2 shows periods of common resonant orbits, chosen in the interval between $\pi/5$ and π, with a maximum of $N = 2$, with $M, N \in \mathbb{N}^+$ indicating respectively, the number of revolutions around libration point and the number of revolutions of primaries.

Table 4.2: *Orbital period of common resonant orbits.*

T [nondim]	M:N
1.26	5:1
1.40	9:2
1.57	4:1
1.79	7:2
2.09	3:1
2.51	5:2
3.14	2:1
4.19	3:2
6.28	1:1

Concerning CR3BP solutions, the existence of resonant motion in the Halo families can be established by comparing Table 4.1 with Table 4.2. Resonant 3:1 and 5:2 Halo orbits exist around L1 and L2, both in the case of Earth-Moon and Sun-Earth system. In the Earth-Moon system, the L2 family has a slightly wider period range with respect to the L1 family and includes 7:2 and 2:1 resonant orbits as well. In the Sun-Earth system, Halo orbits with lower periods exist in the L1 family and 4:1 resonance is found. A significantly larger period is observed for Halo orbits about the L3 point. In this case the period is on the order of 2π and a 1:1 resonant behaviour is observed for orbits of the L3 Halo families in the Sun-Earth system. As for the case of vertical and planar Lyapunov families, 3:2 resonance is found in all families around L1 and L2, in both Earth-Moon and Sun-Earth systems, and 2:1 resonance is found in most of them. Families of Lyapunov about L3 have period of approximately 2π, as in the case of Halo orbit families, leading to 1:1 resonant motion with primaries.

Single-revolution orbits

Single-revolution orbits in the ER3BP are associated to 1:1 resonance with the motion of the primaries: the spacecraft completes one orbit as the primaries do the same around the barycentre of the system. Suitable initial guess for periodic motion in ER3BP typically refer to 1:1 resonant orbits

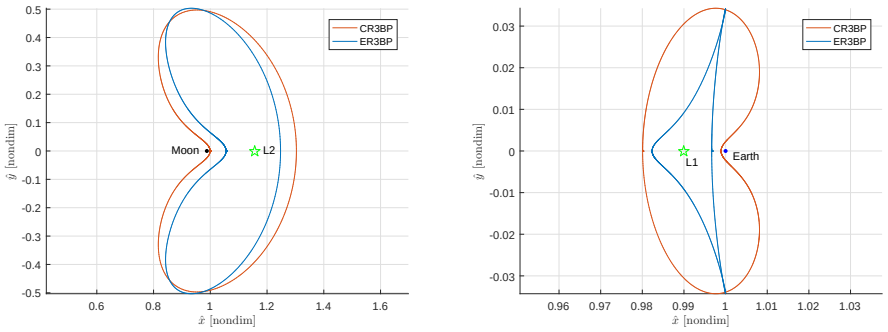

(a) (b)

Figure 4.1: *Single-revolution orbits: planar Lyapunov in CR3BP (red) and ER3BP (blue). (a) L2 orbit in the Earth-Moon system (1:1 in the CR3BP). (b) L1 orbit in the Sun-Earth system (5:2 in the CR3BP).*

in the circular problem. In particular, solutions around L3 are of interest, as well as large Lyapunov orbits, with period of 2π. An example, referring to a planar Lyapunov orbit about L2 in the Earth-Moon system, is shown in Figure 4.1(a). The picture shows the initial guess given to the correction algorithm in red (the 1:1 Lyapunov resonant orbit in the CR3BP) and the periodic solution after correction in the Earth-Moon ER3BP in blue, as seen from the nondimensional rotating-pulsating frame. The eccentricity of the problem is shown to have an effect on the orbit, as it shrinks the amplitude of the orbit along the x axis. However, apart from this small effect, no significant deviation from the circular case is found. This kind of behaviour is observed for many 1:1 orbits, including those around L3, which are then not very much affected by the eccentricity of the system.

A further example of single-revolution motion is shown in Figure 4.1(b), with the case of a periodic orbit in the ER3BP generated from a 5:2 planar Lyapunov orbit about L1 in the CR3BP. The corrector converges to a single revolution orbit, of period 2π despite the different resonance properties of the same orbit in the CR3BP, which completes 5 revolutions every two revolutions of primaries. In addition to the different period, the geometry of the solution appears to be different and a greater deviation is observed with respect to the previous case.

Single-revolution orbits appear to be the only possible periodic motion around L3: no multiple-revolution orbits are observed about L3. The reason is found in typical orbital periods of L3 orbits, which are in the order of 2π. Only 1:1 resonance motion is observed in this particular location.

Double-revolution orbits

Double-revolution orbits are found starting from 2:1 resonance in the circular problem. Since such periodic motion exists in Halo and Lyapunov families around L1 and L2 points, double-revolution orbits are found to be quite common solutions in the ER3BP. Examples related to Halo, vertical and planar Lyapunov are shown here.

Figure 4.2 shows examples of double-revolution orbits in the Earth-Moon system. Periodic motion is depicted both in the nondimensional rotating-pulsating frame (figures on the left side) and in the Moon centred inertial frame (figures on the right side). Figures 4.2(a) and 4.2(b) refer to a planar solution found starting from a Lyapunov orbit about L1. As any other orbit shown in this work, the orbit is symmetric with respect to the x-z plane. Due to its symmetry, the time between two consecutive perpendicular crossings with the x-z plane is π. This result is in agreement with the aforementioned mirror theorem, since every perpendicular crossing occurs when the primaries are at an apse (every π). The orbit is made of two loops and a half (symmetric) orbit includes the two halves of each loop. Each loop has a period of approximately π, as the initial guess orbit in the CR3BP. In particular, the smaller loop has a period slightly larger than π, while the bigger loop is flown in a shorter time. Figures 4.2(c) and 4.2(d) shows a three-dimensional periodic solution, found starting from a Halo orbit around L2 in the CR3BP. The three-dimensional view is shown together with the projection of the ER3BP orbit on the x-y, x-z and y-z planes. The same is shown for the periodic orbit in Figure 4.2(e) and 4.2(f), which refer to a solution generating from a vertical Lyapunov near the L1 point. For the case of double-revolution orbits shown in this work, all periodic solutions appear to have similar properties in terms of geometry and period with respect to their corresponding CR3BP orbit. Both Halo, planar and vertical Lyapunov orbits in the CR3BP have period of π (they replicate their initial state after 2π as well) and they split into two geometrically similar orbits in the ER3BP. The nonzero eccentricity has the effect of duplicating the single orbit into two semi-orbits, which does not replicate itself after π as in the CR3BP, but becomes periodic of period 2π in the ER3BP. More in detail, the two semi-orbits appear to be symmetric along the x axis, with a contact point shared with their CR3BP reference orbit. The presence of the contact point between ER3BP and CR3BP solutions is enforced by the single-shooting numerical correction algorithm in use, to find a periodic solution in the ER3BP associated to the specific (resonant) solution in the CR3BP. Trajectories as seen from the Moon centred inertial frame are

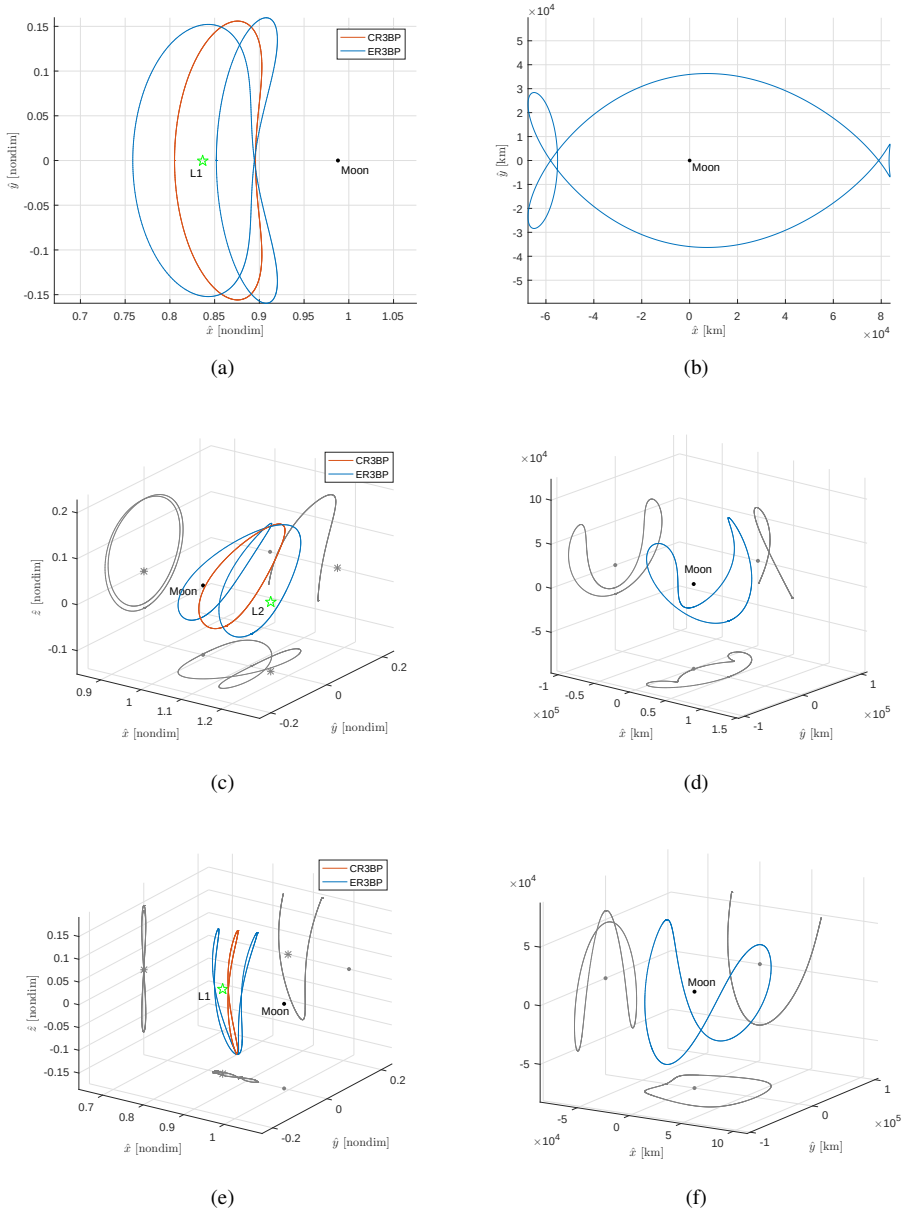

Figure 4.2: *Double-revolution orbits (Earth-Moon system) shown in nondimensional rotating-pulsating frame (left) and Moon centred inertial frame (right). Solutions generated from 2:1 resonant orbits in CR3BP: (a,b) planar Lyapunov about L1, (c,d) Halo about L2, (e,f) vertical Lyapunov about L1. Projections of 3D ER3BP orbits on x-y, x-z and y-z planes are shown in gray.*

also of interest. Since the motion is in resonance with primaries, it results to be periodic in the inertial frame as well. Interesting behaviour appears both for the planar case (Figure 4.2(b)) and for the three-dimensional cases (Figure 4.2(d) and Figure 4.2(f)), where the orbits are shown to surround the Moon with very peculiar oscillating paths.

Triple-revolution orbits

As for the case of double-revolution orbits, the existence of 3:1 resonance in all families of Halo and Lyapunov orbits about L1 and L2 makes triple-revolution orbits quite common solutions in the ER3BP. Figure 4.3 shows some examples of triple revolution orbits, obtained from corresponding periodic motion in the CR3BP. In this case, periodicity in the state is reached after three orbital loops. With analogy to what was observed at the double-revolution cases, a similar orbit to that of CR3BP is replicated three times. In the case of Figures 4.3(a) and 4.3(b), the periodic motion in the ER3BP is found starting from a 3:1 resonant Halo orbit about L2 in the CR3BP. Such orbit possesses orbital period of $2\pi/3$. This example is in analogy with the case shown in Figure 4.2(c) and 4.2(d): both cases refer to a Halo orbit about L2, but with different orbital period. Figures 4.3(c) and 4.3(d) show an ER3BP solution associated to a 3:2 vertical Lyapunov about L1 in the CR3BP. In this case, the CR3BP guess has an orbital period of $4\pi/3$, since it completes three orbital loops as the primaries revolve two times around the barycentre of the system. The orbital period is doubled with respect to the case shown in Figures 4.3(a) and 4.3(b). Accordingly, the resulting trajectory in the ER3BP is periodic with period 4π. Geometrically, the outcome is similar to those observed so far: the orbit makes three loops and is periodic both in the synodic and in the inertial frame. Same considerations apply for the case of Figures 4.3(e) and 4.3(f), which refer to a periodic ER3BP solution generated from a 3:2 resonant vertical Lyapunov about L2 in the CR3BP. Periodicity is also observed after two revolutions of primaries (4π). Very interesting behaviour is observed for triple-revolution orbits, as seen from the Moon centred inertial point of view. As for the case of double-revolution orbits, the trajectory path surrounds the Moon with oscillations associated to the three orbital loops that characterize triple-revolution motion.

A very interesting solution is obtained when providing a 3:1 resonant Halo orbit about L1 in the CR3BP as initial guess. In this case the starting point is a orbit with period $2\pi/3$ and three loops are obtained in the ER3BP, in order to match the period of 2π. The correction algorithm converges into a peculiar solution, that connects motion between the neighborhoods of L1

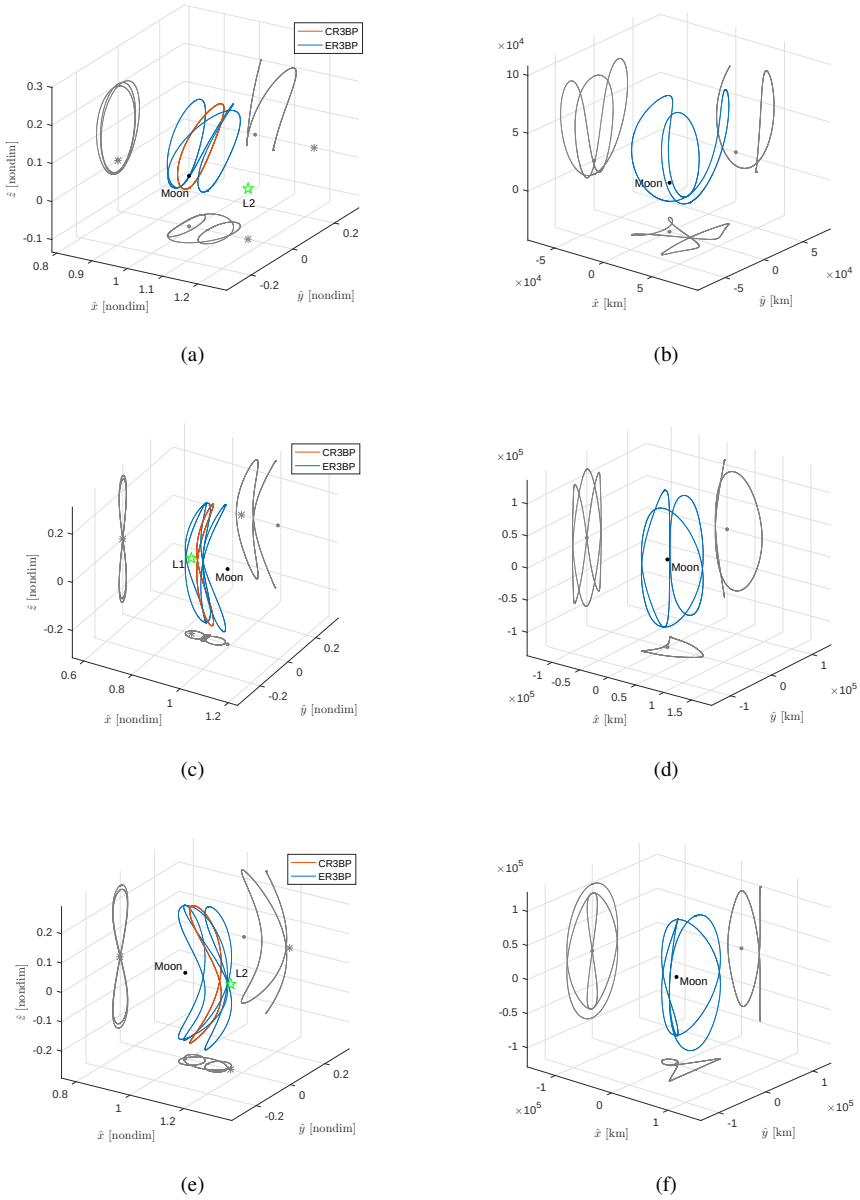

Figure 4.3: *Triple-revolution orbits (Earth-Moon system) shown in nondimensional rotating-pulsating frame (left) and Moon centred inertial frame (right). Solution generated from 3:1 resonant Halo about L2 in CR3BP (a,b). Solutions generated from 3:2 resonant orbits in CR3BP: (c,d) vertical Lyapunov about L1, (e,f) vertical Lyapunov about L2. Projections of ER3BP orbits on x-y, x-z and y-z planes are shown in gray.*

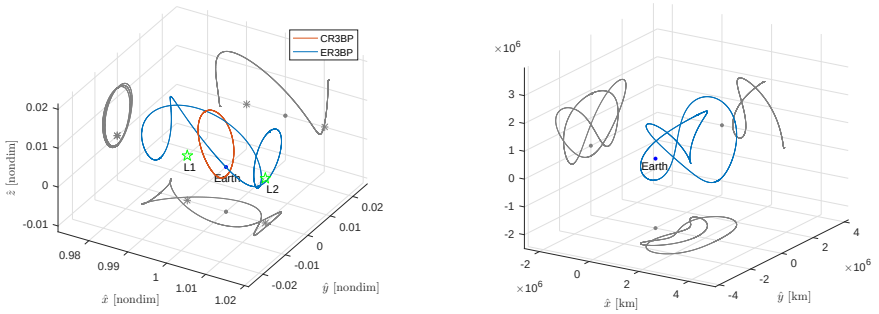

(a) (b)

Figure 4.4: *Triple-revolution orbit (Sun-Earth system) shown in (a) nondimensional rotating-pulsating frame and (b) Earth centred inertial frame. Solution generated from 3:1 resonant Halo about L1 in CR3BP. Projections of ER3BP orbit on x-y, x-z and y-z planes are shown in gray.*

and L2 points. Such solution is in fact a heteroclinic connection between a solution around L1 and a solution around L2. This periodic orbit might be of great interest for space applications, since it provides free motion between L1 and L2 and follows the higher fidelity dynamics associated to ER3BP.

Quadruple-revolution orbits

The last class of periodic motion reported here is quadruple-revolution motion. Few cases of 4:1 resonance exist in the families of vertical and planar Lyapunov. No 4:1 resonance orbit exists in the Halo families about L1, L2 or L3 in the Earth-Moon system. As for the case studied in this work, such resonance is observed only in the family of Halo orbits around L1, in the Sun-Earth system. Figure 4.5(a) and 4.5(b) show an example of four-revolution solution obtained from the 4:1 Halo about L1 in the Sun-Earth CR3BP. As for the last case of triple-revolution orbits shown, the corrector converges to a heteroclinic connection between L1 and L2 solutions. In this case, the initial guess orbit possesses period of $\pi/2$ and then, the ER3BP orbit is periodic after looping four times between L1 and L2. The looping behaviour is clearly seen when looking at the projection of the motion in the synodic frame on the y-z axis.

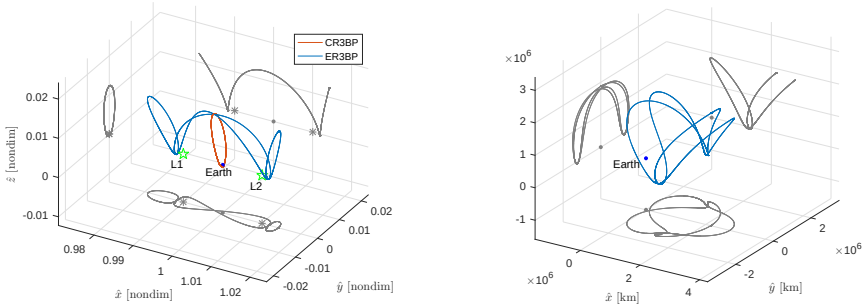

(a) (b)

Figure 4.5: *Quadruple-revolution orbit (Sun-Earth system) shown in (a) nondimensional rotating-pulsating frame and (b) Earth centred inertial frame. Solution generated from 4:1 resonant Halo orbit about L1 in the CR3BP. Projections of ER3BP orbit on x-y, x-z and y-z planes are shown in gray.*

4.1.3 Small celestial bodies

Examples of periodic motion computation in the proximity of a binary asteroid system are provided in Figure 4.6. Halo and Lyapunov families around L1 and L2 points are computed using a shape-based model of Didymos binary asteroid system. Following the scheme discussed in Section 3.2.3, the initial guess is provided using families of orbits in the Didymos CR3BP. Periodic solutions were subsequently obtained in the higher fidelity shape-based Didymos model. Didymain (bigger asteroid of the couple) is modeled as a constant density polyhedron, while Didymoon (smaller asteroid) as a constant density ellipsoid. Further details on the shape-based model of Didymos system are provided in Section 5.2.1. As discussed, the orbit in the shape-based model is obtained by slightly varying the shape of the primaries from spherical to the actual ones. Such an approach benefits the space mission design, since it provides more accurate and realistic solutions to the designer.

4.2 Asteroid mascon models

Following the method described in Section 3.4, the purpose is to study the gravitational aggregation process of a cluster of boulders and to investigate favorable conditions for the formation of a stable aggregate. The simulation setup related to the NEA scenario to be studied is presented in Section 4.2.1. The problem to be investigated is twofold: the study of gravitational aggre-

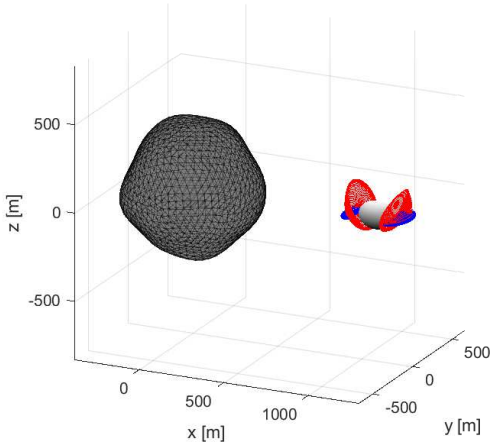

Figure 4.6: *Halo (red) and Lyapunov (blue) families about L1 and L2 in the shape-based model of Didymos system*

gation dynamics, and the study of the physical and dynamical properties of the final aggregate. The first aspect includes the analysis and numerical simulation of typical scenarios, for small and medium-size (hundreds of meters) asteroid aggregation, to identify dynamical conditions that lead to the formation of the aggregate or to the dispersion of the particle cloud. The dynamical evolution of the system, up to the formation (or non-formation) of a stable aggregate is studied in Section 4.2.2. The aggregation process is studied by looking at the time profile of the orbital angular momentum of the N-body system, and by monitoring the evolution of the relative position of all bodies. The second aspect is related to what happens after the transient. In case the system has converged to a stable asteroidal aggregate, the resulting physical and geometrical properties are studied and compared to the properties of known asteroids. Shape and inertia properties of the aggregate and their dependence on initial conditions are investigated. Results are shown in Section 4.2.3 for all simulation sets. Significant quantities extracted from the simulation scenarios include the bulk density (mean density, including void fraction) of the aggregate, its inertial elongation (ratio between maximum and minimum principal inertia moments) and rotation state. In this respect, future work would include the generation of a catalogue of asteroid aggregates suitable to represent the mass distribution of different classes of bodies.

4.2.1 Simulation set up

The parameters are selected to simulate the aggregation process of common asteroids of small/medium size, with a characteristic size of hundreds of meters. The physical properties of the asteroids are chosen among typical values of objects belonging either to the main asteroid belt or to the Near Earth Asteroids (NEA) population [76, 78]. Table 4.3 summarizes all simulation parameters in use. In the simulations, 200 bodies are randomly generated in a three-dimensional cube whose side is 5 km long. The bodies are medium size boulders of 130 m characteristic size on average, with the smallest ones of 40 m. As mentioned earlier, this is likely the case of re-accumulation after fragmentation due to a collision event. The aggregate is then a "rubble pile" of loosely aggregated boulders. The material density is set to 3000 kg/m^3, which is typical for metallic-based asteroids [111]. As discussed in Section 3.4, gravity interactions are slow and the integrator time step can be of the order of 10^3 s. However, a time step of 10 s is chosen to correctly integrate collision dynamics, which are much faster and need shorter integration time steps. With these figures, aggregation processes reach a stable configuration after a transient of few tens of hours, corresponding to computational times on the order of few minutes.

Table 4.3: *Simulation parameters*

Parameter	Symbol	Value
number of bodies	N	200
characteristic size of bodies [min-average]	L^*	40-130 m
material density	ρ	3000 kg/m^3
initial position cube side length	L_0	5 km
integration time step	t_{step}	10 s

Simulations are performed considering different sets of initial conditions. The norms of linear and angular velocity vectors of each body range from 0 (no relative motion between bodies) to the maximum values specified in Table 4.4. Analogously, different cases are explored concerning the angular velocity of the rotating frame, which ranges from 0 to the maximum value in Table 4.4. Maximum values specified in Table 4.4 are identified as thresholds above which there is no aggregation of the bodies, which are scattered apart from each other by too high relative velocities or centrifugal force.

Table 4.4 defines boundaries on the magnitude of the velocities. Without any loss of generality, the inertial frame (XYZ) is oriented such that $\mathbf{\Omega}$ is

Table 4.4: *Range of values for initial conditions set*

Parameter	Symbol	Max value
linear relative velocity of bodies	v_0	$0.15\ m/s$
angular relative velocity of bodies	ω_0	$10^{-2}\ rad/s$
angular velocity of rotating frame	Ω	$5 \cdot 10^{-5}\ rad/s$

directed towards the positive Z axis, with $\mathbf{\Omega} = \Omega\hat{\mathbf{Z}} = \Omega\hat{\mathbf{z}}$

$$\mathbf{\Omega} = \Omega \begin{Bmatrix} 0 \\ 0 \\ 1 \end{Bmatrix} \tag{4.1}$$

The direction of the linear and angular velocity of each body is randomly generated.

The simulation campaign is performed by imposing to the system several initial condition sets, in order to cover different aggregation scenarios and to explore the combined effects between the initial conditions. Table 4.5 summarizes all simulation sets considered. Each simulation set is labeled using an ID, to provide references during the analysis of results.

Table 4.5: *Simulation sets*

Simulation set	ID	$v_0\ [m/s]$	$\omega_0\ [rad/s]$	$\Omega\ [rad/s]$
0 - no initial motion	0	0	0	0
1 - single parameter	1.1	$0 - 0.15$	0	0
	1.2	0	$0 - 10^{-2}$	0
	1.3	0	0	$0 - 5 \cdot 10^{-5}$
2 - double parameter	2.1	$0 - 0.15$	$0 - 10^{-2}$	0
	2.2	$0 - 0.15$	0	$0 - 5 \cdot 10^{-5}$
	2.3	0	$0 - 10^{-2}$	$0 - 5 \cdot 10^{-5}$
3 - all parameters	3	$0 - 0.15$	$0 - 10^{-2}$	$0 - 5 \cdot 10^{-5}$

The case with no initial motion between bodies and no rotation imposed is marked ID '0'. The first simulation set (ID '1') includes the analysis of the effect of one initial condition at a time, with the remaining set to zero. The second set (ID '2') analyzes the effect of two parameters at a time. Finally, the third set of simulations (ID '3') investigates the effect of simultaneous action of all initial conditions.

4.2.2 Aggregation dynamics

An example of aggregation sequence is shown in Figure 4.7 for case ID '0'. The N bodies are driven solely by their mutual attraction, with no effects due to rotation of the reference frame. When boulders start to interact, few small bodies are scattered away because of collisions and others depart after reaching escape velocity conditions without any collision interaction. In this case, after a dynamical transient, a stable aggregate eventually forms.

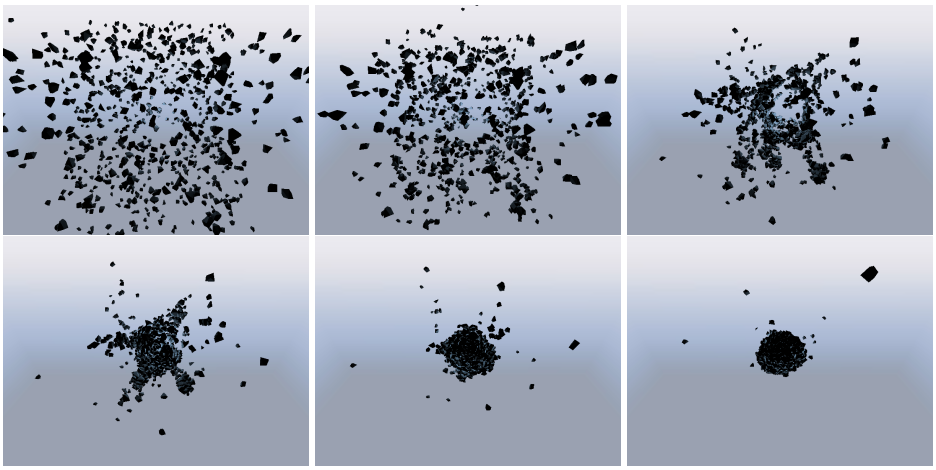

Figure 4.7: *Aggregation sequence: case ID '0' (example with 1000 bodies).*

Figures 4.8 and 4.9 show the time profile of the orbital angular momentum of the system $\mathbf{H}$ with respect to the origin of the inertial frame, computed as the vectorial sum of orbital angular momenta $\mathbf{h}_i$ of the N bodies

$$\mathbf{H} = \sum_{i=1}^{N} \mathbf{h}_i = \sum_{i=1}^{N} m_i \mathbf{r}_i \times \mathbf{v}_i \tag{4.2}$$

The orbital angular momentum $\mathbf{h}_i$ refers to the orbital motion of the centre of mass of the *i*-th body, where $\mathbf{r}_i$ and $\mathbf{v}_i$ are its velocity and position with respect to the origin of the inertial frame. The contribution due to the spinning motion of the *i*-th body is not accounted in $\mathbf{h}_i$. In the case of stable aggregate formation, the orbital angular momentum of the N-body system is also the rotational spinning angular momentum of the final aggregate. For this reason, $\mathbf{H}$ is also referenced as rotational energy of the aggregate.

The norm and the three Cartesian components of $\mathbf{H}$ are shown as a function of simulation time. Case ID '0' is shown in Figure 4.8(a). At t_0, the system is at rest; after a few hours, the first collisions between bodies take

place. Most of the collisions occur between 5 and 10 hours after t_0. After the transient, the system turns into a single aggregate. The system is initially at rest and after the aggregation process, the final aggregate rotates with a period of about 10^3 hours (slow rotator). A different case, extracted from set ID 1.3, is shown in Figure 4.8(b). In this case, the centre of mass of the *N* bodies are initially provided with a common orbital angular velocity ($\Omega = 1.5 \cdot 10^{-5}$ rad/s). The orbital energy of the system is partially dissipated by collision events (between 5 and 10 hours after t_0), but in the end most of it is converted to rotational energy of the final aggregate. The final cluster rotates with a period of a few hours (fast rotator).

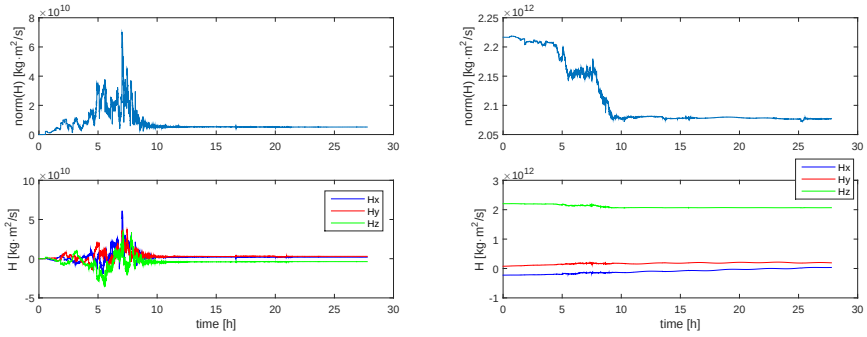

Figure 4.8: *Orbital angular momentum of the N-body system: (a) case ID '0' (b) case extracted from set ID '1.3'* ($\Omega = 1.5 \cdot 10^{-5}$).

Figure 4.9(a) shows a simulation case extracted from set ID 1.2. The bodies are provided with a given spinning velocity about their body axes ($\omega_0 = 4 \cdot 10^{-3}$ rad/s). The spinning state of each single body is transmitted between boulders through collisions up to the formation of a single aggregate, which have nonzero angular velocity despite the absence of initial orbital motion of the N bodies. In this specific case, the final aggregate is left with a rotation period of some tens of hours (slow rotator). The effect of combined initial conditions in ω_0 and Ω is shown in Figure 4.9(b). The effect due to collisions of dissipating the kinetic energy associated with rotation and of transferring orbital angular momentum among bodies is balanced in this case. The orbital angular momentum of the system stabilizes at about its initial value after the collisions transient. The resulting aggregate is a fast-spinning asteroid.

Maximum breakup values (Table 4.4) identify the values of v_0, ω_0 and Ω above which no aggregation occurs for the case of study specified in

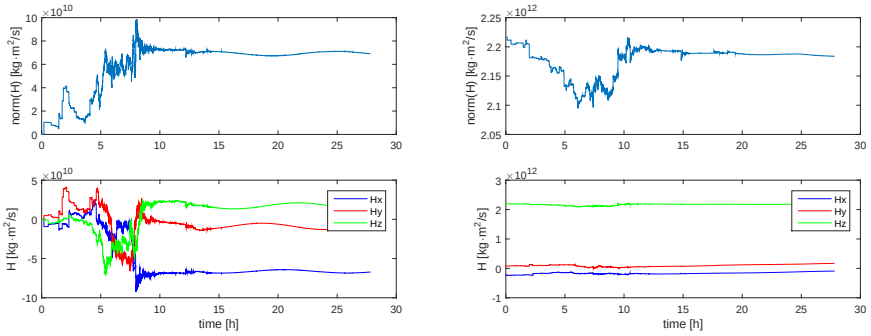

(a) (b)

Figure 4.9: *Orbital angular momentum of the N-body system: (a)* $\omega_0 = 4 \cdot 10^{-3}$ *rad/s (from set ID '1.2') (b)* $\omega_0 = 7 \cdot 10^{-3}$,$\Omega_0 = 1.5 \cdot 10^{-5}$ *rad/s (from set ID '2.3').*

Table 4.3. The results in terms of breakup values show good agreement with data from the literature: as mentioned in [111], no stable aggregate larger than 200 m is observed to spin faster than critical breakup period, which is approximately 2.2 h for strength-less bodies of density ∼3000 kg/m^3. Also, aggregation is found for relative speeds between fragments lower than surface escape velocity from the stable aggregate, which is found in the range between 0.4 and 0.8 m/s for the case under study.

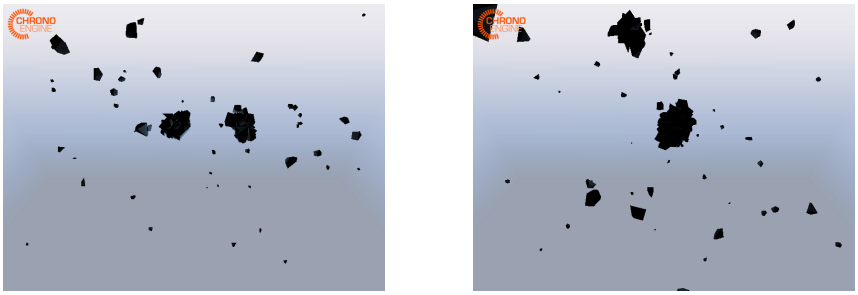

Figure 4.10: *Formation of two main aggregates, extracted from simulation set ID 2.3 and ID 2.2.*

The formation of more than one aggregate is observed when initial conditions are close to their maximum breakup values. A very common behaviour is that of two-lobed asteroids, which are very common in the Solar System asteroidal population, as it will be discussed in Section 5.1.1. As observed from the simulation performed, it is very likely for boulders to combine into two main aggregates, which after a certain time collide with

each other to form one bigger aggregate, or become a close or contact binary asteroid. Figure 4.10 shows two phases of such process, with the formation of two main aggregates.

4.2.3 Asteroid aggregate

Different kinds of aggregates were obtained from the simulation campaign. This Section identifies the properties of the aggregates and compares them with known asteroids to verify the ability of the numerical code of representing gravitational aggregation phenomena. Once the asteroid is found and its shape identified through the alpha shape algorithm (Section 3.4.3), its characteristics are studied. Significant properties of asteroids are briefly defined here. The first quantity considered is the *inertial elongation* (or simply *elongation* in the following) λ, that is defined as the ratio between the maximum and the minimum principal inertia moments. It is always greater than or equal to one: the larger λ is, the more elongated the asteroid is. Note that this property refers to the mass distribution of the asteroid, not to its geometry. An important quantity for the case of asteroids is the *bulk density* ρ_b, that refers to the mean density of the asteroid, including internal voids. Accordingly, the porosity P is defined as

$$P = 1 - \frac{\rho_b}{\rho} \tag{4.3}$$

where ρ is the material density (Table 4.3). In the following, T_{agg} is used to indicate the period of rotation of the aggregate, M_{agg} its total mass, and N_{agg} the number of bodies (out of 200) in the final aggregate.

Figure 4.11 shows how inertial elongation, rotation period and number of bodies in the aggregate are affected by initial conditions on v_0 (blue asterisks), ω_0 (green stars) and Ω (red diamonds) for the case of study (Table 4.3). Exponential or polynomial fitting curves are displayed to separately show the trend of each contribution. The values of the initial conditions refer to a normalized range on the abscissa: each parameter ranges from 0 to 1, with 0 as their minimum value ($v_0 = \omega_0 = \Omega = 0$) and 1 their maximum value ($v_0 = v_{0_{\text{max}}}$, $\omega_0 = \omega_{0_{\text{max}}}$, $\Omega = \Omega_{\text{max}}$ from Table 4.4). The upper plot shows that high elongations are obtained for high Ω or for low v_0, while no precise trend can be derived for ω_0. On the other plots, all parameters are observed to share a common trend characterizing their effect on rotation period and number of bodies in the aggregate. As far as the former is concerned, small relative motion and rotation produce slowly rotating asteroids and vice versa: fast rotators are formed when the bodies are initialized with high angular and linear velocities. In particular, within the

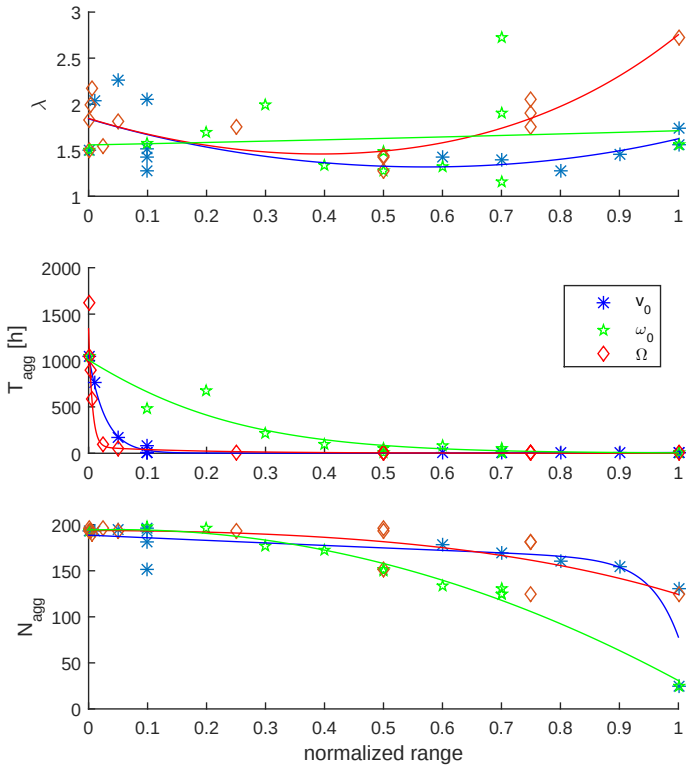

Figure 4.11: *Properties of the final aggregate as a function of normalized initial conditions: simulation results and best fitting curves.*

validity domain of this case of study, Ω is observed to produce the strongest effect and ω_0 the weakest one. As for the last case, the number of bodies aggregating in the final asteroid decreases as velocities increase, with ω_0 playing a dominant role.

Figure 4.12 shows simulation results that correlate the rotation period of the asteroid to its elongation and total mass. Results are shown on semi-logarithmic plots (the rotation period scale is logarithmic). A clear trend can be extracted from the plot on the right: as far as gravitational aggregates are concerned, smaller asteroids rotate faster than more massive ones. This is found in agreement with balancing between centrifugal force and gravitational attraction predicted by the theory [111].

Figures 4.13 and 4.14 show examples of asteroids obtained by envelop-

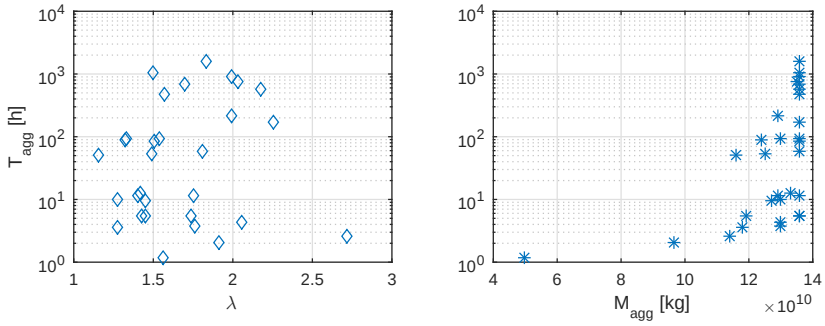

Figure 4.12: *Simulation results: rotation period as a function of inertial elongation and total mass in the asteroid population.*

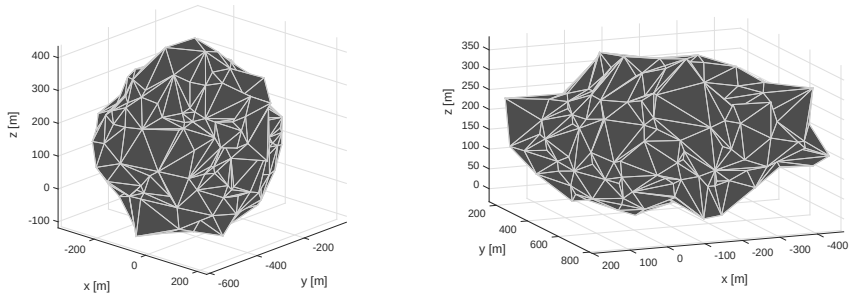

(a) (b)

Figure 4.13: *Shape of the final aggregate: (a) minimum (from set ID '1.2') and (b) maximum (from set ID '2.3') inertial elongation case.*

ing all aggregating bodies after the dynamical transient. Minimum (Figure 4.13(a)) and maximum (Figure 4.13(b)) elongation cases are shown, in a population of asteroids ranging from quasi-spherical shapes ($\lambda_{\text{min}} \simeq 1.15$) to highly elongated ones ($\lambda_{\text{max}} \simeq 2.7$).

For what concerns the porosity (or equivalently the bulk density) of the aggregates, the results show that very little variability exists for the case of study. Porosity is found between 34% and 40% for all large stable aggregates found, corresponding to $\rho_b \simeq 1900$ kg/m^3. This is found to be in good agreement with theory and observations concerning asteroids porosity fraction after shattering and reassembling, estimated to be within 20% and 40% [111]. A different result is obtained for the case of the small aggregate depicted in Figure 4.14(b), for which $P \simeq 14\%$, correspond-

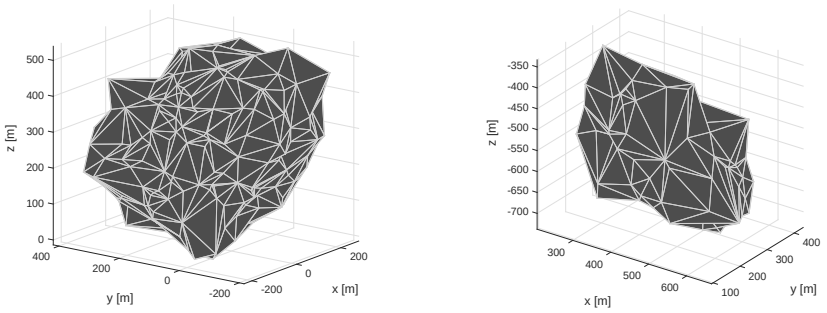

(a) (b)

Figure 4.14: *Shape of the final aggregate: (a) minimum (from set ID '1.2') and (b) maximum (from set ID '2.1') bulk density.*

ing to $\rho_b \simeq 2500$ kg/m^3. This result agrees with general trend observing that smaller asteroids are more compact, with a lower fraction of interior voids [111]. The lower level of porosity, compared to what is reported in [111] can be explained by the low number of bodies forming the final aggregate: only 25 out of 200 bodies are found in the final stable aggregate, while aggregates with higher porosity have more than 125 bodies in the final aggregate.

CHAPTER 5

Mission Analysis Scenarios

Rendezvous missions to small celestial bodies of our Solar System are the current frontier of space exploration. Recently, Near Earth Asteroids (NEA) have become of great interest for human space exploration. NASA identified them as the intermediate step to be pursued on the mankind's way to Mars, being one of the motivations behind NASA's Asteroid Redirect Mission (ARM) [14,56,84]. Motivated by a great scientific interest and invaluable technological demonstration opportunities, the close-proximity exploration of asteroids and comets is among the latest challenges of modern astrodynamics. Nowadays, the problem of landing a space probe on such celestial bodies is studied for the first time and the research on this topic still is a very young field. Among the small body population, a great interest is given on binary asteroid systems since 1993, when the first natural satellite of an asteroid was discovered by the Galileo spacecraft that imaged Dactyl while performing a flyby near its bigger companion 243 Ida [8]. In the last few decades, many multiple asteroid systems were discovered and it is currently estimated that about 16% of NEA are binaries [88, 91]. The study of binary asteroids can be very interesting under many aspects. These kinds of systems possess peculiar properties that make them good candidates for scientific and technological studies. The binary

asteroid environment is the ideal place to study gravitational dynamics, to enhance the understanding of how celestial bodies in the Solar System were formed and how they evolve. More in detail, they offer the unique opportunity to determine precisely asteroid masses and densities: nowadays, mass and density are accurately known only for a few tens of small body objects. In case of binary systems, the mass of the asteroids can be accurately computed after the orbit of the satellite object is measured [12]. In addition, it represents an ideal place for technology demonstration missions, as a test bench for In-Orbit-Demonstration (IOD) experiments. For these reasons, the study of the dynamical environment near an asteroid pair is an extremely relevant topic for future missions design.

This chapter discusses Mission Analysis applications for the exploration of binary asteroid systems. Three scenarios are studied. The first one (Section 5.1) presents a novel patched strategy for trajectory design in the proximity of a binary asteroid pair, when the primary asteroid is of a dog-bone, elongated or contact binary kind. The concept of Surface Of Equivalence (SOE) is introduced to deal with the patched problem and its transitions. A landing design strategy based on Poincaré map analysis is proposed and suitable landing solutions are identified for the case under study. The second scenario (Section 5.2) discusses the design options for a ballistic landing on the secondary of Didymos binary system, with explicit reference to the ongoing design of the Asteroid Impact Mission (AIM). The mission analysis strategy is outlined and taylored to the peculiar dynamics and requirements related to the AIM mission. Relevant design parameters are identified and their effect on the ballistic landing design is discussed. Expected landing results and proposed mission analysis design solution are also presented. The third scenario (Section 5.3) refers to relative motion within a binary system. Free formation flying is studied and preferred initial configurations are sought to fully exploit the natural dynamics and to maximize some desired formation keeping performance.

5.1 Binary system with two-lobed primary

As discussed in Chapter 2, different strategies can be adopted to model the gravity field about binary asteroid systems according to different levels of accuracy [6, 53, 122]. Apart from the different representation of the single asteroid mass distribution, all cited approaches start from the basic idea that, because of the presence of two main gravitational sources, the dynamics of a spacecraft in the proximity of a binary system can be naturally modeled with a restricted three-body problem. This consideration

represents the starting point of this study as well.

The trajectory design strategy proposed here models the dynamics around a binary asteroid system by using two patched Three-Body Problems. The patched three-body strategy is a generalization of the classical patched conics approach [5]. The latter exploits a Keplerian decomposition (one attractor at the time) of the three-dimensional space, to design a trajectory in an N-body model by patching different two-body solutions. Analogously, three-body solutions can be patched together by considering two attractors at the time [59, 82]. The transition between different gravity models is driven by the definition of regions of influence, where different models apply. To this aim, the concept of Sphere Of Influence (SOI) [115] is usually adopted.

The study proposes a novel patched approach. In analogy with the SOI, the concept of Surface Of Equivalence (SOE) was developed to handle transitions between different dynamical models, with specific applications to binary asteroids. In particular, but without any loss of generality, applications related to Circular Restricted Three-Body Problem (CR3BP) are shown. The design approach and numerical methods can be easily generalized to other restricted dynamical models (Elliptic Three-Body Problem, Full Three-Body Problem, ...), as well as to other representation of the asteroid gravity field (polyhedron, ellipsoid, ...). The binary asteroid model is described in Section 5.1.2, where the different three-body systems in use are defined. The patched three-body model introduces some degrees of freedom with respect to a classical two-body approach and it is intended to model with higher accuracy the peculiar dynamical properties of such irregular and low gravity field bodies, while keeping the advantages of having a full analytical formulation and low computational cost. The neighborhood of the asteroid couple is split into two regions of influence where two different Three-Body Problems describe the dynamics of the spacecraft. These regions were identified by introducing the concept of SOE as defined in Section 5.1.3, a three-dimensional surface that serves as boundary between the regions of influence of each dynamical model. A potential scenario that may benefit of such an approach in solving its mission analysis is eventually presented in Section 5.1.4. Cost-effective solutions to land a vehicle on the surface of a low gravity body are found by patching stable and unstable manifolds associated to the two different three-body systems by means of Poincaré maps analysis on the SOE.

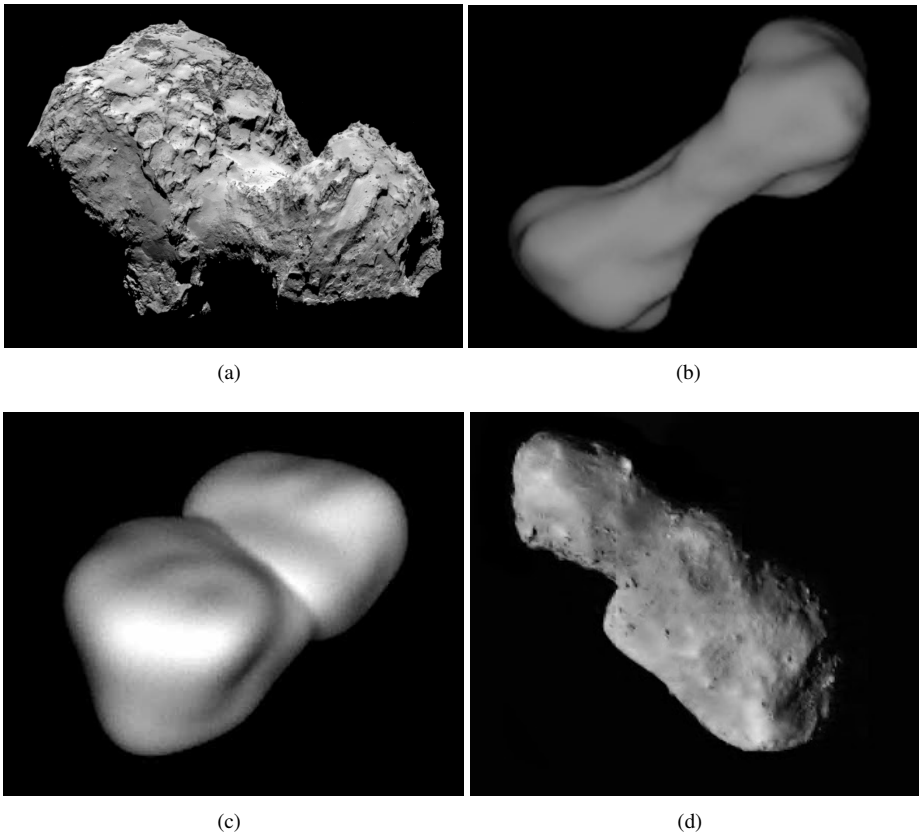

Figure 5.1: *Example of two-lobed small bodies (a) Comet 67P/Churyumov-Gerasimenko. Credits: OSIRIS/Rosetta, ESA, 2014 (b) 216 Kleopatra. Credits: Stephen Ostro et al., Arecibo Radio Telescope, NASA/JPL, 2000 (c) 4769 Castalia. Credits: Stephen Ostro et al., Arecibo Radio Telescope, NASA/JPL, 1990 (d) 4179 Toutatis. Credits: Chang'e 2, CNSA, 2012.*

5.1.1 Model validity within the small body population

The model implemented is suitable for certain classes of binary asteroids. More in detail, a "big+small" binary couple is here considered. This is a reasonable choice and not a very restrictive assumption with respect to the binary asteroid population, since it is known that the mass of most of known NEA binary systems is not evenly distributed among the two asteroids [76] where the couple usually consists of one big asteroid (primary) and a smaller one (secondary). As a further assumption, the work focuses on binaries whose primary asteroid is elongated or dipole-shaped. This assumption is also quite realistic, confirmed by radar imaging of NEA and

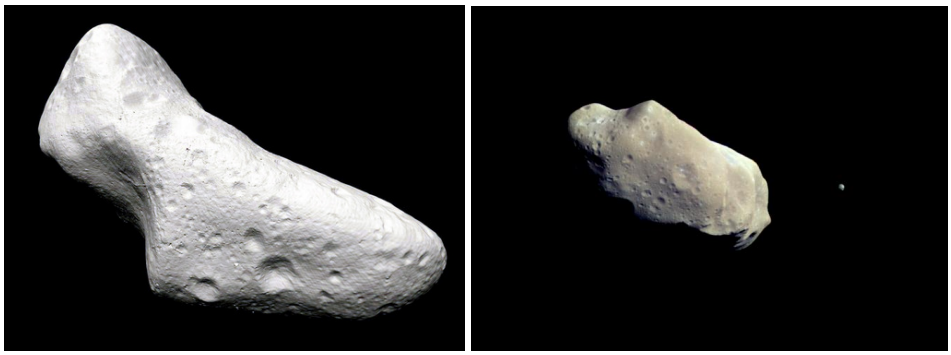

(a) (b)

Figure 5.2: *Example of elongated small bodies (a) 433 Eros. Credits: NEAR, NASA, 2001 (b) 243 Ida. Credits: Galileo, NASA, 1993.*

by the increasing information on asteroid shape available from rendezvous missions and flybys. A large variety of natural bodies are suitable to be represented with a mass dipole, since it is very common for small celestial bodies to have two distinct lobes. It is the case of asteroids such as 4769 Castalia [100], 216 Kleopatra (the "dogbone" asteroid) [101], 2963 Bacchus [9], 4179 Toutatis [102], 12 Victoria [95] and 624 Hektor [26], as well as comet 67P/Churyumov-Gerasimenko [125]. Some of them are shown in Figure 5.1, using images provided by either spacecraft or radar observations from Earth. Elongated asteroids are also very common, few examples are given: 1620 Geographos [103] (the mostly elongated body known in the Solar System), 433 Eros [139] and 243 Ida [7, 8]. The latter two are shown in Figure 5.2, as imaged by, respectively, NASA's NEAR mission in 2001 and by the NASA's Galileo spacecraft in 1993.

The goal of the study is to demonstrate the effectiveness of the patched three-body approach presented here. For this reason, perturbing actions external to the binary system were not included at this stage. Such effects might include SRP and gravity of the Sun, as well as more accurate models of the mass distribution of the asteroid (see Section 1) to model with higher accuracy the gravity field of the asteroid and the dynamics of the spacecraft. Concerning SRP, it is known that its effect becomes relevant when long-term missions are considered. In this work the dynamical model is used to compute short-time trajectories, hence the accuracy of the dynamics is not compromised by the absence of such an effect. The assumption of neglecting the gravity of the Sun is motivated by the fact that the mission analysis is confined within the Sphere Of Influence (SOI) of the binary

system. The radius of the SOI is here computed according to its classical formulation [115]:

$$r_{\text{SOI}} = r_{Sun} \left(\frac{m_A}{m_S} \right)^{\frac{2}{5}} = 8.61 \text{ km} \tag{5.1}$$

where m_A is the total mass of the binary system, m_S is the mass of the Sun and r_{Sun} is the distance of the binary from the Sun, with data referring to the study case as reported in Table 5.3. As shown in Figure 5.8, the dynamical environment under study is confined well below the distance of 8.61 km from the barycentre of the binary system.

5.1.2 Binary asteroid model

This section presents the assumptions made to define the dynamical model and the binary system configuration. The dynamical model of the binary asteroid system is built here using two rotating dipoles. As mentioned, the gravity field associated to each dipole is modeled using the CR3BP formulation. The first rotating dipole is identified with the binary couple itself: the two asteroids are modeled as point masses and represent the primaries of the first three-body problem. This system will be addressed in the text as *external system*. The second rotating dipole is the result of approximating the gravity potential of the primary asteroid with the potential of two masses (two-mass concentrated model or two-mascon in the followings). These two masses are the primaries of the second three-body problem, which will be addressed as *internal system*. When considering the dynamics of the primary and secondary asteroid, this model can be seen as a simplification of the Kokoriev-Kirpichnikov problem [62], which models the planar motion of a point mass and a symmetric rigid body whose gravity field is approximated using a two-mascon model. As discussed in Section 5.1.1, the latest assumption makes the model appropriate to represent particular classes of bodies, such as elongated, dog-bone shaped or two-lobed asteroids. Asteroids 4769 Castalia, 2963 Bacchus, 624 Hektor and 216 Kleopatra, due to their peculiar shape, are thought to be contact or close binaries and therefore their mass distribution fits very well with the two-mascon model. A particularly suitable candidate to be represented with the proposed patched three-body model is asteroid 243 Ida, already identified as a good candidate for proving the dynamical properties of the Kokoriev-Kirpichnikov problem [62] with a real celestial body: asteroid 243 Ida is elongated and also, it has a small moon (Dactyl) orbiting around it (Figure 5.2(b)).

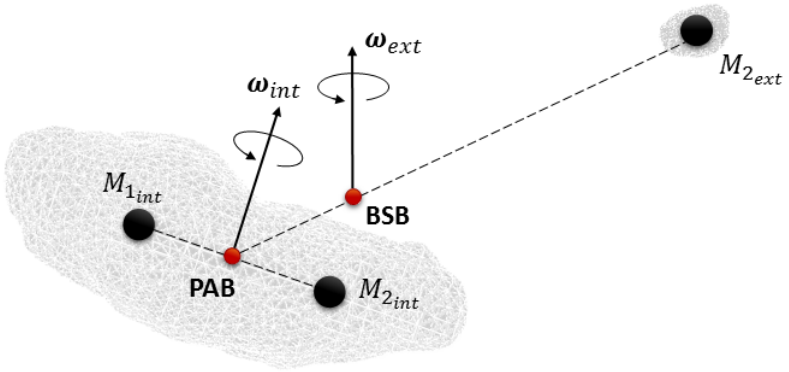

Figure 5.3: *Binary system in the three-dimensional space. Rotational motions around Primary Asteroid Barycentre (PAB) and Binary System Barycentre (BSB) are represented using angular velocities of the two dipoles*

Figure 5.3 shows the orientation in the three-dimensional space of the two asteroids and the angular velocity associated to the two rotating dipoles. With reference to Figure 5.3, the Primary Asteroid Barycentre (PAB) and the secondary asteroid ($M_{2_{\text{ext}}}$) are the primaries of the external system (PAB is also referred as $M_{1_{\text{ext}}}$) and rotate with angular velocity $\boldsymbol{\omega}_{\text{ext}}$ around the Binary System Barycentre (BSB). On the other hand, $M_{1_{\text{int}}}$ and $M_{2_{\text{int}}}$ identify the primaries of the internal system, which rotate with angular velocity $\boldsymbol{\omega}_{\text{int}}$ about the PAB. Note that $M_{1_{\text{ext}}}$ refers to the primary asteroid, as well as the couple $M_{1_{\text{int}}}, M_{2_{\text{int}}}$ and therefore, the following relation holds

$$M_{1_{\text{ext}}} = M_{1_{\text{int}}} + M_{2_{\text{int}}} \tag{5.2}$$

Relative kinematics between asteroids

As shown in Section 2.1.1, the nondimensional equations of motion of the third body (Eq. (2.27)), expressed in the rotating frame of a single dipole, depend only on the mass ratio μ between the primaries. When two different rotating dipoles and their relative orientation in the 3D space are considered, other parameters must be settled to define the overall dynamical system. In particular, dimensional quantities (or common nondimensional ones) are to be considered as well as relative three-dimensional kinematics between the two systems have to be defined. The term *relative kinematics* is used here to indicate the relative motion between the rotation of the primary asteroid about its barycentre ($\boldsymbol{\omega}_{\text{int}}$) and the revolution of the asteroid couple (or *revolution of the secondary* in the followings) about the BSB

($\boldsymbol{\omega}_{\text{ext}}$). Reduction to special cases can be considered with respect to the general kinematic problem. Four possible cases are identified to describe the relative kinematics between two rotating dipoles in the binary asteroid scenario.

(a) General case: the rotation of the primary is not coupled with the revolution of the secondary as the two dipoles rotate independently in the space, with $\boldsymbol{\omega}_{\text{int}}$ not aligned to $\boldsymbol{\omega}_{\text{ext}}$ and $\|\boldsymbol{\omega}_{\text{int}}\| \neq \|\boldsymbol{\omega}_{\text{ext}}\|$ (Figure 5.3).

(b) Planar motion: $\boldsymbol{\omega}_{\text{int}}$ is aligned to $\boldsymbol{\omega}_{\text{ext}}$, in this case the primaries of both rotating dipoles lie on the same plane. The two systems differ by a relative rotation since $\|\boldsymbol{\omega}_{\text{int}}\| \neq \|\boldsymbol{\omega}_{\text{ext}}\|$ (Figure 5.4).

(c) Synchronous motion: the rotation of the primary is coupled with the revolution of the secondary, but the angular velocity vectors are not aligned. The resulting patched system is periodic and the motion of the primaries is three-dimensional.

(d) Planar and synchronous motion: angular velocity vectors are equal both in magnitude and direction ($\boldsymbol{\omega}_{\text{int}} = \boldsymbol{\omega}_{\text{ext}}$). The motion of the primaries is planar and no relative rotation exists between the two rotating dipoles.

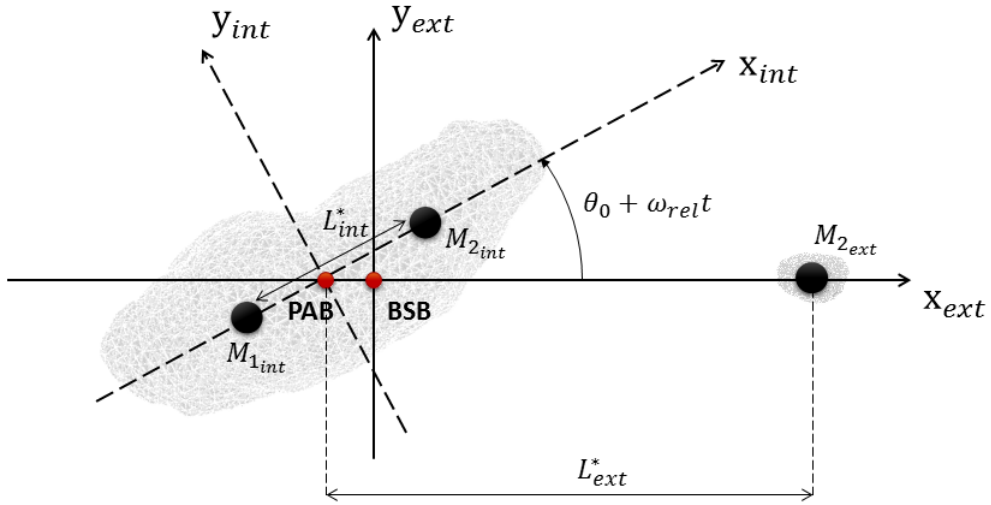

Figure 5.4: *Relative kinematics between internal and external dipoles (case (b), planar motion)*

As previously recalled, the mass ratio μ is sufficient to retrieve the equations of motion of the CR3BP in the nondimensional rotating frame. In

Table 5.1: *Set of parameters to tune the patched CR3BP system*

Relative kinematics case	set of parameters		
(a) General case	$\{\mu, L^*, \boldsymbol{\omega}\}_{\text{ext}}$	$\{\mu, L^*, \boldsymbol{\omega}\}_{\text{int}}$	+IC
(b) Planar motion	$\{\mu, L^*, \|\boldsymbol{\omega}\|\}_{\text{ext}}$	$\{\mu, L^*, \|\boldsymbol{\omega}\|\}_{\text{int}}$	+IC
(c) Synchronous motion	$\{\mu, L^*, \hat{\boldsymbol{\omega}}\}_{\text{ext}}$	$\{\mu, L^*, \hat{\boldsymbol{\omega}}\}_{\text{int}}$	+IC
(d) Planar and synchronous motion	$\{\mu, L^*\}_{\text{ext}}$	$\{\mu, L^*\}_{\text{int}}$	+IC

addition, the characteristic length L^* is required to represent the three-body system in dimensional coordinates, and the angular velocity vector is required to correctly represent the rotation of the dipole in the space. In general, when two patched CR3BP are to be considered, the full set of parameter $\{\mu, L^*, \boldsymbol{\omega}\}$ is required for each dipole, plus the information on the relative orientation of the bodies at a certain epoch (Initial Condition or IC in the followings). When special relative dynamics between the two rotating dipoles are considered (cases (b), (c) and (d)), the set of required parameters to unequivocally define the patched CR3BP system is reduced due to constraints on the relative angular velocity. More in detail, case (b) constrains the relative orientation of the angular velocity to be null, while case (c) leaves as only degree of freedom their unitary directions ($\hat{\boldsymbol{\omega}}$). Case (d) refers to null relative angular velocity vector, both in magnitude and direction. This special case, if seen from their common rotating frame, constrains the primaries of the two dipoles to be fixed on a plane. It is a reduction of case (b), hence it can be represented with Figure 5.4, when the relative angular velocity $\omega_{\text{rel}} = 0$ (with $\omega_{\text{rel}} = \|\boldsymbol{\omega}_{\text{int}} - \boldsymbol{\omega}_{\text{ext}}\|$). The assumption of zero relative angular velocity between the two rotating dipoles can be made to design a trajectory in the patched three-body system for slow rotating targets. In this case, the time spent on the trajectory is much less than the time the asteroid takes to complete one rotation: hence, during the time the spacecraft flies its trajectory, the relative position between the two asteroids in the rotating frame has not changed significantly. In the latest case, the two CR3BP are unequivocally defined by $\{\mu_{\text{ext}}, L^*_{\text{ext}}, \mu_{\text{int}}, L^*_{\text{int}}\}$ and by selecting the IC (θ_0, with reference to Figure 5.4), which constrains the relative position of the four primaries. Table 5.1 summarizes the sets of parameters to be fixed to unequivocally tune the patched CR3BP system, depending on its relative kinematics.

Dynamics of the spacecraft

The dynamical environment driving the motion of the spacecraft in the proximity of the binary system is described here. As mentioned above, the classical patched conics approach considers different regions of influence, bounded by the SOI computed around a single attractor, to model the dynamics of the spacecraft. Similarly, the dynamical environment in the proximity of the binary couple is split into two regions of influence, bounded by the SOE computed around the primary asteroid. A qualitative definition of the SOE is given here. Further details on its mathematical definition and numerical computation are given in Section 5.1.3.

Intuitively, it can be assumed that the dynamics of the spacecraft are dominated by the gravitational effect of the primary asteroid when it is near to it, with the effect of the smaller asteroid negligible ($M_{1_{\text{ext}}} >> M_{2_{\text{ext}}}$). This region is considered to be *internal* with respect to the SOE and the motion of the spacecraft is governed by the internal CR3BP. With reference to section 2.1.1, the equations of motion of the spacecraft are represented by system (2.27) and can be equivalently rewritten in vectorial form as

$$\tilde{\boldsymbol{a}}_{\text{int}} = \left\{ \begin{array}{c} 2\dot{\tilde{y}} + U_{\tilde{x}} \\ -2\dot{\tilde{x}} + U_{\tilde{y}} \\ U_{\tilde{z}} \end{array} \right\}_{\text{int}} \tag{5.3}$$

with notation referring to the internal nondimensional system, normalized to have unitary angular velocity (ω_{int}), total mass of the system ($M_{1_{\text{int}}} + M_{2_{\text{int}}}$) and distance between primaries.

Far from the primary asteroid, its gravity field is approximated with a simple central field, as the effects due to its non-homogeneous mass distribution are negligible. In addition, the effect of the smaller asteroid turns to be relevant as the primary field becomes weaker. This region is considered to be *external* with respect to the SOE and the dynamics of the third body is driven by the combined gravitational field of the binary couple (external CR3BP). In analogy to what is done for internal system, the equations of motion of the spacecraft moving outside the SOE are represented by system (2.27), which in vectorial form reads

$$\tilde{\boldsymbol{a}}_{\text{ext}} = \left\{ \begin{array}{c} 2\dot{\tilde{y}} + U_{\tilde{x}} \\ -2\dot{\tilde{x}} + U_{\tilde{y}} \\ U_{\tilde{z}} \end{array} \right\}_{\text{ext}} \tag{5.4}$$

with notation referring to the external nondimensional system, normalized

to have unitary angular velocity (ω_{ext}), total mass of the system ($M_{1_{\text{ext}}} + M_{2_{\text{ext}}}$) and distance between primaries.

The schematics of the dynamical system are shown in Figure 5.5: the SOE represents the boundary between internal and external CR3BP.

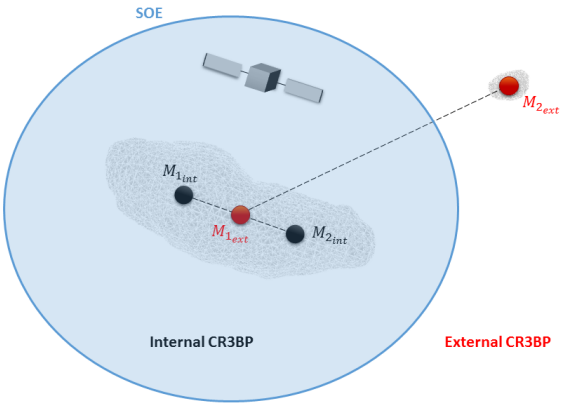

Figure 5.5: *Schematics of the dynamical system. SOE as boundary between regions of applicability of internal and external CR3BP*

5.1.3 Surface Of Equivalence

This section discusses the mathematical definition of the SOE and its numerical computation for the landing scenario studied in Section 5.1.4. The data used to produce results and figures presented here refer to data reported in Section 5.1.4.

Definition of the SOE

The concept of Surface Of Equivalence is developed here to cover specific needs related to the study and the design of trajectories in a patched three-body model. The SOE is defined as the implicit surface

$$\mathcal{F}(\boldsymbol{G}, \boldsymbol{H}) = 0 \tag{5.5}$$

where $\boldsymbol{G}$ and $\boldsymbol{H}$ are vector fields, as defined in the following paragraph. The SOE is used to compare such vector fields and, according to the properties of the fields and by selecting the proper $\mathcal{F}(\boldsymbol{G}, \boldsymbol{H})$, to establish boundaries of equivalent regions between them. The definition of the SOE provided here applies to the case study, as shown in the followings, to compare gravity fields.

SOE to compare gravity models

A simple application of the SOE concept is shown here to compare acceleration fields associated to different gravity models. More in detail, the purpose is to identify regions in the three-dimensional space where two different gravity models produce *equivalent* acceleration fields. It is here highlighted that *equivalent* does not mean *equal*, but it does refer to specific applications for which two acceleration fields, even if not equal, produce equivalent results according to a specified accuracy. E.g. a massive attractor can be modeled according to different mathematical models (single central field, mass distributed model, mass concentrated model, polyhedron model,...) and, depending on the specific application (e.g. distance of the spacecraft), these models can be seen as equivalent or not. It is known that the intensity of the acceleration field is inversely proportional to the square of the distance from the attractor: intuitively, different models of the same attractor can be considered equivalent far enough from the singularities of the field (gravity sources). Equivalence criteria are established through the definition of the SOE since they are directly linked with the selection of $\mathcal{F}(\boldsymbol{G}, \boldsymbol{H})$.

Referring to the case study, the SOE is computed here to confine equivalence regions between representation of primary asteroid gravity field with the single mass or with the two-mascon model. $\boldsymbol{G}$ and $\boldsymbol{H}$ represent the acceleration fields of, respectively, the two-mascon model (CR3BP, referred as $\boldsymbol{a}_{\text{int}}$, as in Eq. (5.3)) and the single mass model (Restricted Two-Body Problem, or R2BP, referred as $\boldsymbol{a_{2B}}$). It is convenient to evaluate both acceleration fields in the rotating frame associated to the two-mascon model (referred as internal system in Section 5.1.2), such that the asteroid remains fixed in the space. In this particular reference frame, vector fields are time-invariant and their functional expression read as

$$\boldsymbol{G} = \boldsymbol{G}(x, y, z) \qquad \boldsymbol{H} = \boldsymbol{H}(x, y, z)$$

To facilitate the comparison between acceleration fields, dimensional units are used. More in detail, the dimensional form of Eq. (5.3) can be written as

$$\boldsymbol{a}_{\text{int}} = \left\{ \begin{array}{c} \omega_{\text{int}}^2 x + 2\omega_{\text{int}}\dot{y} - G\left(\frac{M_{1_{\text{int}}}}{r_1^3}(x + x_1) + \frac{M_{2_{\text{int}}}}{r_2^3}(x - x_2)\right) \\ \omega_{\text{int}}^2 y - 2\omega_{\text{int}}\dot{x} - Gy\left(\frac{M_{1_{\text{int}}}}{r_1^3} + \frac{M_{2_{\text{int}}}}{r_2^3}\right) \\ -Gz\left(\frac{M_{1_{\text{int}}}}{r_1^3} + \frac{M_{2_{\text{int}}}}{r_2^3}\right) \end{array} \right\}_{\text{int}} \tag{5.6}$$

where x, y, z refer to the dimensional coordinates in the internal CR3BP, x_1, x_2 represent the position of the two primaries on the x axis, r_1, r_2 the

distance of the third body from the primaries and G is the universal gravitational constant.

The contribution due to the single mass representation of the primary, in the rotating frame reads as

$$\boldsymbol{a}_{\text{2B}} = \left\{ \begin{array}{c} \omega_{\text{int}}^2 x + 2\omega_{\text{int}}\dot{y} - G\frac{M_{1_{\text{int}}}+M_{2_{\text{int}}}}{r^3}x \\ \omega_{\text{int}}^2 y - 2\omega_{\text{int}}\dot{x} - G\frac{M_{1_{\text{int}}}+M_{2_{\text{int}}}}{r^3}y \\ -G\frac{M_{1_{\text{int}}}+M_{2_{\text{int}}}}{r^3}z \end{array} \right\}_{\text{int}} \tag{5.7}$$

with r representing the distance of the spacecraft from the barycentre of the system.

Since the vector field is being evaluated with spacecraft at rest ($\dot{x} = \dot{y} = \dot{z} = 0$), Coriolis terms in equations (5.6) and (5.7) result to be zero and then the equations can be simplified into the form used to define the SOE:

$$\boldsymbol{a}_{\text{int}} = \left\{ \begin{array}{c} \omega_{\text{int}}^2 x - G\left(\frac{M_{1_{\text{int}}}}{r_1^3}(x+x_1) + \frac{M_{2_{\text{int}}}}{r_2^3}(x-x_2)\right) \\ \omega_{\text{int}}^2 y - Gy\left(\frac{M_{1_{\text{int}}}}{r_1^3} + \frac{M_{2_{\text{int}}}}{r_2^3}\right) \\ -Gz\left(\frac{M_{1_{\text{int}}}}{r_1^3} + \frac{M_{2_{\text{int}}}}{r_2^3}\right) \end{array} \right\}_{\text{int}} = \boldsymbol{G}(x,y,z) \tag{5.8}$$

and

$$\boldsymbol{a}_{\text{2B}} = \left\{ \begin{array}{c} \omega_{\text{int}}^2 x - G\frac{M_{1_{\text{int}}}+M_{2_{\text{int}}}}{r^3}x \\ \omega_{\text{int}}^2 y - G\frac{M_{1_{\text{int}}}+M_{2_{\text{int}}}}{r^3}y \\ -G\frac{M_{1_{\text{int}}}+M_{2_{\text{int}}}}{r^3}z \end{array} \right\}_{\text{int}} = \boldsymbol{H}(x,y,z) \tag{5.9}$$

SOE example: relative difference in magnitude

In this paragraph, the SOE is computed by comparing the magnitude of different acceleration fields. Figure 5.6(a) shows contour lines of the function $f(x,y,z)$, which represents the relative difference in magnitude between fields

$$f(x,y,z) = \frac{\|\boldsymbol{a}_{\text{int}} - \boldsymbol{a}_{2B}\|}{\|\boldsymbol{a}_{\text{int}}\|} \tag{5.10}$$

The value of f in each point (x,y,z) of the domain corresponds to the difference in magnitude between central field and two-mascon model as percentage of the latter. As expected, the difference between the fields is maximum near the asteroid and decreases monotonically moving away from it.

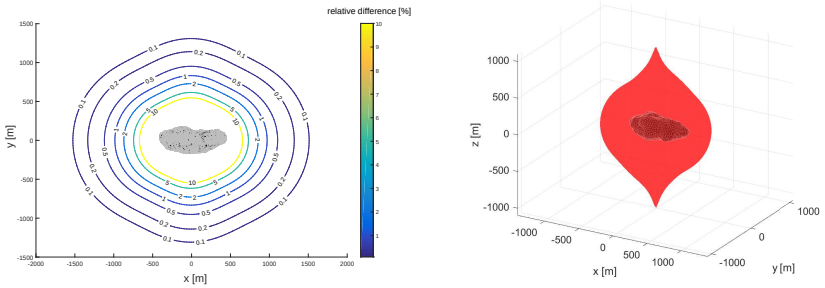

(a) (b)

Figure 5.6: *(a) Contour lines of function $f(x, y, z)$ (Eq. (5.10)): projection on x, y plane. Relative difference in magnitude expressed as percentage of $\|\boldsymbol{a}_{int}\|$. (b) Three-dimensional view of the SOE (with $\kappa = 5\%$). Magnitude of acceleration fields is compared*

Equation (5.10) is included in the definition of the SOE (5.5), which is expressed as the implicit surface

$$\mathcal{F}(\boldsymbol{G}, \boldsymbol{H}) = \frac{\|\boldsymbol{G} - \boldsymbol{H}\|}{\|\boldsymbol{G}\|} - \kappa = 0 \tag{5.11}$$

or equivalently

$$\frac{\|\boldsymbol{a}_{\text{int}} - \boldsymbol{a}_{2B}\|}{\|\boldsymbol{a}_{\text{int}}\|} = \kappa \tag{5.12}$$

being κ a scalar value representing the norm of the vectorial difference between the fields normalized to $\|\boldsymbol{a}_{\text{int}}\|$ or, in other words, the percentage of difference between the models. The analytical expression of the SOE can be written in the dimensional rotating frame by substituting equations (5.8) and (5.9) into Eq. (5.12): it results into a nonlinear scalar equation to be solved for the value κ. Figure 5.6(b) shows the three-dimensional SOE computed for $\kappa = 5\%$. As mentioned, the SOE bounds regions of equivalence of different models, according to a specific accuracy. In this case, as it appears clear from Figure 5.6(a), the SOE divides the domain into two regions: the internal region (where $f > 5\%$) and the external region (where $f < 5\%$). A region of *equivalence* between the two models, within the accuracy of 5%, is then identified outside the SOE.

SOE example: relative difference in direction

Other SOEs can be computed according to different equivalence criteria. The equivalence of two acceleration fields can be assessed in terms of vec-

tor orientation (other than vector magnitude). In analogy to what is done for the case of magnitude comparison, the relative difference in direction between fields is defined as $g(x, y, z)$

$$g(x, y, z) = \arccos\left(\frac{\boldsymbol{a}_{\text{int}} \cdot \boldsymbol{a}_{2B}}{\|\boldsymbol{a}_{\text{int}}\|\|\boldsymbol{a}_{2B}\|}\right) \tag{5.13}$$

Figure 5.7(a) shows contour lines of the function $g(x, y, z)$ being the relative difference in directions, expressed in degrees, between the vector fields under study. Again, the difference between the fields is maximum near the asteroid and decreases away from it.

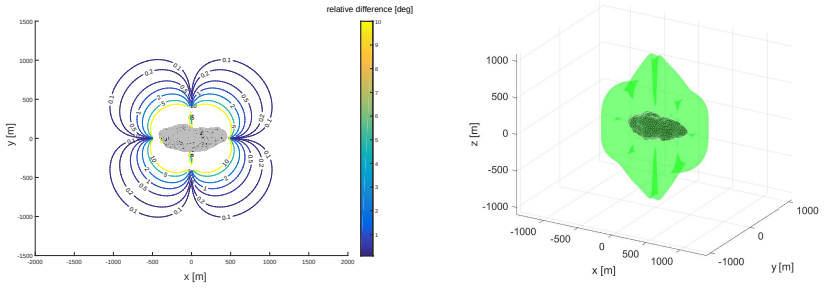

(a) (b)

Figure 5.7: *(a) Contour lines of function $g(x, y, z)$ (Eq.* (5.13)*): projection on x, y plane. Relative difference in direction expressed in degrees. (b) Three-dimensional view of the SOE (with $\gamma = 2°$). Direction of acceleration fields is compared*

In this case, the SOE is defined as

$$\arccos\left(\frac{\boldsymbol{a}_{\text{int}} \cdot \boldsymbol{a}_{2B}}{\|\boldsymbol{a}_{\text{int}}\|\|\boldsymbol{a}_{2B}\|}\right) = \gamma \tag{5.14}$$

where γ is the angle between vectors of the different fields. Figure 5.7(b) shows the three-dimensional SOE computed when $\gamma = 2°$. In analogy to the magnitude comparison case, the region of *equivalence* between the two models, within the accuracy of $2°$, is identified outside the SOE.

5.1.4 Landing scenario

This section presents a space exploration scenario to a NEA binary system. The patched three-body strategy described above is adopted here for close proximity operations and to design the landing trajectory of a space probe. With reference to Section 5.1.2, the relative kinematics of the target

binary system and the dynamical environment are described, using the SOE concept defined in Section 5.1.3.

Binary system data

All data used for the scenario under study are reported here. A target binary system was defined by using typical physical values of asteroids among the wide binary NEA population [76]: Table 5.2 reports the ranges of properties relevant for the case study. With reference to notation introduced in Section 5.1.2, table 5.3 lists the selected values.

Table 5.2: *NEA binary population (data from Johnston's archive [76])*

	quantity	range of values
Asteroid couple	heliocentric semi-major axis	$[0.6 - 3]$ AU
	mass ratio	$[10^{-4} - 10^{-1}]$
	distance between primaries	$[0.25 - 8]$ km
Primary asteroid	diameter	$[120 - 8200]$ m
Secondary asteroid	diameter	$[50 - 800]$ m

Table 5.3: *Physical values used for the case study*

	quantity	symbol	Value
Asteroid couple	mass ratio	μ_{ext}	0.0065
	characteristic length	L^*_{ext}	1100 m
	relative orientation	θ_0	0°
	distance from the Sun	r_{Sun}	1.64 AU
	total mass	m_A	$4.59 \cdot 10^{11}$ kg
Primary asteroid	mass ratio	μ_{int}	0.5
	characteristic length	L^*_{int}	400 m
	size (ellipsoid semi-axis)	(a_x, a_y, a_z)	(400, 200, 200) m
Secondary asteroid	size (sphere radius)	R_2	75 m

It is remarked here that for this case study, the shapes of the asteroids are used only for representing their surface during the landing design: the sizes of primary and secondary asteroids refer to their representation as ellipsoid (or sphere).

Relative kinematics of the binary system

The case study presented here refers to the simplest case in terms of relative kinematics between asteroids among those presented in Section 5.1.2: it is assumed that planar and synchronous motion applies for the binary system under study (case (d)). This assumption simplifies the computations but it does not affect the validity and meaningfulness of the design process. The relative kinematics of the binary systems do not affect the motion of the two rotating dipoles and therefore the applicability of the CR3BP in their domain of interest: relative kinematics between asteroids are important only at the SOE, where the transition between internal and external CR3BP occurs instantaneously. In this respect, case (d) is equivalent to the general non-synchronous and three-dimensional motion (case (a)), with the two rotating dipoles aligned only during transition at the SOE. Moreover, a simpler study case fits better than a more complex case with the needs of showing and explaining a novel design approach, which is the goal of this section. The patched approach shown here can be easily applied to any general, more complex study case.

As shown in Table 5.1, when case (d) applies, the patched three-body system is tuned by fixing the following set $\boldsymbol{P}$ of parameters, with reference to Figure 5.4

$$\boldsymbol{P} = \{\mu_{\text{ext}}, L^*_{\text{ext}}, \mu_{\text{int}}, L^*_{\text{int}}, \theta_0\} \tag{5.15}$$

The set $\boldsymbol{P}$ is selected according to the targeted binary system and refer to properties of both binary couple and primary asteroid. Parameters related to the external system μ_{ext} and L^*_{ext} refer to the asteroid couple since they represent the mass ratio between the two asteroids and relative distance between them. Parameters of the internal system μ_{int} and L^*_{int} are the degrees of freedom to model the gravity field of the primary asteroid: the mass ratio and distance of the two masses is used to approximate the mass distribution of the natural body. Last, θ_0 fixes the relative position of the four primaries $\{M_{1_{\text{ext}}}, M_{2_{\text{ext}}}, M_{1_{\text{int}}}, M_{2_{\text{int}}}\}$ in their common rotating frame. Values of $\boldsymbol{P}$ refer to Table 5.3. The targeted binary configuration is shown in Figure 5.8: all primaries are collinear and lie on the x axis of the common rotating frame. According to [120], if two asteroids are modeled as ellipsoids, the smaller asteroid being aligned with the minimum inertia axis of the primary represents an equilibrium configuration, which can be of stable equilibrium depending on the values of angular momentum, mass ratio and inertia properties of the asteroid couple. The design case under study is however found to stay in the region of instability, due to the chosen mass ratio between the asteroids. Nevertheless, the choice of the configuration is

justified by the fact that the two dipoles interacts dynamically only during transition at SOE: from the particle dynamics point of view, this patched model can be representative of the case in which the primaries move with a general non-synchronous, three-dimensional motion (case (a)), with instantaneous transition at SOE during alignment of the dipoles. The relative kinematics do not affect the dynamics of internal and external CR3BP in their domain and, since the transition at the SOE between patched three-body problems is instantaneous, the rotating dipoles need to be aligned only when the spacecraft is at the SOE.

Two ellipsoids are used to approximate the surface of the asteroids to design the landing trajectory and for visualization purposes.

Dynamical environment

The spacecraft moves in the proximity of the asteroid couple following the dynamics described in Section 5.1.2. The computation of the SOE to confine internal and external system is presented here for the study case.

Section 5.1.3 presents the mathematical definition of the SOE and shows some examples of its computation around the primary asteroid. The magnitude of vectors between two different acceleration fields are compared and serve to define condition (5.5) to compute the SOE. The results shown in Section 5.1.3 are applied to the binary system case and used to compute the SOE for the case of study presented here: inside the SOE the dynamics are driven by the internal CR3BP (with effects due to the smaller asteroid negligible), outside the SOE the dynamics are driven by the external CR3BP, with the primary modeled as single mass.

The case of study considers the magnitude SOE (Figure 5.6(b)) computed in Section 5.1.3. The surface is defined as

$$\frac{\|\boldsymbol{a}_{\text{int}} - \boldsymbol{a}_{2B}\|}{\|\boldsymbol{a}_{\text{int}}\|} = \kappa \tag{5.16}$$

with the threshold value κ used in Section 5.1.3:

$$\kappa = 5\% \tag{5.17}$$

This value was selected with the goal of satisfying constraints on the geometry of the problem (SOE not smaller than primary asteroid and not bigger than the binary system) while keeping a satisfactory representation of the dynamics: the internal three-body system is considered as the real world model to represent the primary asteroid and the SOE represents a boundary beyond which the gravity contribution of the primary is modeled to a

lower accuracy (if SOE is too small the accuracy of the model of the primary is too low, if the SOE is too big the effect of the secondary inside it is too high to be discarded). Since the differences in magnitude decreases by moving away from the primary asteroid (Figure 5.6(a)), outside the SOE the acceleration fields satisfy condition

$$\frac{\|\boldsymbol{a}_{\text{int}} - \boldsymbol{a}_{2B}\|}{\|\boldsymbol{a}_{\text{int}}\|} < \kappa \tag{5.18}$$

meaning that, outside the SOE, the acceleration fields are *equivalent*, within the accuracy specified in (5.17).

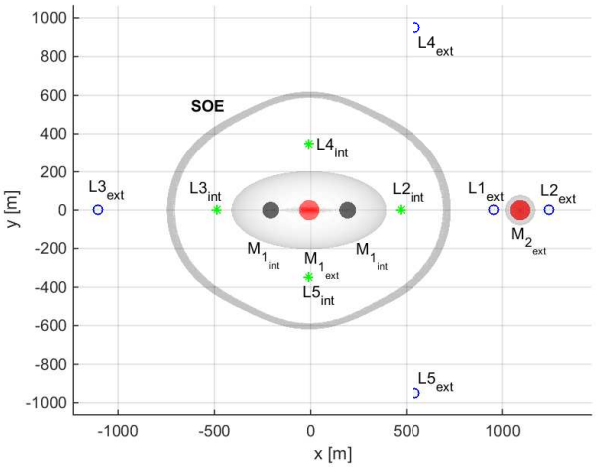

Figure 5.8: *Dynamical system, with two CR3BP and their libration points in the rotating frame: green stars indicate libration point of the internal system, blue circles indicate libration points of the external system*

Figure 5.8 shows the dynamical environment to support trajectory design for the case study. The x, y projection of the SOE is shown here, splitting the neighborhood of the binary couple into two regions where internal and external CR3BP apply. Libration points of both internal and external systems are shown.

The patched three-body approach

An example of how the patched three-body system can be employed to support the design of a potential mission scenario is presented. Solutions to land a vehicle on the surface of the primary asteroid are selected by exploiting manifold dynamics of the two three-body systems. The interaction

between the three-body problems was solved by means of Poincaré maps analysis on the SOE.

The mission scenario considers a spacecraft initially following a periodic orbit about the L1 point of the external CR3BP. During the landing phase, the spacecraft follows the dynamics of the external system to reach the SOE and then, after transition to internal CR3BP, it reaches the surface of the primary asteroid. The landing trajectory is designed by patching together two trajectories of the external and internal CR3BP. More in detail, the landing phase is initiated when the spacecraft leaves the initial orbit exploiting its unstable manifolds, which drive the spacecraft towards the primary asteroid, up to the SOE. At the SOE, the transition from external to internal CR3BP occurs and a manoeuvre is performed to reach stable manifolds that drive the spacecraft towards the surface of the asteroid. A planar transfer case is compared to a full three-dimensional one.

The following paragraphs show trajectories computed in the external and internal systems, and then discuss the landing solution found after patching external with internal trajectories.

Trajectories in the external CR3BP

It is assumed that initial orbits are imposed by mission requirements and constrained to keep the spacecraft permanently within the two asteroids, for observation purposes. For this reason, a lyapunov and a halo orbit about L1 are chosen as starting point for the planar and 3D landing solution (Figure 5.9).

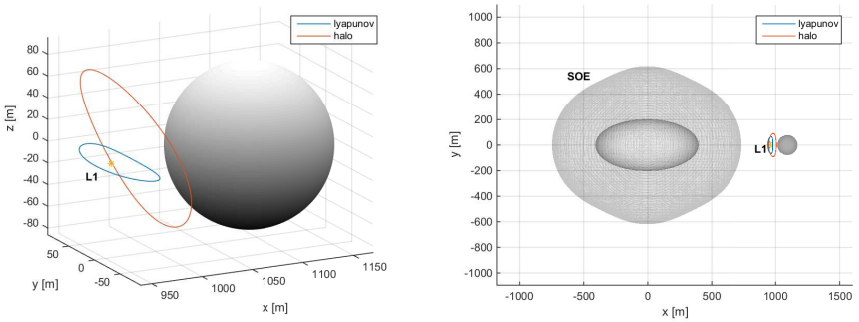

(a) (b)

Figure 5.9: *Initial orbits in the external CR3BP: lyapunov (planar case) and halo (3D case) orbits about the L1 point (a) close up view in the proximity of the smaller asteroid (b) x-y projection in the binary system*

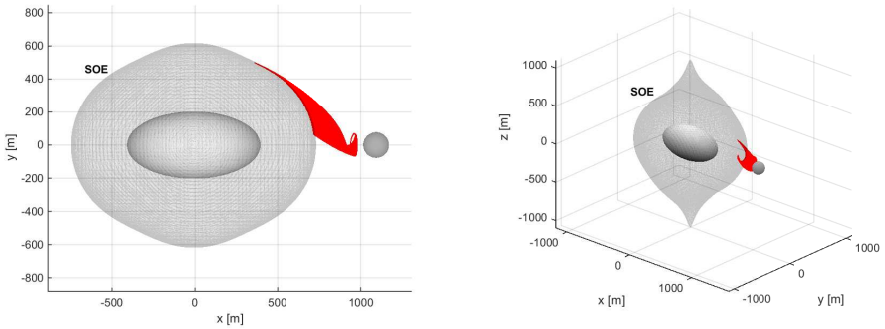

(a) (b)

Figure 5.10: *Unstable manifolds associated to (a) lyapunov and (b) halo orbits: forward propagation in the external CR3BP*

To let the spacecraft reach the SOE from its initial orbit, unstable manifolds of both lyapunov and halo orbits are computed and propagated forward within their domain of validity (Figure 5.10). The unstable manifolds computed represent possible solutions for the first phase of the landing trajectory, from the initial orbit to the SOE.

Trajectories in the internal CR3BP

According to the patched three-body model in use, the dynamics of the spacecraft transition from external to internal CR3BP at the SOE.

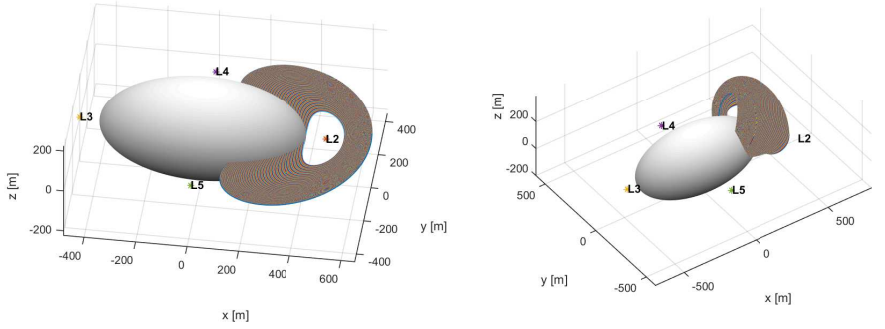

(a) (b)

Figure 5.11: *Families of (a) lyapunov and (b) halo orbits about L2 in the internal CR3BP: suitable landing points are identified by intersections with asteroid surface*

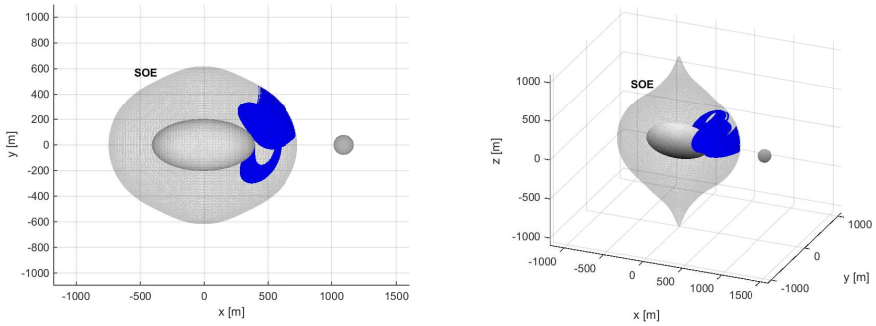

(a) (b)

Figure 5.12: *Stable manifolds associated to (a) lyapunov and (b) halo orbits: backward propagation from landing points in the internal CR3BP*

Trajectories in the internal CR3BP represent the last part of the landing trajectory, from the SOE to the surface of the primary asteroid. Landing points on the asteroid surface are sought first, by computing periodic orbits in the internal CR3BP that intercept the surface of the primary. Figure 5.11 shows families of lyapunov and halo orbits about L2 in the internal CR3BP, which intersects the surface of the asteroids. Suitable trajectories of the spacecraft from the SOE to the asteroid are found by computing stable manifolds associated to periodic orbits depicted in Figure 5.11. Manifolds are propagated backwards starting from identified landing points. Figure 5.12 shows computed stable manifold trajectories starting from suitable landing points, for both planar and three-dimensional cases.

Patched trajectories

Landing solutions are investigated in this paragraph, after patching external with internal trajectories. A connection between unstable (external) and stable (internal) manifolds shall be found on the SOE. To this aim, Poicaré maps are used. Poincaré maps are widely used in dynamical system theory: examples of specific applications to astrodynamics problems can be found in [82]. To patch internal and external trajectories, the SOE is taken as Poincaré section to compute the map.

The planar case is firstly discussed. Lyapunov orbits in internal and external CR3BP and their associated manifolds are considered here and shown in Figure 5.13(a). Since all trajectories are planar, the full six-dimensional problem is reduced to four-dimensional. To find free connections between the stable and unstable manifolds, all four states x, $\dot{x}$, y, $\dot{y}$

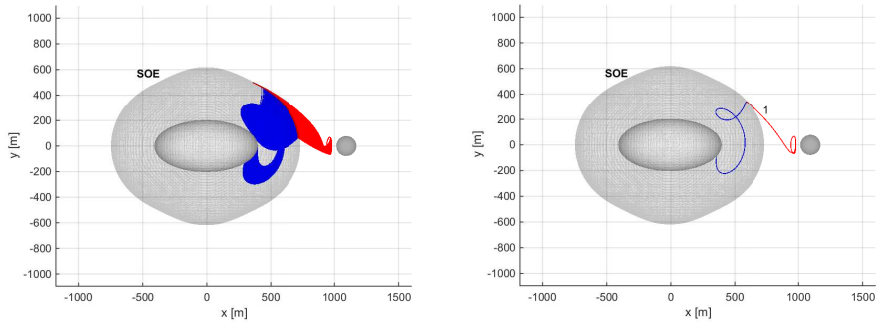

(a) (b)

Figure 5.13: *Unstable (red) and stable (blue) manifolds associated to external and internal CR3BP (planar case): (a) manifold families and (b) chosen solutions*

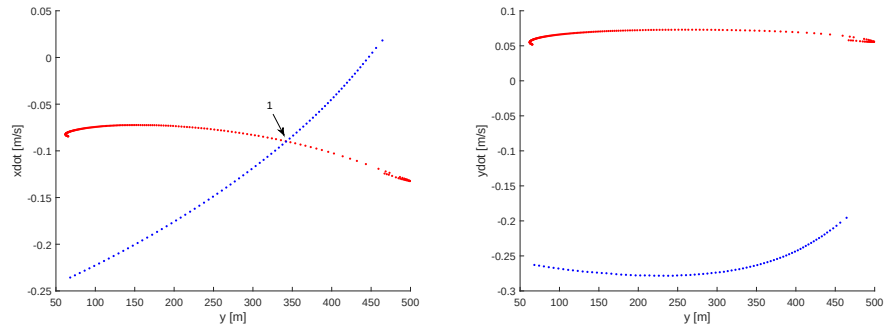

(a) (b)

Figure 5.14: *Poincaré maps associated to the planar landing case: (a) $y, \dot{x}$ and (b) $y, \dot{y}$. Red dots represent unstable (external) manifolds, blue dots represent stable (internal) manifolds*

of internal and external manifolds must match each other on the Poincaré section. However, the four states are not all independents as the location of the Poincaré section constrains one position state. Three states need to be matched at the SOE: one position state (x or y) and both velocity states ($\dot{x}$ and $\dot{y}$). To look at possible free transfers, two different Poincaré maps at the SOE are built. Figure 5.14 shows the maps: red dots represent unstable manifolds associated to the external CR3BP, while blue dots represent stable manifolds associated to the internal CR3BP.

Figures 5.14(a) and 5.14(b) show the projection of manifolds on the SOE in the phase spaces $(y, \dot{x})$ and $(y, \dot{y})$. Stable and unstable manifolds

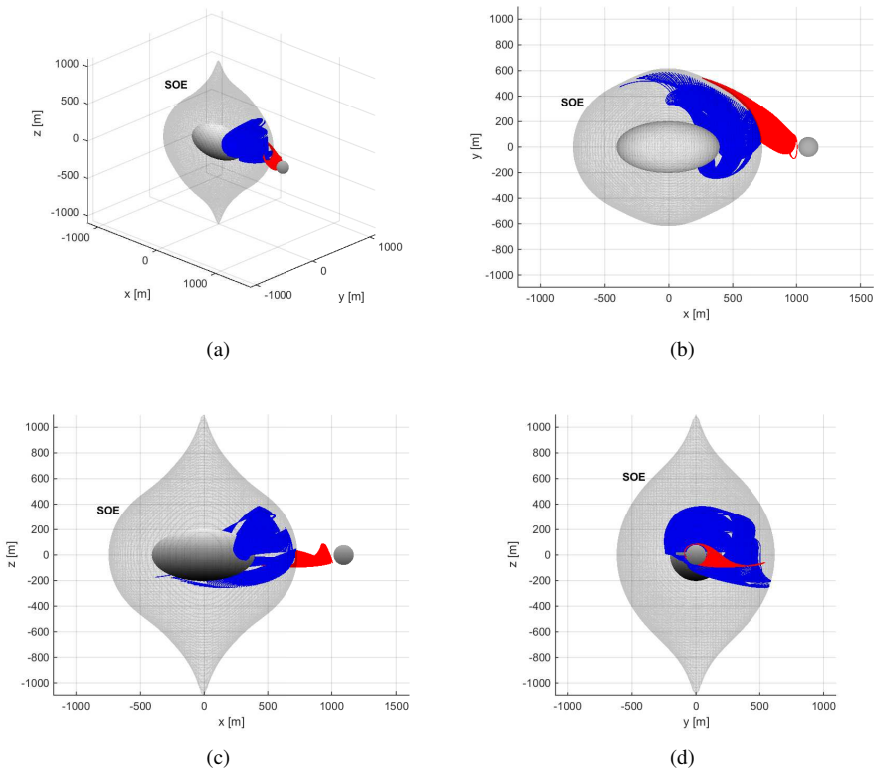

Figure 5.15: *Unstable (red) and stable (blue) manifolds associated to external and internal CR3BP (3D case): (a) three-dimensional view (b) x,y (c) x,z and (d) y,z projections*

have one intersection in the $(y, \dot{x})$ phase space, hence one point on the SOE exists where manifolds have the same position and the same $\dot{x}$. On the other hand, no intersections exist in the $(y, \dot{y})$ plane, and then, no points where the whole state of internal and external manifolds matches exist. Since no free transfer trajectories exist, a manoeuvre shall be performed on the SOE to match the $\dot{y}$ state. The intersection in Figure 5.14(a) is selected as possible landing solution and referred as solution 1 in the followings. Figure 5.13(b) shows the full trajectory associated to landing solution 1 in the x, y plane, as patched trajectory in external and internal systems. Table 5.4 reports the cost of the manoeuvre to be provided at the SOE, which in this case corresponds to a $\Delta\dot{y}$ manoeuvre.

The three-dimensional case is then discussed. Figure 5.15 shows computed manifolds associated to the three-dimensional case and their interaction on the SOE.

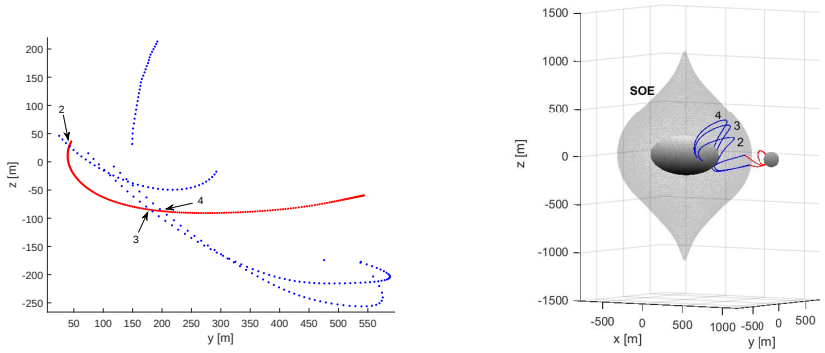

(a) (b)

Figure 5.16: *(a) Poincaré map associated to the 3D case: red dots represent unstable (external) manifolds, blue dots represent stable (internal) manifolds (projection in the x, y plane). (b) Selected landing solution for 3D case*

In this case, connection points are sought to guarantee continuity in position state between internal and external manifolds: three states are to be matched. The Poincaré section is again the SOE, which constraints one position state, and the map is built to represent x, y projection of manifolds on the SOE. Figure 5.16(a) shows the Poincaré map and the three intersections that exist between stable and unstable manifolds. These are referred as landing solutions 2, 3 and 4 in the followings. Blue dots in Figure 5.16(a) are shown to belong to four different curves, which correspond to four different kinds of families of stable manifolds associated to internal CR3BP solutions (Figure 5.12(b)).

Table 5.4: Δv *for selected landing solutions*

ID landing solution	Δv [cm/s]
1 (2D)	33.7
2 (3D)	37.8
3 (3D)	39.4
4 (3D)	41.6

The cost of the manoeuvre to be performed at the SOE is reported in Table 5.4 for all planar and three-dimensional selected solutions.

5.2 Asteroid Impact Mission landing design

Following the heritage of NEAR-Shoemaker, which was the first spacecraft to achieve a soft landing on an asteroid, and of the Rosetta mission, which was the first to achieve a soft landing on a comet nucleus, the Asteroid Impact Mission (AIM) [54, 55, 83] is planned to be the first to rendezvous with a binary asteroid. Designed by ESA, AIM is planned to be launched in 2020 and to arrive at the asteroid system in mid 2022 [1]. The target is the near-Earth binary asteroid 65803 Didymos [124], which will transit close to Earth (less than 0.1 AU) in late 2022. The binary system, whose primary was originally discovered in 1996 and named 1996 GT, was renamed Didymos, the Greek word for "twin", in 2003, after the discovery of a smaller satellite orbiting around the primary [76]. The primary asteroid is informally called Didymain and its small companion Didymoon. As a broader cooperation, AIM mission is part of the Asteroid Impact & Deflection Assessment (AIDA) [22, 23, 92] mission, a joint mission between ESA and NASA. The goal of AIDA is to assess the effectiveness of deflecting the heliocentric path of a threatening NEA for planetary defense purpose. More in detail, AIDA shall monitor the effects of a kinetic impact towards the surface of Didymoon on the heliocentric motion of the binary system. Within AIDA cooperation, AIM has the role of scientific investigator and shall observe the kinetic impact, which is achieved by means of the impactor DART (Double Asteroid Redirection Test) [20, 21, 127], a spacecraft designed by NASA. Such observations will support the study and understanding of the formation of asteroids and binary systems and the evolution of the Solar System regarding collisional evolution of small celestial bodies.

AIM shall rendezvous with Didymos prior to the arrival of DART in late 2022, after a nearly two-year interplanetary transfer. A sketch of AIM's interplanetary trajectory is shown in Figure 5.17(a), together with the orbital path of the Earth and Didymos from launch to arrival, on the ecliptic plane. The strategy to approach and rendezvous Didymos foresees relative navigation with respect to the asteroid system, using the on-board visual camera, to ultimately estimate the actual orbital path of the asteroid and to correctly rendezvous with it. Figure 5.17(b) shows the relative distance and velocity with respect to the target asteroid during the rendezvous phase, which includes five impulsive maneuvers. One week is currently chosen as time between two consecutive manoeuvres, in order to allow a detailed naviga-

[1] At the time of writing this thesis, AIM design underwent phase A and B1. Phase B2 and subsequent ones are currently awaiting for ESA ministry assembly approval.

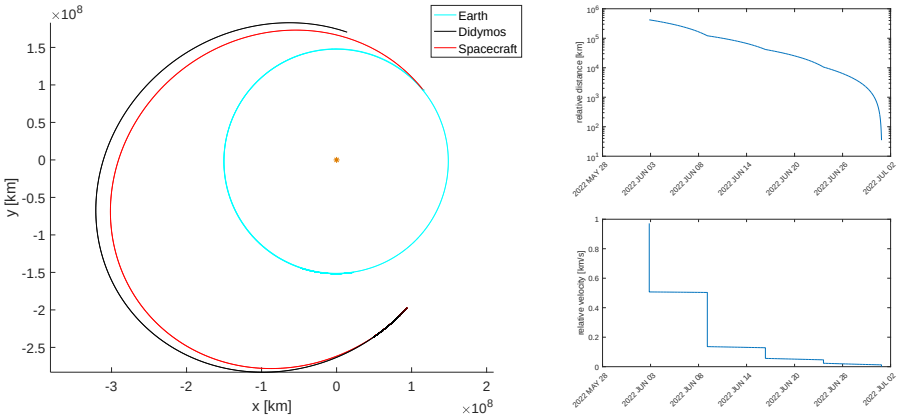

(a) (b)

Figure 5.17: *(a) projection of AIM's interplanetary trajectory on the ecliptic plane (b) relative position and velocity with respect to Didymos during the rendezvous manoeuvre*

tion estimate to correctly rendezvous with the asteroid, and to have enough time to re-schedule the manoeuvre sequence if needed. After rendezvous, the spacecraft is currently designed to pursue its scientific goals and close-proximity operations at the asteroid through the use of stationary points in the neighborhood of the two asteroids. Since out of the scope of this work, interplanetary mission analysis and close proximity operations of AIM are not detailed here. A more detailed description of all phases of the mission and a discussion on the motivation of mission analysis design solutions can be found in [45,46,49]. After arrival, AIM shall operate with a twofold goal, to perform both scientific investigations and technological demonstrations. AIM shall characterize Didymos from a dynamical and geophysical point of view and, after DART's arrival, will assess the consequences of the kinetic impact on the surface of Didymoon. The primary objectives of AIM include the detailed study and characterization of the binary couple, in terms of shape, mass, surface, sub-surface, interior structure, mechanical and thermal properties of the asteroids. Among these, the internal composition of the smaller asteroid will be determined by means of bi-static low frequency radar (LFR) tomography. Similarly to what is done with the CONSERT instrument [69], on board the ESA's Rosetta mission [131], the radar will include a lander-orbiter architecture to host both transmitters and receivers. A small lander, named MASCOT-2, shall be deployed on Didymoon to perform the Moonlet Engineering eXperiment (MEX) that will

demonstrate the ballistic landing and operations of a miniaturized asteroid lander on a binary system. MASCOT-2, a very small (about 13 kg) and completely passive probe, is named after MASCOT [134], the lander on board the Hayabusa-2 mission [132].

The Rosetta mission highlighted the challenges of designing close proximity trajectories and landing a probe on the surface of an extremely irregular body such as comet 67P/Churyumov-Gerasimenko [125], whose shape and mass distribution were completely unknown and unexpected during the mission design phase. In that case, the Philae lander [10] release was challenged by the highly perturbed dynamical environment in the proximity of the comet and by its very low and irregular gravity field. In analogy to the Rosetta mission, AIM will deploy a small and passive probe that will reach the surface of a largely unknown object after a purely ballistic descent. MASCOT-2 lander does not feature any mechanism to anchor to the surface of the asteroid, which makes the landing design even more challenging. Moreover, Didymos system's gravity field is expected to be weaker, with an escape velocity from Didymoon's surface of about 4-6 cm/s, since the asteroids are estimated to be nearly two (Didymain) and four (Didymoon) orders of magnitude less massive than comet 67P/Churyumov-Gerasimenko. In addition, the presence of two gravitational attractors makes the dynamics in the close proximity of the couple highly unstable and chaotic. The accurate knowledge of the dynamics driving the motion of a body in the vicinity of such a binary system is then a key point for the success of the mission, to correctly operate scientific payloads and to effectively land the probe on the asteroid.

An effective strategy for MASCOT-2 release is proposed here. The increased complexity of having two small bodies as gravity source is used here as a potential opportunity to be exploited in the design process, through the use of three-body modeling techniques. The AIM/MASCOT-2 scenario is presented in the following paragraphs as a case study. However, the applied methodology is representative for any asteroid/small body scenario.

5.2.1 Didymos three-body system

The dynamics of MASCOT-2 in the proximity of the binary asteroid system are modeled using a restricted three-body model, as detailed in the following. The landing trajectory and dynamics of MASCOT-2 is studied during close-proximity operations using the most precise up-to-date fidelity model of Didymos. Shape-based models are used to represent the gravitational contribution due to the two asteroids. Three-body solutions are investi-

gated within the Didymos binary system and suitable landing trajectories are selected. More in detail, manifold dynamics near libration points associated to the asteroid three-body system are exploited to find low-energy landing trajectories.

The modeling strategy is based on the CR3BP formulation, refined by including the effects of non-spherical mass distribution when modeling the two asteroids. Didymain and Didymoon are the primaries of a three-body system and their motion is constrained on circular paths around the barycentre of the binary. The classical CR3BP models the primaries using spherical and uniform mass distribution around their centre of mass, which is equivalent to consider point-mass sources. For this reason, the classical CR3BP accurately describes the dynamics around the binary couple only if the mass distribution of the two asteroids is close to be spherical. In general, this is not the case for small celestial bodies. The highly irregular mass distribution of such bodies can lead to very inaccurate results when studying the dynamics in their close proximity. In this work, more accurate models are implemented within a modified CR3BP, by including information on more complex mass distribution into the classical CR3BP. As for the case study, due to the lack of information and direct measurements regarding the mass distribution of the asteroids, the latter is directly recovered from shape information: the mass is considered to be uniformly distributed, within a non-spherical shape of the asteroid. Since it deals with the well-known CR3BP formulation, this strategy takes advantage from the large availability of dynamical solutions for astrodynamics and mission analysis design, by adapting such solutions to the case of modified CR3BP.

Didymos modified CR3BP

The working assumptions of the CR3BP related to the dynamics of the primaries are kept. The two asteroids follow a two-body circular path around the barycentre of the binary and their motion is not influenced by the presence of the third body (MASCOT-2). As usual, the equations of motion of the third body are written in the synodic frame, which rotates together with the primaries (Section 2). Concerning the rotational motion of Didymoon, observations show that the secondary is in a tidally-locked configuration, having the same period of rotation about its axis and revolution about the barycentre of the binary system. This configuration is such that Didymoon shows the same face to Didymain during its motion. More in detail, its smaller principal axis of inertia is aligned to the Didymoon-Didymain direction. The relative configuration between the two primaries is fixed as seen from the three-body synodic frame, with Didymoon's smaller princi-

pal axis lying on the x axis, together with the centres of mass of the primaries, having nondimensional $\tilde{x}$ coordinates of $-\mu$ and $1-\mu$. Figure 5.18 shows Didymos three-body system as seen from the rotating frame, in dimensional coordinates.

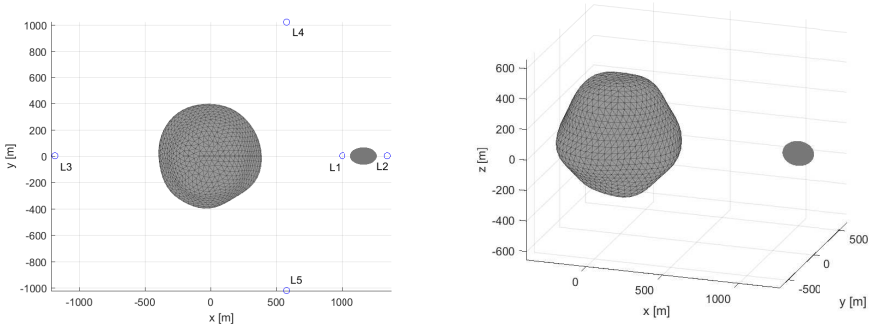

(a) (b)

Figure 5.18: *Didymos three-body system in rotating dimensional frame (a) x-y plane view with libration points (b) three-dimensional view.*

With reference to Section 2.1.1, the nondimensional equations of motion of the spacecraft are written in the synodic frame as

$$\begin{cases} \ddot{\tilde{x}} = \tilde{x} + 2\dot{\tilde{y}} + \tilde{U}_{1_{\tilde{x}}} + \tilde{U}_{2_{\tilde{x}}} \\ \ddot{\tilde{y}} = \tilde{y} - 2\dot{\tilde{x}} + \tilde{U}_{1_{\tilde{y}}} + \tilde{U}_{2_{\tilde{y}}} \\ \ddot{\tilde{z}} = \tilde{U}_{1_{\tilde{z}}} + \tilde{U}_{2_{\tilde{z}}} \end{cases} \tag{5.19}$$

where the subscript $(\cdot)_{\tilde{x}}$, $(\cdot)_{\tilde{y}}$ or $(\cdot)_{\tilde{z}}$ indicate partial derivatives, superscript $\tilde{}$ indicates nondimensional coordinates, $\tilde{U}_1$ and $\tilde{U}_2$ represent the nondimensional gravitational potential due to the primaries P_1 and P_2. Note that $\tilde{U}_1$ and $\tilde{U}_2$ differ from the three-body potential function $\tilde{U}$ defined in Section 2.1.1, the latter including the effects of both primaries and synodic frame rotation. The classical CR3BP formulation considers point-mass (or spherical) gravitational potentials, which can be written as

$$\tilde{U}_1 = \tilde{U}_{1_{\text{sph}}} = \frac{1-\mu}{\tilde{r}_1} \tag{5.20}$$

$$\tilde{U}_2 = \tilde{U}_{2_{\text{sph}}} = \frac{\mu}{\tilde{r}_2} \tag{5.21}$$

The modified version of the CR3BP implements shape based models of the two asteroids. According to the latest observations of Didymos system,

information on the shape of the asteroids are partially available. A face-vertex shape model of Didymain is available[2], while Didymoon's shape is estimated to be an elongated tri-axial ellipsoid. The following paragraphs describes briefly the strategy used to reproduce the asteroids gravity field based on these shape models and recall techniques presented in Section 2.3.1.

The gravity effect of Didymain is modeled using its shape model and its mass distribution is considered to be uniform (constant density polyhedron). The gradient of the polyhedron potential is written with reference to Section 2.3.1 as

$$\begin{Bmatrix} U_{\text{poly}_{\overline{x}_1}} \\ U_{\text{poly}_{\overline{y}_1}} \\ U_{\text{poly}_{\overline{z}_1}} \end{Bmatrix} = G\rho \left(\sum_{f \in \text{faces}} \mathbf{F}_f \cdot \overline{\boldsymbol{r}}_f \overline{\omega}_f - \sum_{e \in \text{edges}} \mathbf{E}_e \cdot \overline{\mathbf{r}}_e \overline{L}_e \right) \tag{5.22}$$

All parameters in Eq. (5.22) refer to Section 2.3.1, with notation $\overline{\square}_1$ referring to coordinates of the field point with respect to the rotating frame centreed at the centre of the polyhedron. Relations between $\overline{x}_1, \overline{y}_1, \overline{z}_1$ and nondimensional coordinates associated to Didymos three-body system are provided by

$$\begin{cases} \overline{x}_1 = (\tilde{x} + \mu) L^* \\ \overline{y}_1 = \tilde{y} L^* \\ \overline{z}_1 = \tilde{z} L^* \end{cases} \tag{5.23}$$

The potential function is nondimensionalized according to characteristic length L^* and time t^* associated to the problem

$$\begin{Bmatrix} \tilde{U}_{\text{poly}_{\tilde{x}}} \\ \tilde{U}_{\text{poly}_{\tilde{y}}} \\ \tilde{U}_{\text{poly}_{\tilde{z}}} \end{Bmatrix} = \begin{Bmatrix} U_{\text{poly}_{\overline{x}_1}} \\ U_{\text{poly}_{\overline{y}_1}} \\ U_{\text{poly}_{\overline{z}_1}} \end{Bmatrix} \frac{t^{*2}}{L^*} \tag{5.24}$$

Concerning Didymoon, the most updated model of its shape considers it as an ellipsoid. Accordingly, its gravity effect is modeled using the potential of a constant density tri-axial ellipsoid. With reference to Section 2.3.1 the gradient of the potential due to the ellipsoid is written as

$$\begin{Bmatrix} U_{\text{ell}_{\overline{x}_2}} \\ U_{\text{ell}_{\overline{y}_2}} \\ U_{\text{ell}_{\overline{z}_2}} \end{Bmatrix} = -2G\rho\pi\alpha\beta\gamma \begin{Bmatrix} \overline{x}_2 \int_{\lambda(\overline{x}_2,\overline{y}_2,\overline{z}_2)}^{\infty} \frac{du}{(\alpha^2+u)\Delta(u)} \\ \overline{y}_2 \int_{\lambda(\overline{x}_2,\overline{y}_2,\overline{z}_2)}^{\infty} \frac{du}{(\beta^2+u)\Delta(u)} \\ \overline{z}_2 \int_{\lambda(\overline{x}_2,\overline{y}_2,\overline{z}_2)}^{\infty} \frac{du}{(\gamma^2+u)\Delta(u)} \end{Bmatrix} \tag{5.25}$$

[2]The Didymain shape model is used in the frame of the AIM contract, however it is still unpublished (courtesy of L. Benner and S. Naidu)

All parameters in Eq. (5.25) refer to notation used in Section 2.3.1. Similarly to what is done for the polyhedron case, notation $\overline{\square}_2$ refer to coordinates of the field point with respect to the dimensional rotating frame oriented as principal axis of the ellipsoid. Relations between such coordinates and coordinates of Didymos three-body system are provided by

$$\begin{cases} \overline{x}_2 = (\tilde{x} - 1 + \mu)L^* \\ \overline{y}_2 = \tilde{y}L^* \\ \overline{z}_2 = \tilde{z}L^* \end{cases} \tag{5.26}$$

As for the polyhedron case, the potential of the ellipsoid is nondimensionalized according to characteristic length L^* and time t^* associated to the problem

$$\begin{Bmatrix} \tilde{U}_{\text{ell}_{\tilde{x}}} \\ \tilde{U}_{\text{ell}_{\tilde{y}}} \\ \tilde{U}_{\text{ell}_{\tilde{z}}} \end{Bmatrix} = \begin{Bmatrix} U_{\text{ell}_{\overline{x}}} \\ U_{\text{ell}_{\overline{y}}} \\ U_{\text{ell}_{\overline{z}}} \end{Bmatrix} \frac{t^{*2}}{L^*} \tag{5.27}$$

To implement the modified CR3BP formulation, the gravity terms due to the asteroids are modified to include the effects of their non-spherical mass distribution: point mass potentials are replaced by nondimensional shape-based potentials $\tilde{U}_{\text{poly}}$ and $\tilde{U}_{\text{ell}}$. Partial derivatives of shape-based potential functions are included in the modified CR3BP equations of motion as follows

$$\begin{cases} \ddot{\tilde{x}} = \tilde{x} + 2\dot{\tilde{y}} + \tilde{U}_{\text{poly}_{\tilde{x}}} + \tilde{U}_{\text{ell}_{\tilde{x}}} \\ \ddot{\tilde{y}} = \tilde{y} - 2\dot{\tilde{x}} + \tilde{U}_{\text{poly}_{\tilde{y}}} + \tilde{U}_{\text{ell}_{\tilde{y}}} \\ \ddot{\tilde{z}} = \tilde{U}_{\text{poly}_{\tilde{z}}} + \tilde{U}_{\text{ell}_{\tilde{z}}} \end{cases} \tag{5.28}$$

Note that only gravity terms due to the primaries acting on the third body are modified. No changes are made on the assumptions regarding the motion of the centre of mass of the two primaries and their mutual interaction.

Model validity

The previous section defines the model used to propagate the dynamics of MASCOT-2 in the proximity of the binary couple. Since the gravity field is extremely low, it might be worth to consider the effects of orbital perturbations due to SRP and fourth-body effect (Sun or Earth). Table 5.5 reports the order of magnitude of orbital perturbations acting on the lander, as compared to Didymos gravity acceleration at 1 km from the primary, which is found to be the only relevant driver for MASCOT-2 dynamics. The most

relevant perturbing effect, the SRP, is indeed three orders of magnitude less important than Didymos gravity. Accordingly, the SRP could be relevant only in case of long time of flights. This is not the case for MASCOT-2, which is foreseen to only have a short ballistic descent of a few hours before reaching the surface of Didymoon. Fourth body perturbations due to Sun and Earth (which is closer than 0.1 AU during MASCOT-2 descent) are shown not to be relevant at all.

Table 5.5: *Dynamical effects acting on MASCOT-2 in the proximity of Didymos system*

	Order of magnitude [m/s^2]
Didymos gravity	10^{-5}
SRP	10^{-8}
Sun's gravity (4$^{\text{th}}$ body)	10^{-11}
Earth's gravity (4$^{\text{th}}$ body)	10^{-13}

The most important source of perturbation will likely be the irregularities of Didymain and Didymoon gravity fields, which act in a very relevant way on MASCOT-2 dynamics during its ballistic descent. Figure 5.19 shows an example of landing trajectory, propagated using different models of the Didymain-Didymoon gravity field. Dotted-dashed line indicate the trajectory in the classical CR3BP model. In this case, the mass distribution of both Didymain and Didymoon is modeled as a uniform sphere (central field). This case is referenced in the figure with sphere-sphere (S1-S2). The second case is referenced as sphere-ellipsoid (S1-E2) and refer to the modeling of Didymain as sphere and Didymoon as ellipsoid. The last case is the most accurate and is the one described in the previous section: polyhedron-ellipsoid (P1-E2), with polyhedral model of Didymain and ellipsoidal model of Didymoon.

Figure 5.19 shows that a significant difference exists in the final trajectory when comparing different modeling strategies of Didymoon, while no relevant effects are observed when modeling Didymain as a sphere or using the polyhedron model. For mission analysis application, S1-E2 and P1-E2 models are shown to be suitable for representing MASCOT-2 dynamics. Concerning results presented in this work, in many cases, the S1-E2 model was preferred for its effectiveness in terms of computational time compared to the P1-E2 model.

Sample solutions

This section presents simple solutions related to the classical CR3BP, i.e. to the sphere-sphere model. Such solutions are used to initiate the design

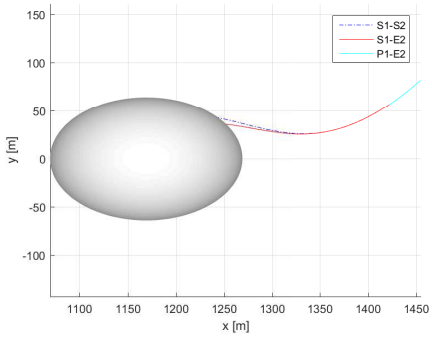

Figure 5.19: *Ballistic descent with different models of Didymain-Didymoon gravity: sphere-sphere (S1-S2), sphere-ellipsoid (S1-E2), polyhedron-ellipsoid (P1-E2).*

process, to investigate MASCOT-2 ballistic descent opportunities. Periodic orbits and invariant manifold families are investigated as suitable solutions. The goal is to investigate solutions to land on Didymoon, hence only L1 and L2 related trajectories are considered here, due to their vicinity to Didymoon asteroid. Trajectories in the proximity of L3, L4 and L5 can be used during close-proximity operations to fulfill specific requirements on payloads and asteroid visibility such as bounded motion in the neighborhood of L4 and L5 or even as disposal strategy for AIM spacecraft on the surface of Didymain through L3 related trajectories. Concerning periodic motion, families of Halo orbits about first and second collinear points are shown in Figure 5.20 and 5.21.

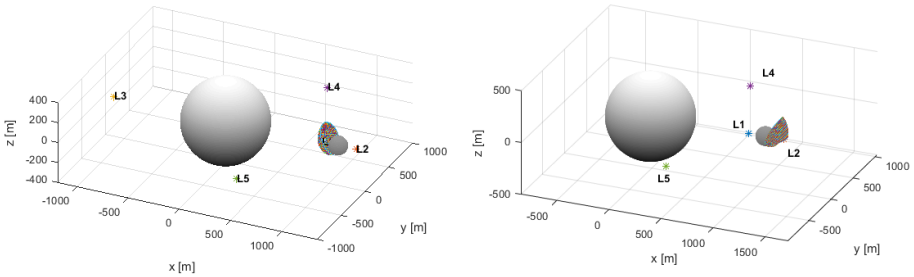

(a) (b)

Figure 5.20: *Families of Halo orbits about (a) L1 and (b) L2, as seen from Didymos system co-rotating frame.*

Some of the orbits in the L1 and L2 family intersect the surface of Didy-

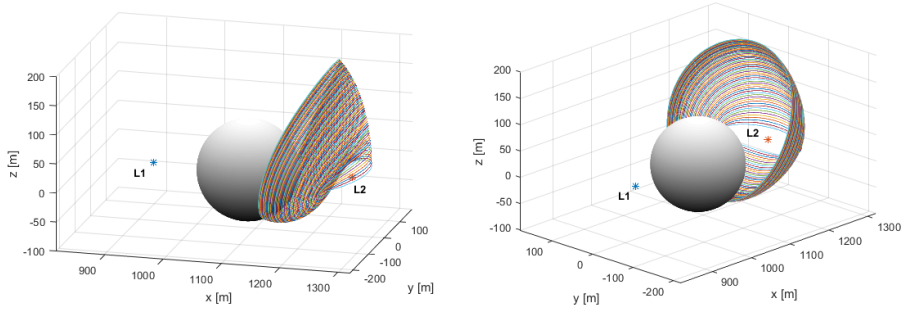

(a) (b)

Figure 5.21: *Family of L2 Halo orbits, enlargement of Figure 5.20(b).*

moon. These can be selected as suitable solutions for landing design: in this case the lander could be directly injected in the impacting orbit. This implies that the release occurs very close to Didymoon's surface, which is not desirable from the AIM spacecraft safety point of view. To avoid this safety issue, it is possible to exploit stable manifold dynamics associated to the orbit. Figure 5.22 shows examples of stable manifolds associated to a Halo orbit about L2. Both x-y and three-dimensional view are shown.

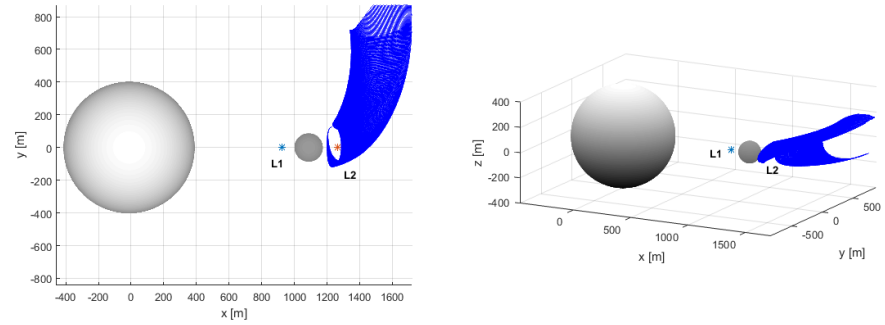

(a) (b)

Figure 5.22: *Stable manifolds associated to a L2 Halo orbit.*

To design the landing trajectory, the manifolds are computed and propagated backwards starting from the point on the orbit that intersects the surface of Didymoon. Some of these three-body solutions are shown in Figure 5.23. More in detail, stable manifolds associated to Halo and Lyapunov orbits about L2 are shown respectively in Figure 5.23(a) and 5.23(b). As

mentioned, such trajectories can be exploited for the last part of the landing manoeuvre, namely the ballistic descent of MASCOT-2 after release.

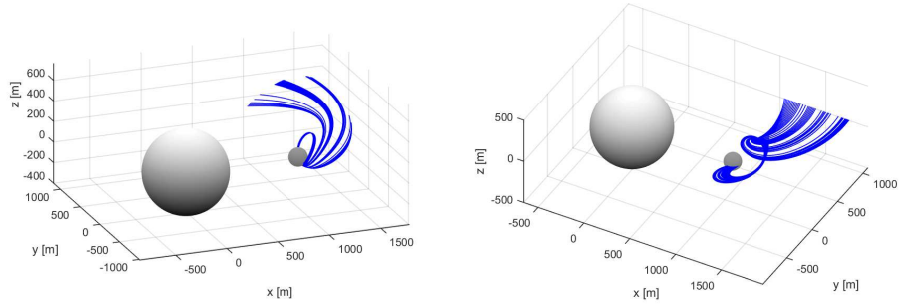

(a) (b)

Figure 5.23: *Stable manifolds associated to a (a) Halo and a (b) Lyapunov orbit about L2, as seen from Didymos system co-rotating frame.*

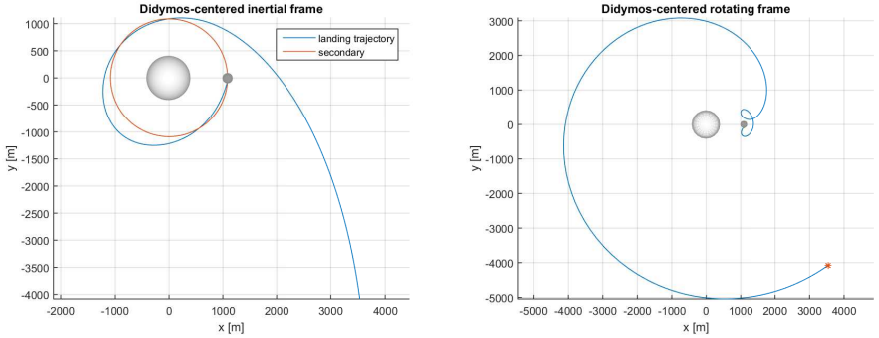

(a) (b)

Figure 5.24: *Example of ballistic descent on a stable manifold associated to a Lyapunov orbit about L2: (a) inertial and (b) rotating frame.*

Figure 5.24 shows an example of a trajectory extracted from the manifolds family associated to a Lyapunov orbit about L2. The trajectory is shown both in the inertial and in the rotating frame. In this example, the ballistic descent could start very far from the surface of Didymoon, depending on the knowledge of the gravity field and on release errors.

5.2.2 Landing design strategy

MASCOT-2, as its predecessor MASCOT (on board the Hayabusa mission), is a completely passive probe. It does not have any device to stop or anchor on Didymoon's surface once there. Also, MASCOT-2 does not have any orbit-controlling device, such as thrusters. For this reason, the landing trajectory must be carefully designed, and a well-designed purely ballistic descent is the only chance to reach Didymoon's surface. The success of the landing is completely depending on the choice of the release condition. Moreover, the safety of AIM spacecraft must be ensured during all phases of the mission, meaning that the release point shall be far enough from both asteroids. Given these requirements, two major criticalities are identified for the MASCOT-2 scenario. The first critical aspect regards the capability of the lander to reach the surface of Didymoon after release. This is an extremely challenging problem under such nonlinear and chaotic dynamics described in Section 5.2.1. A small deviation in the release state could lead to very different trajectories, which might or might not intersect Didymoon's surface. To avoid this problem, the landing trajectory shall be confined in a region with low divergence of the dynamical flow. The second challenge related to the MASCOT-2 landing design appears clearly linked to whether the lander will stay or not on the surface after touch down. The extremely low-gravity environment will likely induce the probe to bounce multiple times until reaching a stable position on Didymoon's surface or, in the worst condition, to escape from the asteroid's gravity field. For this reason, the lander shall be put on a suitable trajectory, that allows the lander to safely reach Didymoon with a sufficiently small touch down velocity, such that it will not bounce away. From the design point of view, the touch down velocity plays a major role, especially when compared to the local escape velocity at the asteroid surface.

In order to better understand the dynamical behaviour of the third body in such peculiar environment, it is worth to highlight the role of the escape velocity and identify the main design options for the case study. In the frame of the classical restricted two-body problem, the escape velocity is defined as the minimum velocity to escape from the gravitational attraction of the body. In this case, the limiting condition corresponds to the velocity to be inserted on a parabolic arc, which reaches the SOI of the attractor after infinite time. Conversely, this means that a body release at the SOI, heading towards the attractor through a pure ballistic descent, will reach its surface with a touch down velocity greater or equal than the minimum escape velocity. This imposes a dynamical constraint to the minimum touch

down velocity reachable from outside the SOI. The only way to decrease the touch down velocity with a pure ballistic descent is to release the probe from within the SOI, in order to let the probe withstand to the gravitational acceleration for a smaller time span. As for the case of Didymos system and when Didymoon's rotation is taken into account, the minimum escape velocity from Didymoon's surface occurs at the equator and it is slightly lower than 8 cm/s. The SOI with respect to the main attractor (Didymain), is approximately 180 m, which corresponds to nearly 100 m altitude from Didymoon's surface. As mentioned, this is valid for the case of restricted two-body problem formulation, which can lead to very inaccurate results in the Didymos case of study.

Analogous concepts can be derived for the case of restricted three-body problem. The R3BP is known not to have an analytical solution of the equations of motion and, unlike the case where a single attractor is present, the escape velocity from Didymoon's surface differs depending on the local latitude and longitude. When dealing with R3BP, it is common to look at the qualitative behaviour of the motion of the third body using the energy approach. More in detail, zero relative velocity surfaces (Hill's curves) can be derived to qualitatively bound the motion of the particle in the proximity of the two primaries (see [118, 128] for further detail). Interesting insights on MASCOT-2 scenario can be derived by following this approach. Analogously to the two-body case, it is possible to define the escape velocity as the minimum velocity allowing a massless body to escape from Didymoon's surface. For a sufficiently low amount of energy, zero relative velocity surfaces will separate clearly the region near P_1 from the region near P_2: in this case, a body near P_2 is trapped to stay in its neighborhood. For a higher energy level, a connection between the two zero relative velocity surfaces opens in correspondence of the L1 point: in this case, the particle is allowed to move between P_1 and P_2 regions, by passing through the L1 neck. With relation to MASCOT-2 scenario, this condition can be seen as the lowest energy for a particle to escape from Didymoon's neighborhood. Figure 5.25 shows an example of low energy trajectory escaped from Didymoon through the L1 neck.

More in detail, the lowest energy trajectory to escape from P_2 region is the stable manifold associated to L1 point. The velocity at intersection between the manifold and the surface of Didymoon corresponds to the minimum escape velocity from Didymoon's surface. This kind of information can be used to assess the existence of a ballistic landing trajectory, from outside the P_2 region. With analogy to the escape problem, a lander can reach the surface from L1 through its unstable manifold. Both landing and

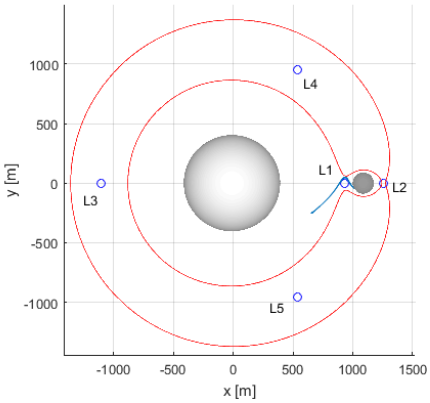

Figure 5.25: *Low energy escape from Didymoon through the L1 neck of Hill's curves.*

escaping trajectories are found at the same level of energy, corresponding to the opening of the L1 neck. Intuitively, the minimum energy correspond to the minimum escape velocity from Didymoon's surface. In the following, this velocity will be referenced as L1 escape velocity, or v_{L1}. As for the case of Didymos, this trajectory corresponds to an escape velocity v_{L1} of about 4.57 cm/s. In analogy to what was discussed for the two-body case, this value represents the minimum touch down velocity when the probe is released from L1 point. It is known that a higher level of energy allows the opening of the L2 neck. In this case, the particle has enough energy to escape from the attraction of both asteroids. The L2 escape velocity (v_{L2}) represents the velocity corresponding to the level of energy for which the L2 neck opens. The same considerations made for L1 apply: in this case, in order to escape from L2 neck the minimum escape velocity v_{L2} is about 5.11 cm/s. Figure 5.26 shows the stable/unstable manifold branches associated to L1 and L2, corresponding respectively, to minimum escape/touch down velocity solutions.

To summarize, no escape is possible for velocities below the L1 point limit v_{L1}, while escape is possible through the L1 neck for $v_{\mathrm{L1}} < v < v_{\mathrm{L2}}$ and through the L2 neck for $v > v_{\mathrm{L2}}$. L1 and L2 escape velocities are reported in Table 5.6 for different cases of Didymos modeling: escape conditions are compared for the case of sphere-sphere (S1-S2), sphere-ellipsoid (S1-E2) and polyhedron-ellipsoid (P1-E2) models. Note that values differs significantly when Didymoon is modeled as sphere or ellipsoid, while there is no substantial dependency on Didymain's modeling strategy.

Figure 5.27 shows a Monte Carlo simulation performed to support en-

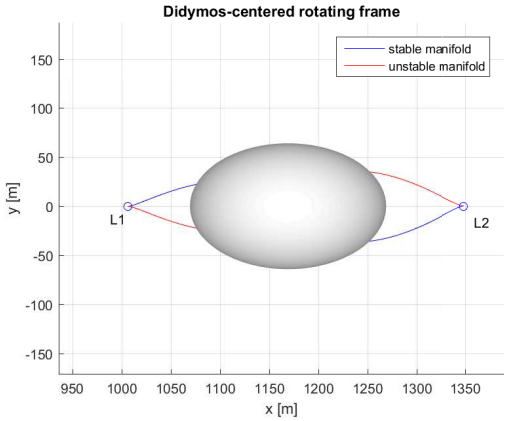

Figure 5.26: *Stable (blue) and unstable (red) manifolds associated to L1 and L2 points. Stable manifolds corresponds to minimum escape velocity solutions, unstable manifolds to minimum touch down velocity solutions*

Table 5.6: *L1 and L2 escape velocities for different Didymos models: sphere-sphere (S1-S2), sphere-ellipsoid (S1-E2) and polyhedron-ellipsoid (P1-E2) [cm/s].*

	S1-S2	**S1-E2**	**P1-E2**
v_{L1}	4.95	4.58	4.57
v_{L2}	5.23	5.11	5.11

ergy considerations when looking at touch down velocities. A uniform distribution of points is considered on the surface of Didymoon and the dynamics are propagated backwards from each of these points, with a given touch down velocity v at the surface, uniformly distributed in direction. It is shown that no trajectories comes from outside the binary system for touch down velocities below the L1 point limit v_{L1} (Figure 5.27(a)), while some trajectories exist through the L1 neck for $v_{L1} < v < v_{L2}$ (Figure 5.27(b)). Trajectories through both L1 and L2 are finally shown for $v > v_{L2}$ (Figure 5.27(c)).

The L1 case is the lower limiting case in terms of energy level of the third body. This solution might be applied to the MASCOT-2 scenario. However, due to safety issues, the L1 solution is discarded in favor of a safer release from L2 side. It is indeed preferable to release the lander from outside the asteroid system (L2 side) rather than from between the two asteroids (L1 side). For these reasons, for MASCOT-2 scenario, low energy trajectories associated to unstable manifold of L2 are investigated as suitable landing solutions. A purely ballistic landing can be achieved

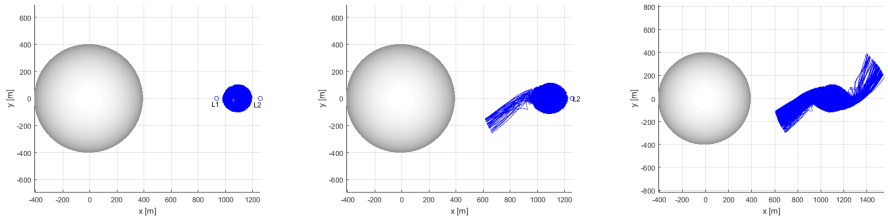

Figure 5.27: *Monte Carlo simulation: backwards integration of dynamics with initial velocity v from the surface of Didymoon (a) $v < v_{L1}$, (b) $v_{L1} < v < v_{L2}$, (c) $v > v_{L2}$.*

by releasing MASCOT-2 from the L2 point, on its unstable manifold. This constraints the release altitude and the AIM spacecraft trajectory to the L2 point. Different and higher release altitudes are desirable from the mission design point of view. To achieve this goal, the design strategy foresees to construct the ballistic descent starting from outside the L2 region, by combining the stable L2 manifold (from release point up to L2) with the unstable manifold (from L2 to Didymoon's surface). The targeted complete ballistic path of MASCOT-2 from release up to touch down is shown in Figure 5.28(a). The chosen manifold solution is also suitable to address the challenge of reaching Didymoon after release, since it provides minimization of the instability and divergence of the dynamical flow. From a mathematical point of view, the L2 point includes a 2D stable and a 2D unstable manifold branch. This means that, once at L2, when switching from stable to unstable manifold, the lander will have the same probability to fall either on the wrong unstable manifold branch (outgoing from Didymos system) or on the right unstable manifold branch (ingoing towards the surface of Didymoon). Since no trajectory control can be operated by MASCOT-2, the lander is released close to the stable manifold, but not exactly on it. The release point is found after propagating backward the state of the landing point associated to the nominal manifold solution, but considering a higher touch down velocity (same direction). The dynamics are backwards propagation until the release distance is reached. This procedure increases the robustness of the landing solution, at the cost of a slightly higher energy and touch down velocity. A more detailed description of the procedure used to find the nominal landing trajectory is provided in Section 5.2.5.

The values in Table 5.6 are important since they represent dynamical constraints for the MASCOT-2 landing problem. Any ballistic trajectory coming from outside the Didymos system towards Didymoon, will reach

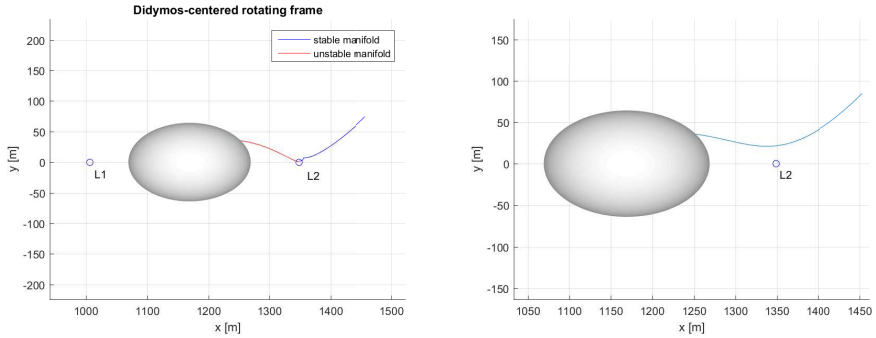

(a) (b)

Figure 5.28: *(a) Stable (blue) manifold branch carries the lander from release point up to L2, where it jumps on the unstable (red) branch to proceed towards the Didymoon's surface. (b) Robust landing trajectory with release in the proximity of L2 stable manifold*

the asteroid with a touch down velocity that is (equal or) higher than v_{L2}. Since the AIM spacecraft, for safety reason, will not deploy MASCOT-2 too close to the two asteroids, v_{L2} represents the minimum touch down velocity for candidate ballistic trajectories related to the AIM/MASCOT-2 scenario. It is highlighted here that manifolds are computed using the modified CR3BP formulation described in Section 5.2.1.

5.2.3 MASCOT-2 landing scenario

MASCOT-2 will be released by the AIM spacecraft at a safe distance of 200 m from Didymoon's surface. As discussed in the previous section, the baseline design strategy foresees the exploitation of the manifold dynamics associated to the L2 point. Numbers and figures refer to physical parameters of Didymos system as reported in [109]. The following paragraphs reports the main assumptions related to the AIM design scenario.

Release

MASCOT-2 will be released by AIM by means of a spring-based mechanism, which will provide a relative velocity between the lander and the orbiter of few cm/s. From the mission design point of view, the chosen ballistic trajectory must be robust to uncertainties in the release event. The nominal trajectory is validated against state dispersion at release. More in detail, errors related to AIM navigation and release mechanism are taken

into account and the information is used to assess the success rate of the release. The following contributions are considered:

- Navigation error: applied on the full release state (both position and velocity) of AIM spacecraft at release. Dispersions are computed according to AIM navigation information.
- Release mechanism error (vector direction): error in relative velocity between MASCOT-2 and AIM spacecraft at release. The error is dispersed around the nominal release velocity provided by the spring. The error in direction is quantified within a half-cone angle of 5 deg (1σ value) around nominal release direction.
- Release mechanism error (vector norm): the error is quantified into the 10% (1σ value) of the nominal release velocity norm.

Interaction with asteroid surface

An important part of MASCOT-2 landing design is to assess and simulate the dynamics of the lander once it gets in contact with the asteroid's soil. The interaction with Didymoon's surface is a crucial point to establish whether MASCOT-2 will escape or not after bouncing. As mentioned, a successful landing will likely see MASCOT-2 bouncing few times on the surface of Didymoon before coming to a rest. The modeling of the surface interaction heads to the definition of the velocity of MASCOT-2 after touch down.

- Velocity after touch down (norm): the most important aspect to be studied is to assess the quantity of energy dissipated at touch down. This effect can be summarized into a single parameter, called restitution coefficient, defined as the ratio between velocity after (v_{TD}^{+}) and before (v_{TD}^{-}) touch down

$$\eta = \frac{v_{\text{TD}}^{+}}{v_{\text{TD}}^{-}} \tag{5.29}$$

  The restitution coefficient ranges from 0 (fully inelastic collision) to 1 (fully elastic collision) and it represents a measure of the energy dissipated at contact ($\eta \leq 1$). As for the case of study, two different effects are considered as dissipative terms: part of the energy at touch down will be absorbed by the structure of MASCOT-2 (η_{struct}), part of it will be absorbed by the asteroid's soil (η_{soil}):

$$\eta = \eta_{\text{soil}} \cdot \eta_{\text{struct}} \tag{5.30}$$

The restitution coefficient allows to evaluate the amount of energy dissipated by the impact, which essentially turns into a decrease in the norm of the velocity vector after bouncing. The actual parameter, related to the Didymoon/MASCOT-2 scenario, is of course very difficult to be known and it is usually estimated according to the expected surface properties. Missions such as JAXA's Hayabusa [132], ESA's Rosetta [10, 134] and NASA's NEAR-Shoemaker [136] have shown how hard is to accurately estimate such parameter based on the soil's response and that a high level of uncertainty exists. For this reason, a worst case scenario is considered here, with very poor dissipation introduced by a very hard soil ($\eta_{\text{soil}} = 0.9$). The damping effect provided by MASCOT-2 structure was estimated and the overall coefficient of restitution is $\eta = 0.6$.

- Velocity after touch down (direction): uncertainties on the local soil inclination are included in the model to stochastically reproduce the irregularities of the surface. The direction of velocity after touch down is computed according to uniform distribution in azimuth and with gaussian distribution in elevation with mean value of 90 deg and 3σ value dispersion of 70 deg.

5.2.4 Sensitivity analysis to design parameters

In order to properly design an effective landing trajectory and to be robust to real-world conditions, it is important to identify design parameters critical for the success of the manoeuvre. This section presents sensitivity analyses performed on the design parameters. Being related to an ongoing mission design, the analyses presented might refer to different phases of design process. Hence, numbers and figures might not be fully consistent with other provided in the text, due to updates on requirements and data available during the design phase. However, the general results in terms of behaviour and identification of criticalities hold.

Sensitivity to Didymos properties

A great source of uncertainty could reside in the actual mass of Didymos. In particular, concerning the three-body dynamics, the ratio between the two masses is the relevant parameter. Table 5.7 shows escape L1 and L2 velocities for the nominal and limiting cases, when the mass ratio is taken as

$$M_2/M_1 = 0.0093 \pm 0.0013 \tag{5.31}$$

Results show that the higher M_2/M_1, the higher the success rate. A very low value of M_2/M_1 can critically affect the success of the landing manoeuvre, while no problem is expected for mass ratio equal or greater than its nominal value.

Table 5.7: *L1 and L2 escape velocities in [cm/s] for different mass ratio between Didymos primaries*

M_2/M_1	v_{L1}	v_{L2}
0.0080	4.03	4.50
0.0093	4.61	5.14
0.0106	5.16	5.76

Sensitivity to release condition

As far as the spacecraft design is concerned, the major source of error in MASCOT-2 trajectory is surely due to uncertainty in release conditions. General sensitivity analyses showed that position error can be tolerated up to tens of meters, while the dynamics imposes a much more stringent requirement on velocity dispersion which cannot be tolerated to be above a few cm/s. The effects associated to each separate contribution due to navigation, release mechanism error in direction and in norm of velocity vector are investigated. Nominal error are defined, with reference to Section 5.2.3. The relevance of each effect is identified by means of Monte Carlo simulation performed using different values of uncertainty. In the attempt to increase landing performance, lower errors with respect to nominal one are investigated. The aim is to identify critical parameters whose reduction of uncertainty can be effective to increase the landing performance. Monte Carlo simulations are performed using a fraction of the nominal error (10%, 20%,...) associated to the three aforementioned effects when considered separately: when one effect's uncertainty is decreased, the remaining two are taken with their nominal uncertainty. Sensitivity on successful landing probability is shown in Figure 5.29, for the case of release from 200 m and 300 m altitude. Each point in the curves represents a Monte Carlo simulation performed. Each curve represents the simulations performed while varying one parameter associated to dispersion. The blue line refers to navigation error: several Monte Carlo simulations are ran using nominal (100%) release mechanism errors and variable error on navigation error, from 10% up to nominal (100%). The percentage is directly applied on the error to be summed to the release state of AIM (both position and velocity). The same applies for the other two cases. The red line refers to variation

in the error associated to the norm of release mechanism velocity, which ranges between the 10% of its nominal value (that correspond to 1% of velocity) and its nominal value (10% of velocity) while keeping the other effect as nominal. Finally, the yellow line refers to errors in the direction of release mechanism velocity, which ranges between 10% of its nominal value (half cone angle of 0.5 deg) and its nominal value (half cone angle of 5 deg). Figure 5.29 shows clearly that the most relevant error that affect the success rate of the landing is due to the norm of release mechanism velocity. It is shown indeed that a decrease in this error gives a substantial increase in success rate. The same is not true for the other errors: the increase of navigation accuracy and the increase in release mechanism direction release accuracy do not affect in a relevant fashion the success of MASCOT-2 landing.

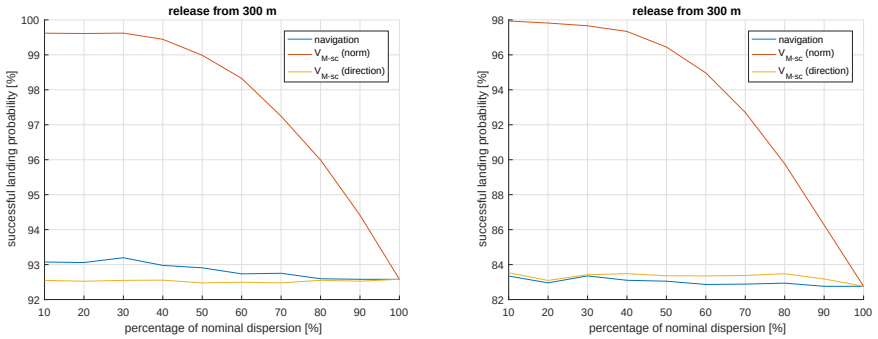

(a) (b)

Figure 5.29: *Successful landing probability with release from (a) 200 m and (b) 300 m altitude*

Similarly to what is done with success rate, the sensitivity of landing point location to dispersion is also studied for the cases of release from 200 m and 300 m altitudes. Figure 5.30 and 5.31 show the 3σ dispersion of latitude and longitude bands of the landing point for the case of, respectively, release from 200 m and 300 m. The results show that both errors in norm and direction of release mechanism velocity are relevant with respect to dispersion in longitude, while navigation error plays a minor role. Concerning the effects on latitude dispersion, the difference is shown to be very low (about 5 deg) between worst and best cases. The latitude is therefore not very affected by release errors.

As a further relevant parameter to be studied, the sensitivity analysis is also performed on the time of flight during ballistic descent, from release

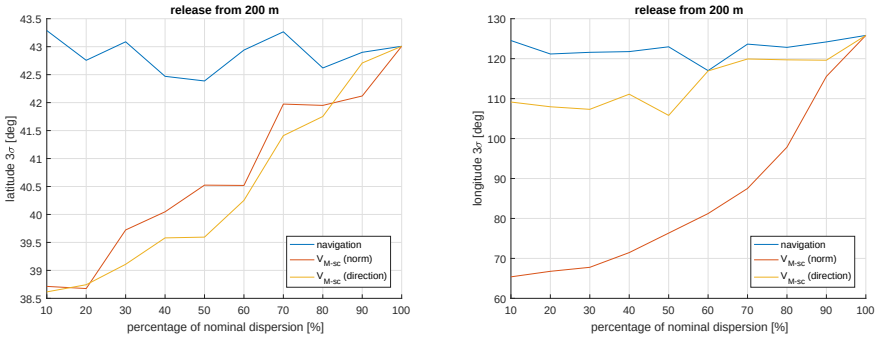

(a) (b)

Figure 5.30: *3σ dispersion of (a) latitude and (b) longitude bands of landing point with release from 200 m*

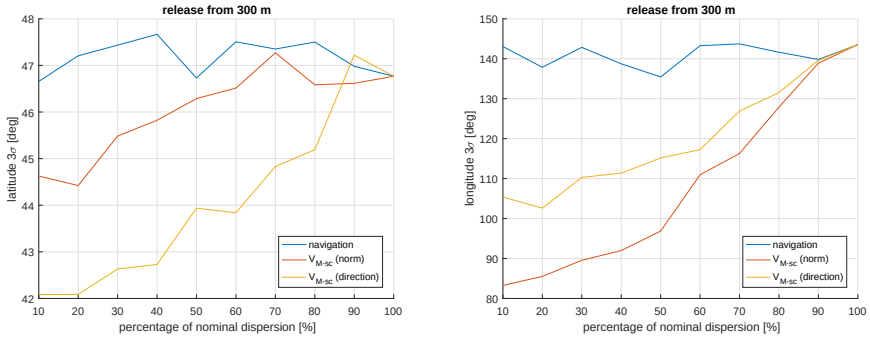

(a) (b)

Figure 5.31: *3σ dispersion of (a) latitude and (b) longitude bands of landing point with release from 300 m*

until rest on Didymoon's surface. Figure 5.32 shows results for the cases under study. As for the case of landing point, the time of flight is shown to be affected by both errors in norm and direction of the release mechanism velocity.

Sensitivity to touch down conditions

A very important issue to be addressed is the assessment of escape probability after touch down. With this respect, the key parameter is the restitution coefficient η defined in Section 5.2.3, namely the ratio between the velocity of the lander after and before touch down. Results are here presented related to different restitution coefficient to reproduce the interaction between

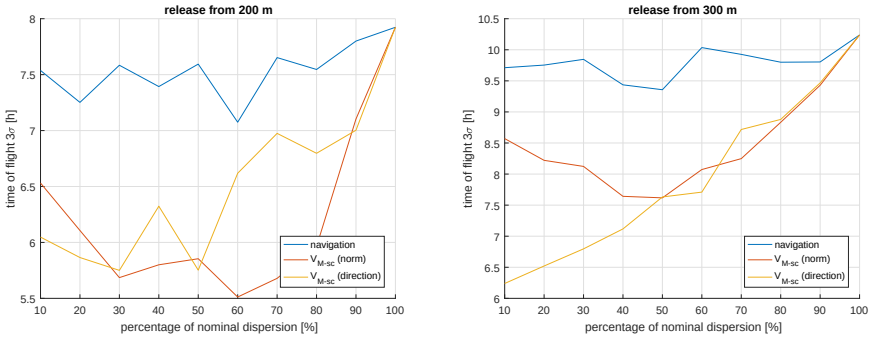

(a) (b)

Figure 5.32: *3σ dispersion of time of flight until rest on surface with release from (a) 200 m and (b) 300 m altitude*

MASCOT-2 and Didymoon's surface.

- Dissipation of velocity normal to the surface ($\eta_n = 0.5, \eta_t = 1$). In this case the effects of the restitution coefficient are subdivided into tangential and normal contributions. The absolute value of the velocity after touch down is dissipated of $\eta_n = 0.5$ in the direction normal to the surface, while its component tangent to the surface is not dissipated at all ($\eta_t = 1$). To assess the probability of escaping due to bouncing after the first touch down, a Monte Carlo simulation is run. All dispersed landing points (first touch down) are considered. The trajectory after the first bouncing is then computed for each landing point solution by assuming a uniformly distributed direction of velocity vector after touch down. This strategy is driven by the uncertainties in the relative geometry between the lander and the soil at the landing points and it allows to take into considerations all possible inclinations of Didymoon's surface. Figure 5.33 shows an example of bouncing dynamics until rest. The relevant aspect to be highlighted is that with no dissipation of tangential component of velocity, the lander keeps bouncing towards the equatorial latitude band, with very large longitude footprint.

- Hard soil and low energy dissipation by MASCOT-2 structure ($\eta = 0.9$). In this case touch down dynamics is modeled using an extremely conservative assumption for the restitution coefficient. Figure 5.34(a) shows dispersed trajectories after first touch down for a single bouncing and for a single landing trajectory. The height after bouncing is

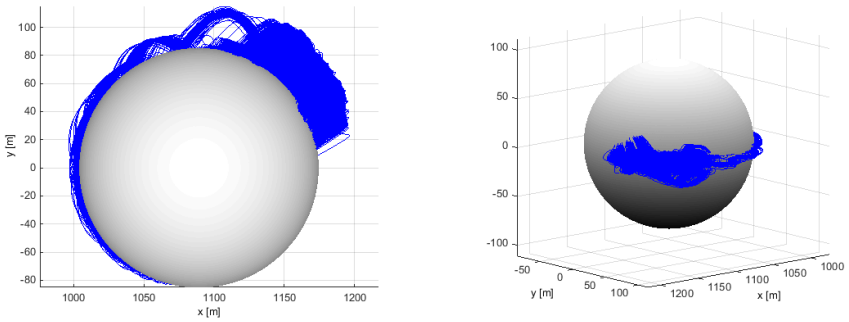

(a) (b)

Figure 5.33: *Bouncing until rest associated to velocity dissipation normal to the surface: (a) x, y view (b) 3D view (early spherical Didymoon model)*

very high, since very little energy is dissipated after touch down. The dynamics clearly show a westwards trend, since the majority of second landing points are located further west with respect to the first landing point.

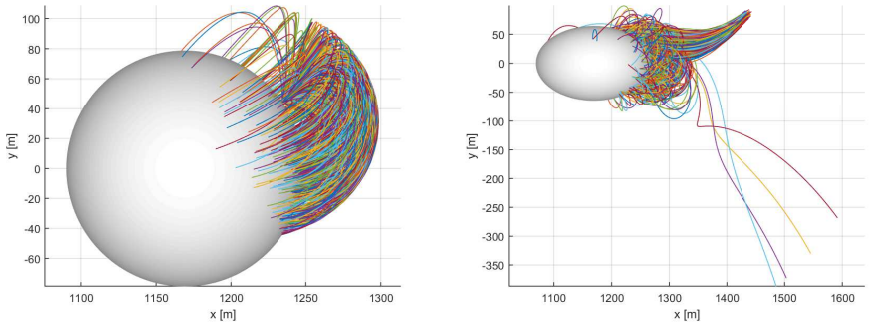

(a) (b)

Figure 5.34: *Hard soil and low structural dissipation case: (a) trajectories after first touch down (early spherical Didymoon model) and (b) bouncing until rest*

Figure 5.34(b) shows an example of full simulation from release up to rest on Didymoon or escape. This specific case refer to very good condition in terms of release, which is very robust since all trajectories reach Didymoon. However, due to the high η and the low dissipation of energy, some of them escape after the first touch down.

5.2.5 Mission analysis results

This section presents results related to MASCOT-2 ballistic landing. The way the nominal landing trajectory is computed is presented first. Suitable release geometry is then discussed from the orbiter (AIM spacecraft) point of view. Conditions for optimal release are identified to minimize the effect of the error induced by the release mechanism on MASCOT-2. Finally, results in terms of successful landing probability and landing point dispersion on Didymoon's surface are shown.

Nominal landing

As discussed in Section 5.2.2, the nominal release strategy is based on the exploitation of manifold dynamics associated to L2. MASCOT-2 will be released near the stable manifold and will transit near L2 to the unstable manifold branch to reach Didymoon's surface. The strategy to compute such trajectory is described and discussed here.

The nominal trajectory is computed starting from the inner branch (between Didymoon and L2) of the unstable manifold solution associated to the L2 point. The manifold is computed with the technique described in Section 3.3, starting from the L2 point and propagating the dynamics forward until the surface of Didymoon is intersected. Unstable L2 manifold dynamics would naturally push the lander towards the surface, even after bouncing. For this reason, the intersection of the manifold with the surface is a favorable location to be targeted for MASCOT-2 landing. As mentioned, a direct release on the stable manifold with transition to the unstable manifold at L2 is not robust from the mission design point of view, since the lander, once at L2, would have a 50% chance to follow either the ingoing or the outgoing manifold branch. For this reason, a higher energy solution is adopted. Due to its favorable location, the landing position identified by the manifold's intersection with Didymoon's surface is kept fixed. The higher energy solution is found by increasing the velocity at touch down and by integrating the dynamics backwards, until the desired release distance from Didymoon is reached. Higher energy trajectories generated through this strategy are shown in Figure 5.35 to cross the upper part of the L2 neck of the Hill's curves. This region is close to the stable ingoing branch of the L2 manifold. The trajectories found are natural connections between the stable ingoing L2 manifold and the unstable ingoing L2 manifold and fits with the goal of the design strategy.

The drawback of choosing a higher energy solution is that, due to a higher touch down velocity, the risk the lander escapes after bouncing is

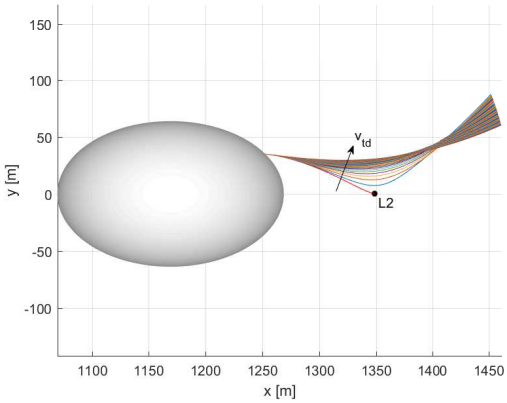

Figure 5.35: *Landing trajectories based on unstable L2 manifold solution for increasing touch down velocities.*

higher. However, analyses and investigations performed (Section 5.2.4) have shown that favorable conditions near the unstable manifold landing point guarantee very low risk of escape. After extensive investigation on sensitivity due to the different parameters involved in the design, as shown in Section 5.2.4, a touch down velocity of about 6.2 cm/s was selected to generate the nominal ballistic landing trajectory.

Optimal AIM release conditions

As described in Section 5.2.3, MASCOT-2 release uncertainties depend both on release mechanism and on AIM spacecraft navigation. Uncertainty in release position is only dependent on AIM navigation accuracy, whereas uncertainty in release velocity is due to the combined effect between AIM navigation accuracy and release mechanism accuracy. Figure 5.36 shows examples of release velocities, referring to two different release strategies (plain and dashed arrows). $\boldsymbol{V}_{\mathrm{M}}$ indicates the velocity of MASCOT-2 at release in the synodic three-body reference frame. This value is common for both strategies, since it is chosen a priori in order to release the lander near manifold dynamics and it is provided by the initial condition on the nominal landing trajectory. $\boldsymbol{V}_{\mathrm{M}}$ is then a constraint from the design point of view, to ensure high landing successful probability. $\boldsymbol{V}_{\mathrm{sc}}$ is the velocity of AIM spacecraft, while $\boldsymbol{V}_{\mathrm{M\text{-}sc}}$ is the relative velocity between MASCOT-2 and AIM spacecraft. The following vectorial relation holds:

$$\boldsymbol{V}_{\mathrm{M}} = \boldsymbol{V}_{\mathrm{sc}} + \boldsymbol{V}_{\mathrm{M\text{-}sc}} \tag{5.32}$$

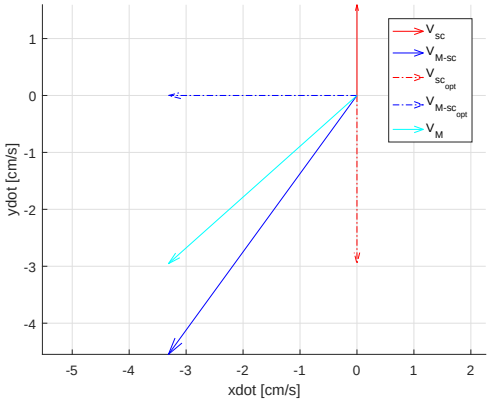

Figure 5.36: *Release velocities: optimal release (dashed) compared to general one (plain).*

As mentioned in Section 5.2.3, the error in the norm of the release velocity $\boldsymbol{V}_{\text{M-sc}}$ due to spring mechanism equals the 10% (1σ) of its nominal value. For this reason, it is convenient to minimize $\|\boldsymbol{V}_{\text{M-sc}}\|$ when designing AIM release conditions. The term *optimal* refers here to release conditions that minimize the errors at the release event. The minimization includes the fulfillment of some constraints: $\boldsymbol{V}_{\text{M}}$ is constrained since it represents the initial conditions for the ballistic descent close to the stable L2 manifold. Also, for safety reasons, AIM is constrained on a hyperbolic-kind orbit, with pericentre at release point. In that case, $\boldsymbol{V}_{\text{sc}}$ is constrained to be orthogonal to the x axis and aligned to the y axis. Given such constraints together with Eq. (5.32), the optimal release condition occur when $\boldsymbol{V}_{\text{M-sc}}$ is aligned with the x axis and equal to the x component of $\boldsymbol{V}_{\text{M}}$, while $\boldsymbol{V}_{\text{sc}}$ equals the y component of $\boldsymbol{V}_{\text{M}}$. It can be easily proven that this condition minimizes $\|\boldsymbol{V}_{\text{M-sc}}\|$ and consequently minimizes the 10% error on it.

Success rate

The results presented here refer to the nominal trajectory case, under the assumptions related to the mission scenario presented in Section 5.2.3. The robustness of the ballistic landing solution is validated against release and touch down uncertainties, to guarantee the success of the landing strategy. A Monte Carlo analysis is performed to assess successful landing probability. The dispersed release conditions are propagated forward using the hi-fidelity polyhedron/ellipsoid three-body model described in Section 5.2.1. The dynamics of the lander are propagated until MASCOT-2 comes to a

rest on Didymoon's surface, or escapes from Didymos system. Bouncing dynamics is modeled as described in Section 5.2.3 and the resting condition is associated to the residual vertical velocity of the lander after bouncing. More into detail, MASCOT-2 is considered at rest when its vertical velocity is lower than 0.5 cm/s.

Monte Carlo analysis is run with 200 000 points for each different release altitude under study. More in detail, release altitudes of 100, 150, 200, 250 and 300 m from Didymoon's surface are considered.

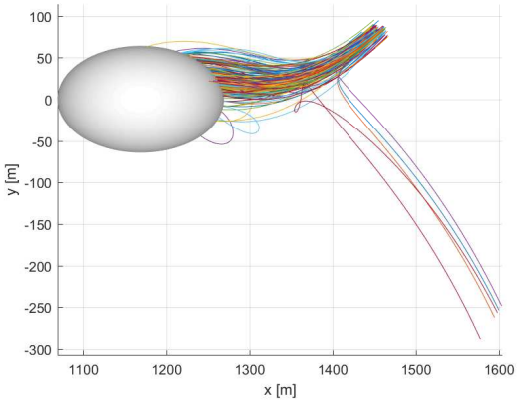

Figure 5.37: *Dispersed landing trajectories from release altitude of 200 m.*

Figure 5.37 shows an example of dispersed release conditions and landing trajectories associated to the case of 200 m altitude release. The figure is included only for visualization purpose, since only 200 trajectories (out of 200 000) are displayed.

Table 5.8: *Escape probability from Didymoon.*

Release altitude [m]	Escaped trajectories [%] after release	after touch down	TOTAL
100	1.14	0.00	1.14
150	1.26	0.00	1.26
200	3.18	0.01	3.19
250	5.79	0.04	5.83
300	6.03	0.32	6.35

Table 5.8 shows the percentage of escaped trajectory after release dispersion, for all considered release altitudes. Escape rate is divided into escaped after release and escaped after touch down. In the first case, the uncertainty drives MASCOT-2 on a different path, which, due to the extremely chaotic

nature of the dynamics, does not allow the lander to reach the surface of Didymoon. The second case accounts for MASCOT-2 state after first touch down and in particular, for the cases when the lander is put on an escape trajectory after bouncing on the asteroid. As expected, the success rate of the ballistic landing increases as the release altitude decreases. Successful probability ranges from a worst case value of 93.65% for release from 300 m altitude, to a maximum of 98.86% in the case of release from 100 m altitude. Results in terms of success rate are in agreement with a similar analysis performed by DLR [129] on MASCOT-2 landing probability.

Landing dispersion

After assessing the successful rate of the release strategy, it is important to study the outcome of the successful landing in terms of final landing point dispersion. Table 5.9 reports the latitude and longitude bands related to MASCOT-2's point at rest on Didymoon, for the different release altitude cases. The time of flight (ToF) during ballistic descent and bouncing, from release up to rest on Didymoon is also reported. Uncertainty range is included and specified according to a Gaussian 3σ distribution.

Table 5.9: *Landing dispersion on Didymoon's surface at rest: latitude/longitude bands and time of flight between release and rest.*

Release altitude [m]	Dispersion at rest [$\mu \pm 3\sigma$] Latitude [deg]	Longitude [deg]	ToF [h]
100	0.2 ± 32.5	23.3 ± 87.9	1.81 ± 0.95
150	0.0 ± 31.5	20.1 ± 66.7	2.19 ± 1.06
200	0.1 ± 32.9	19.7 ± 60.5	2.50 ± 1.21
250	-0.1 ± 36.6	20.5 ± 64.8	2.77 ± 1.41
300	0.1 ± 44.3	19.5 ± 86.0	2.95 ± 1.35

With reference to the case of 200 m release altitude in Table 5.9, Figure 5.38 shows the landing dispersion on the surface of Didymoon when the lander is at rest. More in detail, the latitude-longitude map is shown in Figure 5.38(a), while the three-dimensional view of all landing points on Didymoon's surface is shown in Figure 5.38(b). Latitude and longitude distributions of resting point are displayed, respectively, in Figure 5.38(c) and 5.38(d).

It must be highlighted that the dynamical behaviour of the lander after touch down is heavily dependent on the choice of the restitution coefficient η, defined in Section 5.2.3. According to latest assumptions on release parameters and restitution coefficient, the results show that the landing region can be estimated within an uncertainty in the latitude-longitude region on

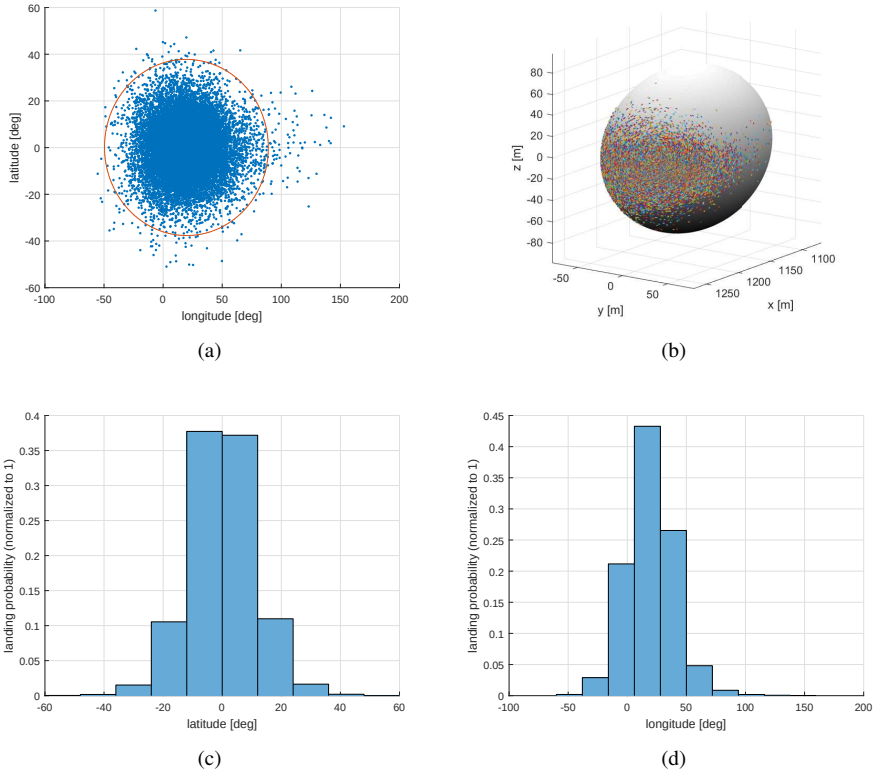

Figure 5.38: *Landing dispersion at rest for the case of 200 m altitude release. (a) latitude-longitude map (b) three-dimensional view of Didymoon (c) latitude and (d) longitude distribution of points.*

the order of tens of degrees. This allows to state that the lander will likely come to a rest in the hemisphere of Didymoon opposite to Didymain.

5.2.6 Critical aspects of MASCOT-2 landing problem

As mentioned in the previous sections and proved by the results and analyses presented, the problem of MASCOT-2 landing is extremely challenging. A summary of the problem's criticalities is provided here. Two main critical aspects can be identified: the first is related to the capability of MASCOT-2 to reach Didymoon after release and a pure ballistic landing. The second is related to the capability of MASCOT-2 of staying on the surface of Didymoon after touch down, without escaping from its weak gravity attraction. Relevant design parameters and physical properties of Didymos affecting such capabilities are summarized here.

Capability to reach Didymoon

Reaching Didymoon is the most critical aspect regarding MASCOT-2 descent because the gravity environment around the Didymos binary system is extremely chaotic, and a very small deviation of release conditions can drive the lander far from Didymoon. The most relevant parameters are:

- Mass distribution among Didymos system (mass ratio between Didymoon and Didymain): it is shown that the higher M_2/M_1, the better it is in terms of success rate. This parameter can be very critical for values $M_2/M_1 < 0.0093$ (nominal up-to-date value), while not critical for $M_2/M_1 \geq 0.0093$
- Nominal release: it is extremely important to select the release point conditions in Didymoon three-body system. As discussed in Section 5.2.2, nominal release is chosen exploiting manifold dynamics associated to the L2 point. The success rate decreases dramatically and the landing can never be achieved when manifold dynamics is not exploited.
- Release uncertainties: as discussed, position uncertainty is not an issue and can be tolerated up to tens of meters. On the other hand, velocity dispersion can be very critical for values above few cm/s. More into detail, sensitivity analyses performed (Section 5.2.4) showed that uncertainties due to the norm of velocity release mechanism can be very critical concerning the success rate of the landing manoeuvre. A strategy to mitigate such effect is discussed in Section 5.2.5.

Capability to stay on Didymoon

Staying of Didymoon after touch down is very critical for MASCOT-2 landing design, due to the very low gravity attraction of Didymoon and, consequently, to its very low escape velocity. Relevant parameters to this problem are:

- Mass ratio between Didymoon and Didymain: the escape velocity increases as the mass of Didymoon increases. Analogously to the previous case, the higher M_2/M_1, the better it is.
- Restitution coefficient: this parameter is the key parameter to model the interaction between the soil and MASCOT-2. It is shown to be very critical for values $\eta > 0.7$, while not critical for $\eta \leq 0.7$.
- Uncertainty in soil inclination: this has shown not to be critical in terms of success rate.

- Nominal release: due to its peculiar dynamics, the escape velocity from the surface of Didymoon is not constant but it depends on latitude and longitude. For this reason it is very important to land on a region with low escape velocity. As discussed in Section 5.2.1, such region is that associated to unstable manifold dynamics. As for the case selected, unstable manifold dynamics associated to the L2 point provide a low energy solution (low touch down velocity) that pushes MASCOT-2 away from L2 point, and then towards Didymoon's surface, even after touch down.

5.3 Triangular formation flying

A further investigated scenario concerns a very challenging problem of modern astrodynamics. The design of formations of spacecraft in a non-Keplerian environment represents one of the most promising research fields for future space mission design. Two or more cooperating spacecraft can greatly answer some very complex mission goals, not achievable by a single spacecraft. Many scientific fields find possible applications and benefit from this peculiar coupling: observation and basic science, from telecommunications to space exploration. When designing classical formations of spacecraft, the cost to be paid is the resolution of a highly challenging trajectory and station keeping problem solving, to satisfy tight requirements on relative dynamics between each member of the formation. The exploitation of low acceleration regions such as the proximity of equilibrium points associated to a three-body system opens to a wide range of design opportunities, and three-body dynamics can be conveniently used to reduce such trajectory and station keeping needs. The evolution of a free formation orbiting in the proximity of periodic orbits about collinear libration points is investigated here.

The problem of formation flying was extensively studied in the past decades and many missions employing such architecture were designed. However, very few concepts of formations of spacecraft were studied to exploit three-body dynamics. Several studies aimed to the design of control strategies for formations of spacecraft under a three-body dynamics exist, but very few of them studies the free relative motion between the spacecraft as they are subjected to this highly unstable and non-linear environment. Among them, Barden and Howell [4] exploited the natural motion on the centre manifold near periodic orbits to reproduce tori of quasi-periodic trajectories that can be useful for the design of naturally bounded formations of spacecraft. Few years later, Gómez, Marcote, Masdemont and Mondelo [60] derived regions around periodic orbits with zero relative velocity and radial acceleration, which ideally keep unchanged the relative distances between the spacecraft in the formation. Finally, Héritier and Howell [70] extended the analysis done by Gómez et al. and derived low drift regions (low relative velocity and acceleration) around periodic orbits, as quadric surfaces. Ferrari and Lavagna [37] generalized the work by Héritier and Howell to the whole three-body domain, identifying regions of zero relative acceleration and velocity (ZRAV loci) for large formations of spacecraft. Also, the relative dynamics of a three-spacecraft triangular formation were investigated and suitable initial conditions were found in the Earth-

Moon system [37]. Controlled formations were studied under the ER3BP formulation [3] but still there is very little known about the free relative dynamics within this particular dynamical environment.

A three spacecraft triangularly-shaped formation is assumed as a representative geometry to be investigated. One example of such a formation arrangement is the Laser Interferometer Space Antenna (LISA) [11], which consists of three identical spacecraft, placed around a reference point that orbits the Sun, following a circular path. Other examples of similar configurations are given by Cluster II [65] and Magnetospheric Multiscale Mission (MMS) [31]: both of them employ a tetrahedral (triangular pyramid) formation to study Earth's magnetosphere. The study identifies initial configurations that provide good performance in terms of formation keeping, and investigates key parameters that control the relative dynamics between the spacecraft within the three-body system. Simulated scenarios include the dynamics within Earth-Moon and Sun-Earth three-body systems. This choice is made to reproduce scenarios with similar geometry with respect to past or existing formation flying missions. However, the analysis can be easily generalized to any choice of mass ratio μ between primaries of any three-body system. Formation keeping performance is quantified by monitoring shape and size changes of the triangular formation. Some constraints are imposed to the relative dynamics within the formation and the best solution, in terms of free and uncontrolled dynamics is identified within a specific set of initial conditions. The analysis is performed under several degrees of freedom to define the geometry, the orientation and the location of the triangle in the synodic rotating frame: one parameter defines the size of the triangle and five parameters describe unequivocally its location and orientation in the rotating frame. The solution is provided in terms of initial configuration of the formation which fits at best the constraint imposed on the formation dynamics. Two different strategies are implemented and compared to find the initial configurations that maximize performance indexes: a *brute force* Monte Carlo approach (Section 5.3.2) is compared with a global optimization approach (Section 5.3.3).

5.3.1 Statement of the problem

This section presents the problem addressed, showing how numerical simulations and the optimization problem are set and what is the domain of validity of the study. As mentioned, the study focuses on the free dynamics of a formation of satellites, with the goal to find suitable initial configurations leading to good performance in terms of formation keeping. In the

present section, the reader will find explanation to what is referenced with the term *initial configuration* and to what is meant by formation keeping performance. In addition, criteria driving the selection of suitable initial configurations will be defined and motivated.

The problem is formulated as follows. An uncontrolled three-spacecraft formation undergoes non-Keplerian dynamics, with applications studied under the CR3BP and ER3BP formulations. The dynamical state of the formation is initiated by selecting relative initial position and velocity between the spacecraft. Also, the initial location of the formation in the three-dimensional space shall be selected. In this study, the motion close to libration point orbits in CR3BP and ER3BP is investigated and formations are initially located around such orbits (*reference orbits* in the followings). The dynamics of the spacecraft are integrated forward and their relative positions are monitored in time.

Formation flying geometry

Three identical spacecraft are located at the vertexes of an equilateral triangle. The initial configuration of the formation is specified by a set of parameters representing the initial size and orientation of the triangle.

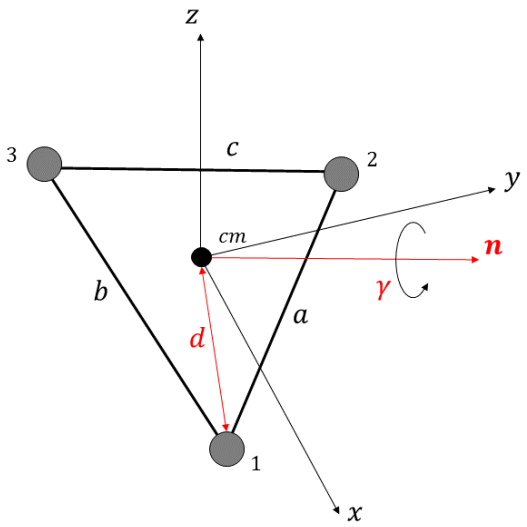

Figure 5.39: *Triangular formation in the local frame*

Figure 5.39 shows a possible initial configuration of the formation with respect to the *local* frame, which is centred in the barycentre of the forma-

tion and defined such that x, y and z are directed as the axes of the three-body synodic frame. The initial size of the triangle is identified by the parameter d, which represents the distance between each spacecraft and the barycentre of the equilateral triangle. The initial orientation of the formation is found using the vector normal to the triangle plane $\boldsymbol{n}$ and the angle γ which represent positive rotation about $\boldsymbol{n}$ axis as shown in Figure 5.39. Five parameters are used to unequivocally define the geometry and the orientation of the formation in the rotating frame. Lastly, the barycentre of the formation is located on the reference orbit, which has to be chosen. Summarizing, to define the initial configuration of the formation the following parameters shall be fixed:

- d: distance between each spacecraft and the centre of mass of the formation
- $\boldsymbol{n}$: normal to the triangle plane (three-component unit vector)
- γ: rotation about $\boldsymbol{n}$ axis
- X_{ref}: reference orbit (initial conditions)

Once the initial configuration is selected, meaning the initial state of the three spacecraft, the equations of motion are integrated forward in time for each spacecraft as they evolve near the reference trajectory. The evolution of the formation is monitored. As mentioned, the aim of the study is to investigate the effect that different initial configurations have on the relative dynamics between the three spacecraft and to identify the best cases.

Performance factors

The ideal formation keeping condition can be synthesized with no change in shape and size of the initial triangular configuration as the spacecraft fly near the reference orbit. The ideal condition is, of course, impossible to obtain if the formation is free and uncontrolled, in the extremely chaotic and nonlinear three-body environment. Nonetheless, it is possible to seek preferred initial configurations which lead to small changes in shape and size of the formation after given time intervals, which means cheaper formation keeping needs. In order to evaluate how the formation is maintained, it is important to monitor how the shape and the size of the triangular formation change during the evolution of the three spacecraft along the orbit. It is proposed here a strategy to measure formation keeping performance, by quantifying both shape and size changes, in order to identify initial conditions sets leading to good formation keeping maintenance. To this purpose,

two performance factors are used: the *Shape Factor (SF)*, which takes into account for the change in the shape of the triangle, and the *Size* or *Dimension Factor (DF)*, which takes into account for the change in size of the triangular formation. These performance indexes were introduced by the author in a previous work [37]. Their analytical expressions and mathematical definitions are recalled in the following paragraphs.

- *Shape Factor (SF)*: to evaluate and quantify the shape changes of the triangular formation during its evolution on the reference orbit, the Shape Factor is been defined and conveniently expressed in a mathematical way. The analytical expression of the SF is selected to guarantee some features that should be performed by such a function. First of all, a nondimensional factor should be considered, in order to allow comparisons between different systems and investigations, this would also help to keep the expression as general as possible. Most important, the variables of the function, shall meaningfully allow the monitoring of the shape changes. A good choice is to select as variables the ratios of the sides of the triangle. Referring to Figure 5.39:

$$\varepsilon_1 = \frac{a}{b} \qquad \varepsilon_2 = \frac{a}{c} \qquad \varepsilon_3 = \frac{b}{c} \tag{5.33}$$

  These three parameters allow the monitoring of the shape changes: it can be easily noticed that the shape is unchanged if and only if

$$\varepsilon_1 = \varepsilon_2 = \varepsilon_3 = 1 \tag{5.34}$$

  and therefore they can provide a good way of determining where the shape is unchanged. Note that only two of these parameters are independent: ε_1 and ε_2 are chosen here as variables to write the expression of the SF function

$$SF = f(\varepsilon_1, \varepsilon_2) \tag{5.35}$$

  Next, the mathematical expression of the Shape Factor function is built. To proceed, some constraints are introduced, in order to shape the mathematical function in a convenient way. For the purpose of the study, it is convenient to consider a function which is equal to one if and only if the shape of the triangle is unchanged. It is also useful to set this function such that it can range from 0 to 1 in a monotonic way, so that the lower its value, the worse the condition in terms of shape maintenance. Considering then the selected variables, both ε_1 and ε_2 are always greater than zero, being the ratios of two positive numbers.

For this reason, it is better to consider a function whose variables' domain is always greater than zero. Moreover, since the choice of the ratios (5.33) is arbitrary, it is convenient to have a function which is symmetric with respect to ε and $\frac{1}{\varepsilon}$, having an expression which is not dependent on the definition of the ratios. For example, considering two sides of the triangle:

$$a = 1 \quad \text{[length unit]}$$
$$b = 5 \quad \text{[length unit]}$$

the SF function shall return the same result if the ratio is defined as both

$$\varepsilon = \frac{a}{b} = \frac{1}{5} \qquad \text{or} \qquad \varepsilon = \frac{b}{a} = 5$$

Based on these considerations, the following expression is selected as SF function

$$SF = e^{-\sqrt{(\ln \varepsilon_1)^2 + (\ln \varepsilon_2)^2}} \tag{5.36}$$

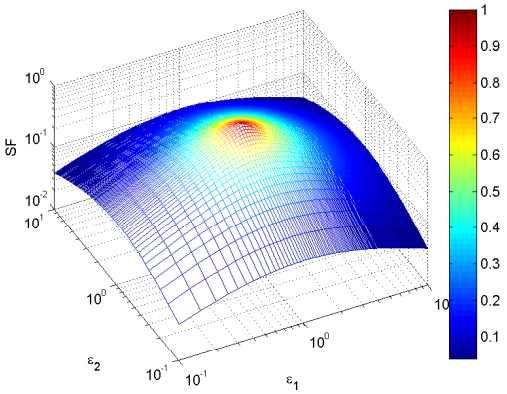

Figure 5.40: *Shape Factor (logarithmic scale)*

Figure 5.40 shows the 3D graphics of Equation (5.36) and represents the SF function. Note that the numerical value of the SF depends on the choice of the ratio to use: for example, the choice (ε_1, ε_2) will provide different numerical results form the choice (ε_1, ε_3) or (ε_2, ε_3). It is possible to make the Shape Factor independent also from that choice by computing SF for all three possible choices and then taking the average value. However, without any loss of generality, the analyses performed in this work relate to Equation (5.36), and not to the averaged SF.

- *Size or Dimension Factor (DF)*: the second key aspect to be monitored during the evolution of the formation on its orbit is the size of the triangular formation. It can happen that the distance between the spacecraft grows very fast without changes (or with little changes) in the shape of the formation: this situation is not detected by a change in the SF. The DF is introduced to identify such behaviours. Similarly to what done for the SF, a nondimensional parameter is considered. Also in this case ratios between sides of the triangle are considered as variables, but the ratio is computed here for each side, with respect to its initial length. Referring to Figure 5.39:

$$\zeta_1 = \frac{a}{a_0} \qquad \zeta_2 = \frac{b}{b_0} \qquad \zeta_3 = \frac{c}{c_0} \tag{5.37}$$

  where the subscript $_0$ denotes the initial length of the sides (initial configuration, $a_0 = b_0 = c_0$). From the mathematical point of view, the only condition to be verified is that the DF equals one only at the initial time and if the average size of the formation is maintained. It shall be also considered that, once again, the variables represent ratios of positive numbers. A very simple form is adopted, by averaging the three ratios ζ_1, ζ_2 and ζ_3

$$DF = \frac{\zeta_1 + \zeta_2 + \zeta_3}{3} \tag{5.38}$$

  Equation (5.38) is able to tell whether the three spacecraft are getting farther or closer to each other and if the size of the formation is growing or reducing. Differently from the SF, the DF needs information on the initial state of the formation and provides a measure of the size of the triangle at a certain time after initial time. Roughly speaking, DF=5 at $t = t_1$ (with $t_1 > t_0$) means that the triangle is, on average, five times bigger than its initial size at $t = t_0$.

Examples of how performance factors behave in time during the evolution of the formation near its reference orbit are shown in Figure 5.41. Performance factors are evaluated for different initial orientations of the formation. In this case, with reference to Figure 5.39, the results refer to a formation lying in the (y, z) plane, with $\boldsymbol{n}$ directed as the positive x axis. Accordingly, γ refers to a simple rotation about the x axis. Rotations are computed here starting from $\gamma = 0$, found when one spacecraft is along the positive z axis and the remaining two are below the (x, y) plane. Nondimensional time is shown on the abscissa, referring to the percentage of orbital period of the reference orbit (the time span goes from 0 to one period T_{orb}).

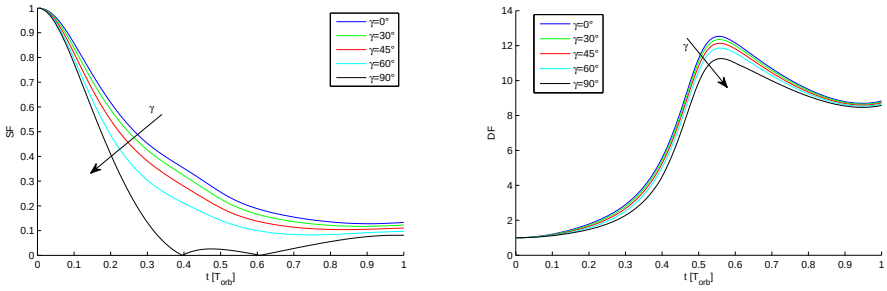

(a) (b)

Figure 5.41: *Time evolution of (a) Shape Factor and (b) Dimension Factor for different initial orientations (with $\boldsymbol{n}$ directed as the positive x axis)*

To compare different initial conditions sets, the value of the performance factors is evaluated after one period of the reference orbit. The behaviour of performance factors is studied to find the closest conditions to the ideal situation (no change in shape and size of the formation), which is given by

$$SF = 1 \qquad DF = 1 \tag{5.39}$$

5.3.2 Monte Carlo approach

A simulation campaign is set up to explore a wide set of initial configurations. As mentioned in Section 5.3.1, the initial orientation of the triangle, the initial size of the formation and the reference orbit are the free parameters investigated. The order of magnitude of the size d of the formation is chosen by analogy with existing missions employing similar formation configurations: for example, the size of Cluster II [65] and MMS [31] formations varies from few kilometers up to few thousands of kilometers. For the general analysis, the simulation campaign is set up by considering the $d = 1, 10, 100$ km. For what concerns the orbital path of the spacecraft, the study is performed by considering only planar reference orbits. In particular, the following Lyapunov orbits about L1, L2 and L3 of Earth-Moon system are considered:

L1	$Ay = 8\,246,$	$44\,582,$	$88\,339$	km
L2	$Ay = 7\,334,$	$75\,019,$	$145\,740$	km
L3	$Ay = 6\,874,$	$100\,719,$	$338\,888$	km

where Ay represents the maximum semi-amplitude of the orbit in the y direction. In the followings, the orbits will be referenced as L1(1), L1(2),

L1(3), L2(1), L2(2),... where the numbers in the brackets indicates which orbit, from the smallest (1) to the largest (3), is being referenced. For example, L3(2) refers to the intermediate orbit about L3 with $Ay = 100\,719$ km. Figure 5.42 shows the orbits used as reference, in the Earth-Moon rotating frame. Overall, three values of size d, nine reference orbits and several initial orientations of the formation with respect ot the rotating frame are considered.

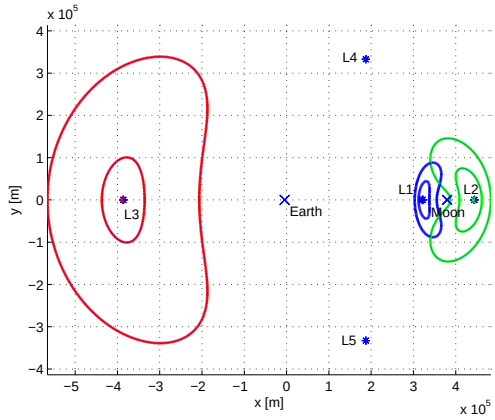

Figure 5.42: *Reference Lyapunov orbits in the Earth-Moon system*

The functions in Figures 5.41(a) and 5.41(b) are evaluated at $t = T_{orb}$ for any different initial orientation and size d of the formation and for any of the selected reference orbits.

Results

Interesting results can be obtained by comparing all simulated scenarios. Figure 5.43 shows the outcome of the simulation campaign. The value of performance factors after one period is computed for any possible case: each set of parameters is represented by a point in the SF-DF plane. Note that DF increases on the abscissa, while SF decreases on the ordinate: the ideal formation keeping condition (5.39) is then located at the left-bottom corner of the graph, where both performance factors equal one. The best conditions must be sought then in the left/lower region of the plot.

Blue triangles represent solutions associated to formations orbiting L1, green dots are associated to formations orbiting L2 and red stars to formations orbiting L3. The first thing to be noticed is that there are big differences in terms of final size of the formation (DF) depending on the libration point the reference orbit is about. Limited to the simulation domain under

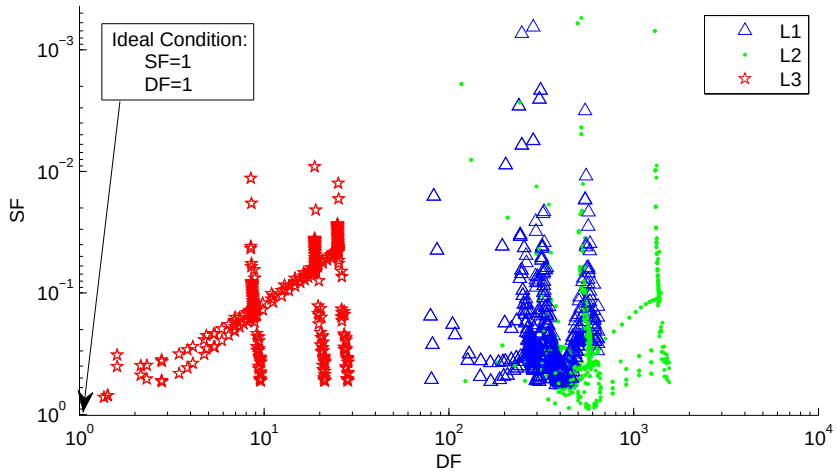

Figure 5.43: *Totality of solutions (limited to the case of study)*

study, L3 orbits appears by far the best place to host a formation of satellites: all solutions related to L3 orbits exhibit a lower DF then any other solution about L1 or L2. Looking at numbers, the final value of DF is always lower than 25 if L3 orbits are considered, while it is always greater than 80 for L1 orbits and it is always greater than 120 for L2 orbits. For what concern formation keeping, the orbits considered here about L1 and L2 appear not to be good candidates to host a triangular formation of satellites, since after one orbital period the size of the triangle increases dramatically and the spacecraft lose their initial relative configuration.

Discarding all solutions related to L1 and L2 orbits, the analysis is carried forward by focusing on L3 orbits only. Figure 5.44 show an enlargement of Figure 5.43, considering only solutions associated to L3 orbits. The effects of the initial orientation of the formation are studied. Interesting patterns can be identified, when looking at simple rotations, i.e. when $\boldsymbol{n}$ is directed towards x, y or z axes. Blue triangles represent cases with normal directed as the x axis, green dots are associated to formation plane normal to the y axis and red stars to cases with normal towards the z axis. Each point refers to a different value of in-plane rotation angle γ (ranging from 0 to 2π), initial size of the formation d and initial orbit about L3. The figure shows that the best performance is achieved when considering the formation lying on the (x, z) plane, that is when $\boldsymbol{n}$ is directed towards y axis. Figure 5.45 shows the same solutions depicted in Figure 5.44 (only L3 orbits) sorted by reference orbit (smaller to larger orbit about L3). The

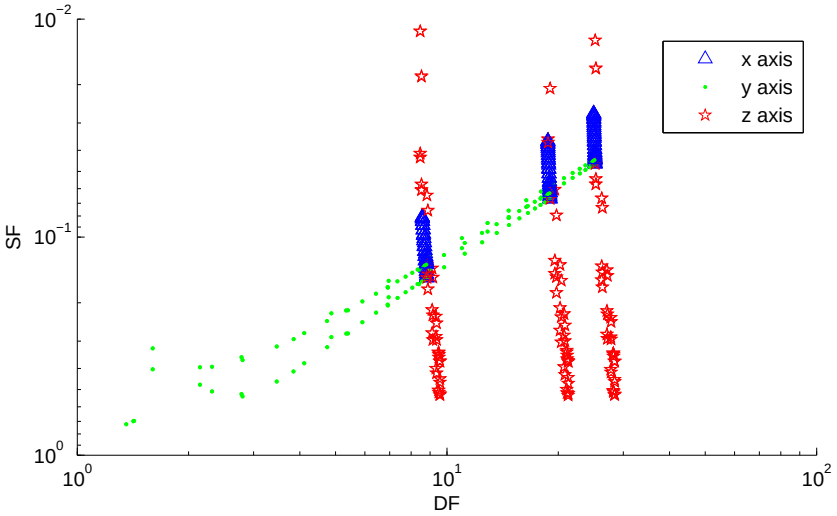

Figure 5.44: *Solutions associated to L3 orbits (**n** directed as positive x, y, z axes)*

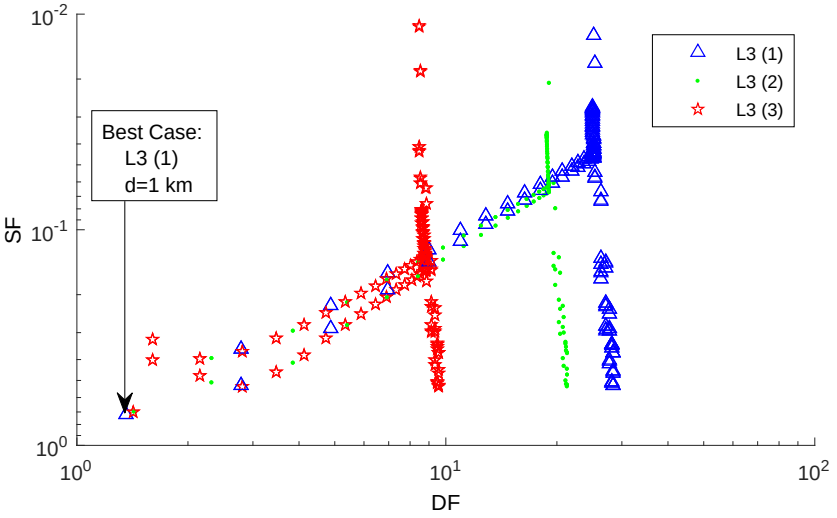

Figure 5.45: *Solutions associated to L3 orbits (according to the reference orbit)*

selection of the orbit produces different results in terms of DF values: the bigger the orbit, the smaller the maximum DF experienced by the formation. However, while being true for the maxima, this is not true for the DF minima since the overall best case is found for a formation flying about the smallest orbit about L3. Concerning the initial size of the formation, no

relevant effects are observed for the different d values investigated.

5.3.3 Global optimization approach

The goal of the optimization problem is to explore a large domain of initial conditions and to find the optimal set in terms of maximization of formation keeping performance, quantified thanks to some performance factors. To this aim, the optimizer is chosen to implement a genetic algorithm. The followings discuss the set up of the optimization problem, including the description of the initial population set, the boundaries of the search space domain and the fitness function.

Search space domain

The initial population set includes all parameters needed to initiate the numerical integration of the spacecraft dynamics. With reference to Section 5.3.1, several parameters are used to unequivocally define the initial geometry, location and orientation of the triangular formation. In addition, the velocity of each spacecraft ($\boldsymbol{v}_1, \boldsymbol{v}_2, \boldsymbol{v}_3$) at the beginning of the numerical integration is also included here as a free parameter.

To set up the optimization process, the search space is clearly defined, by identifying boundaries the parameters are allowed to range within. The order of magnitude of the size of the formation d is chosen by analogy with existing missions employing similar formation flying configurations: for example, the size of Cluster II [65] and MMS [31] formations varies from few kilometers up to few thousands of kilometers. In this work, a significantly wider range of variability is allowed for the initial size of the triangle that can range between 1 m and 10^5 km. No constraints are imposed on the relative orientation of the triangle, meaning that no limitations are imposed on $\boldsymbol{n}$ and γ, except for the numerical need of keeping $\boldsymbol{n}$ as an unit norm vector. For what concerns the orbital path of the spacecraft, the analysis is performed by considering families of Lyapunov and Halo orbits about L1, L2 and L3 in the Sun-Earth three-body system. Each component of the initial velocity vector of each spacecraft is allowed to range within $\pm 20\%$ range with respect to the velocity on the reference orbit $\boldsymbol{v}_{\text{ref}}$. Table 5.10 summarizes the initial population set, highlighting the effect of the parameter on the initial configuration of the formation and its limiting range.

Fitness function

After the initial population is settled, the dynamics of the three spacecraft are integrated forward in time as they evolve near the reference orbit. The

Table 5.10: *Initial population set*

Parameter	Range
d	1 m - 10^5 km
$\boldsymbol{n}$	any direction, $\|\boldsymbol{n}\| = 1$
θ	0 - 2π
$\boldsymbol{X}_{\text{ref}}$	L1,L2,L3 Lyapunov and Halo families
$\boldsymbol{v}_1$	$\boldsymbol{v}_{\text{ref}} \pm 20\%$
$\boldsymbol{v}_2$	$\boldsymbol{v}_{\text{ref}} \pm 20\%$
$\boldsymbol{v}_3$	$\boldsymbol{v}_{\text{ref}} \pm 20\%$

fitness function refers to the evaluation of formation keeping performance after one complete orbital period associated to the reference orbit and it is based on the performance factors defined in Section 5.3.1. From the numerical implementation point of view, the evaluation of the fitness function $f(\xi)$ includes the integration of the equations of motion for all three spacecraft and the evaluation of SF and DF after one period of the reference orbit. The figure to be minimized by the optimizer is written as

$$f(\xi) = (1 - SF(\xi)) + |1 - DF(\xi)| \tag{5.40}$$

where ξ indicates the initial population set and both SF and DF are computed after the numerical integration of the dynamics. Equation 5.40 is equal to zero if $SF = DF = 1$, meaning that its minimum corresponds to the optimal initial condition set in terms of formation keeping performance. More in detail, Eq. (5.40) can be written as

$$f(\xi) = (1 - (e^{-\sqrt{\left(\ln\frac{a}{b}\right)^2 + \left(\ln\frac{a}{c}\right)^2}})) + |1 - \frac{\frac{a}{a_0} + \frac{b}{b_0} + \frac{c}{c_0}}{3}| \tag{5.41}$$

where the effects of initial conditions (a_0, b_0, c_0) and of the outcome of the integration of the dynamics (a, b, c) are clearly visible.

Results

The results of the optimization process are presented here. The optimal initial configurations, limited to the domain of parameters defined in the previous section, are found. Table 5.11 summarizes the results of the optimization, grouped according to the family of reference orbit. The results show that the optimizer does not converge to a good solution for the case of L1 orbits, whereas suitable solutions are found concerning L2 and L3 orbits. In agreement with what obtained with the Monte Carlo approach (Section 5.3.2), the overall best case is found for orbits about L3.

Table 5.11: *Results of the optimization: best performance factor achieved*

Reference orbit		SF	DF
L1	Lyapunov	2e-3	59
	Halo	4e-3	24
L2	Lyapunov	1.00	1.07
	Halo	0.75	1.00
L3	Lyapunov	1.00	1.00
	Halo	1.00	1.00

Regarding L2 solutions, the optimizer is shown to converge to good results, in particular for the case of lyapunov orbits. Figure 5.46 shows that the geometry of the formation is preserved after one orbital period (indeed SF=1.00, DF=1.07) while its orientation changes with respect to its initial configuration.

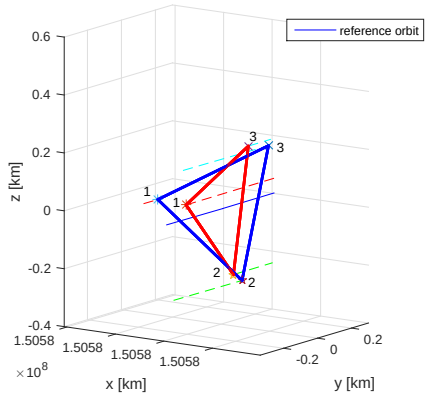

Figure 5.46: *Triangular formation at time t_0 (red) and after one orbital period (blue) (L2 Lyapunov)*

The best solutions are found when considering orbits about L3. In this case the geometry and orientation of the formation is fully preserved after one orbital period, as shown in Figure 5.47(a), where the formation at t_0 is almost overwritten by the formation after one orbital period. The three spacecraft are located on nearly periodic orbits nearby the reference halo orbit, since their motion is periodic with about the same period of the reference orbit.

Figure 5.47(b) shows the time behaviour of performance factors during the evolution of the formation on the reference orbit. The abscissa rep-

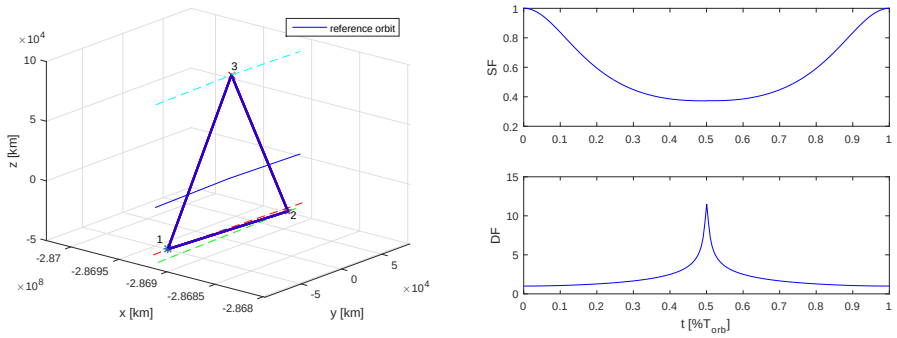

(a) (b)

Figure 5.47: *L3 Halo: (a) triangular formation at time t_0 (red) and after one orbital period (blue) (b) performance factors as function of time*

resents nondimensional time, normalized to one period of the reference orbit (the time spans from 0 to T_{orb}). As mentioned, the fitness function includes the evaluation of formation keeping performance at $t = T_{orb}$. SF and DF functions exhibit a periodic behaviour: in both cases the performance reaches a minimum after half orbit and it increases towards the optimal condition at the end of the orbital period. This means that the geometry of the formation is not kept constantly as it evolves along its orbit, but it reaches the optimum periodically, with a period equal to the period of the reference orbit.

In the case of lyapunov family about L3 the optimizer converges to a small orbit, and the formation has a characteristic size comparable to the amplitude of the orbit. Figure 5.48(a) shows the evolution of the triangular formation during one orbit and Figure 5.48(b) shows the behaviour in time of performance factors. In this case the formation changes shape during one period, with lowest formation keeping performance reached at 1/4 T_{ref} and 3/4 T_{ref}. At that points, the triangle collapses nearly onto a line and naturally gets back to its initial geometrical configuration after $T_{ref}/2$ from t_0. It is worth to notice that the three spacecraft experience periodic motion and their paths are actually out-of-plane orbits in the proximity of the reference lyapunov orbit (Figure 5.49).

The optimal initial configuration, in case of L3 halo and lyapunov orbits are shown in Figure 5.50(a) and in Figure 5.50(b). The overall optimal case is indeed achieved when the $\boldsymbol{n}$ unity vector is directed towards the x axis, that is when the triangular formation lies initially on the y, z plane.

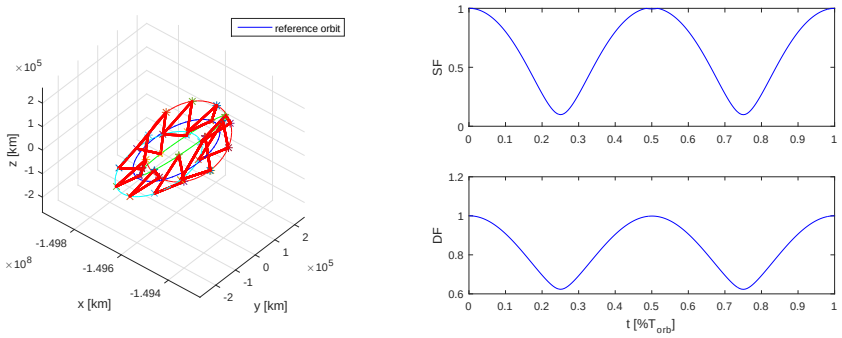

(a) (b)

Figure 5.48: *L3 Lyapunov: (a) time evolution of the triangular formation (b) performance factors as function of time*

5.3.4 Refinement of solution under the ER3BP

The previous section shows results related to CR3BP dynamics. Both Monte Carlo and global optimization approach agree on the fact that best solutions are achieved when L3 orbits are considered. Here, the analysis is replicated for the more realistic case of ER3BP dynamics. As detailed in Section 3.2.2, finding periodic motion in ER3BP is more challenging than in the CR3BP, due to the fact that the elliptic problem is not autonomous and explicitly depends on time. In order to investigate how the solution of the free triangular formation problem under study is affected by such change in the dynamics, one reference orbit about L3 in ER3BP is considered. The orbit is depicted in Figure 5.51 and represents a resonant 1:1 periodic orbit with one-year period about L3 in the Sun-Earth system. As described in Section 4.1.2, the orbit is generated starting from a resonant 1:1 orbit in the CR3BP about L3, through eccentricity continuation. The maximum amplitudes of the orbit in the y and z directions are

$$\Delta y = 3.88 \cdot 10^8 \quad \text{km}$$
$$\Delta z = 3.39 \cdot 10^4 \quad \text{km}$$

Note that the out-of-plane amplitude (Δz) is significantly lower than amplitudes along x and y directions: for this reason the orbit is classified here as a quasi-planar Halo orbit.

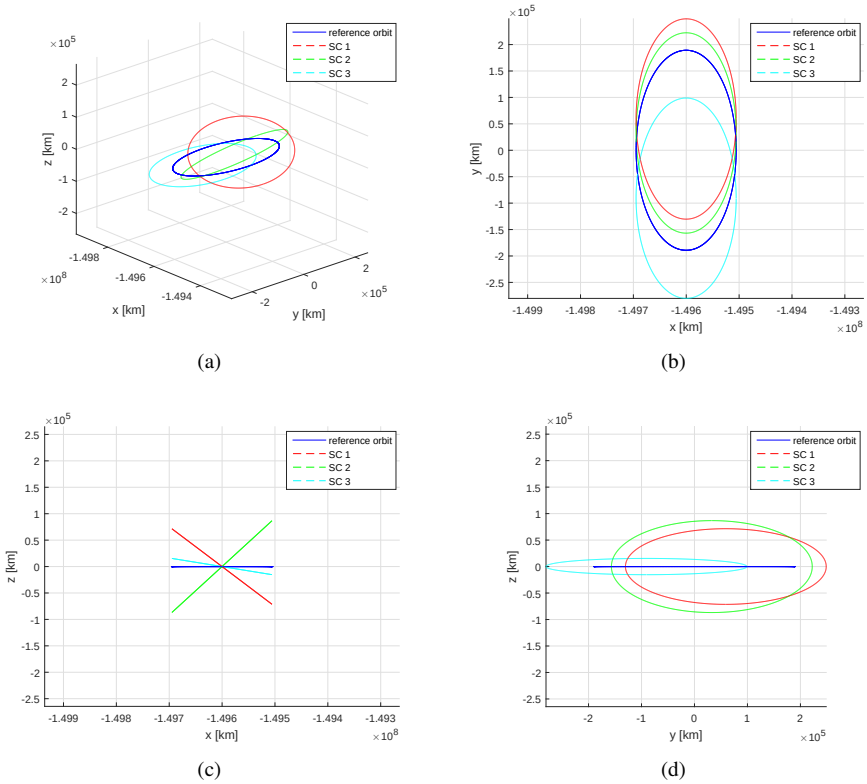

Figure 5.49: *Orbital paths of spacecraft around reference lyapunov orbit about L3 (a) 3D (b) x-y (c) x-z (d) y-z views*

Monte Carlo Approach

A Monte Carlo simulation campaign is set up and several initial configurations of formations in L3 are explored. Different initial orientations of the triangle $(\boldsymbol{n}, \gamma)$ and initial sizes of the formation (d) are considered. In this second step of the study, the simulation campaign is set up by considering the following values to initialize the size of the formation:

$$d = 10^N \text{ m} \quad \text{with} \quad N = 0, 1, 2, \ldots, 8$$

meaning that the size of the triangle varies from a minimum of 1 m up to a maximum of 10^5 km.

The orientation of the formation is generated randomly, with a uniform spherical distribution. Figure 5.52 shows the distribution associated to the orientation of the triangle. Each point in Figure 5.52 represents a different orientation of the formation: the normal to the triangle $\boldsymbol{n}$ is the vector con-

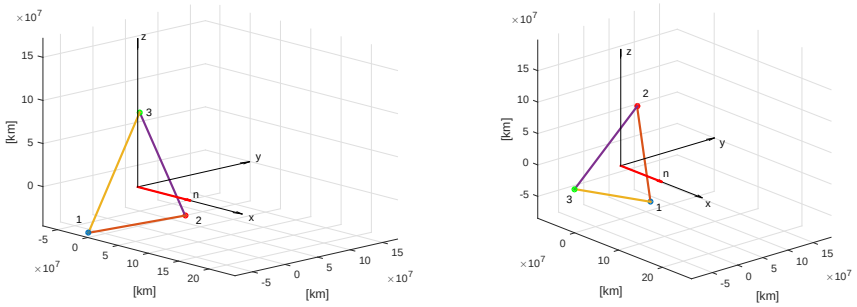

Figure 5.50: *Optimal configuration (a) halo (b) lyapunov about L3*

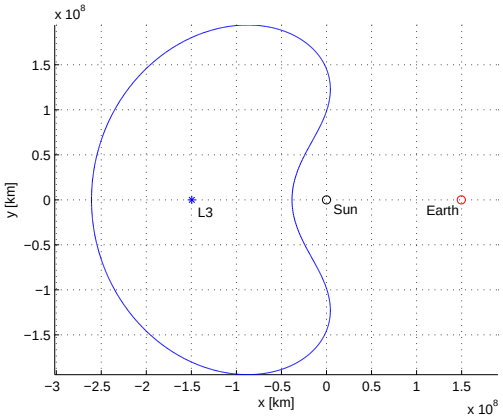

Figure 5.51: *Reference orbit*

necting the origin of the reference frame to the point on the sphere, which is centred in the barycentre of the formation. In this work 10^4 points are used to generate initial conditions for vector $\boldsymbol{n}$. For each $\boldsymbol{n}$ case, different values of angle γ are considered, ranging between 0 and $360°$, with an incremental value of $5°$. This leads to 72 different values of γ for each normal vector to the triangle plane. Summarizing, the simulation scenario includes 9 different initial sizes of the formation, 10^4 different normal vectors to the triangle plane, 72 different rotation angles γ and one reference orbit, for a total amount of 9 x 10^4 x $72 = 6.48$ millions of different cases simulated.

After computing SF and DF performance for each different set of parameters, it is useful to look at aggregated results, to identify the best initial configurations. Figure 5.53 shows the results for $d = 1$ km. Each set of

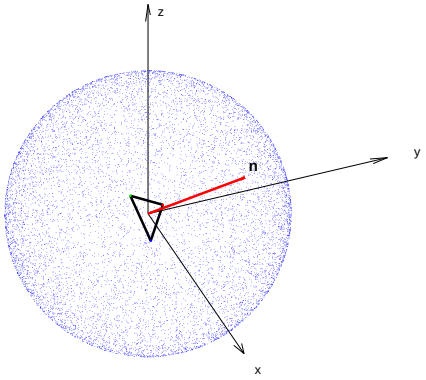

Figure 5.52: *Orientation of the formation, uniform spherical distribution to set up Monte Carlo simulation (10^4 points)*

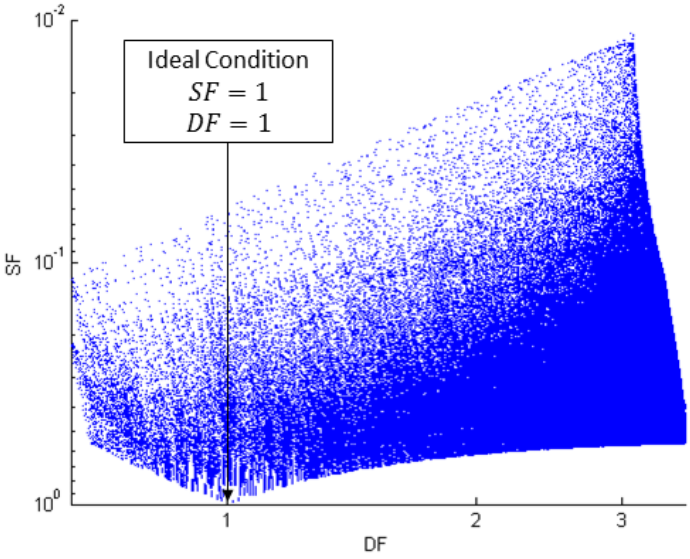

Figure 5.53: *Solutions for $d = 1$ km (72 x 10^4 points)*

initial conditions (72 x 10^4 different sets in this case) is represented by a point in the SF-DF plane. The coordinates of each point represent the value of SF and DF after integrating the equations of motion starting from that particular set of initial conditions, for one period of the reference orbit.

Concerning the initial size of the formation, no relevant effects are observed for the different d values explored. Aggregated results associated to

different d values looks very similar between them and when compared to Figure 5.53. The identification of the best case between different sets of results shows also very little dependence on the parameter d. It can be then concluded that, under the domain investigated in this work, the initial size of the formation has no relevant effect on the relative dynamics between spacecraft in the proximity of the chosen reference trajectory. This result agrees with the results of the analysis performed under the CR3BP formulation (Section 5.3.2). Formation keeping performance depends mainly on the initial orientation of the triangle plane $(\boldsymbol{n}, \gamma)$. The first step is to identify convenient solutions in terms of $\boldsymbol{n}$, that is the normal unity vector to the triangle surface.

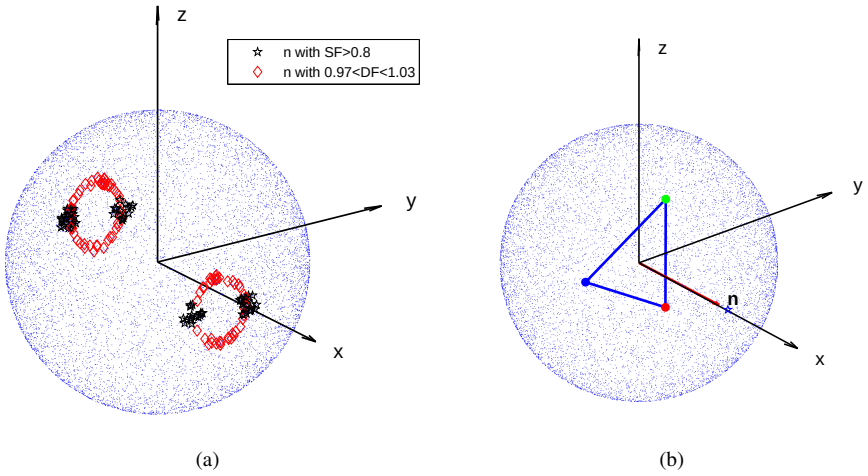

Figure 5.54: *(a) $\boldsymbol{n}$ ensuring highest performance (b) Best initial configuration*

Figure 5.54(a) shows regions on the overall distribution sphere where $\boldsymbol{n}$ (vector joining the origin with point on the sphere) leads to $SF < 0.8$ (black stars) or to a DF between 0.97 and 1.03 (red diamonds). The intersections between these regions correspond to the points in the neighborhood of the ideal point in Figure 5.53. Note that as far as the cases highlighted by Figure 5.54(a) are concerned, the triangle lies on the y, z plane or slightly inclined with respect to it. Figure 5.54(b) shows the overall best case, achieved when the $\boldsymbol{n}$ unity vector is directed towards the x axis, that is when the triangular formation lies initially on the y, z plane. For what concern the last parameter (γ), the results show that the best performance is always achieved when one of the spacecraft lies on the (positive or negative) y axis of the rotating frame. This initial configuration leads to values

of SF and DF after one period of

$$SF = 0.98$$
$$DF = 1.02$$

which is nearly equal to the ideal condition (5.39) of unchanged shape and size of the formation.

As mentioned in the previous paragraphs, performance is evaluated only at the end of the period, without considering the evolution of the formation along the reference orbit. It is interesting to look at the behaviour of the formation while it orbits near the reference path.

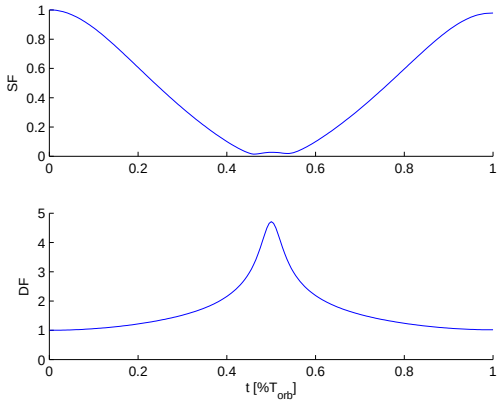

Figure 5.55: *SF (top) and DF (bottom) behaviour in time during one orbit, best initial configuration case*

Figure 5.55 shows the time behaviour of the two performance factors during a complete orbital period. Note that the two functions oscillates with the same period of the orbit, reaching the lowest performance nearly at half orbit. At that point, the triangle collapses nearly onto a line (Figure 5.56(a)), but finally it got back to almost its initial configuration (Figure 5.56(b)).

Global optimization approach

The optimization process is replied for the case of elliptic problem. The aim is to study whether any change occurs in the results of the optimization, under a different dynamical model. To this goal, only the best case coming out from the previous analysis is considered for comparison (orbits about L3).

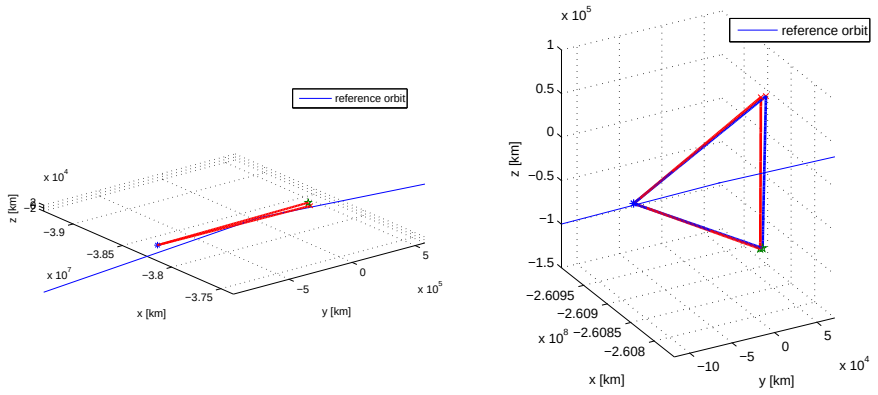

(a) (b)

Figure 5.56: *Triangular formation after (a) half period (b) one period: comparison between initial (red) and final (blue) formation*

The results confirm what was obtained so far. The two performance factors after one period reach the optimal condition

$$SF = 1.00$$
$$DF = 1.00$$

and the initial orientation is found to be lying in the y-z plane (Figure 5.57), in agreement with previously obtained results.

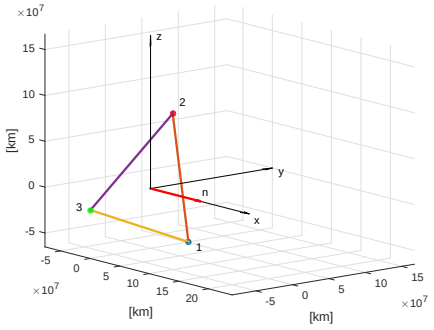

Figure 5.57: *Optimal initial configuration for the elliptical case*

Perturbed case: Solar Radiation Pressure

Finally, the found solution is propagated using a higher fidelity model of the dynamics, considering both the effect of the eccentricity of Earth's orbit around the Sun (ER3BP) and the effect due to SRP. This small perturbation is included into the dynamics of the three spacecraft, to model the effects on their orbital path. Values of mass and surface properties are selected in analogy with LISA, Cluster II and other formation flying missions cited in the introduction to this section, keeping the relevant parameters on the same order of magnitude. In particular, the analysis is set up with the followings values:

- $m = 200 \quad \text{kg}$
- $C_r = 0.2$
- $A = 2 \quad m^2$

with reference to notation in use in Section 2.4 and the acceleration is quantified using Eq. (2.83). With such assumptions, the resulting effect of the Solar Radiation Pressure is very low: the ratio between accelerations due to SRP and to the gravity of the Sun results to be on the order of

$$\beta = \frac{a_{\text{SRP}}}{a_{\text{grav}}} \sim 10^{-5} \tag{5.42}$$

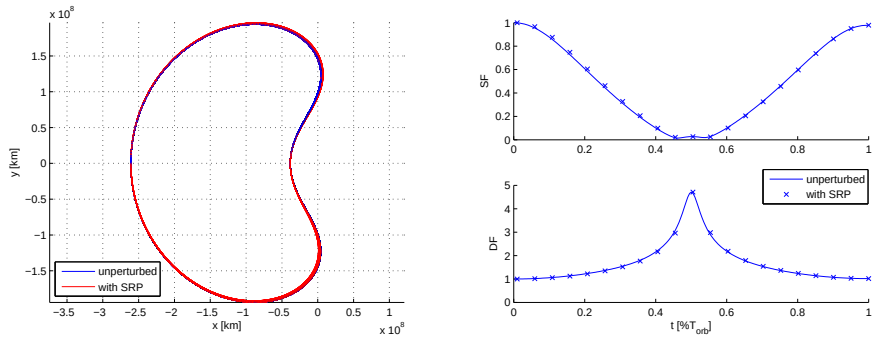

(a) (b)

Figure 5.58: *(a) Perturbed orbit (200 years) (b) SF (top) and DF (bottom) behaviour in time during one orbit with Solar Radiation Pressure Perturbation, best initial configuration case*

Figure 5.58(a) shows a simulation of orbital propagation, where the perturbed equations of motion are integrated for 200 T_{orb} (200 years) and compared to the unperturbed orbit. The chosen orbit appear to be very stable, as

the perturbed trajectory remains in the proximity of the unperturbed orbit. Finally the motion of the three spacecraft of the formation are integrated in time considering the perturbing effect. Figure 5.58(b) shows the effect of the perturbation, with respect to the unperturbed dynamics. As for the reference orbit, the effect on the spacecraft trajectories is very small and the formation keeping performance does not vary in a significant way.

5.3.5 Interpretation of results using manifold dynamics

It is useful to compare results obtained through Monte Carlo analysis and global optimization with considerations based on the dynamic nature of the system. Since the work considers periodic orbits, the problem can be studied by analyzing the eigenstructure of the monodromy matrix (STM after one orbital revolution, Section 2.1). The analysis through monodromy matrix inspection is performed for all reference orbits under study, both in the circular and elliptic case.

As detailed in the previous sections, the best initial configurations are associated to L3 reference orbits. Such orbits are stable, since they have a 6D centre manifold eigenstructure, with the monodromy matrix having 3 pair of complex conjugate eigenvalues. Since the spacecraft move in the centre manifold associate to the periodic orbit, the formation has a bounded motion near the reference trajectory, with no risk of departing from it. This is confirmed from results shown in Figure 5.53, where the DF does never reach very high values, as it does for the case of L1 or L2 orbits. In the L3 case, the orientation is only important to preserve the geometry of the formation, since the motion is bounded anyway. This is no longer true for L1 and L2 cases, where unstable orbits are to be considered. In that case, the eigenstructure of the monodromy matrix include a 2D (or 4D) stable/unstable manifold, and a 4D (or 2D) centre manifold. Being such a case, the eigendirections of the monodromy matrix play a major role not only for shape preservation, but also for assessing the possibility to have bounded motion in the proximity of the reference orbit. Figure 5.59 shows the directions of eigenvectors of the monodromy matrix, that is the direction tangent to the manifolds associated to the periodic orbit. Few cases are displayed, with one Halo and Lyapunov orbit chosen near L1 and L2. For all cases, the centre manifold is shown to be tangent to the orbit and directed as the y axis. Also, it belongs to the (y, z) plane. This is shown to be in agreement with results from Monte Carlo and global optimization analyses, where the best solution is found when the triangular formation initially lies on the (y, z) plane.

Overall, the relative orientation of the formation with respect to the eigendrections of the monodromy matrix associated to the reference orbit is of main importance in terms of formation keeping performance. This is confirmed by the fact that results shows that performance does not depend on the size of the initial equilateral triangle, but only by its orientation. This fact is shown to be always true for the cases under study and even more relevant for the case of unstable reference orbits.

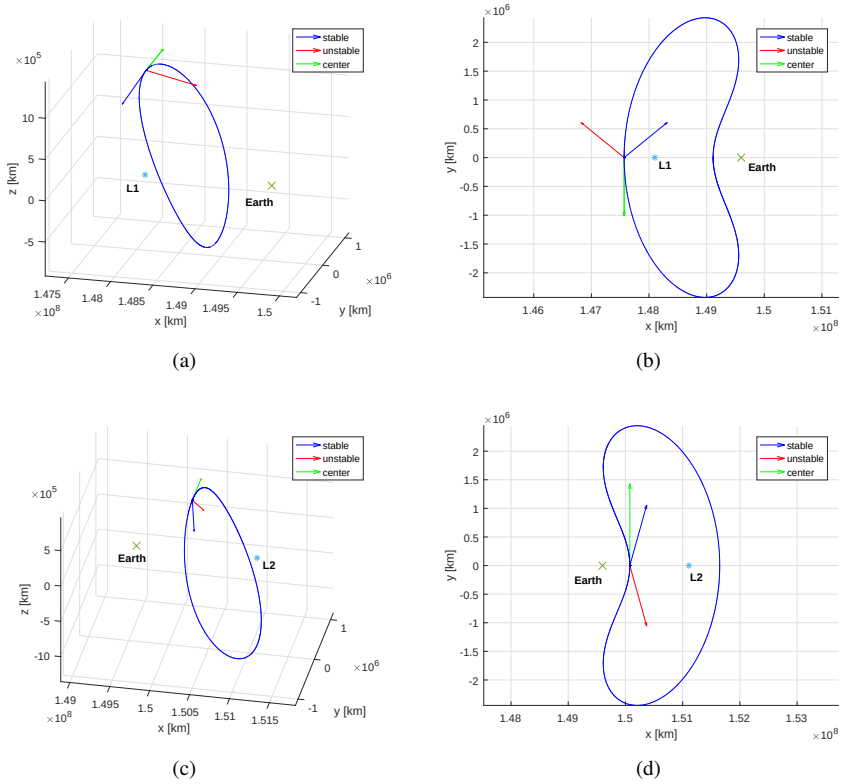

Figure 5.59: *Tangent to manifold directions at t_0 for (a) L1 Halo (b) L1 Lyapunov (c) L2 Halo (d) L2 Lyapunov*

CHAPTER 6

Conclusion

This thesis deals with non-Keplerian dynamics and their applications related to trajectory design of space missions. Different aspects of the problem were faced and investigated. This chapter summarizes the major findings and results of this work, by recalling the work done and its usefulness when related to mission analysis applications, highlighting the elements of innovations with respect to existing knowledge and previous works in the field. Possible directions and opportunities for future work are eventually discussed.

The first element of innovation that was introduced, relates to the general-purpose method presented in Section 3.1. As mentioned in Chapter 1, a lot of studies on motion under non-Keplerian and multi-body dynamics exist. However, the software in use in often tuned to the specific case under study and in most cases the same algorithms do not have general validity and are not applicable to other problems without implementing modifications on the code. Very few implementations of general purpose codes exist. The software architecture proposed here is intended to be a very astrodynamics-related tool, to support space mission analysis and design. The software provides ready-to-use libraries for the modeling of the most common systems for astrodynamics applications: restricted three-

body problems (CR3BP, ER3BP) and small body dynamics (shape-based, mascon models). The novelty of the implementation proposed here is the ability of joining all most popular available methods for periodic orbit computation into a harmonized and user-friendly software architecture. The goal was to enhance understanding of the applicability of the different techniques available, depending on the kind of dynamics and relevant parameters. Classical and recent techniques for non-linear system dynamics are used and integrated together to build new algorithms, in the attempt of creating more efficient schemes, that can be customized to the properties of the system. Also, the approach proposed for finding solutions around small bodies is innovative. As mentioned in Section 1, some studies on periodic motion around such irregular bodies exist, but still the topic is very new and unexplored. Existing studies investigate possible solutions directly by searching for peculiar configurations of the dynamics around small bodies. This method is useful to identify periodic motion or trajectories within a certain well-defined dynamical system, i.e. a given asteroid or comet. However, the results obtained can hardly be generalized to be valid to any other targeted celestial body. Conclusions drawn from a single investigation cannot be, in general, applied to other cases of celestial bodies with a different mass distribution. The approach proposed here is intended to be much more general and systematic: the properties of the attractor (which generates the dynamical environment) are slightly varying and periodic solutions are found as the primary changes its shape and mass distribution. The properties of periodic orbits are monitored and their dependency to the mass distribution of the primary is studied. In this way, it is possible to study in detail the effects that influences the existence and nature of periodic motion around such irregular bodies. The procedure can be followed for several typical shapes of common asteroids (diamond, dog-bone, elongated, ...), in order to create a database of what to expect from these particular dynamical environments in terms of periodic motion. The thesis objectives included the creation of a catalogue of periodic orbits for the most common systems relevant for space mission applications, and also, the definition of guidelines related to the applicability of the numerical methodologies to the different dynamical problems under study. The ultimate goal was to enhance the comprehension of the dynamics in a specific system, in order to foresee a priori what kind of periodic solutions can be expected to be found.

Concerning applications related to asteroid aggregation dynamics, a new implementation is presented to deal with N-body gravitational dynamics. Current capabilities of N-body integrators include the ability to simulate

the aggregation dynamics between hundreds of bodies of simple (spherical) shape. The proposed implementation is able to handle the simultaneous gravitational interaction between hundreds of bodies, including contact dynamics between bodies of complex (non spherical) shape. To test and validate the implementation, significant scenarios were analyzed in the framework of asteroid formation processes and different sets of initial conditions were investigated. The initial dynamical state of the N bodies is found to play a fundamental role in the evolution of the cloud of boulders. In detail, the state of the N bodies was initialized by either imposing no initial relative motion between them, or by imposing a given rotational and relative motion. The presented results show good agreement with theoretical predictions and observations, and suggest the ability of the numerical code to predict natural aggregation phenomena. The outcome of the aggregation process in used as a high-fidelity model of the asteroid's mass distribution. Such models are suitable to represent "rubble pile" asteroids and small celestial bodies with a significant amount of porosity. Space mission scenarios can be reproduced to compute trajectories and simulate the motion of a spacecraft under the complex gravity field of such highly irregular bodies.

Concerning mission analysis scenarios under study, the dynamical model of a binary asteroid is built with a patched three-body approach. Relative kinematics between asteroids was investigated for the case of binary systems and design parameters was identified for the specific relative configuration under study. The dynamical model appears to be particularly suitable to model certain classes of bodies, which are very common among asteroid population, such as elongated and dog-bone shaped asteroids, as well as contact or close binaries. To confine regions of applicability of the patched three-body problems, the concept of SOE is introduced and defined. The dynamical model was used to simulate possible mission scenarios aimed to the exploration of a NEA binary system. Landing trajectories are identified by means of manifolds interaction between patched three-body problems, resolved through Poincaré analysis on the SOE. The dynamical model defined in this work can serve as an easy and useful tool to identify trajectories in such complex dynamical systems. The patched three-body approach allows the exploitation of the peculiar dynamical properties of the CR3BP and cost-effective trajectories can be computed starting from periodic or quasi-periodic orbits and their invariant manifolds. The SOE, defined in this work, represents a tool to compare different vectorial fields: within the patched three-body approach, the SOE is exploited as a valuable alternative to the SOI, in case small and low-massive systems, such as asteroids, are

considered as sources of gravity field. When the assumptions on the distribution of mass in the binary system are valid, the physical system is well represented by the dual three-body model; hence it is possible to rely on its solution, avoiding the expensive computational effort required by higher fidelity models. The resulting trajectory can be used as a suitable first guess solution, to be differentially corrected towards a higher fidelity model for further mission analysis refinements.

The MASCOT-2 landing scenario, in the framework of AIM and AIDA missions, is presented. The strategy to design a ballistic trajectory to land a small and passive probe to the surface of Didymoon is discussed and suitable solutions to satisfy mission objectives are presented. Results show that the extremely low gravity environment does not guarantee the lander to stay on the surface after touch down, and MASCOT-2 will most likely bounce until reaching a stable position of Didymoon. Successful landing probability is assessed for the case study and landing dispersion is evaluated. Critical parameters affecting the success of the landing manoeuvre are identified and solutions to mitigate the risk are proposed by convenient exploitation of the three-body environment. Compared to solutions found using classical Keplerian models, three-body dynamics are found to be much more effective to increase the success rate of the landing manoeuvre, to lower the risk of rebounding on the surface of the secondary, and to increase the safety of the overall release manoeuvre to be performed by AIM. More in detail, the modeling of the gravity field near the binary asteroid through the use of non-Keplerian dynamics is shown to be crucial to the effective landing design, since no solutions compliant with requirements can be found using the simpler Keplerian model. Non-Keplerian dynamics is also needed to accurately simulate the behaviour of the lander after release, since the simpler central field is unacceptably inaccurate for the AIM/MASCOT-2 landing scenario.

The free dynamics of an equilateral triangular formation of spacecraft under the CR3BP and ER3BP formulations are studied. The relative dynamics between spacecraft of the formation were investigated by considering several initial configurations sets, in terms of orientation, size and location of the formation with respect to the three-body synodic frame. To quantify and compare formation keeping performance, two performance factors were defined to monitor both shape and size changes of the triangular formation in time. Suitable initial configurations of the formation, leading to good natural formation keeping performance, were identified thanks to combined Monte Carlo and global optimization methods. More in detail, the results of the study highlight that within the domain of study, perfor-

mance is not dependent on the size of the triangle, while it strongly depends on the initial orientation and on the reference orbit the formation is orbiting about. This result is further supported by considerations on the manifold structure associated to the reference orbit and confirmed by Monodromy matrix analysis performed on the periodic orbits considered. As far as the present study is concerned, the best performance is achieved for formations orbiting about L3, and in particular when the triangle lies on the y, z plane of the synodic reference frame, with one spacecraft on the x, y plane. It is important to remark that only free dynamics is considered, meaning that the formation comes back to nearly its initial configuration without any control action, but only through a convenient exploitation of three-body dynamics. When designing such kind of missions, to lower formation keeping needs to be provided to the three spacecraft, the initial orientation and reference orbit of the formation must be chosen carefully.

Future work

As a general consideration, the work presented in this thesis can be extended and generalized to include more mission scenarios and trajectory design solutions. Concerning the software architecture presented here, it can be enriched by means of more efficient schemes and algorithms to be implemented. As mentioned, applications of this scheme can be used to produce comprehensive catalogues of solutions related to known small celestial bodies. This would help the mission analysis process and trajectory design, since it would provide *a priori* ideas and hints on how motion within such chaotic dynamics can be. To support this, the catalogue of periodic solutions can be coupled with a further enriched catalogue of asteroid models, related both to homogeneous shape-based models, or to N-body mascon models, which can be generated for different classes of asteroids by using the N-body aggregation scheme presented in this thesis. As far as the N-body aggregation model is concerned, future work includes the need of considering a larger number of bodies in the simulation. The cost of evaluating gravity is N^2, but it can be reduced to $N \log(N)$ by clustering the interaction effect between far clusters of bodies. Such clustering can be pursued by means of partitioning the domain using octrees, and GPU-based parallelization of gravitational and contact forces computation. This would increase the capability of the implementation to handle a higher number of bodies, extending the possibility to simulate different dynamical scenarios, including impact and disruption ones.

Postface

This thesis is a comprehensive work based on the work carried out during the Ph.D. period. The work on Asteroid Impact Mission has been performed by the author under ESA contract with Politecnico di Milano, during the phase A and B1 of AIM mission design. Part of the work and results discussed in this thesis has been published as journal papers or presented at conferences. A list of major publications is here provided.

- F Ferrari, M Lavagna, and K C Howell. Dynamical model of binary asteroid systems through patched three-body problems. *Celestial Mechanics and Dynamical Astronomy*, 125(4):413–433, 2016

- F Ferrari, A Tasora, P Masarati, and M Lavagna. N-body gravitational and contact dynamics for asteroid aggregation. *Multibody System Dynamics*, 39(1):3–20, 2017

- F Ferrari and M Lavagna. Suitable configurations for triangular formation flying about collinear libration points under the circular and elliptic restricted three-body problems. *Acta Astronautica*, 2016

- F Ferrari, M Lavagna, and K C Howell. Trajectory design about binary asteroids through coupled three-body problems. In *Spaceflight Mechanics 2014, Roby S. Wilson et al. (Eds.)*, pages 2093–2110, Santa Fe, NM, USA, 2014

- F Ferrari and M Lavagna. Formation flying and relative dynamics under the circular restricted three-body problem formulation. In *Spaceflight*

Mechanics 2014, Roby S. Wilson et al. (Eds.), pages 185–204, Santa Fe, NM, USA, 2014

- F Ferrari and M Lavagna. Asteroid impact monitoring mission: Mission analysis and innovative strategies for close proximity maneuvering. In *Proceedings of the 4th IAA Planetary Defense Conference*, Frascati, Italy, 2015

- F Ferrari and M Lavagna. Triangular formation flying under the elliptic restricted three-body formulation. In *Proceedings of 65th International Astronautical Congress*, Toronto, CA, 2014

- F Ferrari and M Lavagna. Design drivers for formation flying near collinear libration points in the circular and elliptic restricted three-body problems. In *Proceedings of the 8th International Workshop on Satellite Constellations and Formation Flying*, 2015

- F Ferrari and M Lavagna. Asteroid impact mission: A possible approach to design effective close proximity operations to release mascot-2 lander. In *Proceedings of AIAA/AAS Astrodynamics Specialist Conference*, Vail, CO, USA, 2015

- F Ferrari and M Lavagna. Consolidated phase a design of asteroid impact mission: Mascot-2 landing on binary asteroid didymos. In *Proceedings of the 26th AAS/AIAA Space Flight Mechanics Meeting*, Napa, CA, USA, 2016

- F Ferrari, M Lavagna, and I Carnelli. Coupling high fidelity body modeling with non-keplerian dynamics to design aim-mascot-2 landing trajectories on didymos binary asteroid. In *Proceedings of the 6th International Conference on Astrodynamics Tools and Techniques*, Darmstadt, DE, 2016

List of Acronyms

3BP	Three-Body Problem
AIDA	Asteroid Impact and Deflection Assessment
AIM	Asteroid Impact Mission
ARM	Asteroid Redirect Mission
BSB	Binary System Barycentre
C::E	Chrono::Engine
CNSA	China National Space Administration
CR3BP	Circular Restricted Three-Body Problem
DART	Double Asteroid Redirection Test
DF	Dimension Factor
ER3BP	Elliptic Restricted Three-Body Problem
ESA	European Space Agency
IOD	In-Orbit-Demonstration
ISAS	Institute of Space and Astronautical Science
ISEE-3	International Sun/Earth Explorer 3

JAXA	Japan Aerospace eXploration Agency
JPL	Jet Propulsion Laboratory
LFR	low frequency radar
LISA	Laser Interferometer Space Antenna
MASCOT	Mobile Asteroid Surface SCOuT
MEX	Moonlet Engineering eXperiment
MMS	Magnetospheric Multiscale Mission
NASA	National Aeronautics and Space Administration
NBP	N-Body Problem
NEA	Near Earth Asteroid
NEAR-Shoemaker	Near Earth Asteroid Rendezvous
P1-E2	polyhedron-ellipsoid
PAB	Primary Asteroid Barycentre
R3BP	Restricted Three-Body Problem
S1-E2	sphere-ellipsoid
S1-S2	sphere-sphere
SF	Shape Factor
SOE	Surface Of Equivalence
SOI	Sphere Of Influence
SRP	Solar Radiation Pressure
STM	State Transition Matrix
ToF	time of flight
ZRAV loci	zero relative acceleration and velocity
ZVC	Zero Velocity Curves

Bibliography

[1] S J Aarseth. Nbody2: A direct n-body integration code. *New Astronomy*, 6:277–291, 2001.

[2] R L Anderson and M W Lo. A dynamical systems analysis of resonant flybys: Ballistic case. *Journal of the Astronautical Sciences*, 58(2):167–194, 2011.

[3] M Bando and A Ichikawa. Periodic orbits and formation flying near the libration points.

[4] B T Barden and Howell K C. Formation flying in the vicinity of libration point orbits. *AAS 98-169*, 1998.

[5] R R Bate, D D Mueller, and J E White. *Fundamentals of Astrodynamics*. Dover, New York, 1971.

[6] J Bellerose and D J Scheeres. General dynamics in the restricted full three body problem. *Acta Astronautica*, 62:563–576, 2008.

[7] M J S Belton, C R Chapman, P C Thomas, M E Davies, R Greenberg, K P Klaasen, D Byrnes, L D'Amario, S Synnott, T V Johnson, A McEwen, W J Merline, D R Davis, J M Petit, A Storrs, J Veverka, and B Zellner. Bulk density of asteroid 243 ida from the orbit of its satellite dactyl. *Nature*, 374(6525):785–788, 1995.

[8] M J S Belton, C R Chapman, J Veverka, K P Klaasen, A Harch, R Greeley, R Greenberg, J W Head III, A McEwen, D Morrison, P C Thomas, M E Davies, M H Carr, G Neukum, F P Fanale, D R Davis, C Anger, P J Gierasch, A P Ingersoll, and C B Pilcher. First images of asteroid 243 ida. *Science*, 265:1543–1547, 1994.

[9] L A M Benner, R S Hudson, S J Ostro, K D Rosema, J D Giorgini, D K Yeomans, R F Jurgens, D L Mitchell, R Winkler, R Rose, M A Slade, and L M Thomas. Radar observations of asteroid 2063 bacchus. *Icarus*, 139:309–327, 1999.

[10] J Biele and S Ulamec. Capabilities of philae, the rosetta lander. *Space Science Review*, 138:275–289, 2008.

[11] J J C M Bik, P N A M Visser, and O Jenrich. Stabilization of the triangular lisa satellite formation.

[12] W F Bottke Jr., A Cellino, P Paolicchi, and R P Binzel, editors. *Asteroids III*. University of Arizona Press, 2002.

[13] J V Breakwell and J V Brown. The 'halo' family of 3-dimensional periodic orbits in the earth-moon restricted three-body problem. *Celestial Mechanics*, 7(6):389–404, 1969.

[14] J R Brophy, L Friedman, N J Strange, T A Prince, D Landau, T Jones, R Schweickart, C Lewicki, M Elvis, and D Manzella. Synergies of robotic asteroid redirection technologies and human space exploration. In *Procedings of the 65th International Astronautical Congress, Toronto, Canada*, 2014.

[15] R Broucke. Stability of periodic orbits in the elliptic, restricted three-body problem. *AIAA Journal*, 7(6):1003–1009, 1969.

[16] R C Calleja, E J Doedel, A R Humphries, A Lemus-Rodríguez, and E B Oldeman. Boundary-value problem formulations for computing invariant manifolds and connecting orbits in the circular restricted three-body problem. *Celestial Mechanics and Dynamical Astronomy*, 114:77–106, 2012.

[17] S Campagnola, M Lo, and P Newton. Subregions of motion and elliptic halo orbits in the elliptic restricted three-body problem. In *Proceedings of 18th AAS/AIAA Space Flight Mechanics Meeting*, Galveston, TX, USA, 2008.

[18] J E Chambers. A hybrid symplectic integrator that permits close encounters between massive bodies. *Monthly Notices of the Royal Astronomical Society*, 304:793–799, 1999.

[19] C R Chapman. Asteroid collisions, craters, regolith and lifetimes. *In Asteroids: An Exploration Assessment. NASA Conf. Publ.*, 2053:145–160, 1978.

[20] A Cheng, A Stickle, J Atchison, O Barnouin, A Rivkin, P Michel, S Ulamec, and AIDA Team. Asteroid impact and deflection assessment mission: Double asteroid redirection test (dart). In *Proceedings of the 4th IAA Planetary Defense Conference*, Frascati, Italy, 2015.

[21] A F Cheng, P Michel, C Reed, A Galvez, and I Carnelli. Dart: Double asteroid redirection test. In *Proceedings of the European Planetary Science Congress*, Madrid, Spain, 2012.

[22] A F Cheng, P Michel, C Reed, A Galvez, and I Carnelli. Aida: Asteroid impact & deflection assessment. In *Proceedings of the IAA Planetary Defense Conference*, Flagstaff, AZ, USA, 2013.

[23] A.F Cheng, J Atchison, B Kantsiper, A.S Rivkin, A Stickle, C Reed, A Galvez, I Carnelli, P Michel, and S Ulamec. Asteroid impact and deflection assessment mission. *Acta Astronautica*, 115:262–269, 2015.

[24] V A Chobotov. *Orbital Mechanics*. AIAA Education Series, 1991.

[25] A Colagrossi, F Ferrari, M Lavagna, and K C Howell. Dynamical evolution about asteroids with high fidelity gravity field and perturbations modeling. In *Proceedings of the AIAA/AAS Astrodynamics Specialist Conference*, Napa, CA, USA, 2015.

[26] D P Cruikshank, C M Dalle Ore, T R Geballe, T L Rouch, T C Owen, M Cash, C de Bergh, and Hartmann W K. Trojan asteroid 624 hektor: Constraints on surface composition. *Bull. Am. Astron. Soc.*, 32, 2000.

[27] D J Dichmann, E J Doedel, and R C Paffenroth. The computation of periodic solutions of the 3-body problem using the numerical continuation software auto. In *Proceedings of the International Conference on Libration Point Orbits and Applications*, Aiguablava, ES, 2002.

[28] E Doedel, H B Keller, and J P Kernevez. Numerical analysis and control of bifurcation problems. *International Journal of Bifurcation and Chaos*, 1(3):493–520, 1991.

[29] E Doedel, R C Paffenroth, H B Keller, D J Dichmann, J Galán-Vioque, and A Vanderbauwhede. Computation of periodic solutions of conservative systems with application to the 3-body problem. *International Journal of Bifurcation and Chaos*, 13(6):1353–1381, 2003.

[30] E N Dorband, M Hemsendorf, and D Merritt. Systolic and hyper-systolic algorithms for the gravitational n-body problem, with an application to brownian motion. *Journal of Computational Physics*, 185:484–511, 2003.

[31] J Dow, S Matussi, R Mugellesi Dow, M Schmidt, and M Warhaut. The implementation of the cluster ii constellation. *Acta Astronautica*, 54:657–669, 2004.

[32] M J Duncan, H F Levison, and M H Lee. A multiple time step symplectic algorithm for integrating close encounters. *Astronomical Journal*, 116:2067–2077, 1998.

[33] H Edelsbrunner and E P Mücke. Three-dimensional alpha shapes. *Transactions on Graphics*, 13(1):43–72, 1994.

[34] R W Farquhar. *The Control and Use of Libration-Point Satellites*. PhD thesis, Stanford University, Department of Aeronautics and Astronautics, Stanford, CA, USA, 1968.

[35] R W Farquhar. The flight of isee-3/ice: Origins, mission history, and a legacy. *Journal of the Astronautical Sciences*, 49, 1998.

[36] R W Farquhar and A A Kamel. Quasi-periodic orbits about the translunar libration point. *Celestial Mechanics*, 7:458–473, 1973.

[37] F Ferrari and M Lavagna. Formation flying and relative dynamics under the circular restricted three-body problem formulation. In *Spaceflight Mechanics 2014, Roby S. Wilson et al. (Eds.)*, pages 185–204, Santa Fe, NM, USA, 2014.

[38] F Ferrari and M Lavagna. Triangular formation flying under the elliptic restricted three-body formulation. In *Proceedings of 65th International Astronautical Congress*, Toronto, CA, 2014.

[39] F Ferrari and M Lavagna. Asteroid impact mission: A possible approach to design effective close proximity operations to release mascot-2 lander. In *Proceedings of AIAA/AAS Astrodynamics Specialist Conference*, Vail, CO, USA, 2015.

[40] F Ferrari and M Lavagna. Asteroid impact monitoring mission: Mission analysis and innovative strategies for close proximity maneuvering. In *Proceedings of the 4th IAA Planetary Defense Conference*, Frascati, Italy, 2015.

[41] F Ferrari and M Lavagna. Design drivers for formation flying near collinear libration points in the circular and elliptic restricted three-body problems. In *Proceedings of the 8th International Workshop on Satellite Constellations and Formation Flying*, 2015.

[42] F Ferrari and M Lavagna. Consolidated phase a design of asteroid impact mission: Mascot-2 landing on binary asteroid didymos. In *Proceedings of the 26th AAS/AIAA Space Flight Mechanics Meeting*, Napa, CA, USA, 2016.

[43] F Ferrari and M Lavagna. Suitable configurations for triangular formation flying about collinear libration points under the circular and elliptic restricted three-body problems. *Acta Astronautica*, 2016.

[44] F Ferrari, M Lavagna, and I Carnelli. Coupling high fidelity body modeling with non-keplerian dynamics to design aim-mascot-2 landing trajectories on didymos binary asteroid. In *Proceedings of the 6th International Conference on Astrodynamics Tools and Techniques*, Darmstadt, DE, 2016.

[45] F Ferrari, M Lavagna, I Carnelli, B Burmann, I Gerth, and M Scheper. Esa's asteroid impact mission: Mission analysis ans payload operations state of the art. In *Proceedings of the 6th International Conference on Astrodynamics Tools and Techniques*, 2016.

[46] F Ferrari, M Lavagna, I Gerth, B Burmann, M Scheper, and I Carnelli. The asteroid impact mission: Consolidated mission analysis and scientific payload operations at binary asteroid didymos. In *Proceedings of the 25th International Symposium of Space Flight Dynamics (ISSFD)*, 2015.

[47] F Ferrari, M Lavagna, and K C Howell. Trajectory design about binary asteroids through coupled three-body problems. In *Spaceflight Mechanics 2014, Roby S. Wilson et al. (Eds.)*, pages 2093–2110, Santa Fe, NM, USA, 2014.

[48] F Ferrari, M Lavagna, and K C Howell. Dynamical model of binary asteroid systems through patched three-body problems. *Celestial Mechanics and Dynamical Astronomy*, 125(4):413–433, 2016.

[49] F Ferrari, M Lavagna, M Scheper, B Burmann, and I Carnelli. The european asteroid impact mission: Phase a design and mission analysis. In *Proceedings of AIAA/AAS Astrodynamics Specialist Conference*, Vail, CO, USA, 2015.

[50] F Ferrari, A Tasora, P Masarati, and M Lavagna. Numerical simulation of n-body asteroid aggregation. In *Multibody Dynamics, Josep M. Font-Llagunes (Ed.)*, pages 936–947, Barcelona, ES, 2015.

[51] F Ferrari, A Tasora, P Masarati, and M Lavagna. N-body gravitational and contact dynamics for asteroid aggregation. *Multibody System Dynamics*, 39(1):3–20, 2017.

[52] D C Folta, N Bosanac, D Guzzetti, and K C Howell. An earth-moon system trajectory design reference catalog. *Acta Astronautica*, 110:341–353, 2015.

[53] F Gabern, W S Koon, and J E Marsden. Parking a spacecraft near an asteroid pair. *Journal of Guidance, Control and Dynamics*, 29(3), 2006.

[54] A Galvez, I Carnelli, M Fontaine, and C Corral Van Damme. Asteroid impact mission (aim) & deflection assessment: an opportunity to understand impact dynamics and modelling. In *Proceedings of the European Planetary Science Congress*, Madrid, Spain, 2012.

[55] A Galvez, I Carnelli, M Khan, W Martens, P Michel, S Ulamec, and A Hriscu. Asteroid investigation mission: the european contribution to the aida eu-us cooperation. In *Proceedings of the 24th International Symposium on Space Flight Dynamics*, Laurel, MD, USA, 2014.

[56] M. M. Gates, S Stich, M McDonald, B Muirhead, D Mazanek, P Abell, and P Lopez. The asteroid redirect mission and sustainable human exploration. In *Procedings of the 65th International Astronautical Congress, Toronto, Canada*, 2014.

[57] T Gehrels, editor. *Asteroids*. University of Arizona Press, 1979.

[58] P. Geissler, J. Petit, D. D. Durda, R. Greenberg, W. Bottke, M. Nolan, and J. Moore. Erosion and ejecta reaccretion on 243 ida and its moon. *Icarus*, 120(1):140 – 157, 1996.

[59] G Gómez, W S Koon, M W Lo, J E Marsden, J Masdemont, and S D Ross. Connecting orbits and invariant manifolds in the spatial restricted three-body problem. *Nonlinearity*, 17:1571–1606, 2004.

[60] G Gómez, M Marcote, J J Masdemont, and J M Mondelo. Natural configurations and controlled motions suitable for formation flying. *AAS 05-347*, 2005.

[61] C L Goudas. Three-dimensional periodic orbits and their stability. *Icarus*, (2):1–18, 1963.

[62] K Gozdziewski and A J Maciejewski. Unrestricted planar problem of a symmetric body and a point mass. triangular libration points and their stability. *Celestial Mechanics and Dynamical Astronomy*, (75):251–285, 1999.

[63] P Gurfil and N J Kasdin. Practical geocentric orbits in the sun-earth spatial elliptic restricted three-body problem. In *Proceedings of AIAA/AAS Astrodynamics Specialist Conference*, Monterey, CA, USA, 2002.

[64] P Gurfil and D Meltzer. Stationkeeping on unstable orbits: Generalization to the elliptic restricted three-body problem. *The Journal of the Astronautical Sciences*, 54(1), 2006.

[65] J J Guzmán and A Edery. Mission design for the mms tetrahedron formation. *IEEEAC*.

[66] D Guzzetti, N Bosanac, D C Folta, and K C Howell. A framework for efficient trajectory comparisons in the earth-moon design space. In *Proceedings of AIAA/AAS Astrodynamics Specialist Conference*, San Diego, CA, USA, 2014.

[67] J. K. Hale and H. Kocac. *Dynamics and Bifurcations*, volume 3. Springer-Verlag New York, 1 edition, 1991.

[68] M Hénon. Numerical exploration of the restricted three-body problem. In *The Theory of Orbits in the Solar System and in Stellar Systems*, Thessaloniki, GR, 1964.

[69] A Herique and W Kofman. Definition of the consert / rosetta radar performances. In *Proceedings of the CEOS SAR Workshop*, Tokyo, Japan, 2001.

[70] A Héritier and K C Howell. Regions near the libration points suitable to maintain multiple spacecraft. 2012.

[71] J L Hilton. *Asteroid Masses and Densities*, pages 103–112. University of Arizona Press, 2002.

[72] K C Howell. Three-dimensional periodic 'halo' orbits. *Celestial Mechanics*, 32:53–71, 1984.

[73] K C Howell. Families of orbits in the vicinity of the collinear libration points. *The Journal of the Astronautical Sciences*, 49:107–125, 2001.

[74] K C Howell and J V Breakwell. Almost rectilinear halo orbits. *Celestial Mechanics*, 32:29–52, 1984.

[75] K C Howell and E Campbell. Three-dimensional periodic solutions that bifurcate from halo families in the circular restricted three-body problem. In *Proceedings of AAS/AIAA Space Flight Mechanics Meeting*, Breckenridge, CO, USA, 1999.

[76] R. Johnston. Johnston's archive web pages at johnstonsarchive.net, 2016.

[77] NASA JPL. Ephemerides web pages at ssd.jpl.nasa.gov/?ephemerides, 2016.

[78] NASA JPL. Jpl small-body database web pages at ssd.jpl.nasa.gov, 2016.

[79] G Katsiaris. The three-dimensional elliptic problem. *Recent Advances in Dynamical Astronomy*, 39:118–134, 1973.

[80] W M Kaula. *Theory of Satellite Geodesy*. Blaisdell, Waltham MA, 1966.

[81] H B Keller. Constructive methods for bifurcation and nonlinear eigenvalue problems. *Computing Methods in Applied Sciences and Engineering*, 704:241–251, 1977.

[82] W S Koon, M W Lo, J E Marsden, and S D Ross. *Dynamical Systems, the Three Body Problem and Space Mission Design*. World Scientific, 2006.

[83] M Kueppers, I Carnelli, A Galvez, K Mellab, P Michel, and AIM Team. The asteroid impact mission (aim). In *Proceedings of the European Planetary Science Congress*, Nantes, France, 2015.

[84] K C Laurini and M M Gates. Nasa's space exploration planning: the asteroid mission and the step-wise path to mars. In *Procedings of the 65th International Astronautical Congress, Toronto, Canada*, 2014.

[85] M W Lo. Halo orbit generation using the center manifold. In *Proceedings of the AAS/AIAA Space Flight Mechanics Meeting*, Huntsville, AL, USA, 1997.

[86] G Macris, G A Katsiaris, and C L Goudas. Doubly-symmetric motions in the elliptic problem. *Astrophysics and Space Science*, 33:333–340, 1975.

[87] B Mahajan. *Libration point orbits near small bodies in the elliptic restricted three-body problem*. PhD thesis, Missouri University of Science and Technology, Department of Mechanical and Aerospace Engineering, Rolla, MO, USA, 2013.

[88] J L Margot, M C Nolan, L A M Benner, S J Ostro, R F Jurgens, J D Giorgini, M A Slade, and D B Campbell. Binary asteroids in the near-earth object population. *Science*, 296:1445–1448, 2002.

[89] M S Matthews, R P Binzel, and T Gehrels, editors. *Asteroids II*. University of Arizona Press, 1989.

[90] H Mazhar, T Heyn, A Pazouki, D Melanz, A Seidl, A Barthlomew, A Tasora, and D Negrut. Chrono: A parallel multi-physics library for rigid-body, flexible-body and fluid dynamics. *Mechanical Sciences*, 2013.

[91] W J Merline, S J Weidenschilling, D D Durda, J L Margot, P Pravec, and A D Storrs. *Asteroids Do Have Satellites*, pages 289–312. University of Arizona Press, 2002.

[92] P Michel, A Cheng, A Galvez, C Reed, I Carnelli, P Abell, S Ulamec, A Rivkin, J Biele, and N Murdoch. Aida: Asteroid impact and deflection assessment. *Highlights of Astronomy*, 2009.

[93] P Michel, F E DeMeo, and W F Bottke Jr., editors. *Asteroids IV*. University of Arizona Press, 2015.

[94] P Michel, P Tanga, W Benz, and D C Richardson. Formation of asteroid families by catastrophic disruption: Simulations with fragmentation and gravitational reaccumulation. *Icarus*, 160:10–23, 2002.

[95] D L Mitchell, S J Ostro, K D Rosema, R S Hudson, D B Campbell, J F Chandler, and I I Shapiro. Radar observation of asteroids 7 iris, 9 metis, 12 victoria, 216 kleopatra, and 654 zelinda. *Icarus*, 118:105–131, 1995.

[96] A Morbidelli. Modern integrations of solar system dynamics. *Annual Reviews of Earth and Planetary Sciences*, 30, 2002.

[97] F R Moulton. *Periodic Orbits*. Carnegie Institution of Washington, 1920.

[98] P M Muller and W L Sjogren. Mascons: Lunar mass concentrations. *Science*, 161(3842):680–684, 1968.

[99] M Ollé and J R Pacha. The 3d elliptic restricted three-body problem: periodic orbits which bifurcate from limiting restricted problems. *Astronomy and Astrophysics*, 351:1149–1164, 1999.

[100] S J Ostro, J F Chandler, A A Hine, K D Rosema, I I Shapiro, and D K Yeomans. Radar images of asteroid 1989 pb. *Science*, 248:1523–1528, 1990.

[101] S J Ostro, R S Hudson, M C Nolan, J Margot, D J Scheeres, D B Campbell, C Magri, J D Giorgini, and D K Yeomans. Radar observations of asteroid 216 kleopatra. *Science*, 288:836–839, 2000.

[102] S J Ostro, R S Hudson, K D Rosema, J D Giorgini, R F Jurgens, D K Yeomans, P W Chodas, R Winkler, R Rose, D Choate, R A Cormier, D Kelley, R Littlefair, L A M Benner, L M Thomas, and M A Slade. Asteroid 4179 toutatis: 1996 radar observations. *Icarus*, 137:122–139, 1999.

[103] S J Ostro, K D Rosema, R S Hudson, R F Jurgens, J D Giorgini, R Winkler, D K Yeomans, D Choate, R Rose, M A Slade, S D Howard, and D L Mitchell. Extreme elongation of asteroid 1620 geographos from radar images. *Nature*, 375:474–477, 1995.

[104] J F Palacián, P Yanguas, S Fernández, and M A Nicotra. Searching for periodic orbits of the spatial elliptic restricted three-body problem by double averaging. *Physica D*, 213:15–24, 2006.

[105] J S Parker and R L Anderson. *Low-Energy Lunar Trajectory Design*. JPL Deep Space Communications and Navigation Series, 2013.

[106] H Peng and S Xu. Stability of two groups of multi-revolution elliptic halo orbits in the elliptic restricted three-body problem. *Celestial Mechanics and Dynamical Astronomy*, 123:279–303, 2015.

[107] H J Pernicka. *The Numerical Determination of Nominal Libration Point Trajectories and Development of a Station-Keeping Strategy*. PhD thesis, Purdue University, School of Aeronautics and Astronautics, West Lafayette, IN, USA, 1990.

[108] H Poincaré. *Les Méthodes Nouvelles de la Mécanique Céleste*. 1899.

[109] P Pravec, P Scheirich, P Kušnirák, L Šarounová, S Mottola, G Hahn, P Brown, G Esquerdo, N Kaiser, Z Krzeminski, D P Pray, B D Warner, A W Harris, M C Nolan, E S Howel, L A M Benner, J L Margot, A Galád, W Holliday, M D Hicks, Y N Krugly, D Tholen, R Whiteley, F Marchis, D R DeGraff, A Grauer, S Larson, F P Velichko, W R Cooney Jr, R Stephens, J Zhu, K Kirsch, R Dyvig, L Snyder, V Reddy, S Moore, Š Gajdoš, J Világi, G Masi, D Higgins, G Funkhouser, B Knight, S Slivan, R Behrend, M Grenon, G Burki, R Roy, C Demeautis, D Matter, N Waelchli, Y Revaz, A Klotz, M Rieugné, P Thierry, V Cotrez, L Brunetto, and G Kober. Photometric survey of binary near-earth asteroids. *Icarus*, 181:63–93, 2006.

[110] C D Pruett, J W Rudmin, and J M Lacy. An adaptive n-body algorithm of optimal order. *Journal of Computational Physics*, 187:298–317, 2003.

[111] D C Richardson, Z M Leinhardt, H J Melosh, W F Bottke Jr., and E Asphaug. *Gravitational Aggregates: Evidence and Evolution*, pages 501–515. University of Arizona Press, 2002.

[112] D C Richardson, P Michel, K J Walsh, and K W Flynn. Numerical simulations of asteroids modelled as gravitational aggregates. *Planetary and Space Science*, 57:183–192, 2009.

[113] D C Richardson, T Quinn, J Stadel, and G Lake. Direct large-scale n-body simulations of planetesimal dynamics. *Icarus*, 143:45–59, 2000.

[114] D L Richardson. Analytic construction of periodic orbits about the collinear points. *Celestial Mechanics*, 22:241–253, 1980.

[115] A E Roy. *Orbital Motion*. Adam Hilger, Bristol, 1988.

[116] A E Roy and M W Ovenden. On the occurrence of commensurable mean motions in the solar system. ii the mirror theorem. *Monthly Notices of the Royal Astronomical Society*, 115:296–309, 1955.

[117] E Sarris. Families of symmetric-periodic orbits in the elliptic three-dimensional restricted three-body problem. *Astrophysics and Space Science*, 162:107–122, 1989.

[118] H Schaub and J L Junkins. *Analytical Mechanics of Aerospace Systems*. American Institute Of Aeronautics & Astronautics, 2002.

[119] D J Scheeres. Dynamics about uniformly rotating triaxial ellipsoids: Applications to asteroids. *Icarus*, 110:225–238, 1994.

[120] D J Scheeres. Stability of relative equilibria in the full two-body problem. *Ann. N.Y. Acad. Sci.*, 1017:81–94, 2004.

[121] D. J. Scheeres. *Orbital Motion in Strongly Perturbed Environments*. Praxis Publishing, Springer, 2012.

[122] D J Scheeres and J Bellerose. The restricted hill full 4-body problem: Application to spacecraft motion about binary asteroids. *Dynamical Systems: An International Journal*, 20(1):23–44, 2005.

[123] D J Scheeres, S J Ostro, R S Hudson, E M DeJong, and S Suzuki. Dynamics of orbits close to asteroid 4179 toutatis. *Icarus*, 132:53–79, 1998.

[124] P Scheirich and P Pravec. Modeling of lightcurves of binary asteroids. *Icarus*, 200:531–547, 2009.

[125] H Sierks, C Barbieri, P L Lamy, R Rodrigo, D Koschny, H Rickman, H U Keller, J Agarwal, M F A'Hearn, F Angrilli, A-T Auger, M A Barucci, J-L Bertaux, I Bertini, S Besse, D Bodewits, C Capanna, G Cremonese, V Da Deppo, B Davidsson, S Debei, M De Cecco, F Ferri, S Fornasier, M Fulle, R Gaskell, L Giacomini, O Groussin, P Gutierrez-Marques, P J Gutiérrez, C Güttler, N Hoekzema, S F Hviid, W-H Ip, L Jorda, J Knollenberg, G Kovacs, J R Kramm, E Kührt, M Küppers, F La Forgia, L M Lara, M Lazzarin, C Leyrat, J J Lopez Moreno, S Magrin, S Marchi, F Marzari, M Massironi, H Michalik, R Moissl, S Mottola, G Naletto, N Oklay, M Pajola, M Pertile, F Preusker, L Sabau, F Scholten, C Snodgrass, N Thomas, C Tubiana, J-B Vincent, K-P Wenzel, M Zaccariotto, and M Pätzold. On the nucleus structure and activity of comet 67p/churyumov-gerasimenko. *Science*, 347(6220), 2015.

[126] J Stadel. *Cosmological N-body simulations and their analysis*. PhD thesis, University of Washington, Seattle, WA, USA, 2001.

[127] A M Stickle, J A Atchison, O S Barnouin, A F Cheng, C M Ernst, Z Fletcher, D C Richardson, and A S Rivkin. Modeling momentum transfer from the dart spacecraft impact into the moon of didymos. In *Proceedings of the 4th IAA Planetary Defense Conference*, Frascati, Italy, 2015.

[128] V Szebehely. *Theory of Orbits: The Restricted Problem of Three Bodies*. Academic Press, New York and London, 1967.

[129] S Tardivel, C Lange, S Ulamec, and J Biele. The deployment of mascot-2 to didymoon. In *Proceedings of the 26th AAS/AIAA Space Flight Mechanics Meeting*, Napa, CA, USA, 2016.

[130] A Tasora, D Negrut, R Serban, H Mazhar, T Heyn, A Pazouki, and D Melanz. Chrono::engine web pages at projectchrono.org, 2006.

[131] M G G T Taylor, C Alexander, N Altobelli, M Fulle, M Fulchignoni, E Grün, and P Weissman. Rosetta begins its comet tale. *Science*, 347(6220):387–387, 2015.

[132] A Tsuchiyama, M Uesugi, T Matsushima, T Michikami, T Kadono, T Nakamura, K Uesugi, T Nakano, R Sandford, S A nad Noguchi, T Matsumoto, J Matsuno, T Nagano, Y Imai, A Takeuchi, Y Suzuki, T Ogami, J Katagiri, M Ebihara, T R Ireland, F Kitajima, K Nagao, H Naraoka, T Noguchi, R Okazaki, H Yurimoto, M E Zolensky, T Mukai, M Abe, T Yada, A Fujimura, M Yoshikawa, and J Kawaguchi. Three-dimensional structure of hayabusa samples: Origin and evolution of itokawa regolith. *Science*, 333(6046):1125–1128, 2011.

[133] K Uesugi. Results of the muses-a "hiten" mission. *Advances in Space Research*, 18(11):1169–1172, 1996.

[134] S Ulamec, J Biele, P-W Bousquet, P Gaudon, K Geurts, T-M Ho, C Krause, C Lange, R Willnecker, L Witte, Philae, and MASCOT teams. Landing on small bodies: From the rosetta lander to mascot and beyond. *Acta Astronautica*, 93:460–466, 2014.

[135] M Vaquero and K C Howell. Leveraging resonant-orbit manifolds to design transfers between libration-point orbits. *Journal of Guidance, Control, and Dynamics*, 37(4):1143–1157, 2014.

[136] J Veverka, B Farquhar, M. Robinson, P Thomas, S Murchie, A Harch, P G Antreasian, S R Chesley, J K Miller, W M Owen Jr, B G Williams, D Yeomans, D Dunham, G Heyler, M Holdridge, R L Nelson, K E Whittenburg, J C Ray, B Carcich, A Cheng, C Chapman, J F Bell III, M Bell, B Bussey, B Clark, D Domingue, M J Gaffey, E Hawkins, N Izenberg, J Joseph, R Kirk, P Lucey, M Malin, L McFadden, W J Merline, C Peterson, L Prockter, J Warren, and D Wellnitz. The landing of the near-shoemaker spacecraft on asteroid 433 eros. *Nature*, 413:390–393, 2001.

[137] R A Werner and D J Scheeres. Exterior gravitation of a polyhedron derived and compared with harmonic and mascon gravitation representations of asteroid 4769 castalia. *Celestial Mechanics and Dynamical Astronomy*, 65:313–344, 1997.

[138] J Wisdom and M Holman. Symplectic maps for the n-body problem. *Astronomical Journal*, 102:1528–1538, 1991.

[139] M T Zuber, D E Smith, A F Cheng, J B Garvin, O Aharonson, T D Cole, P J Dunn, Y Guo, F G Lemoine, G A Neumann, D D Rowlands, and M H Torrence. The shape of 433 eros from the near-shoemaker laser rangefinder. *Science*, 289:2097–2101, 2000.